Mechanisms and Products of the Breakdown of Contaminant Element-Bearing Jarosites

Adrian Michael Lloyd Smith

A thesis presented for the degree of Doctor of Philosophy

Birkbeck College
University of London

2004

Abstract

Jarosite [$KFe_3(SO_4)_2(OH)_6$] is a mineral commonly found in acidic, sulphate rich environments that forms by the oxidation of sulphides such as pyrite. Jarosite has considerable environmental importance because of its ability to scavenge toxic elements (*e.g.* Pb(II), As(V)), and is thus of great interest to geochemists, geologists and metallurgists. This project aims to determine the mechanisms and products of jarosite breakdown and the related magnitude of potentially hazardous toxic element release. Until now, these have not been known, but they are critical in understanding and modelling such systems.

Potassium jarosite, plumbojarosite, and beudantite were dissolved in pH free-drift dissolution batch experiments in both acidic (pH 2) and alkaline (pH 8) solutions. The acidic and alkali dissolution of potassium jarosite, plumbojarosite, and beudantite can all be described by incongruent dissolution kinetics, due to non-ideal dissolution of the parent solids and in some cases, the precipitation of a secondary phase(s). α-FeOOH and $Fe(OH)_3$ are secondary precipitates in the alkali dissolutions, and $PbSO_4$ forms in both acidic and alkali dissolutions. Pb(II) and As(V) remain in solution in the acidic dissolutions, and, in the alkali dissolutions, Pb(II) is incorporated into the precipitate $PbSO_4$ whilst As(V) is partially absorbed to $Fe(OH)_3$.

Classical atomistic simulations were also made of the jarosite structure. The (012) surface, which has been identified experimentally as the most stable, was found to have two zero net dipole shifts. In contrast to what is found in natural jarosites, structural modelling showed that it is more energetically favourable for Cd(II), Zn(II), and Cu(II) to occupy the A-site rather than the B-site. Due to the degree of iron vacancies present in natural samples, these divalent cations will occupy a distorted B-site to reduce the overall lattice energy. The resulting site distortion, however, may lead to points of weakness during any subsequent breakdown.

Table of Contents

List of Figures

List of Tables

Acknowledgements

This work is dedicated to my family, because without all their patience, support, and blind faith I do not think I could have started this project and without them, I certainly would not have been able to finish it!

1   Introduction

Jarosite [KFe$_3$(SO$_4$)$_2$(OH)$_6$] originates and takes its name from a mine in Barranco Jarosa, Sierra Almagrera, Almeira Province, Andalusia, Spain, and was first described by Breithaupt (1852). It is a common mineral in acidic, sulphate-rich environments formed by the oxidation of sulphides such as pyrite (Baron and Palmer 1996b). Such environments include weathered sulphide ore deposits (Bladh 1982), acid soils formed from sulphide bearing sediments (Van Breeman 1973), acid-hypersaline lake deposits (Alpers et al. 1992, Long et al. 1992), as well as acid mine and rock drainage (Chapman et al. 1983, Alpers et al. 1989). Jarosite-type minerals have also been reported to occur in hydrothermal environments (Keith et al. 1979, Stoffregen and Rye 1992). Precipitation of jarosite is of extreme importance to metallurgists because of its ability to scavenge unwanted elements (*e.g.* Fe, Pb, Cu, Zn, As) from hydrometallurgical ore processing solutions (Dutrizac 1984).

Jarosite, *sensu stricto*, is a mineral with the general formula KFe$_3$(SO$_4$)$_2$(OH)$_6$, but it is also associated with an isostructrual mineral subgroup that has a general formula of AB$_3$(TO$_4$)$_2$(OH)$_6$. Throughout this thesis the term 'jarosite', will refer to this isostructural mineral subgroup, and the term 'potassium jarosite' will represent the mineral form of KFe$_3$(SO$_4$)$_2$(OH)$_6$.

1.1   Importance and stability of the jarosite subgroup of minerals

The jarosite subgroup contains nine minerals with the general formula AB$_3$(TO$_4$)$_2$(OH)$_6$. Of these minerals, the majority are extremely rich in toxic elements such as Pb(II) (plumbojarosite Pb$_{0.5}$Fe$_3$(SO$_4$)$_2$(OH)$_6$) or Tl$^+$ (dorallcharite TlFe$_3$(SO$_4$)$_2$(OH)$_6$), and are commonly found as secondary phases produced by the oxidation of mining residues (Dutrizac and Jambor 2000). Mining activities usually involve ore or coal deposits that have accumulations of such elements as Ag, As, Au, Cd, Co, Cu, Hg, Mo, Ni, Pb, Se, Sb, Tl, and Zn in either economic or sub-economic quantities. These elements occur as mineral sulphides or in gangue minerals (Bigham and Nordstrom 2000). When acid drainage waters are produced by oxidation of mining residues, these elements may be mobilised and transported offsite at concentrations that are sufficiently elevated to be of environmental concern. In such

cases, the precipitation of Fe-rich hydroxylsulphates (jarosites) and oxyhydroxides (goethite, ferrihydrite, and schwertmannite) may attenuate the problem by scavenging associated toxic elements through processes of coprecipiatation (jarosites) and adsorption (oxyhydroxides).   The ability of jarosites to coprecipitate wt. % concentrations of toxic elements from solution should not be underestimated, considering most adsorption mechanisms involving oxyhydroxide substrates remove concentrations of these elements only in the realms of 10s to 1000s ppm (Bigham and Nordstrom 2000).   Although cleansing of mine drainage waters can be achieved by the precipitation of jarosites, mine drainage sediments (Figure 1.1) have a potential to cause contamination through changing pH, temperature and redox conditions.   Their long-term stability in downstream environments is therefore of concern.

Figure 1.1.   Photographs of iron ochre on riverbanks of the River Almond, West Lothian, formed through the impact of acid rock/mine drainage (ARD/AMD).   Jarosite-type minerals are a major constituent of iron ochre.

The essential requirements for the formation and stability of jarosites are a ferric rich, acidic (pH < 3), oxic environment.   These minerals, however, will readily decompose upon removal from their stability region, through subtle changes in pH and/or temperature (Stoffregen and Rye 1992).   Potassium jarosite does not display classical equilibrium relationships with aluminosilicates.   Instead, the principle reaction that limits the stability of potassium jarosite in nature is simply its conversion to iron oxide or oxyhydroxide minerals (Stoffregen et al. 2000).   In ambient conditions, the

conversion of potassium jarosite to goethite is thought to occur through the following reaction:

$$KFe_3(SO_4)_2(OH)_{6(s)} \leftrightarrow 3FeO(OH)_{(Goethite)} + K^+_{(aq)} + 2SO_4^{2-}_{(aq)} + 3H^+_{(aq)} \quad (1.1)$$

although this reaction may be complicated by the formation of metastable phases such as schwertmannite [$Fe_8O_8(OH)_{8-x}(SO_4)_x$] and ferrihydrite [~$Fe_5HO_8 \cdot 4H_2O$] (Nordstrom and Alpers 1999). It should be noted that no proof has yet been found that this(ese) reaction(s) actually occurs.

Considering the narrow range of conditions within which jarosites are stable and with the concentrations of toxic elements (*e.g.* Pb(II), As(V), Cu(II), Zn(II)) potentially present within them, their breakdown and the subsequent element release maybe very detrimental to the natural environment. Cu, Zn, and both Pb and As have WHO drinking water limits set at 2000, 3000, and 10 μg/L, respectively (WHO). Pb and As are considered to be highly toxic elements and primarily affect the central nervous system. In particular, Pb attacks neuromuscular connections and As induces chronic integument (skin) effects along with destroying bone marrow (ILO 1983). Cu and Zn are less toxic than Pb and As, seen by the higher concentration thresholds for drinking water, but in excess quantities, both of these elements can attack the central nervous system (ILO 1983). Concentrations of these elements in benthic algae and invertebrates living in acid mine drainage-contaminated sites are usually highly elevated. Accumulation of these toxic elements in aquatic organisms is ultimately fatal (DeNicola and Stapleton 2001, Gerhardt et al. 2003).

The instability of jarosites could be assessed in the laboratory through series of dissolution experiments, which could gauge the breakdown mechanisms of the jarosite structure and, more importantly, assess the potential release of toxic elements. As natural jarosites contain various mixed quantities of toxic elements, synthetic analogues are typically used in dissolution studies, as it is crucial to establish the exact composition of the starting materials before any interpretations can be made.

1.2 Objectives

The mechanisms and products of jarosite breakdown, and the amount of potentially hazardous toxic elements released as a result of this breakdown, are still relatively unknown, but are critical in understanding and modelling geo-chemical reactions in natural environments.

Therefore, the objectives of this project are to:

(1) monitor the rate of release of toxic elements (Pb, As, Cu, Zn) from synthetic jarosites using dissolution batch experiments;

(2) characterise the new phases formed as a result of these dissolution experiments using a number of different surface- and whole-mineralogical techniques; and

(3) model how toxic elements maybe incorporated within and released from the jarosite structure.

1.3 Outline of the thesis

The methods used to answer the questions above and the results produced are presented and discussed in this thesis. The remainder of this introductory chapter (Chapter 1) presents published literature regarding the structure, occurrences in nature, synthesis of analogues and thermodynamic data on the jarosite subgroup of minerals. A section also deals with the theory and practical applications of dissolution studies. Chapter 2 presents the experimental methods and materials for the synthesis and characterisation of the jarosite analogues' including the initial starting conditions and subsequent aqueous and remaining solid analysis of the acid and alkali dissolution experiments. Chapter 3 covers the characterisation of the synthetic jarosites. Chapters 4 and 5 focus on the acid and alkali dissolutions of the synthetic jarosites, respectively. Chapter 6 is dedicated to computational modelling, where the surface properties and intrinsic and extrinsic defects of the potassium jarosite structure are investigated. A general discussion of all the results and implications is given in Chapter 7. Finally, the conclusions of the study and suggestions for future work are presented in Chapter 8. Appendix A describes the theory of the physical and chemical analytical techniques used in this study.

Appendix B contains additional X-ray diffraction data on the synthetic jarosites. Appendix C contains all the raw aqueous data for both the acid and alkali dissolutions.

1.4 Structure of the jarosite subgroup of minerals

Jarosites are members of the alunite supergroup, which consists of more than 40 minerals with the general formula $AB_3(TO_4)_2(OH)_6$, wherein A represents cation sites with a coordination number greater than or equal to 9, and B and T represent cation sites with octahedral (O) and tetrahedral (T) coordination, respectively (Jambor 1999, Hawthorne et al. 2000). The supergroup is commonly divided into various subgroups, though the primary subdivision is based on the B site cations. In most of the minerals in the supergroup, the B site is filled by Fe(III) or Al(III). The minerals are grouped depending upon whether Fe(III) exceeds or is subordinate to Al(III). Minerals with Fe(III) > Al(III) belong to the jarosite subgroup (termed 'jarosite' in this thesis), and those with Al(III) > Fe(III) are allocated to the alunite subgroup (Table 1.1) (Dutrizac and Jambor 2000).

Table 1.1. A selection of minerals from the alunite supergroup (Dutrizac and Jambor 2000).

Alunite subgroup (Al^{3+}>Fe^{3+})		Jarosite subgroup (Fe^{3+}>Al^{3+})	
alunite	$KAl_3(SO_4)_2(OH)_6$	jarosite	$KFe_3(SO_4)_2(OH)_6$
natrojarosite	$NaAl_3(SO_4)_2(OH)_6$	natrojarosite	$NaFe_3(SO_4)_2(OH)_6$
ammonioalunite	$(NH_4)Al_3(SO_4)_2(OH)_6$	ammoniojarosite	$(NH_4)Fe_3(SO_4)_2(OH)_6$
schlossmacherite	$(H_3O,Ca)Al_3(SO_4)_2(OH)_6$	hydronium jarosite	$(H_3O)Fe_3(SO_4)_2(OH)_6$
-		argentojarosite	$AgFe_3(SO_4)_2(OH)_6$
-		dorallcharite	$TlFe_3(SO_4)_2(OH)_6$
osarizawite	$Pb(Al,Cu)_3(SO_4)_2(OH)_6$	beaverite	$Pb(Fe,Cu)_3(SO_4)_2(OH)_6$
-		plumbojarosite	$Pb_{0.5}Fe_3(SO_4)_2(OH)_6$
hidalogite	$PbAl_3(SO_4)(AsO_4)(OH)_6$	beudantite	$PbFe_3(SO_4)(AsO_4)(OH)_6$

In jarosites, the B site cation is Fe(III). The A site is occupied by a cation in 12-fold coordination, most commonly K^+, Na^+ or H_3O^+ (hydronium), and the T site usually contains a sulphate unit (SO_4^{2-}), though in some cases AsO_4^{3-} can partially occupy this site (e.g. beudantite) (Kubisz 1964, Brophy and Sheridan 1965).

The mineral structures of jarosite subgroup are based on tetrahedral-octahedral-tetrahedral (T-O-T) sheets. Octahedra occur at the vertices of a 6^3 plane net, which form six-membered rings with the octahedra linked by sharing corners.
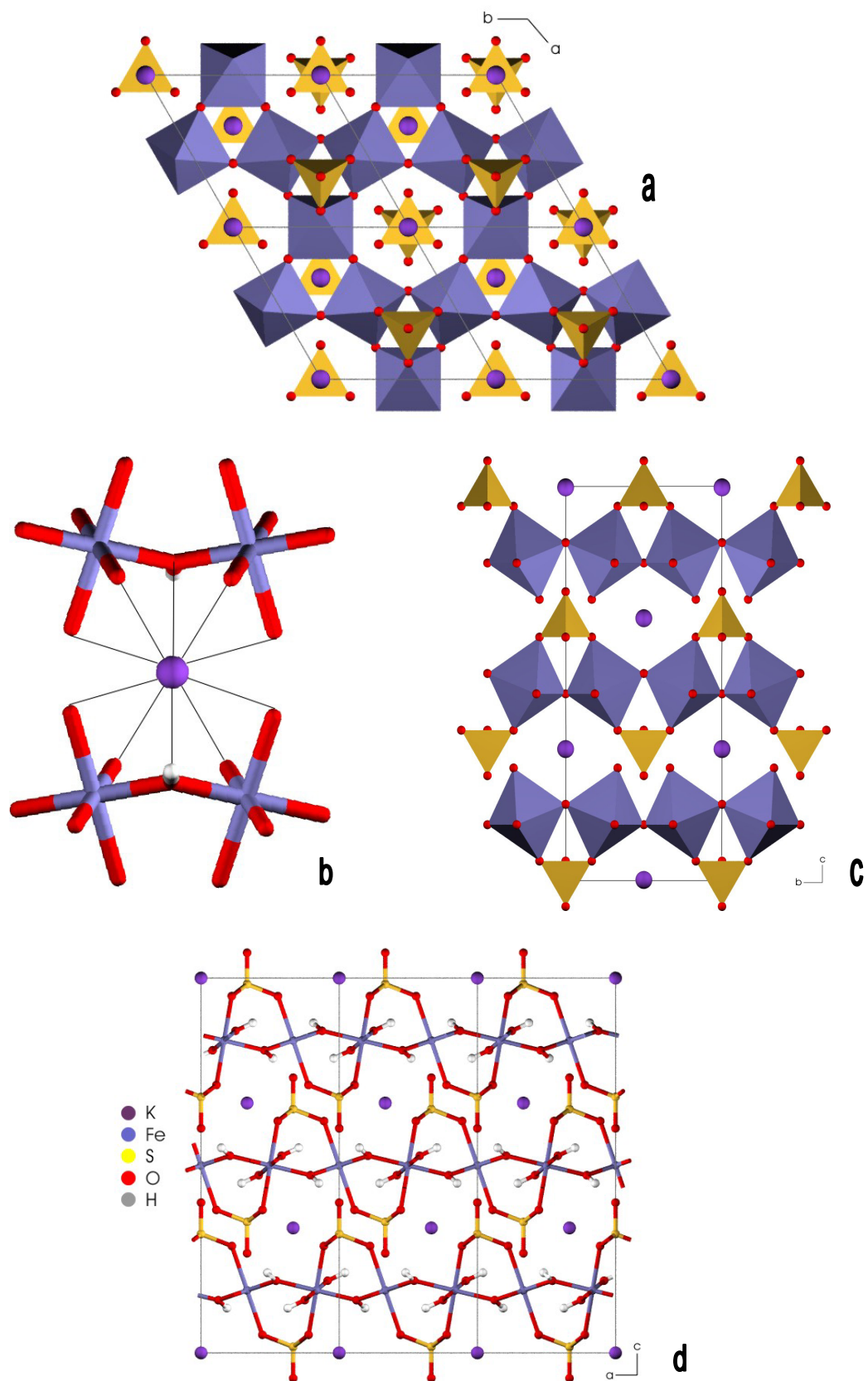
Figure 1.2. (a) c-axis projection illustrating the articulation of the co-ordination polyhedra in the jarosite structure. (b) A K(O,OH)$_{12}$ polyhedron with four surrounding octahedra. (c) and (d) Structure of potassium jarosite, showing the T-O-T layers.

At the junction of the three six-membered rings is a three-membered ring, and one set of apical vertices of those three octahedra linked to a tetrahedron (Figure 1.1). The resultant sheets are held together by interstitial cations and hydrogen bonds (Jambor 1999). Hendricks (1937) first described the crystal structure of potassium jarosite and Wang et al. (1965) confirmed his structural model. The jarosite subgroup belong to the trigonal crystal system in the rhombohedral class with hexagonal axes (a = b ≠ c and $\alpha = \beta = 90^o$, $\gamma = 120^o$), and have a space group of $R\bar{3}m$ (No. 166). Extensive substitution by other ions within the jarosite crystal structure has been reported (Dutrizac and Kaiman 1976).

1.4.1 Structural defects within both natural and synthetic jarosites

A common substitution that is often seen, significantly in some cases, in both natural and synthetic jarosites, is that of hydronium (H_3O^+) partially replacing the A-site cation. Brophy and Sheridan (1965), Kubisz (1970), and Dutrizac and Kaiman (1976) proposed hydronium substitution as an explanation for the presence of excessive amounts of structural water. Ripmeester et al. (1986) demonstrated, with the use of NMR techniques on deuterated samples, that hydronium could be present within the jarosite structure. The degree of hydronium present within any jarosite is calculated indirectly. For synthetic potassium jarosite, the process is relatively straightforward: the potassium concentration is determined and the molar abundance of hydronium is subsequently calculated for the A-site. This is typically expressed as $[H_3O^+_{1-x} K_x]$. For natural jarosites, the procedure for calculating the hydronium concentration is similar, although there are more species parameters that must be considered. In this case, K, Na and hydronium all occupy A-sites up to the molar unit of one, i.e. $[H_3O^+_{1-x} A_x$ where A = Na, K].

Another well-documented structural anomaly present within both synthetic and natural jarosites is Fe(III) vacancies. The degree of Fe deficiency within the structure is typically represented through the Fe:SO_4 molar ratio, where the ideal stoichiometry is 3:2 (Kubisz 1970, Alpers et al. 1989). Typically, the Fe:SO_4 molar ratio is significantly lower than the ideal, with values as low as 2.33:2 (Ripmeester et al. 1986) and 2.20:2 to 2.57:2 (Härtig et al. 1984) reported. Kubisz (1970) was the first to observe that increasing Fe(III) vacancies were accompanied by increased incorporation of water into the jarosite structure, which he termed 'additional water'.

Other authors (Härtig et al. 1984, Ripmeester et al. 1986, Alpers et al. 1989) called this water incorporation 'excess water'. The purpose of this 'additional water' is to charge balance the structure by incorporating additional protons, leading to partial conversion of (OH)$^-$ to H$_2$O. It was not until the NMR work of Ripmeester et al. (1986) on deuterated jarosites, that the hypothesis of Kubisz (1970) on 'additional water' and its role in the structure could be verified.

Considering that both natural and synthetic jarosites have hydronium substitutions and Fe deficiencies, the general formula of AB$_3$(TO$_4$)$_2$(OH)$_6$ is not strictly representative. To appreciate the structural implications of these defects, Kubisz (1970) wisely modified the 'classic' general formula to H$_3$O$_{1-x}$ A$_x$ B$_{3-y}$ [(OH)$_{6-3y}$ (H$_2$O)$_{3y}$ (TO$_4$)$_2$], where A can either be K or Na.

1.5   Occurrences of jarosites in the natural environment

Jarosites are common in nature, and they occur in diverse environments, primarily including: (1) the oxidised parts of sulphide ore deposits or barren pyritiferous rocks; (2) areas of acid sulphate soils; and (3) in clays. Jarosites are also extremely common in wastes produced from the metallurgical extractive industry (Dutrizac and Jambor 2000).

1.5.1 Oxidised sulphide deposits and pyritiferous rocks

Potassium jarosite is formed indirectly from the initial oxidation of a sulphide mineral. In an acid mine/rock drainage environment (AMD/ARD) (Figure 1.1), for example, the sulphide is frequently pyrite (Hudson-Edwards et al. 1999).

$$FeS_{2(s)} + 8H_2O \leftrightarrow Fe^{2+}_{(aq)} + 2SO^{2-}_{4(aq)} + 16H^+_{(aq)} + 14e^- \qquad (1.2)$$

$$4FeS_{2(s)} + 14O_2 + 4H_2O \leftrightarrow 4Fe^{2+}_{(aq)} + 8H^+_{(aq)} + 8SO^{2-}_{4(aq)} \qquad (1.3)$$

$$FeS_{2(s)} + 14Fe^{3+}_{(aq)} + 8H_2O \leftrightarrow 15Fe^{2+}_{(aq)} + 2SO^{2-}_{4(aq)} + 16H^+_{(aq)} \qquad (1.4)$$

Followed by

$$3Fe^{3+}_{(aq)} + K^+_{(aq)} + 2SO^{2-}_{4(aq)} + 6H_2O \rightarrow KFe_3(SO_4)_2OH_{6(s)} + 6H^+_{(aq)} \qquad (1.5)$$
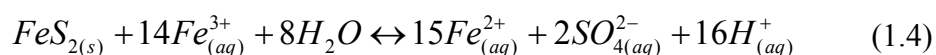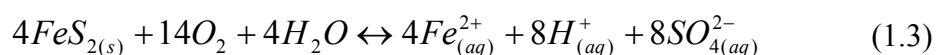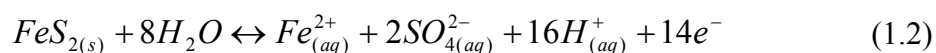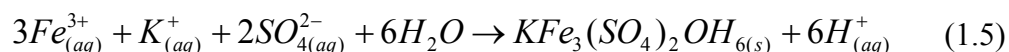
The sulphide undergoes a series of oxidation reactions (Eqs. 1.2-1.4) to yield Fe(II). In the natural environment, however, the Fe(II) rapidly oxidises to Fe(III). The

presence of Fe(III) and pyrite initiates a chain reaction, forming further Fe(II), which in turn oxidises to Fe(III). These reactions catalyse the breakdown of pyrite. Potassium jarosite is eventually formed when Fe(III) and free K in solution rapidly coprecipitate (Eq. 1.5) (Bigham et al. 1996).

Argentojarosite [$AgFe_3(SO_4)_2(OH)_6$] was first observed (Schempp 1925) as a secondary product from the weathering of sulphide-rich ore veins at the Tintic Standard mine, Dividend, Utah. Endmember argentojarosite is rare, likely because of the scarcity of Ag-rich pyritiferous ores, and because Ag commonly precipitates as metallic silver or as a halide mineral (Dutrizac and Jambor 2000). The most extensive mining of silver-bearing jarosite, and certainly the oldest documented instance of such jarosite exploitation, was in the vast pre-Roman workings at Rio Tinto, Spain (Dutrizac and Jambor 1987).

Plumbojarosite [$Pb_{0.5}Fe_3(SO_4)_2(OH)_6$] was first described in 1902 from the occurrence at Cook's Peak, New Mexico (Dutrizac and Jambor 2000). Extensive substitution of alkali ions by lead has been reported for the jarosite subgroup of minerals from several localities (Roca et al. 1999). The iron, lead, and sulphate of the jarosite minerals are probably derived from the oxidation of sulphide minerals, whereas the alkali cations likely come from the acidic dissolution of gangue minerals (Roca et al. 1999). The low mobility of lead in sulphate media is due to the low solubility of lead sulphate; consequently, there is a tendency for plumbojarosite to form in areas rich in lead minerals like galena that have undergone a degree of acidic weathering (Vasilevskaya 1970). Simons and Mapes (1956) stated that plumbojarosite is commonly the last mineral to form during the oxidation of galena.

Beaverite [$Pb(Fe,Cu)_3(SO_4)_2(OH)_6$] is similar to plumbojarosite in that it forms in close proximity to Fe-Pb-Cu sulphide ore bodies. Beaverite was first discovered at the Horn Silver mine, Utah, coexisting with plumbojarosite (Butler 1913). In some of the copper mines in Cornwall, UK, Kingsbury (1952) reported that beaverite occurred as partial pseudomorphs of galena. Kingsbury and Hartley (1957) observed that beaverite from the Lake District, Cumbria, UK, was an alteration product of beudantite [$PbFe_3(SO_4)(AsO_4)(OH)_6$]; eventually beaverite broke down to plumbojarosite.

Alkali-jarosites, like potassium jarosite or natrojarosite [NaFe$_3$(SO$_4$)$_2$(OH)$_6$] commonly occur in oxidised sections of sulphide ore deposits as coatings on, or pseudomorphs of, iron sulphide minerals (Dutrizac and Jambor 2000). Alkali sulphate salts (*e.g.* K$_2$SO$_4$, Na$_2$SO$_4$) are extremely mobile in aqueous environments so it is unsurprising that alkali jarosites can be found considerable distances from the original oxidising ore body. The alkali ions may originate from distally sourced ground water, or from local aluminosilicates that are susceptible to partial dissolution by low pH solutions developed from the original oxidising sulphide body (Jambor et al. 2000).

1.5.2 Acid sulphate soils

Probably the most widespread occurrence of jarosites is in acid soils. Throughout the world, there are extensive regions of acid (pH 3-4) soils that have developed from marine bedrock sediments containing pyrite (Banfield and Nealson 1997). These acidic soils present serious problems for agriculture. Iron oxidising bacteria (mainly *Thiobacillus ferroxidans*) in soils have been shown to play an important role in mineral weathering, and to produce some of the precursor reactants for jarosite formation (Ivarson 1973, Ivarson 1976, Banfield and Welch 2000). The sources of the alkali ions required for jarosite precipitation probably come from local silicate sources, such as potassium- or sodium-rich micas (Jambor 1998).

Potassium jarosite and natrojarosite-bearing soils are extremely widespread and occurrences have been described in Canada (Dudas 1984, 1987, Mermut and Arshad 1987), Germany (Schwertmann 1961), Japan (Hyashi 1994), and Scandinavia (Oeborn and Berggren 1995). Potassium jarosite is probably a constituent of many ochre rich soils, especially those formed from marine sediments containing small amounts of pyrite (Dutrizac and Jambor 2000).

1.5.3 Clays

Jarosites are regularly in clay seams and thick clay beds (Dutrizac and Jambor 2000). It is generally assumed that the iron and sulphate in jarosite originate from the oxidation of pyrite, during which acid leaching of the clay minerals occurs, providing the alkali metals (Warshaw 1956). Alternatively, jarosites can precipitate directly from small isolated 'ponded' solutions during layer silicate formation (Alpers et al.

1992, Long et al. 1992), or from solutions transported into the clay unit from distal sources (Khlybov 1976).

1.5.4 Jarosite and the metallurgical industry

A jarosite precipitation process was developed for the zinc industry to meet the need for an economical means of removing high concentrations of iron, commonly between 5 to 12 wt. % present in Zn-sulphide (sphalerite) ore bodies (Dutrizac 1982). Despite its widespread application in the zinc industry, the jarosite process is not without its problems. Chief among these is the disposal of the jarosite residues, which have little potential use. A zinc refining plant producing 150,000 tonnes of metallic zinc from a concentrate containing 50 wt. % Zn and 12 wt. % Fe will generate about 125,000 tonnes of jarosite containing only 25-36 wt.% Fe (Dutrizac 1982). These wastes are commonly stored in dedicated containment facilities, such as ponds lined with impermeable clay membranes (Dutrizac and Jambor 2000). Other disposal methods have ranged from storage in sole-purpose caverns excavated in mountains to deepwater, oceanic discharge (Berg and Borve 1996).

1.6   Dissolution studies

One method of assessing whether a crystalline phase will tend to dissolve or precipitate is by determining its solubility. To evaluate the solubility of toxic-element bearing jarosites it is first important to define some parameters, equations and relationships. In order to correctly describe equilibrium compositions of natural and experimental water systems (aqueous, gaseous, solid phases) it is initially important that we utilise ion activities rather than concentrations. The advantage of activities is that they take into account the effects of interactions between species (such as intermolecular interactions in reactions of real gases and interatomic forces in electrolyte solutions) (Atkins 1992). The activity of a species i is defined as (Stumm and Morgan 1996):

$$\{i\} = \left(\frac{m_i}{m^o} \right) \gamma_i$$

(1.6)

where m_i is the molal concentration; m^o is the standard concentration of scale (m^o = 1) and γ_i is the molal scale activity coefficient. The activity coefficient specifically contains the additional information on the effects of interactions between species. In dilute solutions, individual ion activity coefficients are commonly expressed through the Extended Debye-Hückel approximation, defined as (Stumm and Morgan 1996):

$$\log f = -Az^2 \frac{\sqrt{I}}{1 + Ba\sqrt{I}}$$

(1.7)

where I is the ionic strength; $A = 1.82 \times 10^6 (\varepsilon T)^{-3/2}$ (where ε = dielectric constant; $A \cong 0.5$ for water at 25°C); z = charge of ion; $B = 50.3(\varepsilon T)^{-1/2}$ ($B \cong 0.33$ in water at 25°C); a = adjustable parameter (angstroms) corresponding to the size of the ion.

The expression for the equilibrium constant for a particular reaction can be written down by inspection of the balanced equation. First, the reaction quotient, Q, is written with the partial pressures or molar concentrations of the products in the numerator and those of the reactants in the denominator, with each one raised to a power equal to the corresponding stoichiometric coefficient. A general example would be:

$$aA + bB \rightarrow cC + dD \qquad Q = \frac{a_C^c a_D^d}{a_A^a a_B^b}$$

(1.8)

$$aA + bB \leftrightarrow cC + dD \qquad Q_{eq} = K$$
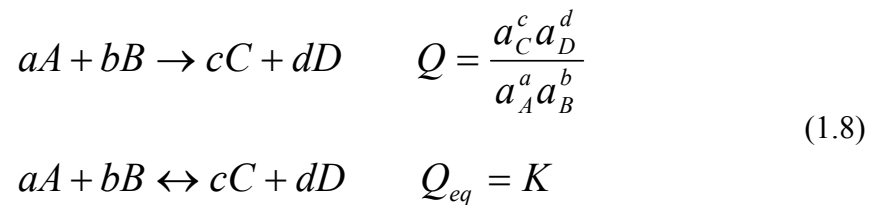
where, at equilibrium, the reaction quotient, Q, equals the equilibrium constant, K. Both are expressed fundamentally in the terms of activities, a (Atkins 1992).

The central relationship in calculating the chemical thermodynamics of mixtures under any conditions is:

$$\Delta G = RT \ln \frac{Q}{K}$$

(1.9)

where ΔG is the free energy of the reaction (kJ mol^{-1}), R is the gas constant (8.3145 J mol^{-1} K^{-1}), T is temperature (K), K is the equilibrium constant and Q is the reaction

quotient. Comparison of Q (actual concentration) with the value of K (equilibrium composition) provides a test for equilibrium (Stumm and Morgan 1996).

The equilibrium between a solid ionic compound, such as calcium carbonate, $CaCO_3$, and its ions in aqueous solution is:

$$CaCO_{3(s)} \leftrightarrow Ca^{2+}_{(aq)} + CO^{2-}_{3(aq)} \qquad (1.10)$$
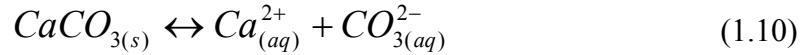
The equilibrium constant for an ionic equilibrium such as this, bearing in mind that the solid does not appear in the equilibrium expression, is called the solubility product, and is denoted K_{SP}:

$$K_{sp} = a(Ca^{2+})a(CO_3^{2-}) \qquad (1.11)$$

In a system where a solid and solution are in contact, the solubility product (K_{SP}) determines the equilibrium concentrations of the elemental components of the solid phase in solution. At equilibrium, the net release of components from the solid phase equals the net precipitation and therefore, the solution is saturated. Solutions that are either super- or undersaturated result in a precipitation or dissolution reaction. In order to test the saturation state of a solution it is necessary to calculate the free energy of dissolution of the solid, (Stumm and Morgan 1996):

$$\Delta G = RT \ln \frac{Q}{K_{sp}}$$

$$= RT \ln \frac{\{Ca^{2+}\}_{act}\{CO_3^{2-}\}_{act}}{\{Ca^{2+}\}_{eq}\{CO_3^{2-}\}_{eq}} = RT \ln \frac{IAP}{K_{sp}} \qquad (1.12)$$

where ΔG is the free energy of dissolution (kJ mol^{-1}), R is the gas constant (8.3145 J mol^{-1} K^{-1}), T is temperature (K), IAP is ion activity product (mol^n l^{-1n}), K_{SP} is the solubility product (mol^n l^{-1n}), and n is the number of lattice components of the solid. The IAP and the K_{SP} may be compared to determine the state of saturation of a solution with respect to a solid as follows (Stumm and Morgan 1996):

IAP > K_{SP} (oversaturated);

IAP = K_{SP} (equilibrium, saturated); and

IAP < K_{SP} (undersaturated).

If in Eq. 1.12 Q/K_{SP} < 1 (ΔG is negative), CaCO$_{3(s)}$ will dissolve; if Q/K_{SP} > 1, CaCO$_3$ will precipitate. The saturation test may often be made by simply comparing the activity (or concentration) of an individual reaction component with the activity (or concentration) the component would have if it were in hypothetical solubility equilibrium. This test is commonly called the saturation index (SI) (Stumm and Morgan 1996).

1.6.1 Dissolution mechanisms

Mineral dissolution takes place through two discrete steps: a reaction at the mineral surface followed by diffusion of ions from the mineral surface to the bulk solution. The slower of these two mechanisms is the dissolution rate-determining step (Stumm and Morgan 1996).

Transport-controlled dissolution is governed by the rate at which dissolution products can be transported, through processes such as diffusion or advection, from the mineral surface to the bulk solution. For a transport-controlled dissolution process, the dissolution rate is described by Eq. 1.13 (Stumm and Morgan 1996):

$$r = \frac{dC}{dt} = k_p t^{-\frac{1}{2}}$$
(1.13)

where r is the dissolution rate (mol s^{-1}), k_p is the reaction rate constant (mol s$^{-1/2}$), C is ion concentration in solution (mol) and t is time (s). By integrating the concentration in solution, C (mol) increases with the square root of time, where C$_O$ is the initial concentration (mol):

$$C = C_O + 2k_p t^{-\frac{1}{2}}$$
(1.14)

Alternatively, when dissolution products detach from the mineral surface via reactions that are so slow that concentrations adjacent to the surface build up to values essentially the same as in the surrounding solution, the mechanism is described as

$$Rate = k_p t^{-1/2}$$

$$C = C_O + 2k_p t^{1/2}$$

A

$$Rate = k[surface\ area]$$

$$C = C_O + kt$$

B
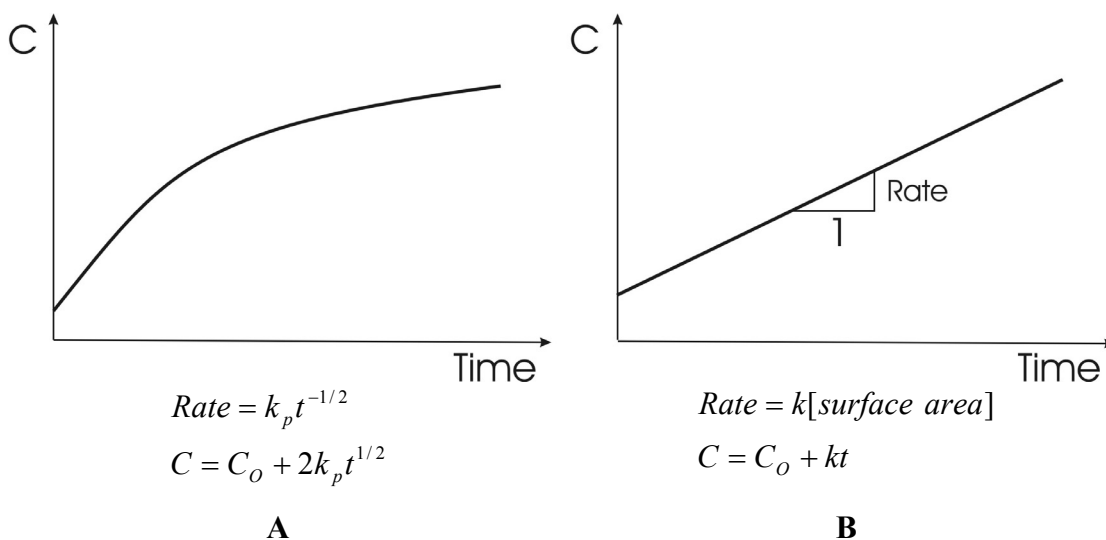
Figure 1.3. (a) Transport vs (b) surface controlled dissolution. Schematic representation of concentration in solution, C, as a function of change in concentration (e.g., in a batch dissolution experiment) is given as a function of time (from Stumm and Morgan 1996).

'surface-controlled'. Under these conditions, the dissolution kinetics follow a zero-order rate law if steady state conditions at the surface prevail. Eq. 1.15 (Stumm and Morgan 1996) describes this relationship:

$$r = \frac{dC}{dt} = kA \qquad (1.15)$$

where r, the dissolution rate (mol s^{-1}), is proportional to the surface area of the mineral, A (m^2), k is the reaction rate constant (mol m^{-2} s^{-1}), C is ion concentration in solution (mol l^{-1}) and t is time (s). According to Stumm and Morgan (1996), the most important dissolution reactions are surface-controlled and most minerals dissolve via this process. Figure 1.3 compares the two control mechanisms.

In certain circumstances, a situation intermediate between transport- and surface-controlled mechanisms, known as a mixed transport-surface kinetic reaction, may develop (Stumm and Morgan 1996).

1.6.2 Experimental methods for studying dissolution process

Various experimental set-ups have been used to determine the kinetics of mineral dissolution (Schnoor 1990):

1. batch reactor method, where the mineral and solution are constantly stirred in a container either open or closed to the atmosphere;

2. flow-through method, where fresh solution is constantly supplied to a reaction chamber containing the mineral, from which the old solution is removed at the same rate; and

3. pH-stat method, an adaptation of the batch reactor method, where the pH of the reaction is kept constant.

Each method has advantages and disadvantages. The batch reactor method is the simplest of the three. It entails the mineral being allowed to dissolve in contact with the same fluid until equilibrium is attained; this method is often used to determine solubility constants (Stumm and Morgan 1996). The two main problems with this method are, first, that as the mineral dissolves, and the solution composition changes, the dissolution rate may change in response to a changing solution. Secondly, as concentrations of ions in solution increase, saturation with respect to any secondary phases may be reached. Once these secondary phases start to precipitate, solution composition reflects both the rate of the primary dissolution and the rate of the secondary phase precipitation. Under certain circumstances, the data could become difficult to interpret in an unambiguous manner (Amacher 1991).

The pH-stat method has similar advantages and disadvantages to those of the batch reactor method, though it has the added benefit that it is possible to study dissolution to equilibrium at a specific pH value. Therefore, it is readily amenable to the determination of the H^+ ion concentration dependence on dissolution rates (Amacher 1991).

Flow-through reactors have an advantage over batch reactors in that the solution composition remains constant and that it is possible to control the saturation state of the solution by changing the flow rate. It is for this reason that this technique is the one commonly used to study the kinetics of mineral dissolution. Flow-through reactors typically come in two configurations: (i) a fluidised bed or (ii) a column

reactor. In fluidised bed reactors, the mineral grains are kept in suspension by a rapid recirculation pump and the dissolution products are rapidly stirred into solution. A problem with this technique is that physical abrasion of mineral grains may occur during stirring, which may affect the dissolution rate. For a column and plug-flow reactor the minerals grains are packed into a tube or column and water is forced through. The contact time with each aliquot of solution with the mineral grains is longer with the column reactor than with the fluidised bed reactors. The reaction products are also stirred into solution less rapidly compared to the fluidised bed, although solution composition near the mineral grains may differ from that of the bulk solution due to reduced flow rates (Amacher 1991).

Solubility products and free energies for dissolution of potassium jarosite (Brown 1970, Allison et al. 1990, Stoffregen 1993, Baron and Palmer 1996b), natrojarosite (Kashkay et al. 1975, Stoffregen 1993) and the chromate analogue of jarosite (Baron and Palmer 1996a, 2002) have been obtained using the batch reactor method (see Section 1.9).

1.6.3 Products of dissolution

When a mineral dissolves, several successive elementary steps may be involved (Stumm and Moran 1996):

1. mass transport of dissolved reactants from bulk solution to the mineral surface;
2. adsorption of solutes;
3. interlattice transfer of reacting species;
4. chemical reactions;
5. detachment of reactants from the surface; and
6. mass transport into the bulk of the solution.

In all solution environments the bare metal ion is in continuous search of a partner. All metal cations in water are hydrated; that is, they form aqua complexes (hydration shell). It is frequently difficult to determine the number of H_2O molecules in the hydration shell, but many metal ions coordinate four or six H_2O molecules per ion. The coordination reactions in which metal cations participate in aqueous solutions are

exchange reactions with the coordinated water molecules exchanged for some preferred ligands (Stumm and Moran 1996).

During mineral dissolution there may come a time when the bulk solution becomes oversaturated; under these conditions a solid phase may be formed from the supersaturated solution. Usually three steps can be distinguished in the nucleation and crystal growth of a solid phase (Stumm and Morgan 1996):

1. The interaction between ions or molecules leads to the formation of a critical cluster or nucleus:

$$X + X \leftrightarrow X_2$$

$$X_2 + X \leftrightarrow X_3$$

$$X_{j-1} + X \leftrightarrow X_j \quad \text{(critical cluster)}$$

$$X_j + X \rightarrow X_{j+1} \quad \text{(nucleation)} \tag{1.16}$$
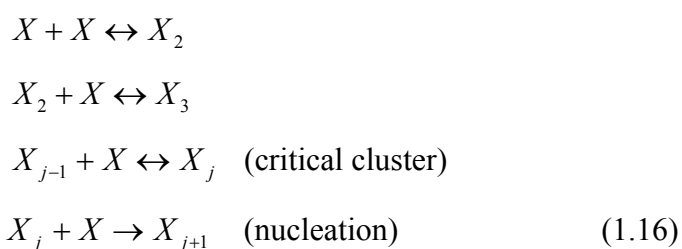
Nucleation corresponds to the formation of the new centres from which spontaneous growth can occur. The nucleation process determines the size and distribution of crystals produced.

2. Subsequently, material is deposited on these nuclei,

$$X_{j+1} + X \rightarrow \text{crystal growth} \tag{1.17}$$
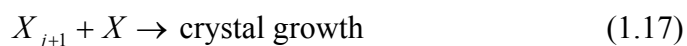
and crystallites are formed (crystal growth).

3. Large crystals may eventually be formed from fine crystallites by a process called ripening.

Adsorption of metal cations in solution on mineral and particle surfaces is extremely important in the attenuation of ARD pollution. The inherent scavenging properties of these compounds are related to their high surface areas, and to their surface charge that is pH dependent (Bigham and Nordstrom 2000). The exchange of H^+ and OH^- ions at the mineral-water interface is responsible for establishing the overall net surface charge for a mineral or particle (Stumm and Morgan 1996). Each surface also has a characteristic point of zero charge (pzc), the pH value at which the net surface charge is zero. The net surface charge is positive at pH values below the pzc but becomes negative at pH values higher than the pzc (Stumm and Morgan 1996, Bigham and Nordstrom 2000).

Foreign toxic metal cations (i.e. Pb(II)) are adsorbed to the surfaces of hydrous Fe oxides by the development of surface complexes that involve the coordination of the foreign ion with oxygen donor atoms to form either monodentate or bidentate complexes, with the release of protons (Bigham and Nordstrom 2000):

$$\text{—Fe—OH} + Pb^{2+} \longleftrightarrow \text{—Fe—OPb}^+ + H^+ \qquad \text{Monodentate}$$

$$\begin{matrix} \text{—Fe—OH} \\ | \\ \text{—Fe—OH} \end{matrix} + Pb^{2+} \longleftrightarrow \begin{matrix} \text{—Fe—O} \\ | \quad \diagdown \\ \quad \quad Pb \\ \text{—Fe—O} \diagup \end{matrix} + 2\,H^+ \quad \text{Bidentate}$$

$$(1.18)$$
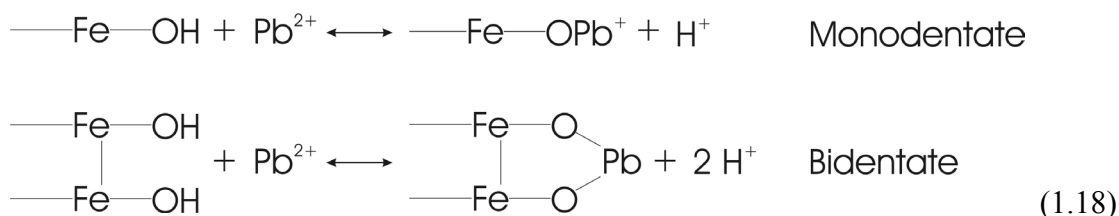
The complexes are considered to be inner-sphere if a mostly covalent bond is formed between the metal and the electron-donating oxygen ions. Otherwise, the complex is outer-sphere, with solute molecules providing the separation between the metal and oxide surface (Stumm and Morgan 1996). As might be expected, the attraction and binding of a foreign metal ion to an oxide surface is strongly pH dependent and is favoured by pH values that produce a net negative surface charge (above the pzc) (Bigham and Nordstrom 2000).

The process of oxyanion (AsO_4^{3-}) accumulation at oxide surfaces is similar to that of metal cations. Unlike metal cations, however, the absorption of oxyanions decreases with increasing pH because of competition with OH^- and electrostatic repulsion by negatively charged oxide surface at pH values above the pzc (Stumm and Morgan 1996). As with metal cations, the surface complexes formed by oxyanion absorption may be inner-sphere or outer-sphere in character. Inner-sphere sorption may result in both monodentate and bidentate surface complexes, and the latter may be bidentate mononuclear or bidentate binuclear (Bigham and Nordstrom 2000):

$$\text{—FeOH}^+ + H_2AsO_4^- \longleftrightarrow \begin{matrix} & O \quad\quad OH \\ & \diagup \diagdown \diagup \\ \text{—Fe} & \quad As \\ & \diagdown \diagup \diagdown \\ & O \quad\quad O \end{matrix} + H_2O \qquad \begin{matrix} \text{Bidentate} \\ \text{Mononuclear} \end{matrix}$$

$$\begin{matrix} \text{—FeOH} \\ | \\ \text{—FeOH} \end{matrix} + H_2AsO_4^- \longleftrightarrow \begin{matrix} \text{—Fe—O} \quad\quad O^- \\ | \quad\quad\quad \diagdown \diagup \\ \quad\quad\quad As \\ \text{—Fe—O} \quad\quad O \end{matrix} + 2\,H_2O \qquad \begin{matrix} \text{Bidentate} \\ \text{Binuclear} \end{matrix}$$

$$(1.19)$$
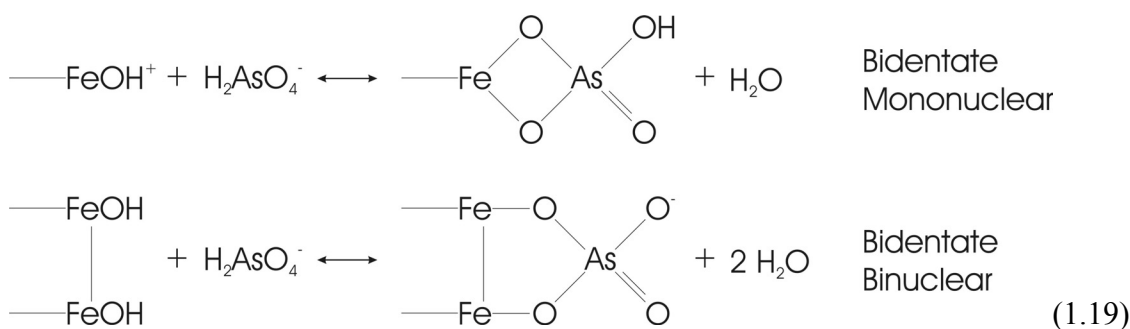
Trivalent oxyanions, such as AsO_4^{3-} and PO_4^{3-}, are much more aggressive in forming inner-sphere complexes as compared to their divalent counterparts (e.g. SO_4^{2-}). As a result, the trivalent species yield absorption edges that are non-reversible (Bigham and Nordstrom 2000).

To understand the process and dynamics of mineral dissolution it is ultimately important to understand the factors that retard dissolution. Obviously, substances that "block" surface functional groups or prevent the approach of dissolution-promoting H^+, OH^-, ligands and reductants to the functional groups inhibit dissolution (Stumm and Morgan 1996). The adsorption of a charged species at a constant pH may change the surface protonation. The formation of a negatively charged surface complex (e.g., by absorption of a multivalent ligand) is accompanied by an increase in surface protonation; the formation of a positively charged surface complex (e.g., due to the adsorption of a cation) is accompanied by a decrease in surface protonation (Sigg and Stumm 1981, Blesa et al. 1994). In doing so, it may cause synergistic or antagonistic effects with respect to the relative acceleration or inhibition of dissolution (Stumm and Morgan 1996). Binuclear or multinuclear surface complexes tend to block surface sites. A much higher activation energy is involved in detaching simultaneously two metal centres from the surface; hence, dissolution is retarded by binuclear species (Bigham and Nordstrom 2000).

It is now worth mentioning some of the possible breakdown phases that might be seen in this study and briefly introduce their mineralogy and adsorption properties.

1.6.3.1 Goethite

Goethite (α-FeOOH) is usually considered to be the most stable form of Fe(III) oxide, and it occurs in almost every type of surface environment (Schwertmann and Taylor 1989, Schwertmann and Fitzpatrick 1992). In mine-drainage precipitates, goethite is commonly observed as a trace or minor constituent, but is rarely the dominant phase (Bigham 1994). Well-crystallised specimens of goethite have needle-like (short rods) crystal habits. Infrared spectra of mine-drainage goethite show diagnostic bands due to OH bending at 890 and 797 cm^{-1} (Brady et al. 1986).

Pb(II) was found to form a monodentate ($\equiv$FeOPb$^+$) complex when absorbed to goethite in an XPS study by Abdel-Samad and Watson (1998). Sherman and Randal

(2003) found, though EXAFS spectroscopy, that AsO_4^{3-} adsorbed to goethite by inner-sphere bidentate binuclear corner and edge-sharing complexes. Also using EXAFS, Peacock and Sherman (2004) found that Cu(II) sorbs to goethite by bidentate $[(\equiv FeOH)_2Cu(OH)_2^0]$ and tridentate $[(\equiv Fe_3O(OH)_2)Cu_2(OH)_3^0]$ surface complexes.

1.6.3.2 Ferrihydrite

Ferrihydrite ($\approx Fe_5OH_8 \cdot 4H_2O$) has become a popular but often misused synonym for "amorphous" ferric hydroxide (Bigham 1994). Ferrihydrite is always poorly crystallised, but can display a range of structural order that gives rise to XRD patterns consisting of anywhere from two (worst crystallised) to six (best-crystallised) broad bands (Carlson and Schwertmann 1981). Natural and synthetic samples both usually consist of highly aggregate, spherical particles with diameters in the order of 2 to 6 nm (Bigham 1994).

In sulphate rich ARD environments, Pb(II), Cu(II), and Zn(II) will all sorb to ferrihydrite to form ternary surface complexes ($\equiv FeOHMeSO_4$, where Me is Pb(II), Cu(II), and Zn(II); Webster et al. 1998, Swedlund and Webster 2001, Swedlund et al. 2003). Sherman and Randal (2003) found that AsO_4^{3-} sorbs to ferrihydrite by forming inner-sphere bidentate binuclear corner and edge-sharing complexes.

1.6.3.3 Schwertmannite

Schwertmannite ($Fe_8O_8(OH)_6SO_4$) is a relatively new mineral and its chemical and physical characteristics were originally described by Bigham et al. (1990). Like ferrihydrite, schwertmannite is a very poorly crystallised mineral characterised by high surface area (100 to 200 m^2/g) and a "pin-cushion" morphology (Bigham 1994). Schwertmannite is also easily distinguished from ferrihydrite and other associated minerals by its XRD profile, which consists of eight broad bands for d > 1.4 Å (Bigham et al. 1990).

In sulphate-rich environments Webster et al. (1998) and Swedlund and Webster (2001) found that Pb(II), Cu(II) and Zn(II) formed ternary surface complexes on the surfaces of schwertmannite. AsO_4^{3-} is thought to sorb to schwertmannite by creating bidentate surface complexes, similar to those seen for goethite and ferrihydrite, though no firm structural (EXAFS) evidence is available at present (Webster et al. 1998). Although schwertmannite is a metastable phase of goethite, Fukushi et al.

(2003) found that the transformation was significantly inhibited by the absorption of AsO_4^{3-}.

1.6.4 Characterisation of dissolution products

There are a large number of techniques available to characterise the products of dissolution. In this short section, the merits of some of the more important techniques will be discussed. Probably the most important and significant is X-ray diffraction. By acquiring a diffraction profile of the residual solid after the completion of a dissolution experiment, it is possible to see if the original mineral structure has changed over the course of being dissolved, and, more importantly, identify any secondary phase(s) that may have formed from the ions in the bulk solution. Another technique that can give significant insight into the structure of the dissolved solid is vibrational spectroscopy, commonly infrared (FTIR) or Raman. By comparing the vibrational assignments of the original solid and the residual recovered after dissolution it is possible to gauge if there are any major structural differences in the dissolved solid and identify any additional modes that could be attributed to a secondary phase(s). Through scanning electron microscopy (SEM), it is possible to compare the morphology of the pre- and post-dissolution solids. This is an important technique as it can help gauge if there is any selective dissolution of the minerals' surface, and to see if a secondary phase(s) has precipitated and, identify its specific crystal habit. The methods used to characterise the dissolution products in this study are discussed in Chapter 2 and Appendix A.

1.7 Synthesis of jarosites

It is possible to determine the amount of toxic element release from the jarosites by conducting dissolution studies on their synthetic analogues. Various members of the alunite supergroup have been synthesised. The jarosite subgroup consists of only nine minerals (Table 1.1). These and their synthetic counterparts are listed in Table 1.2 to illustrate the nomenclature used to distinguish their origins and composition. All the compounds correspond to the general formula of $AB_3(TO_4)_2(OH)_6$. The synthetic analogues can be viewed as a series of elemental substitutions within the general $AB_3(TO_4)_2(OH)_6$ structure and broadly classed together depending upon their valance state (*e.g.* Pb(II) in plumbojarosite, a divalent substitution).

Table 1.2. Minerals of the jarosite subgroup, and synthetic analogues (from Dutrizac and Kaiman 1976).

Idealised Formula	Mineral name	Synthetic equivalent
$KFe_3(SO_4)_2(OH)_6$	jarosite	potassium jarosite
$NaFe_3(SO_4)_2(OH)_6$	natrojarosite	sodium jarosite
$RbFe_3(SO_4)_2(OH)_6$	no mineral equivalent	rubidium jarosite
$AgFe_3(SO_4)_2(OH)_6$	argentojarosite	silver jarosite
$(NH_4)Fe_3(SO_4)_2(OH)_6$	ammoniojarosite	ammonium jarosite
$TlFe_3(SO_4)_2(OH)_6$	dorallcharite	thallium jarosite
$Pb_{0.5}Fe_3(SO_4)_2(OH)_6$	plumbojarosite	lead jarosite
$Hg_{0.5}Fe_3(SO_4)_2(OH)_6$	no mineral equivalent	mercury jarosite
$Pb(Fe,Cu)_3(SO_4)_2(OH,H_2O)_6$	beaverite	lead-copper jarosite
$(H_3O)Fe_3(SO_4)_2(OH)_6$	hydronium jarosite	hydronium jarosite

1.7.1 Monovalent cation substitutions

All the monovalent A-site cations stated below can form near perfect solid solutions with each other, and commonly with additional minor hydronium substitution. The most extensive solid solution made and researched is the Na-K series (Dutrizac and Jambor 2000).

Potassium and sodium. Of the entire jarosite subgroup, potassium and sodium jarosite are the easiest endmembers to synthesise, and consequently the most studied. The reactants commonly used in the synthesis of these two jarosites are ferric sulphate and the corresponding alkali sulphate (Brophy and Sheridan 1965, Brown 1970, Dutrizac and Kaiman 1976, Dutrizac 1983). Baron and Palmer (1996b) synthesised potassium jarosite using an excess of KOH because this produced a purer synthetic analogue than when using potassium sulphate. Generally, it has been observed that potassium is easier to incorporate into the jarosite structure at the A-site than sodium. Potassium jarosite has also been synthesised by Sasaki and Konno (2000) using a novel technique. Fe(III) was provided through the biological oxidation of Fe(II) by *Thiobacillus ferrooxidans* and by the chemical oxidation of Fe(II) by slow and rapid addition of H_2O_2. Potassium was introduced as K_2SO_4.

Ammonium. In hydrometallurgy, ammoniojarosite $[(NH_4)Fe_3(SO_4)_2(OH)_6]$ is formed as a by-product when ammonia is added as a neutralising agent to an iron-rich, hot acid leach solution. Dutrizac (1996) has extensively investigated ammonium incorporation into the jarosite structure. Synthetic ammonium jarosite forms from an

ammonium sulphate salt in similar conditions to that of potassium jarosite and sodium jarosite above (Dutrizac and Kaiman 1976).

Hydronium. Hydronium (H_3O^+) occurs in all natural and synthetic jarosites to charge balance deficiencies of A-site cations (see Section 1.4.1). Under certain conditions, a synthetic hydronium jarosite [$(H_3O)Fe_3(SO_4)_2(OH)_6$] in which no suitable A-site cation is available can be made (Dutrizac and Kaiman 1976). The crystal structure of the isostructural Ga analogue of jarosite (($H_3O)Ga_3(SO_4)_2(OH)_6$) was determined by Johansson (1963), who showed that the alkali cation position was occupied by an O-bearing species which he concluded was most likely H_3O^+ (Dutrizac and Jambor 2000). Many other isostructural analogues of hydronium jarosite have been synthesised (V(III), Wills 2001; Al(III), Wills et al. 2000; Cr(III), Morimoto et al. 2003).

Solution pH is probably the most important parameter controlling the synthesis of pure hydronium jarosite (Dutrizac and Jambor 2000). At 140°C, endmember hydronium jarosite was observed to form over the pH range 0.4-1.4. At lower pH values, no product was produced, and at higher pH, discoloration of the solution suggested partial FeO(OH) precipitation. Seeding with hydronium and constant stirring were essential to suppress the co-precipitation of FeO(OH). Temperature is also a major influence on yield. At 100°C, only traces of hydronium jarosite were precipitated from 1.0 M Fe(III) solution of pH = 0.8 after 24 h, which was seeded with hydronium and well agitated. The yield rose steadily with increasing temperature to approximately 140°C, and then reached a plateau. Above 160°C, hydronium jarosite no longer formed (Dutrizac and Jambor 2000).

Silver. Silver jarosite [$AgFe_3(SO_4)_2(OH)_6$] has been successively synthesised by Fairchild (1933), May et al. (1973) and Dutrizac and Kaiman (1976). Systematic investigations on the formation of silver jarosite by Dutrizac (1983) and Dutrizac & Jambor (1984, 1987a) showed that under certain conditions, silver jarosite was nearly as stable as potassium jarosite. During the formation of potassium jarosite, Ag^+ will be selectively incorporated in preference to Na^+, NH_4^+, Pb(II) or (Pb(II)+Cu(II)) (Dutrizac 1983).

Thallium. Thallium exists in both the monovalent and trivalent states, with Tl^+ by far the more stable. It is theoretically possible to have two Tl-dominant jarosites: $TlFe_3(SO_4)_2(OH)_6$ and $K(Tl^{3+},Fe^{3+})_3(SO_4)_2(OH)_6$ (Dutrizac and Jambor 2000). Yaroslavtsev et al. (1975) reported the co-precipitation of both thallium valences, although the nature of the precipitates was never clarified (Dutrizac and Jambor 2000). However, Dutrizac and Kaiman (1975, 1976) made Tl^+ end-member jarosite relatively successively.

Rubidium. Fairchild (1933) was the first to synthesise rubidium jarosite [$RbFe_3(SO_4)_2(OH)_6$], but the low purity of Rb_2SO_4 available at the time resulted in precipitates containing substantial amounts of K_2O or Na_2O. Fairchild (1933) stated the order of stability for the synthetic jarosites to be K > Rb > Na, which was confirmed by Steintveit (1970). Dutrizac and Kaiman (1976) eventually synthesised rubidium jarosite free of both K and Na, and subsequently characterised it as $Rb_{0.82}(H_3O)_{0.18}Fe_{2.7}(SO_4)_2(OH,H_2O)_6$.

Lithium and Cesium. Although Na, K and Rb substitute into the jarosite structure, it has been demonstrated that neither Li nor Cs produce an endmember jarosite, even though they are all members of Group 1 elements of the periodic table (Dutrizac and Jambor 1987c). The inability to form these endmember species is attributed to the small size of the Li^+ ion (r = 0.60 Å) and the larger size of the Cs^+ ion (r = 1.69 Å) relative to the ions of the other members of the group (Na r = 0.95 Å, K r = 1.33 Å, Rb r = 1.48 Å) (Cotton and Wilkinson 1962). However, Dutrizac and Jambor (2000) state that Cs-bearing potassium, sodium, and rubidium jarosites can be synthesised with a Cs content of > 2 wt. %. The incorporation of Cs was greatest for potassium jarosite and was least for rubidium jarosite. Lithium does not seem to be significantly incorporated in any of the jarosites. The highest Li content detected was 0.1 wt. % Li (Dutrizac and Jambor 2000).

1.7.2 Divalent cation substitutions

Lead. Pb(II) in jarosite will typically occupy only half the available A-sites to preserve charge neutrality [$Pb_{0.5}Fe_3(SO_4)_2(OH)_6$]. Fairchild (1933) was the first to attempt to synthesize plumbojarosite by combining 0.3 g $PbCl_2$, 1.5 M HCl and 1.6 g $Fe_2(SO_4)_3$. The synthesis was especially interesting due to the fact that the jarosite

was produced from an acidic chloride media. Mumme and Scott (1966) prepared plumbojarosite in an autoclave by reacting excess lead sulphate with a 0.125 M $Fe_2(SO_4)_2$ solution at temperatures ranging from 100 to 190°C. Unfortunately, the lead jarosite was contaminated with $PbSO_4$, which was subsequently dissolved and leached from the jarosite by washing with ammonium acetate. Dutrizac and Kaiman (1976) synthesised lead jarosite using a technique whereby the lead was slowly added to a hot ferric nitrate solution. This technique had the advantage that the product was not contaminated with $PbSO_4$.

Dutrizac and Jambor (1987a) observed an 11 Å (003) diffraction line in their synthesis of lead jarosite, thereby indicating that some ordering of the monovalent, alkali-site cations had occurred. The consequence was that the c-axis parameter had doubled to ~ 34 Å. This is discussed in more detail in section 3.1 of this thesis.

Copper and Zinc. Copper and zinc can be incorporated into lead jarosite to produce beaverite [$Pb(Fe,Cu,Zn)_3(SO_4)_2(OH)_6$], where copper and zinc can partially substitute for iron, to the extent that a solid solution series exists. Dutrizac and Dinardo (1983) explored the synthesis of copper and zinc incorporation into lead jarosite concentrating on an autoclave method and a slow-addition technique (see Section 1.8.1).

Dutrizac (1984) determined that potassium jarosite could incorporate about 2.1 wt. % Zn(II), but only half that amount was successfully substituted into sodium jarosite, and even less into ammonium jarosite. Scott (1987) reported a jarosite with 6.3 wt. % Pb and 2.5 wt. % Zn(II), which appears to be the maximum Zn(II) content that has been described for the natural jarosite subgroup. Substitution of Cu(II) in the alkali jarosites is similarly low (Dutrizac and Jambor 2000).

Cadmium, Cobalt, Nickel and Manganese. Cadmium typically has been found in jarosites about 0.05 wt. % or lower (Dutrizac et al. 1996). Substitutions of Co(II) and Mn(II) in sodium jarosite have been reported to be < 0.5 wt. % and about 2 wt. %, respectively (Dutrizac and Jambor 1987a). Dutrizac and Jambor (2000) summarise the order abundance of these metals in the jarosite structure:

$$Cu^{2+} > Zn^{2+} > Co^{2+} \sim Ni^{2+} \sim Mn^{2+} > Cd^{2+}$$
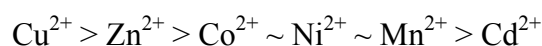
Mercury. Mercury in jarosite is divalent and the formula of the jarosite compound it makes is $Hg_{0.5}Fe_3(SO_4)_2(OH)_6$, analogous to that of plumbojarosite. Mercurian jarosite has not been reported to occur naturally (Dutrizac and Jambor 2000). Dutrizac and Chen (1981) synthesised mercury jarosite by a slow-addition method (see Section 1.8.1). Of all the synthetic jarosites, mercury jarosite is the most sensitive to pH. No product was formed at pH < 1.4, and at pH > 1.8, the product was contaminated with iron sulphates.

1.7.3 Trivalent substitutions

Gallium and Indium. Various elements can substitute for Fe(III) in the minerals of the alunite supergroup. The most notable trivalent solid solution occurs between Fe(III) (jarosites) and Al(III) (alunites). Another trivalent solid solution exists between Ga(III) and Fe(III), which is complete for K, Na, Rb, NH_4, and H_3O synthetic jarosites (Johansson 1963 and Tananaev et al. 1967a,b, Dutrizac and Chen 2000). Dutrizac (1984) synthesised the indium endmember of potassium jarosite. As for the Na system, Dutrizac and Mingmin (1993) showed that In(III) formed a nearly ideal solid solution series with Fe(III) in sodium jarosite.

Vanadium. Dutrizac and Chen (2003) synthesised a variety of V(III) analogues of natrojarosite, potassium jarosite, rubidium-substituted jarosite, dorallcharite (Tl^+), hydronium jarosite, ammonium jarosite and plumbojarosite. The majority of the analogues were made at $100^{\circ}C$ using a standard hydrolysis procedure, although a temperature of $140^{\circ}C$ was required to give a satisfactory yield of the V(III) end-member of hydronium jarosite. The plumbojarosite analogue was synthesised by reacting excessive amounts of lead sulphate at $150^{\circ}C$ and subsequently dissolving un-reacted $PbSO_4$ at room temperature with ammonium acetate. The synthesis of the V(III) end-member of argentojarosite was unsuccessful as the trivalent vanadium reduced the silver ion to metallic silver. Other substitutions, such as Sb(III) (Kolitsch et al. 1999), Cr(III) (Walenta et al. 1982) and Nb(III) (Lottermoser 1990) have also been reported.

1.7.4 T-site substitutions

Arsenic. Arsenic is found in the natural environment in two valence states, 3^+ and 5^+. As(V) as arsenate, AsO_4^{3-}, is the only arsenic species that has been observed in natural

jarosites. Savage et al. (2000) demonstrated arsenate incorporation within jarosite at the T-site using EXAFS analysis.

Dutrizac and Jambor (1987b) and Dutrizac et al. (1987) investigated the incorporation of arsenate in sodium jarosite and potassium jarosite at 97°C and 150°C, respectively. Although extensive precipitation of arsenic occurred in some experiments, the arsenic commonly was present as a discrete arsenate-bearing phase, scorodite ($FeAsO_4$). The studies suggested that only ~ 2 % and ~ 4 % AsO_4^{3-} could be structurally incorporated in either sodium or potassium jarosite, respectively, at these temperatures. Roca et al. (1999) reported specific compositions of jarosite from Rio Tinto gossans containing significant structural concentrations of AsO_4^{3-} and Pb(II) [$(K_{0.58}Pb_{0.39})Fe_{2.98}(SO_4)_{1.65}(AsO_4)_{0.35}(OH,H_2O)_6$]. Alcobe et al. (2001) synthesised a lead-arsenate bearing jarosite with a composition similar to beudantite.

Selenium. Selenium (SeO_4^{2-}), like As (V), replaces SO_4^{2-} in the jarosite structure. The formation of selenate requires strong oxidising conditions, which can occur in some mining areas (Dutrizac and Jambor 2000). Dutrizac et al. (1981) synthesised selenate analogues of sodium and potassium jarosite and subsequently concluded that it was possible to make selenate analogues for all other members of the jarosite subgroup.

Other anions. Phosphate and sulphate show a partial solid solution with Pb(II), Bi(V), and Sr(II) synthetic jarosites (Dutrizac and Jambor 2000). The synthetic chromate analogue of jarosite is also known (Powers et al. 1975, Baron and Palmer 1996b). Substitution of silicate and molybdate at the T-site have been reported but their abundance is rare (Ripp et al. 1998).

1.8   Conditions affecting the synthesis of jarosites

Many physical and chemical parameters (*e.g.* temperature, pH) commonly affect the synthesis of jarosites. The remainder of this section will discuss the important parameters separately.

1.8.1 Experimental technique

There are three principal ways of synthesising jarosites: (1) in a glass reaction vessel, (2) by a slow addition technique and (3) in an autoclave. A glass reaction vessel can

be easily described as a large (commonly 2 L) glass beaker that has a Quickfit lid with a variety of neck adapters, one of which typically has a condenser attached to reduce solution loss through evaporation. The slow addition technique is an adaptation of the reaction vessel technique where a reactant, commonly the A-site cation, is slowly added to the solution through one of the neck adapters connected from the Quickfit lid. Finally, an autoclave allows the solution to react at a variety of temperatures and pressures.

1.8.2 Temperature

Potassium, sodium, and ammonium jarosite can all form at $25^{o}C$ although the rates of formation are very slow (Babcan 1971). Synthetic potassium jarosite precipitates extremely rapidly at about $80^{o}C$ and is nearly complete in several hours at $100^{o}C$ (Brophy et al. 1962, Dutrizac and Kaiman 1979). The reaction rate increases rapidly above $100^{o}C$, but there is an upper limit for jarosite formation that seems to be between 180-200°C, depending upon the solution composition (Haigh 1967, Babcan 1971). Dutrizac (1983) investigated factors affecting alkali jarosite formation and concluded that the majority of alkali jarosites, excluding hydronium jarosite, could be made in a reaction vessel at an optimum temperature of $97^{o}C$. Synthetic hydronium jarosite presently can only form in an autoclave at temperatures varying from 130-160°C (Dutrizac et al. 1980).

All lead-bearing synthetic jarosites examined in the present study (e.g. beaverite, beudantite, and plumbojarosite) can be made at varying temperatures either by an autoclave or by a slow addition type technique. When made via slow addition the optimum temperature is similar to that for alkali jarosite formation in a reaction vessel (i.e. $97^{o}C$) (Dutrizac et al. 1980). For autoclave synthesis, Dutrizac et al. (1980) found that the ideal temperature was $130^{o}C$; small quantities of Fe_2O_3 were detected at $170^{o}C$.

1.8.3 pH

The initial solution pH is extremely important because pH plays a major role in the stability and precipitation of jarosite (Brown 1971, Bingham et al. 1996, Dutrizac and Jambor 2000). A key stage in jarosite formation is the hydrolysis of the ferric iron sulphate, which releases protons. Increasing acidity retards the formation of further

jarosite product (Dutrizac 1983). For this reason, the initial starting pH of the solution is critical to optimising jarosite formation and maximising yield. Jarosite precipitation increases with increasing pH until other Fe compounds are precipitated, which occurs at pH values greater than 2 at 100°C (Brown 1971). Park and Park (1978) found the ideal starting pH to be between 1.5 and 1.6 for jarosite formation at 100°C. Dutrizac (1983) showed that a consistent amount of jarosite is precipitated at pH values less than 1.5. The amount of precipitate, however, decreases sharply at very low pH (< 1.5) values. At an initial pH of ~ 0.5, no precipitate forms because formation of the solid is not thermodynamically favourable.

For the jarosites prepared in this study, all initial solution pHs except that for the synthesis of beudantite, were adjusted to between 1.8 and 1.5, using 0.01-0.03 M H_2SO_4. For the beudantite synthesis, H_3AsO_4 was used to adjust the pH into the correct initial range.

1.8.4 Alkali metal concentration

Iron precipitation increases with increasing M^+/Fe(III) ratio, to a point slightly above the ideal stoichiometric ratio of 1:3; thereafter, the degree of jarosite precipitation is independent of alkali metal concentration (Dutizac and Kaiman 1976, Park and Park 1978, Dutrizac 1983). Early work by Fairchild (1933) and Kubisz (1972) concluded that the ideal stoichiometric ratio of M^+/Fe(III), 1:3, gave a yield closest to the endmember. However, Dutrizac (1983) discovered that higher than theoretical concentrations of alkali ions in solution resulted in jarosites with slightly increased final yields and higher alkali than hydronium contents in the precipitates. Very high alkali metal sulphate concentrations (i.e. > 1.0 M) can result in the precipitation of alkali iron sulphates instead of jarosites (Dutrizac and Jambor 2000).

The alkali metal in synthetic potassium jarosite can be introduced in one of two forms: KOH (Baron and Palmer 1996b) or, more commonly, K_2SO_4 (Dutrizac and Kaiman 1976, Dutrizac 1983). Baron and Palmer (1996b) introduced potassium as a hydroxide rather than a sulphate because they believed the hydroxide would result in higher potassium content in the jarosite-precipitate. The work done by Kubisz (1970) supports the argument of Baron and Palmer (1996b). When preparing synthetic potassium jarosite with K_2SO_4 and ferric sulphate, the molar ratio of SO_3:Fe_2O_3 is 3:1

as opposed to the stoichiometric ideal 4:3. Kubisz (1970) therefore recommended that the A-site alkali cations should be introduced in the form of hydroxides to improve the sulphate to iron ratio and thereby create purer alkali endmember jarosites.

The lead reactant in the lead-bearing jarosites can be either $Pb(NO_3)_2$ for slow addition synthesis or $PbSO_4$ for autoclave synthesis.

1.8.5 Iron concentration

Synthetic jarosites are readily precipitated from sulphate rich solutions containing 0.025 to 3.0 M Fe(III) (Brophy and Sheridan 1965, Brown 1970). The lower limit of Fe(III) for jarosite precipitation is near 0.001 M (Brown 1971). If there are excess alkali metal ions available, the fraction of iron that is precipitated is independent of the iron concentration in solution (Dutrizac and Jambor 2000). Consequently, the total amount of jarosite formed is directionally proportional to the concentration of Fe(III) in solution (Dutrizac and Jambor 1984).

1.8.6 Effects of seeding and agitation

Dutrizac (1983) studied the synthesis of sodium jarosite to investigate the effects of seeding and agitation on alkali jarosites. For the synthesis of sodium jarosite with no jarosite seed, Dutrizac (1983) found at low rotational speeds in the solution, the yield of product was relatively low and the jarosite tended to coat the glassware and the stirring rod. As the rotational speed increased above approximately 400 rpm, the yield increased significantly and most of the jarosite remained in suspension. Above 600 rpm, there was no significant effect on either the amount of jarosite formed or the amount in suspension. From structural analysis of the jarosites formed under various amounts of agitation Dutrizac (1983) found that the iron and alkali content in the final jarosite precipitate was independent of the stirring speed.

Once the jarosite started to form, the precipitate tended to self-seed, but only when the precipitate was well suspended in the solution. Once the precipitate became thoroughly dispersed, further increases in stirring rate had no significant effect on yield and final product composition (Dutrizac 1983). Dutrizac (1983) also discovered that a small amount (< 30 %) of jarosite seed added at the beginning of the synthesis had an insignificant effect on the overall jarosite chemical composition. The only

effect the seed seemed to have upon the synthesis was to increase slightly the overall product yield (Dutrizac 1983).

In autoclave synthesis, the addition of a seed under good mixing conditions was not overtly beneficial, but the seed was useful under poor agitation conditions (Dutrizac et al. 1980). When the solution was not seeded and stirring was minimal, an enriched hydronium lead jarosite formed, but the product made in the presence of a seed always contained more than 12 wt. % lead. The seed prevented the formation of other iron compounds like hydronium jarosite, $FeO(OH)$ or Fe_2O_3. Dutrizac et al. (1980) showed that lead jarosites made in the presence of seed consisted of lead jarosites only, while those made without seed were contaminated with $FeO(OH)$ at low stirring speeds. For plumbojarosite, the yield of product with seeding was as consistent as in its absence; the yield at 200 rpm was nearly the same as at 800 rpm (Dutrizac et al. 1980).

1.8.7 Lead sulphate leaching

One significant challenge in the synthesis of pure lead jarosites is to minimise lead sulphate ($PbSO_4$) impurities in the final precipitated product. The slow addition and autoclave methods both share this $PbSO_4$ impurity problem, but the slow addition technique to a much lesser extent. Mumme and Scott (1966) were the first to attempt to leach lead sulphate impurities from jarosite by washing the product in a 10 % diethylenetriamine solution. Unfortunately, this caused the yellow-coloured product to turn progressively orange and then red. XRD analysis of the amine-leached mixture showed only lead jarosite, suggesting that the colouration was due to the formation of an amorphous decomposition product. Mumme and Scott (1966) abandoned this type of leaching and used 10 % ammonium acetate solutions instead.

Dutrizac et al. (1980) investigated ammonium acetate leaching of lead-bearing jarosites and concluded that an acetate solution did not decompose the lead jarosite at 25 or 35°C. However, they did discover that a slight decomposition of the lead jarosite occurred at 50°C and became significant at 70 to 90°C. They stated that ammonium acetate leaching must be done at low temperature to prevent lead jarosite decomposition. Dutrizac et al. (1980) suggested that, for a 10 g lead jarosite product,

four 1 L washes in 10 % ammonium acetate at 25^oC should be sufficient to remove any lead sulphate from the jarosite product.

1.8.8 Addition of other sulphates

Neither lithium nor magnesium substitute into the jarosite structure (Dutrizac et al. 1980, Dutrizac and Jambor 1987c), and because of this, sulphates of these cations are commonly used as electrolytes to increase the ionic strength during jarosite synthesis (Dutrizac et al. 1980, Dutrizac 1983). High concentrations of Li_2SO_4 or $MgSO_4$ increase Pb(II) incorporation into the jarosite structure at the expense of hydronium (H_3O^+), and this is thought to be due to increased $PbSO_4$ solubilities in the highly concentrated sulphate media (Dutrizac et al. 1980). When lead jarosites are precipitated in the presence of either 2 M Li_2SO_4 or 2 M $MgSO_4$, the Fe(III) concentration in solution must be increased from 0.05 M for low ionic strength solutions to 0.3 M to avoid the precipitation of Fe_2O_3 or α-FeO(OH) (Dutrizac et al. 1980). Dutrizac (1983) investigated the influence of ionic strength on the extent of iron precipitation and composition of alkali jarosites by additions of $MgSO_4$. He found that increasing concentrations of dissolved magnesium sulphate caused a slight decline in the extent of iron precipitation although the effect was imperceptible below 1 M $MgSO_4$. For alkali jarosite compositions such as sodium jarosite, the Na content was found to be essentially independent of the ionic strength (Dutrizac 1983).

1.8.9 Slow addition versus autoclave methodologies

As stated in previous sections the lead-bearing jarosites such as beaverite, beudantite, and plumbojarosite can be made either by a slow addition technique or by using an autoclave. For this project, the slow addition technique was chosen over the autoclave, primarily because the former gave a more pure product. In autoclave synthesis there is a very high probability of lead sulphate impurities in the final product for two reasons. First, lead is introduced to the reaction in the form of lead sulphate and second, the quantity of the reactant is typically twice the stoichiometric amount relative to the iron concentration. Even though Dutrizac et al. (1980) found lead sulphate leaching effective, one of the main objectives of this project is to investigate the degree of toxic element release from the jarosite subgroup by carrying out dissolution studies on synthetic analogues. Considering that lead is in the bulk structure of the majority of the jarosites studied, it would be undesirable to have a

lead-based impurity in the final product. For this reason, a slow addition technique was used in the synthesis of the lead jarosites. By using a slow addition technique, we gained both higher yield and purity at the expense of higher lead and other toxic element concentrations in the structure. Hydrothermal autoclave syntheses commonly create purer end-member products with greater crystallinity (Dutrizac et al. 1980).

1.9 Thermodynamic data on the jarosite subgroup

There are only a few experimental studies investigating the solubility of the jarosite subgroup, concentrated mainly on potassium jarosite and to a much lesser extent, natrojarosite. Until Drouet and Navrotsky (2003) published definitive calorimetric data on the K-Na-H$_3$O jarosite solid solution series, the recommend thermodynamic values correlated by Stoffregen et al. (2000) for the enthalpy of formation, entropy and heat capacity of potassium jarosite and natrojarosite were derived from approximations and estimations (Stoffregen 1993) rather than direct determinations.

There is still a large degree of uncertainty about its thermodynamic properties, despite the amount of data available for the solubility of potassium jarosite. For the potassium jarosite dissolution reaction:

$$KFe_3(SO_4)_2(OH)_{6(s)} + 6H^+_{(aq)} \leftrightarrow 3Fe^{3+}_{(aq)} + K^+_{(aq)} + 2SO^{2-}_{4(aq)} + 6H_2O_{(l)} \quad (1.20)$$
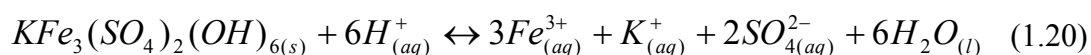
log K_{sp} has been reported to vary from -7.12 to -14.8 and $\Delta G^o_{f,298}$ from -3317.9 to -3192 ± 25 kJ mol^{-1} (Stoffregen et al. 2000). Baron and Palmer (1996b) give a comprehensive summary on available thermodynamic data for potassium jarosite. They claim that one important source for the variation in the values for the free energy of formation of potassium jarosite is the use of different values for the free energies for the ions. Stoffregen et al. (2000) and Drouet and Navrotsky (2003) both recommend the use of $\Delta G^o_{f,298}$ -3309.8±1.7 kJ mol^{-1}, as reported by Baron and Palmer (1996b). There are only a few published values of $\Delta G^o_{f,298}$ for natrojarosite; the recommended value is -3256.7 kJ mol^{-1} (Kashkay et al. 1975, Stoffregen et al. 1993).

Drouet and Navrotsky (2003) were the first to experimentally determine the enthalpy of formation for potassium jarosite, natrojarosite and hydronium jarosite by high-temperature drop solution calorimetry. They reported $\Delta H^o_{f,298}$ of -3829.6 ± 8.3,

-3783.4 ± 8.3, and -3741.6 ± 8.3 kJ mol^{-1} for potassium, sodium and hydronium jarosites, respectively.

Table 1.3. Recommended thermodynamic data for jarosite endmembers

at 298 K, 1 bar	$KFe_3(SO_4)_2(OH)_6$	$NaFe_3(SO_4)_2(OH)_6$	$(H_3O)Fe_3(SO_4)_2(OH)_6$	$KFe_3(CrO_4)_2(OH)_6$
ΔH°_f (kJ mol^{-1})	-3829.6 ± 8.3[a]	-3783.4 ± 8.3[a]	-3741.6 ± 8.3[a]	-3762.5 ± 8.0[e]
ΔG°_f (J mol^{-1} K^{-1})	388.9[b]	382.4[b]	563.5[b]	388.9[e]
S° (J mol^{-1} K^{-1})	-1648.8[a]	-1642.9[a]	-1709.1[a]	-1648.8[e]
ΔS°_f (kJ mol^{-1})	-3309.8 ± 1.7[c]	-3256.7 ± 8.4[d]	-3232.3± 8.4[d]	-3309.8 ± 1.7[f]

[a] Drouet and Navrotsky (2003)   [b] Calculated by Stoffregen (1993)   [c] Baron and Palmer (1996b)
[d] Kashkay et al. (1975)   [e] Drouet et al. (2003)   [f] Baron and Palmer (1996a)

Baron and Palmer (1996a) have calculated log K_{sp} and $\Delta G^o_{f,298}$ for the dichromate analogue of potassium jarosite [$KFe_3(CrO_4)_2(OH)_6$] to be -18.4 ± 0.6 and -3305.5 ± 3.4 kJ mol^{-1}, respectively. Drouet et al. (2003) calculated the $\Delta H^o_{f,298}$, S^o_{298}, $\Delta S^o_{f,298}$ for Baron and Palmer (1996a)'s dichromate jarosite to be -3762.5 ± 8.0 kJ mol^{-1}, 388.9 J mol^{-1} K^{-1}, and -1648.8 -3309.8 ± 1.7 J mol^{-1} K^{-1}. Table 1.3 shows recommended enthalpy and entropy values for synthetic potassium jarosite, natrojarosite, hydronium jarosite and $KFe_3(CrO_4)(OH)_6$.

1.10 Frustrated magnetism and the jarosite structure

Chemists and physicists are particularly interested in jarosites, as they supply the best models for Kagomé antiferromagnets (Wills et al. 2000). The magnetic properties of the jarosite structure are produced by two-dimensional layers of octahedrally coordinated Fe(III) ions that lie on the vertices of a Kagomé network. Kagomé type lattices, of which jarosite is one, comprise of a network of vertex sharing triangles in two dimensions. The organisation of these triangles on a regular lattice leads to geometrical frustration. The combination of antiferromagetic interactions and a Kagomé lattice in a structure such as jarosite leads to interesting frustration effects, such as the reduction of magnetic ordering, exotic magnetic states, and frustration (Morimoto et al. 2003). Wills et al. (2000) and the references within contain a significantly more in-depth appraisal of the magnetism of jarosite-type structures.

1.11 Summary

- The general jarosite structure can accommodate a variety of toxic elements (Pb(II), Cu(II), Zn(II), As(V)) in significant quantities (wt. %), to form a wide variety of minerals.

- Jarosites are inherently unstable and will easily decompose upon removal from their stability region, through either subtle changes in pH and / or temperature.

- Currently there is no mechanistic evidence of how jarosites decompose.

- Jarosites are found in three principal environments: (1) the oxidised parts of sulphide ore deposits or barren pyritiferous rocks; (2) acid sulphate soils; and (3) clays.

- Both natural and synthetic jarosites have hydronium substitutions and Fe deficiencies. These structural defects resulted in the general formula of $AB_3(TO_4)_2(OH)_6$ being modified to $H_3O_{1-x} A_x(K, Na) B_{3-y} [(OH)_{6-3y} (H_2O)_{3y} (TO_4)_2]$.

- Batch reactor dissolution experiments are the most suitable to determine the mechanisms and breakdown products of jarosites, and to gauge the amount of potentially hazardous toxic elements released.

- Many synthetic jarosite endmembers exist; lead-bearing analogues should be synthesised by a slow addition technique to avoid $PbSO_4$ impurities.

- There are very little experimental thermochemistry data available on jarosites. Of the data available, the majority of it is for potassium jarosite and, to a much lesser extent, natrojarosite.

2 Experimental methods and materials

Chapter 2 describes the methods and materials used to synthesise five jarosite analogues including the experimental set-up used in their characterisation. A description of the method and analyses of the dissolution experiments, and an overall summary are given.

2.1 Synthesis

To gauge the degree of toxic element release (*e.g.* Pb, Cu, Zn, As) from the minerals of the jarosite subgroup, five synthetic jarosite analogues were made: potassium jarosite [$KFe_3(SO_4)_2(OH)_6$], plumbojarosite [$Pb_{0.5}Fe_3(SO_4)_2(OH)_6$], beaverite-Cu [$Pb(Fe,Cu)_3(SO_4)_2(OH)_6$], beaverite-Zn [$Pb(Fe,Zn)_3(SO_4)_2(OH)_6$] and beudantite [$PbFe_3(AsO_4)(SO_4)(OH)_6$]. The potassium jarosite analogue was added to this study to help understand the breakdown mechanisms of "pure" non-toxic jarosite.

Of the four lead-rich jarosites made for this study, *sensu stricto*, they should be referred to using their specific synthetic names (Table 1.2) (i.e. a synthetic sample of plumbojarosite should be called lead-rich jarosite); however, this convention is never practically adhered to. More commonly, jarosite endmembers are called simply either natural or synthetic, and this general rule is adopted throughout the remainder of this study.

To appraise the crystal chemistry of the synthetic jarosites, natural samples of potassium jarosite, plumbojarosite, and beaverite were obtained in varying degrees of quality and quantity from the mineral collection of the Natural History Museum. Similar characterisation techniques were used on both synthetic and natural jarosite samples, described in more detain in section 2.2. Due to very restrictive quantities of some of the natural samples, it was not possible to characterise them as fully as the synthetic samples. Generally, combinations of techniques were used, ultimately dictated by sample requirements.

Aldrich Reagent-grade chemicals were used for all syntheses, except for arsenic acid (H_3AsO_4) which was received as a gift from William Blythe Ltd., Accrington, Lancashire, UK. Figure 2.1 is a schematic diagram of the synthesis rig; a 2 L glass Quickfit reaction vessel was immersed in a sand bath, which was heated and

magnetically stirred by a hot plate stirrer. An external temperature probe was used to control the temperature of the solution. A spiral condenser minimised solution evaporation, and lead sulphate was added via a separating funnel, both were attached to the lid of the reaction vessel by one of its appendages. Table 2.1 summaries the initial reactant concentrations for the five synthetic jarosite analogues.

Table 2.1. Synthesis conditions

(mol L^{-1})	Potassium Jarosite	Plumbojarosite	Beaverite-Cu	Beaverite-Zn	Beudantite
KOH	1.0	-	-	-	-
Pb(NO$_3$)$_2$$^\blacklozenge$	-	0.03	0.03	0.03	0.03
Fe$_2$(SO$_4$)$_3$·5H$_2$O	0.351	0.054	0.054	0.054	0.054
CuSO$_4$·5H$_2$O	-	-	0.315	-	-
ZnSO$_4$·7H$_2$O	-	-	-	0.306	-
H$_3$AsO$_4$	-	-	-	-	0.00946
H$_2$SO$_4$	-	0.01	0.02	0.02	-

$^\blacklozenge$ Pb(NO$_3$)$_2$ concentration is that of a 200ml solution.

2.1.1 Potassium jarosite

Potassium jarosite was synthesised according to the methods of Baron and Palmer (1996b). A 100 ml solution of 1.0 M KOH and 0.351 M Fe$_2$(SO$_4$)$_3$·5H$_2$O was heated to 95°C with constant stirring at 400 rpm in a covered 400 ml beaker at 1 atm. After 4 hrs, the precipitate was allowed to settle and the residual solution was decanted. The precipitate was then thoroughly washed with ultrapure water (18 MΩ cm^{-1}) and dried at 110°C for 24 h.

2.1.2 Plumbojarosite

The synthesis of plumbojarosite was based on the work of Dutrizac and Kaiman (1976) and Dutrizac et al. (1980). To prepare plumbojarosite, a one litre solution containing 0.054 M Fe$_2$(SO$_4$)$_3$·5H$_2$O and 0.01 M H$_2$SO$_4$ was heated to 95°C with constant stirring at 400 rpm in a 2 L glass reaction vessel at 1 atm. When the solution reached 95°C, a 200 ml solution of 0.03 M Pb(NO$_3$)$_2$ was slowly added at a rate of 6 ml hr^{-1}. Once all the Pb(NO$_3$)$_2$ had been added, the precipitate was allowed to settle and the residual solution was decanted. The precipitate was then thoroughly washed with ultrapure water (18 MΩ cm^{-1}) and dried at 110°C for 24 h.

Figure 2.1. Schematic diagram of the synthesis rig used to make the lead-bearing jarosites.

2.1.3 Beaverite-Cu/Zn

For the two end-members of beaverite, Cu and Zn, their synthesis was based on the work of Dutrizac and Dinardo (1983), and Jambor and Dutrizac (1983, 1985). Each beaverite endmember was made from a one litre solution containing 0.054 M $Fe_2(SO_4)_3 \cdot 5H_2O$ and 0.02 M H_2SO_4, with the addition of either 0.315M $CuSO_4 \cdot 5H_2O$ or 0.306 M $ZnSO_4 \cdot 7H_2O$. The solution was heated to 95°C with constant stirring at 400 rpm in a 2 L glass reaction vessel at 1 atm. When the solution reached 95°C, a 200 ml solution of 0.03 M $Pb(NO_3)_2$ was slowly added at a rate of 6 ml hr^{-1}. Once all the $Pb(NO_3)_2$ had been added, the precipitate was allowed to settle and the residual solution was decanted. The precipitate was then thoroughly washed with ultrapure water (18 MΩ cm^{-1}) and dried at 110°C for 24 h.

2.1.4 Beudantite

The synthesis of beudantite was loosely based around the work of Alcobe et al. (2001). Beudantite was made from a one litre solution containing 0.054 M $Fe_2(SO_4)_3 \cdot 5H_2O$ and 0.00946 M H_3AsO_4. The solution was heated to 95°C with

constant stirring at 400 rpm in a 2 L glass reaction vessel at 1 atm. When the solution reached 95°C, a 200 ml solution of 0.03 M Pb(NO$_3$)$_2$ was slowly added at a rate of 6 ml hr^{-1}. Once all the Pb(NO$_3$)$_2$ had been added, the precipitate was allowed to settle and the residual solution was decanted. The precipitate was then thoroughly washed with ultrapure water (18 MΩ cm^{-1}) and dried at 110°C for 24 h.

2.2   Characterisation methods

Six distinct experimental methods were used to characterise the five synthetic jarosite analogues. Combinations of four experimental methods were also used to characterise natural potassium jarosite, plumbojarosite, and beudantite. X-ray powder diffraction was used to determine phase purity. Stoichiometric analysis enabled the actual formula of the synthetic and natural jarosites to be calculated. Thermal gravimetric and differential thermal analysis gave behavioural and quantitative structural analysis of the changes to the jarosite analogues upon heating. Infrared vibrational spectroscopy provided a great deal of information about the structure and bonding. Scanning electron microscopy was used to determine particle morphology. Finally, BET analysis determined the surface area of the jarosites. The critical operating conditions for each technique are stated below. General background theory of the techniques employed can be found in Appendix A.

2.2.1 X-ray powder diffraction

Powder X-ray diffraction (XRD) patterns of the synthetic jarosites were collected in Bragg-Brentano refection geometry on a Philips PW1050 vertical powder diffractometer operated at 35 kV and 30 mA at room temperature. The diffractometer produced Co Kα_1Kα_2 radiation ($\lambda\alpha_1$ = 1.788965 Å and $\lambda\alpha_2$ = 1.792850 Å); and the X-ray tube was a long fine-focus type (0.8 x 12 mm). The starting and the final 2θ angles were 5 and 155° respectively. The step size was 0.025° 2θ and the measuring time was 10 seconds per step. The lattice parameters were calculated in collaboration with Dr A. S. Wills (UCL, University of London) through Rietveld refinement. Refinement of the lattice parameters was carried out using GSAS (Larson and Von Dreele 1998) and the 'model free' Le Bial Method (Le Bial et al. 1988) where

individual "$|F_{obs}|$"[1] are obtained by Rietveld decomposition from arbitrarily identical values. In addition to the structure factors, free refinement was made of the lattice parameters constrained according to the rhombohedral symmetry of the space group in the centred hexagonal setting, background, profile parameters, and the instrumental zero-point. In all cases, a pseudo-voigt profile made up a Lorentzian convoluted with a Gaussian was used.

A powder XRD pattern of a crystalline natural plumbojarosite sample was collected in Bragg-Brentano refection geometry on a Bruker D8 diffractometer operated at 40 kV and 40 mA at room temperature. The diffractometer was fitted with a Ge (111) monochromator, producing Cu Kα_1 radiation (λ = 1.54056). The monochromator slit was 2 mm and the exit slit was 0.6 mm. A position sensitive detector (PSD) was used. The sample was mounted on a Bruker zero background silicon (510) sample holder. The starting and the final 2θ angles were 5 and 60° respectively. The step size was 0.007° 2θ and the measuring time was 0.5 seconds per step.

2.2.2 Stoichiometric analysis

Due to hydronium incorporation and iron impurities within the jarosite subgroup the classic general formula of $AB_3(SO_4)_2(OH)_6$ is not truly representative, and the improved one devised by Kubisz (1970), $H_3O_{1-x} A_x(K, Na) Fe_{3-y} [(OH)_{6-3y} (H_2O)_{3y} (SO_4)_2]$ had to be used. The Kubisz (1970) formula requires the elemental ratios of the A- and B-site cations to be determined against sulphate, where it is assumed that there are always two sulphate units per unit formula. The exception to this is beudantite $[PbFe_3(AsO_4)(SO_4)(OH)_6]$ where there is only one sulphate unit per unit formula. For the synthetic jarosites involved in this study total elemental concentrations were required for K, Pb, Fe, Cu, Zn, As and S, where, the total values for S and As were expressed as sulphate (SO_4^{2-}) and arsenate (AsO_4^{3-}) respectively. The concentrations of these species were calculated by wet chemistry. An analytical SEM was also used to determine the elemental species present in the synthetic potassium jarosite sample.

---

[1] The quotation marks are used, as there is a bias in the partitioning of overlapping reflections according to F_{calc}.

Table 2.2. ICP-OES operating conditions

Argon coolant flow	15 l min^{-1}
Argon auxiliary flow	1.50 l min^{-1}
Argon nebuliser flow	0.80 l min^{-1}
Rf forward power	1200 W

Approximately 60 mg of each synthetic jarosite was taken to perform quantitative wet chemical analysis. Each precipitate was dissolved in a polypropylene beaker by adding HCl dropwise, until no solid remained. Afterwards the dissolved samples were made up to volume with 2 % HNO$_3$. The solutions were analysed for their individual species, a combination of K, Pb, Fe, Cu, Zn, As or S by an inductively coupled plasma optical emission spectrometer (ICP-OES) on a Varian Vista-Pro (axial), using a simultaneous solid-state detector (CCD). Table 2.2 shows the standard ICP-OES operating conditions and Table 2.3 shows which spectral lines were used to calculate the total elemental concentrations and their overall detection limits.

Table 2.3. ICP-OES spectral wavelengths for elemental species and their overall detection limits

Elemental Species	Spectral Wavelengths (detection limits)
K	766.491, 769.897 nm (10 ppb)
Fe	234.350, 238.204, 261.187 nm (0.05 ppb)
S	180.669, 181.972, 182.562 nm (10 ppb)
Pb	182.143, 217.000, 220.353, 283.305 nm (5 ppb)
As	188.980, 193.696, 197.198, 228.812, 234.984 nm (25 ppb)
Cu	213.598, 223.009, 324.754, 327.395 nm (1 ppb)
Zn	202.548, 206.200, 213.857, 330.258, 334.502 nm (2 ppb)

The stoichiometry of synthetic potassium jarosite was also determined indirectly by an analytical SEM. For this technique some of the synthetic jarosite was mounted into a cylindrical block (Ø25 mm) of SPECIFIX epoxy resin. Once hardened the block was polished and the sample surface was coated in carbon. The sample was then placed into a Jeol JSM-5900LV SEM combined with an Oxford Instruments INCA system energy dispersive X-ray spectrometer (EDX) backscatter detector, where the accelerating voltage was 20 kV. The analysis calculated K, Fe and S in compound weight percent.

The stoichiometry of the crystalline natural potassium jarosite and plumbojarosite were determined by quantitative elemental analysis with a Cameca SX-50 electron microprobe. Potassium bromide KBr, galena PbS, hematite α-Fe$_2$O$_3$, and barium

sulphate $BaSO_4$ were chosen as standards for K, Pb, Fe, and S respectively; where the analysis was calculated in compound weight percent. Similar to the synthetic sample above, the two natural samples were mounted into cylindrical blocks (Ø25 mm) of SPECIFIX epoxy resin; once hardened the blocks were polished and the sample surfaces were coated in carbon. The operating conditions for the potassium jarosite analysis were an accelerating voltage of 20 kV, current 20 nA, and a spot size of 20 μm. Due to the high water content in plumbojarosite, all three of the above operating parameters for potassium jarosite had to be reduced to avoid sample beam damage. The parameters for the plumbojarosite analysis were: accelerating voltage of 15 kV, current 15 nA, and a spot size of 10 μm.

2.2.3 Thermal gravimetric and differential thermal analysis

Thermal gravimetric (TG) and differential thermal analysis (DTA) were conducted simultaneously on a Remetric STA 1500H. Table 2.4 shows the exact starting weights of each individual sample that was heated from 25.0 to $1100^{\circ}C$ at a rate of $10^{\circ}C$ min^{-1}, under an atmosphere of argon at a rate of 30 ml min^{-1}. Data sampling occurred every second.

Table 2.4. Sample weights for TGA/DTA analysis

Synthetic analogue	Weight (mg)
Potassium jarosite	14.390
Plumbojarosite	10.590
Beaverite-Cu	14.040
Beaverite-Zn	12.960
Beudantite	7.110

X-ray diffraction analyses were preformed after heating the samples under argon to various relevant temperatures selected from the TG-DTA profiles. The powder XRD patterns were collected in Bragg-Brentano refection geometry on a Siemens D500 diffractometer operated at 40 kV and 40 mA at room temperature. Cu Kα radiation (λ = 1.54056 Å) was used in conjunction with a secondary graphite monochromator and a scintillation counter. The divergence slit was of 1° and the receiving slit of 0.05°. The samples were mounted on a Bruker zero background silicon (510) sample holder. The starting and the final 2θ angles were 10 and 70° respectively. The step size was 0.020° 2θ and the measuring time was 18 seconds per step.

2.2.4 Fourier transform infrared spectroscopy

Fourier transform infrared spectroscopy (FTIR) was used to characterize the vibrational modes present within the five synthetic jarosite samples and the natural crystalline potassium jarosite and plumbojarosite. The FTIR spectra of the synthetic jarosite analogues and the natural samples were collected with a PerkinElmer Spectrum One FTIR Spectrometer using the KBr pellet (Ø13 mm) technique. The spectrums were recorded in transmission mode immediately after pellet preparation; the range was $400 - 4000$ cm^{-1} wavenumbers with a resolution of 4 cm^{-1}, and five scans were accumulated.

2.2.5 Scanning electron microscopy

A Philips XL30 FEG scanning electron microscope (SEM) was used to determine the particle morphology of the synthetic jarosites and of natural potassium jarosite, plumbojarosite, and beaverite. Each sample was mounted on an Ø5 mm aluminum stub by araldite adhesive, once dry the samples were coated in 95 % Au and 5 % Pd. The operating conditions for the SEM were typically 7.0 kV accelerating voltage, at a spot size of 2.0 and an SE detector was used. Each electron micrograph shown in this thesis has its individual operating characteristics superimposed upon it.

2.2.6 Surface area

A Micromeritics Gemini III 2375 Surface Area Analyser was used to determine the surface area of the synthetic jarosites from this study. Each sample was de-gassed in N_2 for 24 h at 100°C prior to analysis. The surface areas were calculated through a multi-point (5 points) Brunauer, Emmett, and Teller (BET) method using N_2 gas as the absorbate.

2.3 Dissolution experiments

One of the primary objectives of this study was to gauge the degree of toxic element release from five synthetic jarosites by determining their solubility through dissolution. Due to time constraints, it was not possible to investigate the solubility of either beaverite-Cu or –Zn. A series of dissolution experiments were ultimately undertaken for potassium jarosite, plumbojarosite, and beudantite in both acid and alkali regimes. The acid regime was designed to mimic an environment that had been devastated by acid mine/rock (AMD/ARD) drainage, where the surface waters had

very low pH and were highly oxic. The alkali regime was created to resemble an environment that had been recently remediated with slaked lime $(Ca(OH)_2)$. Calcium hydroxide is commonly used in industry to raise the pH of polluted AMD/ARD waters to values close to neutral (Roca et al. 1999, Miller et al. 2003). Another critical objective of this study was to characterise any new phases formed as a result of these dissolution experiments using a number of different surface- and whole-mineralogical techniques. This section, therefore, is split in two; the first part describes the experimental set-up of the dissolution experiments and the second concentrates on the techniques used to analyse the aqueous and residual solid fractions produced due to the dissolution process.

2.3.1 Batch reactor configuration

All dissolution experiments carried out in this study were of a batch reactor design (Figure 2.2). The general experimental set-up was influenced by the work of Baron and Palmer (1996b).

Figure 2.2. Picture of the batch reactor set-up for all dissolution experiments, where the rollers rotated at a fixed speed of 33 rpm, and rose and fell 16 mm.

100 mg of each synthetic jarosite was added to 500 ml of ultrapure water (18 MΩ cm^{-1}). For the acid dissolution, the initial pH was set to 2.0 by the addition of concentrated $HClO_4$. In the alkali dissolution, the initial pH was adjusted to 8.0 by the addition of a 0.01 M solution of $Ca(OH)_2$. The experiments were not buffered and this resulted in free drift pH conditions. The experiments were conducted at 20°C and at 1 atm. All pH measurements were taken on an Accument AP50 meter in conjunction with a Russel Emerald pH electrode where the meter and electrode were calibrated by a 3-point calibration, at values of 4.003, 7.002 and 9.993 after temperature correction. The solutions were transferred to 750 ml pre-acid washed Amber HDPE plastic bottles, where they were stirred upon a Stuart SRT2 Roller Mixer (Figure 2.2). The rollers rotated at a fixed speed of 33 rpm, and they rose and fell 16 mm. Samples from the bulk solution were extracted at periodic intervals; Table 2.5 illustrates the typical sampling frequency.

Table 2.5. General dissolution sampling rate

No of weeks	Sampling rate
1-3	Daily
3-6	Every 2 days
6-10	Every 4 days
10-12	Every week
12-14	Every 2 weeks

To make sure that the bulk solutions had been sampled, an overhead stirrer (~ 50 rpm) kept the overall mixture in suspension. The samples consisted of a 10 ml aliquot that had been removed from the bulk solution by pipette. The aliquot was filtered through a 0.025 μm MF Millipore filter via a syringe. A 4.5 ml aliquot of filtered sample was then acidified to make a 1 % v/v HNO_3 matrix, and was used for Fe_{tot}, K_{tot}, Pb_{tot}, Zn_{tot}, Cu_{tot}, As_{tot} and S_{tot} analysis, depending on the type of jarosite being dissolved. The remainder of the filtered solution (un-acidified) was used to determine both $SO_4^{2-}{}_{tot}$ and $AsO_4^{3-}{}_{tot}$. The pH of the bulk solution was measured during each sampling episode. At the end of each experiment, the residual jarosite solid was recovered by filtration on a 0.22μm MF Millipore filter. The residual solids were then left to air dry in a desiccator, and stored in a plastic vial. All experiments were conducted in triplicate.

2.3.2 Analysis

General background theory of the techniques employed can be found in Appendix A.

Aqueous species determination

Total concentrations of Fe, K, Pb, Zn, Cu, As and S were calculated by an ICP-OES on a Varian Vista-Pro (axial), using a simultaneous solid state detector (CCD). Operating conditions were identical to those reported in Section 2.2.2.

High-performance liquid chromatography (HPLC) was employed to calculate the sulphate concentrations (SO_4^{2-}). The machine used was a DIONEX DX-300 System, with a pulsed electrochemical detector (PED), and operating conditions were flow rate, 2.0 ml min^{-1}, a Na_2CO_3 / $NaHCO_3$ eluent, and an anion column.

Arsenate (AsO_4^{3-}) concentrations were calculated on an ion pair (IP) reverse phase (RP) narrow-bore HPLC coupled on-line with an inductively coupled plasma mass spectrometer (ICP-MS). Wangkarn and Pergantis (2000) devised the HPLC-ICP-MS technique used in this study, and the analysis was carried out in collaboration with Dr S. Pergantis (Birkbeck, University of London). The ICP-MS was a VG PlasmaQuad III with a quadrupole mass analyser operated in single-ion monitoring mode (*m/z* 75) for detecting arsenic, and in the peak jump mode (*m/z* 75 and 77) was used for detecting arsenic and monitoring argon-chloride interferences. A Micromist low-uptake nebuliser was attached to the ICP-MS water-cooled spray chamber. A narrow-bore HPLC stainless steel column was connected to the Micromist nebuliser via PEEK tubing (90 cm long x 0.13 id). A displacement pump (Rheos 4000, Flux Instruments, Basel, Switzerland) was used to the deliver mobile phase into the ICP-MS at a flow rate of 0.7 ml min^{-1}. Samples were injected onto the narrow-bore HPLC column via a micro-injector fitted with a 1.0-μl internal chamber (Rheodyne 7520, Cotati, CA, USA). An in-line 2-μl filter was placed between the injector and the HPLC column. The total arsenic speciation run took approximately 2 minutes. Table 2.6 shows the typical ICP-MS and LC conditions.

Unfortunately, the HPLC-ICP-MS analysis to determine arsenate concentrations proved inconclusive, as some of the samples came back positive for arsenite, the As^{3+} valence state of arsenic. A plausible explanation for the reduction of the base unit of arsenic in beudantite from arsenate to arsenite during the HPLC-ICP-MS analysis is

particle micro-bacterial reduction. It is thought the bacteria may have come from the ultra pure deionised water (Pergantis per comm. 2003). Considering that the arsenic in beudantite is in the form of arsenate, and the experiment was conducted in a highly oxidising environment, it is highly likely that the major As species in the dissolution solutions is As^{5+} in the form of the arsenate anion. The arsenate values used to plot Figures 4.4 and 5.4 have been calculated based on total arsenic concentrations determined by ICP-OES.

Table 2.6. ICP-MS and LC conditions for arsenate species determination

ICP-MS conditions-	
Argon coolant flow	12.5-14.5 l min^{-1}
Argon auxiliary flow	0.4-0.6 l min^{-1}
Argon nebuliser flow	0.76-0.80 l min^{-1}
Rf forward power	1350 W
Nebuliser	Micromist nebuliser
Spray chamber	Water cooled (5°C) impact bead type
Sample cone	Nickel; aperture diameter 1.0 mm
Skimmer cone	Nickel; aperture diameter 0.75 mm
Data acquisition mode	Single ion monitoring or peak jump mode
LC conditions-	
Column	Discovery C$_{18}$ (150 mm x 2.1 mm id)
Mobile phase	5, 10, or 15mM tetrabutylammonium hydroxide, pH 5.25-7.0
Mobile phase flow rate	0.7 ml min^{-1}

Residual solid characterisation

Solid phase identifications were attained from powder XRD patterns in Bragg-Brentano refection geometry on a Siemens D500 diffractometer operated at 40 kV and 40 mA at room temperature. Cu Kα radiation (λ = 1.54056 Å) was used in conjunction with a secondary graphite monochromator and a scintillation counter. The divergence slit was of 1° and the receiving slit of 0.05^{o}. The samples were mounted on a Bruker zero background silicon (510) sample holder. The starting and the final 2θ angles were 10 and 70° respectively. The step size was 0.020^{o} 2θ and the measuring time was 18 seconds per step.

Quantitative wet chemical analyses (by ICP-OES, see Section 2.2.2 for operating conditions) of the residual solids were performed to calculate total concentrations of K, Pb, Fe, S, and As. From these concentrations, molar ratios were calculated for each individual residual solid so that they could be compared to the original stoichiometry of the corresponding synthetic jarosite.

To see how the particle morphology might have changed after the dissolution of the synthetic jarosites, SEM micrographs were taken on a Philips XL30 FEG SEM. The general operating conditions were similar to those described in Section 2.2.5.

Finally, FTIR spectroscopy was performed on the solid fractions to see what effect the dissolutions might have had on the vibrational modes present within the bulk structure of the jarosites. The operating conditions for this technique were similar to those reported in Section 2.2.4.

2.4 Summary

- Five synthetic endmember jarosites were made in this study. Potassium jarosite was synthesised in a glass reaction vessel, and for the four lead-bearing jarosites (e.g. plumbojarosite, beaverite-Cu and -Zn, beudantite) a slow addition technique was used.

- Six distinctive experimental methods were used to characterise the five synthetic jarosite analogues: XRD, stoichiometric analysis, TG-DTA, FTIR, SEM, and BET surface area analysis.

- Samples of natural potassium jarosite, plumbojarosite, and beaverite were characterised by combinations of XRD, stoichiometric analysis, FTIR, and SEM.

- All dissolution experiments carried out in this study were of a batch reactor design.

- The liquid samples taken from the bulk solutions over the duration of the dissolutions were analysed for total concentrations of the aqueous species present by ICP-OES, and SO_4^{2-} by HPLC.

- The solid fractions remaining at the end of the dissolutions were recovered for phase characterisation, involving XRD, elemental analysis, SEM, and FTIR.

3   Characterisation of the synthetic jarosites

Chapter 3 is dedicated to the characterisation results and discussion of the five synthetic jarosites made for this study. The chapter consists of five sections: X-ray diffraction and formula determination, thermal analysis, Fourier transform infrared spectroscopy, morphology and surface area of the precipitates, and conclusions and summary.

3.1   X-ray diffraction and formula determination

A series of five yellow precipitates formed from the jarosite synthesis; a photograph of the precipitates and their Munsell colours are presented in Figure 3.1 and Table 3.1 respectively. The five precipitates were identified as endmember potassium jarosite, plumbojarosite, two beaverite samples, and beudantite, by comparing their powder X-ray diffraction patterns with those reported in the International Centre for Diffraction Data Powder Diffraction Files (ICDD PDF) 22-0827, 33-0759, 17-0476, and 19-0689, respectively. It should be noted that no ICDD PDF files exist for synthetic beaverite or beudantite; for this reason, ICDD PDF files for natural beaverite (17-0476) and beudantite (19-0689) were used to identify the synthetic analogues. Figures 3.2-3.6 illustrate the X-ray powder diffraction patterns of the five synthetic jarosites. All the peaks produced by the precipitates could be identified as ones relating to the structure of their individual synthetic analogues. The absence of unidentified peaks in the patterns indicated that no other phases were present at detectable levels. This is clearly seen in the Rietveld refinement profiles (Figures 3.2b-3.6b), by the fact that all the Bragg peaks from the diffraction patterns perfectly match predicted reflection markers for the individual jarosite structures. Both of the diffraction patterns for the Cu- and Zn- enriched beaverite samples could be identified as the beaverite structure from the ICDD PDF file 17-0476. The corresponding d-spacings and Miller indices for the five synthetic jarosites are given in Appendix B.

Table 3.1. Corresponding Munsell colour descriptions of the synthetic jarosites.

Synthetic analogue	Munsell colour
Potassium jarosite	10YR 8/7
Plumbojarosite	10YR 6.5/7
Beaverite-Cu	10YR 7/5
Beaverite-Zn	10YR 7/6
Beudantite	10YR 8/8

Figure 3.1. Photograph showing the subtle colour changes throughout the five synthetic jarosites, where: (a) potassium jarosite, (b) plumbojarosite, (c) beaverite-Cu, (d) beaverite-Zn, and (e) beudantite.
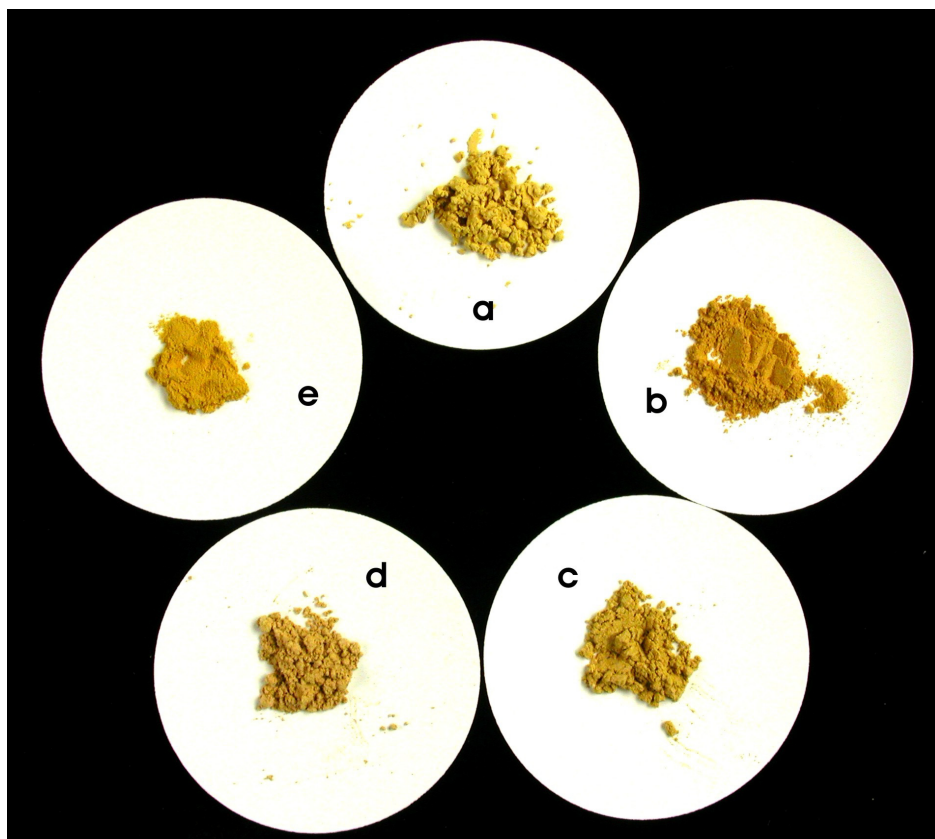
The lattice parameters of the five synthetic jarosites were calculated with Rietveld refinement using the GSAS suite of programs (Larson and Von Dreele 1998). The cell dimensions were refined on the basis that the jarosite subgroup belongs to the trigonal crystal system, in the rhombohedral class with hexagonal axes (a = b ≠ c and α = β = 90°, γ = 120°), where the space group is $R\bar{3}m$ (No. 166). The Rietveld refinement observed and calculated profiles for the five synthetic jarosites are given in Figures 3.2b-3.6b. Some of the strong Bragg reflections are not modelled that well by the pseudo-voigt profile, this is a consequence of anisotropic broadening due to crystallographic defects (the refinement of the beaverite-Zn structure shows up this problem particularly well, Figure 3.5b). In the jarosites, these are presumed to be stacking defects in the crystal structure caused by mismatch in crystallographic planes perpendicular to the hexagonal c-axis. Despite this difficulty, inspection of the individual reflections reveals that the values of the lattice parameters are not significantly affected (Wills per comm. 2004) (Table 3.2).

Synthetic Potassium Jarosite
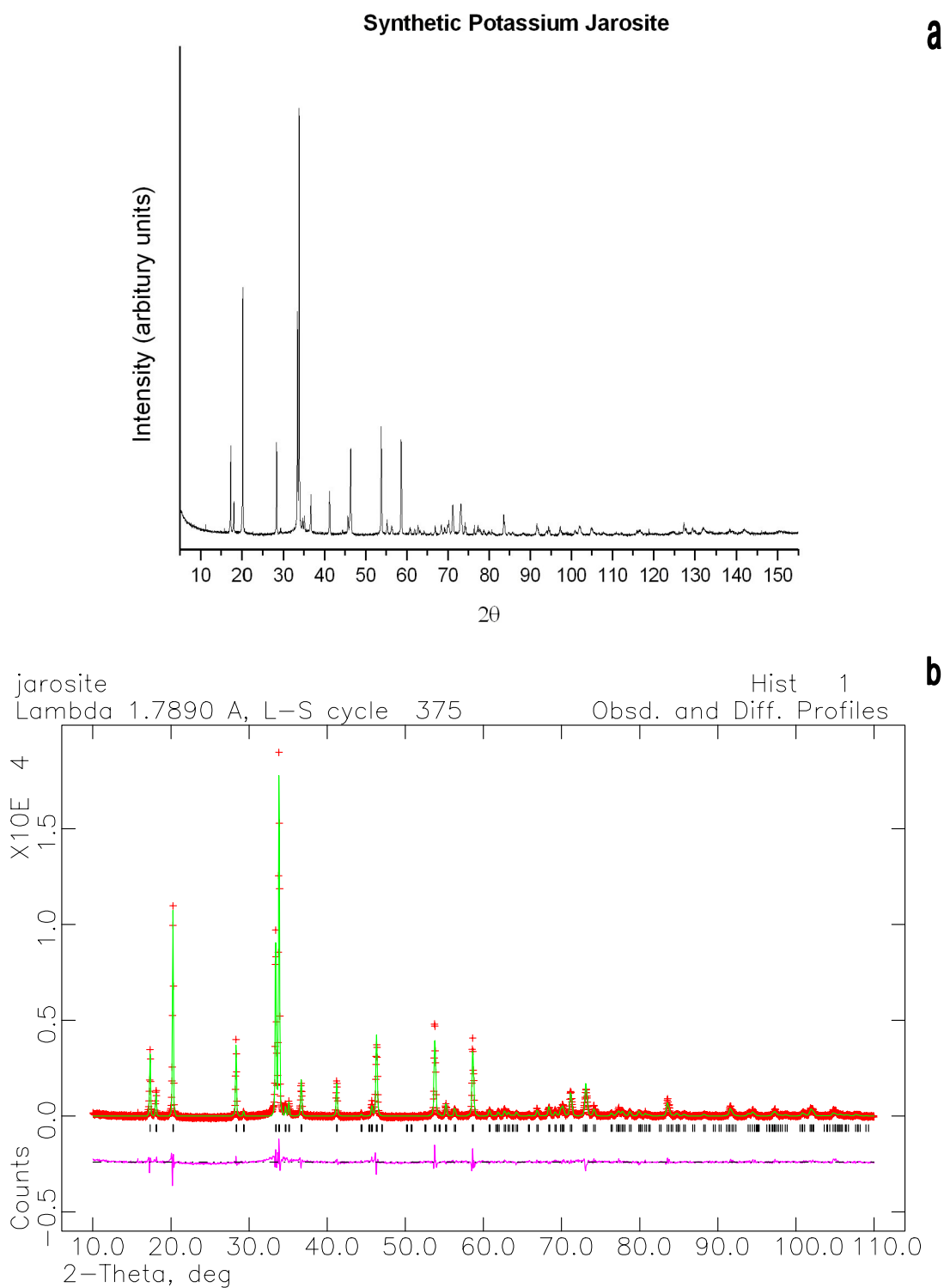
Figure 3.2. (a) Powder X-ray diffraction pattern of synthetic potassium jarosite using Co $K\alpha_1 K\alpha_2$ ($\lambda\alpha_1$ = 1.788965 Å and $\lambda\alpha_2$ = 1.792850 Å) source, 2-theta range 5-155°, step size 0.025°, step time 10s. (b) Rietveld refinement observed (red +) and calculated (green line) profiles, with a difference plot (pink line), for synthetic potassium jarosite, 2-theta range 10-110°. The vertical black lines under the Bragg peaks are the calculated reflection markers for the modelled structure.
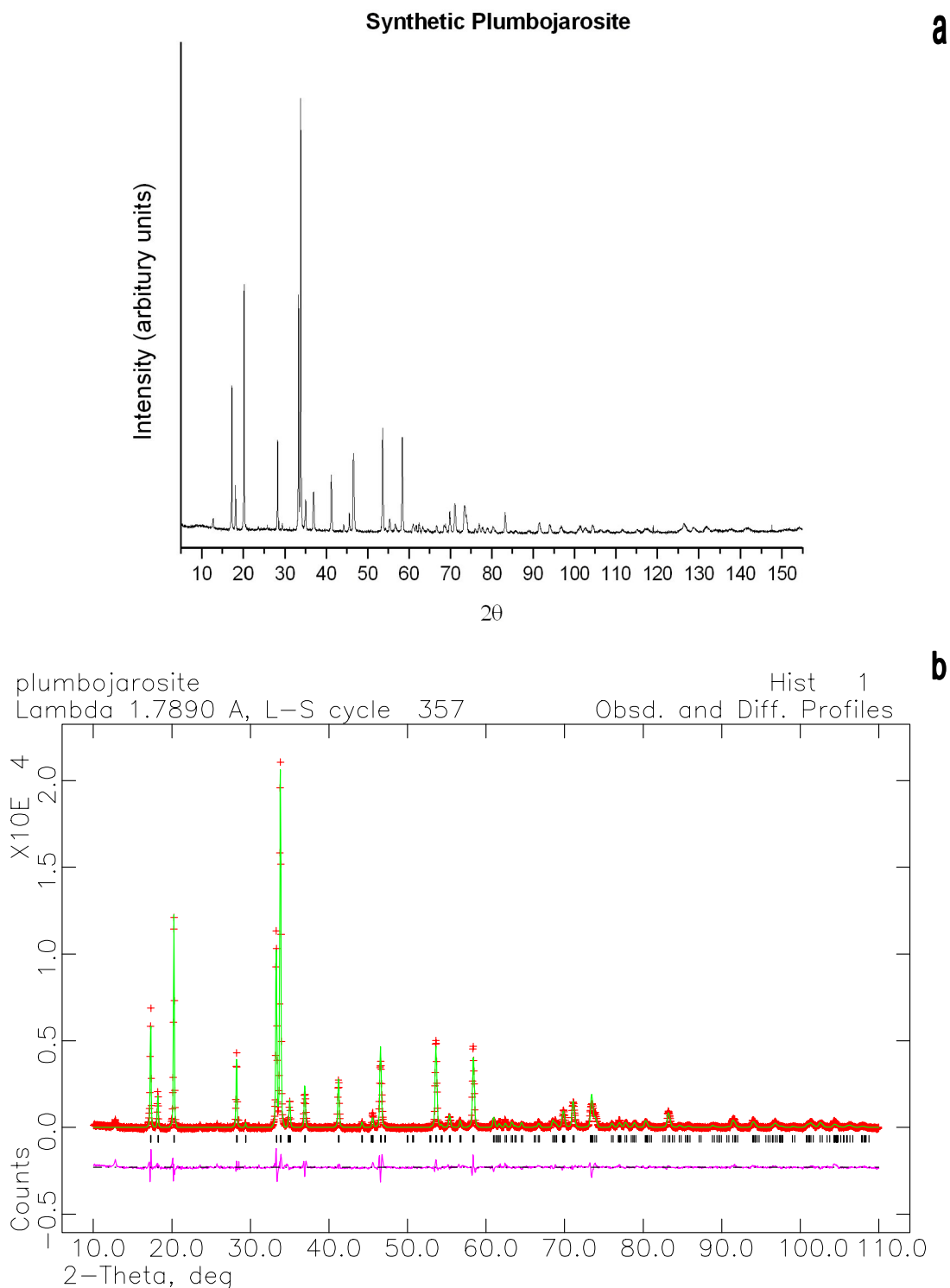
Figure 3.3. (a) Powder X-ray diffraction pattern of synthetic plumbojarosite using Co $K\alpha_1K\alpha_2$ ($\lambda\alpha_1$ = 1.788965 Å and $\lambda\alpha_2$ = 1.792850 Å) source, 2-theta range 5-155°, step size 0.025°, step time 10s. (b) Rietveld refinement observed (red +) and calculated (green line) profiles, with a difference plot (pink line), for synthetic plumbojarosite, 2-theta range 10-110°. The vertical black lines under the Bragg peaks are the calculated reflection markers for the modelled structure.
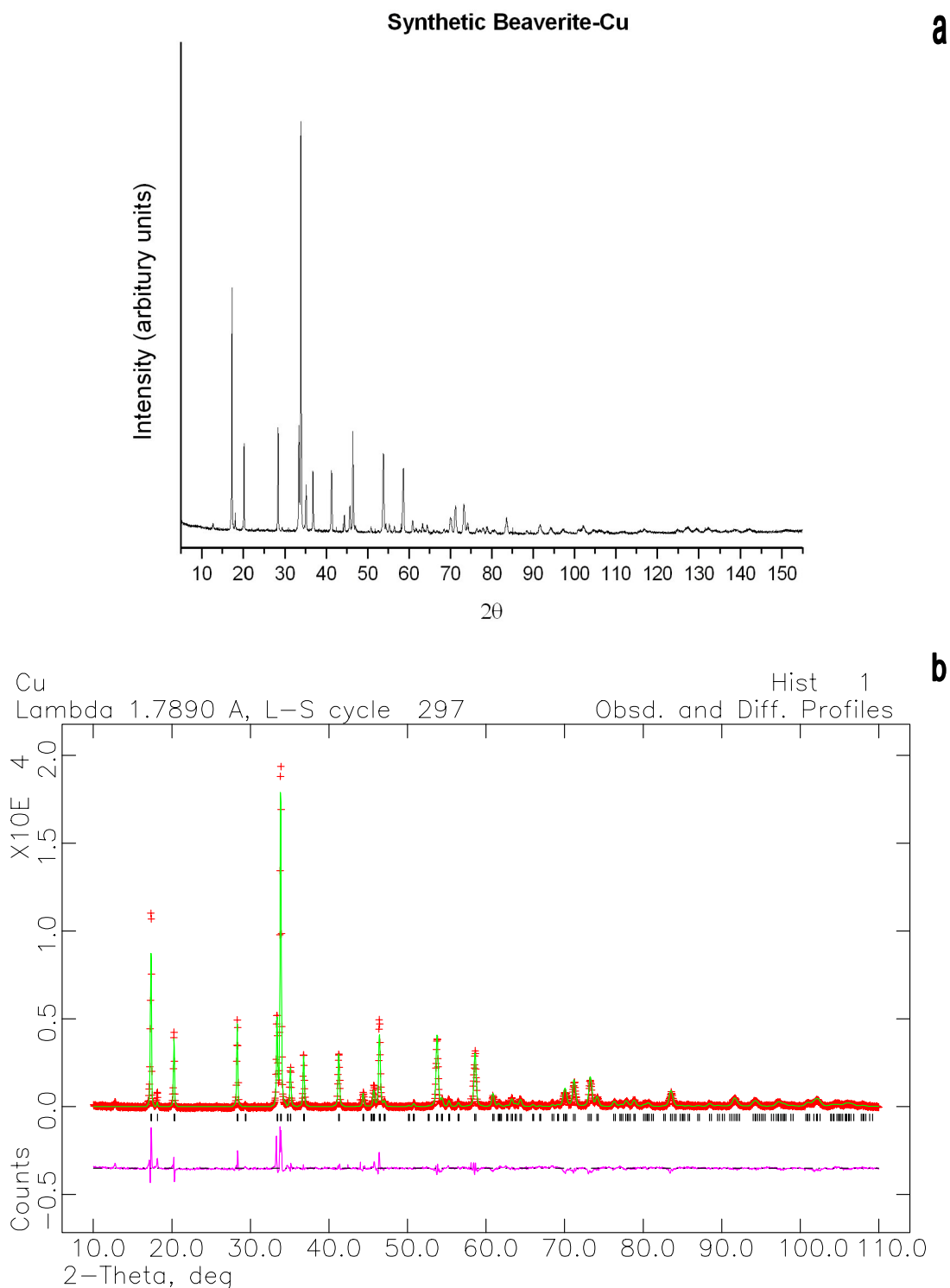
Figure 3.4. (a) Powder X-ray diffraction pattern of synthetic beaverite-Cu using Co $K\alpha_1 K\alpha_2$ ($\lambda\alpha_1 = 1.788965$ Å and $\lambda\alpha_2 = 1.792850$ Å) source, 2-theta range 5-155°, step size 0.025°, step time 10s. (b) Rietveld refinement observed (red +) and calculated (green line) profiles, with a difference plot (pink line), for synthetic beaverite-Cu, 2-theta range 10-110°. The vertical black lines under the Bragg peaks are the calculated reflection markers for the modelled structure.
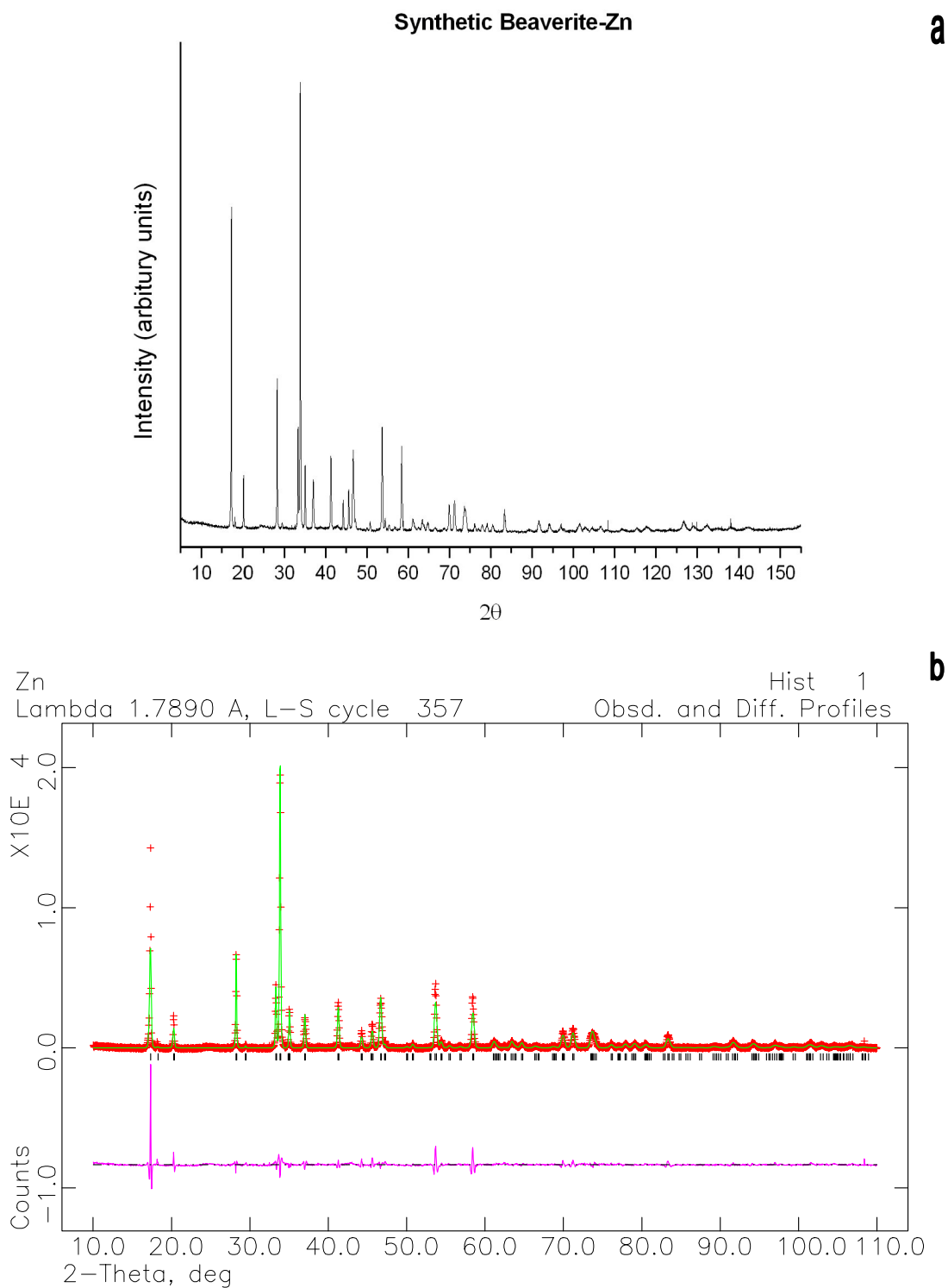
Figure 3.5. (a) Powder X-ray diffraction pattern of synthetic beaverite-Zn using Co $K\alpha_1 K\alpha_2$ ($\lambda\alpha_1 = 1.788965$ Å and $\lambda\alpha_2 = 1.792850$ Å) source, 2-theta range 5-155°, step size 0.025°, step time 10s. (b) Rietveld refinement observed (red +) and calculated (green line) profiles, with a difference plot (pink line), for synthetic beaverite-Zn, 2-theta range 10-110°. The vertical black lines under the Bragg peaks are the calculated reflection markers for the modelled structure.

Synthetic Beudantite
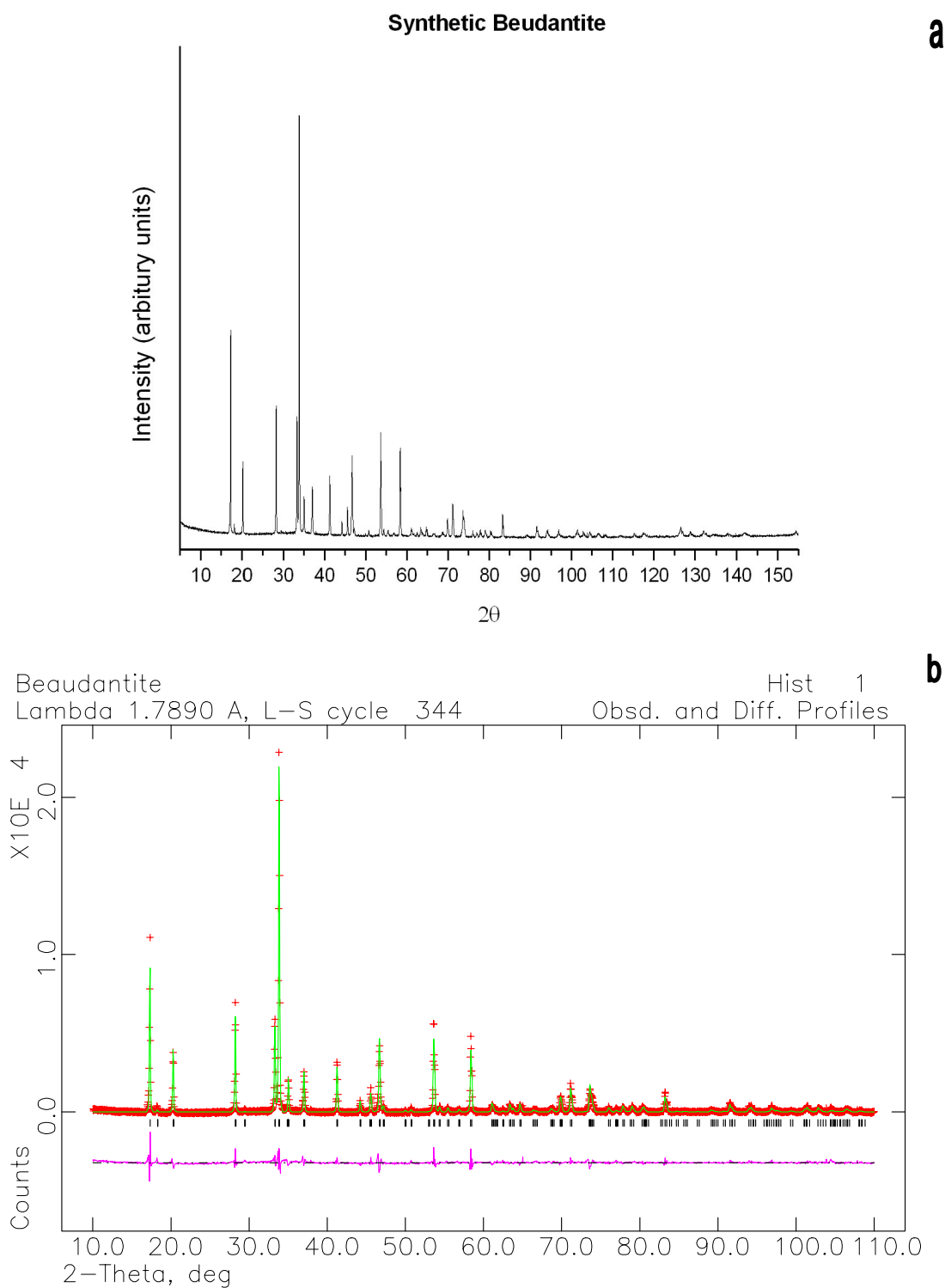
Figure 3.6. (a) Powder X-ray diffraction pattern of synthetic beaverite using Co $K\alpha_1 K\alpha_2$ ($\lambda\alpha_1 =$ 1.788965 Å and $\lambda\alpha_2 =$ 1.792850 Å) source, 2-theta range 5-155°, step size 0.025°, step time 10s. (b) Rietveld refinement observed (red +) and calculated (green line) profiles, with a difference plot (pink line), for synthetic beaverite, 2-theta range 10-110°. The vertical black lines under the Bragg peaks are the calculated reflection markers for the modelled structure.

Table 3.2 compares the calculated lattice parameters of the five synthetic jarosites to those from the standard ICDD PDF files used to identify them.

Table 3.2. Lattice parameters for the five synthetic jarosites and their corresponding dimensions stated in the ICDD PDF files.

| Compound | ICDD PDF No. | Lattice Parameters (Å) | | | |
| | | This study | | ICDD PDF | |
		a_o	c_o	a_o	c_o
potassium jarosite	22-0827	7.3137(6)	17.0730(5)	7.29	17.13
plumbojarosite	33-0759	7.3347(7)	16.9700(5)	7.335(1)	33.850(8)
beaverite-Cu	17-0476	7.3208(8)	17.0336(7)	7.20	16.94
beaverite-Zn	17-0476	7.3373(7)	16.9268(7)	7.20	16.94
beudantite	19-0689	7.3417(8)	16.9213(6)	7.32	17.02

The lattice parameters for synthetic potassium jarosite are comparable to those reported for the synthetic endmember on ICDD PDF file 22-0827. Hydronium jarosite has a_o values in the range of 7.34 to 7.36 Å, and jarosite structures with appreciable hydronium in solid solution have elongated a-axis dimensions compared to their corresponding theoretical endmember (Alpers et al. 1989). The calculated value for the c_o parameter is slightly smaller than that reported on the ICDD PDF standard. Kubisz (1970) recognised a connection between c-axis contractions and calculated deficiencies in the iron molar ratio for synthetic potassium jarosite. Kubisz (1970) proposed that the degree of contraction was a rough guide to the amount of iron deficiency that may be present within the structure, where a lower c_o implied a higher degree of deficiency away from the ideal value. The synthetic potassium jarosite appears to have very small quantities of structural hydronium present, as the a-axis value is 7.31 Å, compared with an ideal of 7.29 Å. The greatest impurity appears to arise from a small deficiency within the iron parameter.

The c_o value for synthetic plumbojarosite (Table 3.2) is noticeably different from that of the ICDD PDF standard (33-0759), in that the c-axes have not doubled in size from ~ 17 to ~ 34 Å seen in most natural samples of plumbojarosite and occasionally in synthetic samples (Jambor and Dutrizac 1985). The synthetic plumbojarosite from this study was refined with a single and a doubled unit cell, the 'goodness of fit parameter', χ^2, for the refinements was found to be lower for a single cell (2.4) rather than a doubled one (3.2). Furthermore, there were no super lattice reflections seen in the diffraction pattern (Figure 3.3) for synthetic plumbojarosite indicating a doubled unit cell. Although the A-site ions are generally thought to have little effect on a_o,

they are theoretically responsible for the main variations in c_o (Jambor and Dutrizac 1983). Jambor and Dutrizac (1985) investigated this assumption by comparing the c_o values for plumbojarosite, beaverite, and hydronium jarosite endmembers. The results were interesting in that there appeared to be an apparent lack of response of c_o to Pb(II) content, they concluded that this might arise simply because additional Pb(II) ions can be accommodated in existing A-site vacancies without disturbing the structure. In plumbojarosite only half the available A-sites are filled, but the synthetic jarosite compositions show that the structure can readily tolerate additional Pb(II), $(H_3O)^+$, or additional vacancies (Jambor and Dutrizac 1985). Jambor and Dutrizac (1985) found that less than a third of the A-sites were required to be filled by Pb(II) to attain a 34 Å c-axis. As for the synthetic plumbojarosite made for this study, the lattice parameters were nearly half of those reported for the synthetic endmember standard in ICDD PDF file 33-0759.

It was found that doubling the unit cell for Cu- and Zn-rich beaverites did not improve the overall refinement of the lattice parameters, in contrast to the work done by Jambor and Dutrizac (1983, 1985). χ^2 values for single and doubled unit cells for beaverite-Cu and beaverite-Zn were 2.57 and 5.97, and 2.45 and 4.16, respectively. Another consideration when comparing the experimental lattice parameters (Table 3.2) for the two-beaverite samples to those on ICDD PDF file 17-0476 is that the ICDD PDF standard is from a natural rather than a synthetic sample. For this reason, discrepancies in lattice parameters would be expected due to differences in site occupancy and crystallinity. A generalised comparison can be accomplished, however, with relative certainty. Giuseppetti and Tadini (1980) carried out a structural study of osarizawaite, the isostructural alunite equivalent of beaverite. They found that Al(III), Fe(III) and Cu(II) had random occupancy in the B-sites and that a replacement of Fe(III) (r = 0.67 Å) and Al(III) (r = 0.50 Å) by Cu(II) (r = 0.83 Å) should expand the T-O-T jarosite structure mainly along a_o. The length of c_o was predicted to remain relatively constant, however, because expansion along a_o permits greater interpenetration of neighbouring sheets, thus reducing the amount of increase otherwise expected. Jambor and Dutrizac (1983) investigated synthetic beaverite with Zn(II) (r = 0.74 Å) as the only divalent ion in the B-site and found that the c-axis was similar or slightly smaller, and the a-axis larger, than that of the beaverite with Cu(II) in the B-site. Therefore, although Cu and Zn are divalent ions of similar size, their

effects on the cell parameters are distinctly different. Jambor and Dutrizac (1983) concluded that the length of a_o seemed to be governed principally by the proportion of Fe(III), Cu(II), Zn(II), and the total number of ions in the B-site. When comparing the two synthetic beaverite samples to that of the ICDD PDF standard, the difference in a_o is quite striking. The main reason for this is the different amounts of Fe(III), Cu(II), Zn(II) in the B-site; the natural sample will probably have fewer vacancies and therefore higher site occupancy in comparison to the synthetic.

Looking at the diffraction patterns of the two-beaverite samples in detail, it can be recognised that the beaverite-Zn pattern has slightly shifted to both higher and lower 2-theta angles compared to the beaverite-Cu profile (Figure 3.7). The peak shifts can be explained once again by the different cations, in the B-site (Cu(II) or Zn(II)). Generally, these peak shifts account for the difference in lattice parameters between the two-beaverite samples (Table 3.2).
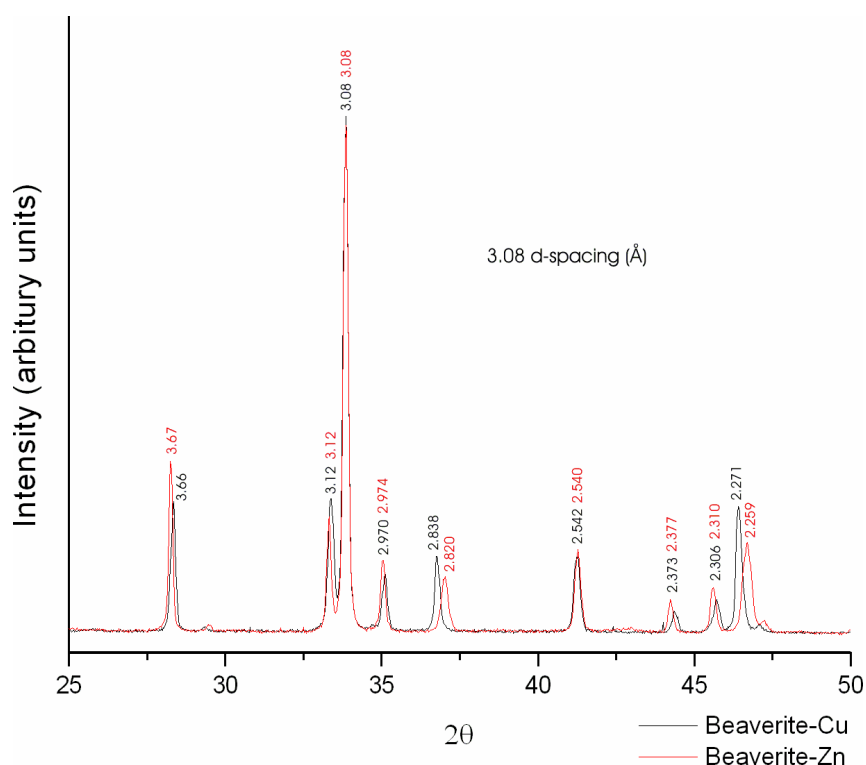
Figure 3.7. Superimposed powder X-ray diffraction patterns of synthetic beaverite-Cu and beaverite-Zn. The figure shows the peak shift of beaverite-Zn to higher 2-theta values in comparison to beaverite-Cu, this illustrates the implications of changing the B-site cation in the beaverite structure on the powder diffraction profile. d-spacings have been indicated for the strongest peaks.

The beudantite synthetic sample also shows no evidence of doubling of the c-axis (χ^2 values for single and doubled unit cells were 2.3 and 4.78, respectively); these results are similar to those of Alcobe et al. (2001). The beudantite sample poses similar problems to those of beaverite, in that there is no synthetic ICDD PDF file available. In the end, a natural beudantite reference was used (ICDD PDF file 19-0689). Unlike the two synthetic beaverite samples, the beudantite sample has good unit cell agreement with the ICDD PDF standard, considering that they probably vary in crystallinity and site occupancy. The synthetic beudantite sample has the longest a-axes out of the remaining four synthetic jarosites, and this can be explained by the partial incorporation of larger arsenate units for sulphate in the T-site.

A few authors (Jambor and Dutrizac 1983, 1985; Dutrizac and Chen 2003) have reported an 11 Å (003) reflection, mostly in natural lead-rich jarosites. For synthetic analogues, the peak is commonly extremely weak or absent. Jambor and Dutrizac (1983) state that the most reliable method of detecting the 11 Å line is to use Debye-Scherrer cameras of 114.6 mm diameter, and radiation with a wavelength longer than that of copper, such as cobalt.
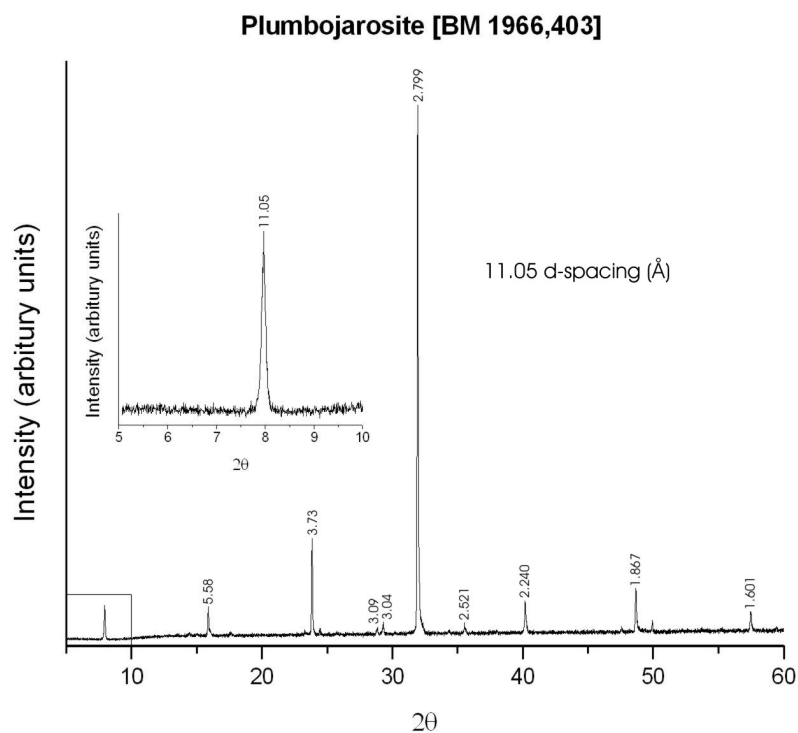
Figure 3.8. Powder X-ray diffraction of a natural plumbojarosite [BM 1966,403] using Cu Kα radiation (λ = 1.54056 Å) source, 2-theta range 5-60°, step size 0.007°, step time 0.5s. The inset diagram is a blow-up of 5-10° 2-theta, indicating an 11Å peak around 8°. d-spacings have been indicated for the strongest peaks.

When comparing the diffraction patterns of the four lead bearing synthetic jarosites (i.e. plumbojarosite, beaverite-Cu, beaverite-Zn and beudantite) (Figures 3.3-3.6); it is noticeable that none of the four patterns reveal an 11 Å reflection. For Co $K\alpha_1 K\alpha_2$ ($\lambda\alpha_1$ = 1.788965 Å and $\lambda\alpha_2$ = 1.792850 Å) radiation this 11 Å reflection should appear around 9° 2-theta. A natural sample of plumbojarosite from Tintic mine, Dividend, Juab County, Utah, USA [BM 1966,403] was analysed by X-ray diffraction (Figure 3.8), and an 11 Å reflection is clearly evident around 8° 2-theta (in this instance Cu Kα (λ = 1.54056 Å) radiation was used).

Jambor and Dutrizac (1983) synthesised two solid solutions of both beaverite endmembers, Cu or Zn, and in particular studied the relative intensity of the 11 Å powder diffraction line as they increased the lead content going from plumbojarosite to the two-beaverite endmembers. They found that the presence or absence of the 11 Å line did not seem predictable from the bulk composition of the jarosite sample. Therefore, the 11 Å reflection appeared to be independent of the total lead content in the jarosite structure. Dutrizac and Chen (2003) proposed that the 11 Å reflection, which is common in some natural examples of plumbojarosite and occasionally in synthetic samples, indicates a high degree of ordering of Pb(II) ions and vacancies. The absence of an 11 Å reflection in any of the synthetic lead-rich analogues made for this study would infer no ordering of the Pb(II) ions and vacancies within these analogues.

Due to the well-documented structural evidence (Brophy and Sheridan 1965, Kubisz 1970, Dutrizac and Kaiman 1976, Ripmeester et al. 1986, Alpers et al. 1989) that synthetic jarosites contain hydronium substitutions in the A-site and vacancies on the B-site, the general formula of $AB_3(TO_4)(OH)_6$ is not strictly representative. To appreciate the structural implications of these defects, Kubisz (1970) wisely modified the 'classic' general formula to $H_3O_{1-x} A_x(K, Na) B_{3-y} [(OH)_{6-3y} (H_2O)_{3y} (TO_4)_2]$. This formula is calculated based on SO_4 = 2, since this yields the most consistent interpretations from both the chemical and structural points of view (Jambor and Dutrizac 1985). The quantity of hydronium substitution, which cannot be directly measured, for lead or other alkali-site elements, precludes using the A-site component as the basis. The substitution of Cu(II) and Zn(II) for Fe, as well as evidence of Fe

vacancies, rules out Fe as a basis for comparison as well (Kubisz 1970, Jambor and Dutrizac 1983, 1985). The hydroxyl ion is determined by difference and is not accurately or directly known (Kubisz 1970). Therefore, SO_4 is the best species for chemical comparison and has the further advantage of being saturated in the jarosite structure; i.e., an excess or deficit of SO_4 is unlikely to be structurally tolerated (Jambor and Dutrizac 1985). For the beudantite sample, where the T-site is mixed between sulphate and arsenate, it is assumed that there is an overall 100 % site occupancy, and once the amount of structural SO_4 has been calculated, both the A- and B-sites are scaled accordingly.

For the five synthetic jarosites, atomic percentages of the A-, B- and T-site elements were determined by wet chemical analysis. Their formulae were calculated using the modified formula of Kubisz (1970) and the results presented in Table 3.3. All analytical ICP-OES results were within one standard deviation of the mean.

Table 3.3. Formulas for the synthetic jarosites calculated from elemental analysis.

Compound	Ideal formula	Actual formula
potassium jarosite	$KFe_3(SO_4)_2(OH)_6$	$(H_3O)_{0.16}K_{0.84}Fe_{2.46}(SO_4)_2(OH)_{4.38}(H_2O)_{1.62}$
plumbojarosite	$Pb_{0.5}Fe_3(SO_4)_2(OH)_6$	$(H_3O)_{0.74}Pb_{0.13}Fe_{2.92}(SO_4)_2(OH)_{5.76}(H_2O)_{0.24}$
beaverite-Cu	$Pb(Fe,Cu)_3(SO_4)_2(OH)_6$	$(H_3O)_{0.67}Pb_{0.33}Fe_{2.71}Cu_{0.25}(SO_4)_2(OH)_{5.96}(H_2O)_{0.04}$
beaverite-Zn	$Pb(Fe,Zn)_3(SO_4)_2(OH)_6$	$(H_3O)_{0.57}Pb_{0.43}Fe_{2.70}Zn_{0.21}(SO_4)_2(OH)_{5.95}(H_2O)_{0.05}$
beudantite	$PbFe_3(SO_4)(AsO_4)(OH)_6$	$(H_3O)_{0.68}Pb_{0.32}Fe_{2.86}(SO_4)_{1.69}(AsO_4)_{0.31}(OH)_{5.59}(H_2O)_{0.41}$

In the measured formula for the synthetic potassium jarosite, the most striking anomaly is the low Fe occupation at the B-site. The ideal potassium jarosite endmember stoichiometry for Fe should be 3.00, but in the sample prepared for this study it is 2.46, which is the lowest Fe occupation of all five synthetic jarosites (Table 3.3). The large number of Fe vacancies would explain the lower than expected c-axis value for this sample compared to the ICDD PDF standard, and support the hypothesis of structural defects in the A- and B-sites put forward by Kubisz (1970). A natural crystalline sample of potassium jarosite from the Margaritas mine, Mexico was analysed by quantitative electron analysis and was found to have a formula corresponding to K and Fe occupancy of 0.99 and 2.99, respectively (Table 3.4). Even for this most ideal of potassium jarosite samples, there are obviously hydronium substitutions and Fe deficiencies within its structure, ultimately similar to the synthetic potassium jarosite created for this study.

Table 3.4. Formulas for samples of natural potassium jarosite and plumbojarosite calculated from EPMA.

Compound	Ideal formula	Actual formula
potassium jarosite, Margaritas mine.	$KFe_3(SO_4)_2(OH)_6$	$(H_3O)_{0.01}K_{0.99}Fe_{2.99}(SO_4)_2(OH)_{5.97}(H_2O)_{0.03}$
plumbojarosite [BM 1966,403]	$Pb_{0.5}Fe_3(SO_4)_2(OH)_6$	$(H_3O)_{0.02}Pb_{0.49}Fe_{2.99}(SO_4)_2(OH)_{5.97}(H_2O)_{0.03}$

In the plumbojarosite structure, the Pb(II) occupancy in the A-site is set at a theoretical ideal of 0.5, in comparison to the beaverite-Cu and –Zn, or the beudantite structures that have full Pb(II) occupancy of 1.0. The crucial difference in Pb(II) occupation in plumbojarosite means that when the formula of any plumbojarosite sample is calculated, it is more likely that the A-site will be charge ordered, rather than site ordered. A-site ordering is commonly applied when calculating the formulas of the remaining three lead rich jarosites (Dutrizac and Kaiman 1976, Dutrizac et al. 1980, Jambor and Dutrizac 1983, Alcobe et al. 2001, Dutrizac and Chen 2003). Under these conditions the synthetic plumbojarosite sample made for this study has a Pb(II) occupation of 0.13, and will have 0.74 units of structural hydronium (H_3O^+) present in the A-site, so that the total charge of this site equals +1.0 (Table 3.3). A natural crystalline sample of plumbojarosite from the Tintic mine, USA [BM 1966,403] was analysed by quantitative electron analysis and was found to have a formula corresponding to Pb(II) and Fe occupancy of 0.49 and 2.99, respectively (Table 3.4). The very high Pb(II) occupancy in this natural sample means that the A-site is only deficient of 0.02 units of positive of charge; this is ultimately charge balanced with hydronium (H_3O^+). The reason why the charge ordered method is not used in jarosite structures such as beaverite or beudantite is that these structures have ideal Pb(II) occupancy of 1.0, resulting in the A-site occupying +2.0 units of charge. For a beaverite structure with a Pb(II) occupancy of 0.8, for example, the A-site would need 0.4 units of hydronium under the charge ordered method, which would result in 1.2 units of ions being present at the A-site. The A-site can theoretically only occupy 1.0 unit of ions in jarosite structures. It is for this reason why the two-beaverite and beudantite structures had their formulas calculated under a site-ordering basis, as exceeding the theoretical occupancy of the A-site is impossible (Table 3.3). The A-site will always be deficient in charge, but this is easily rectified by protonation of hydroxyl groups to form structural water.

Comparing the calculated formulae of the two synthetic beaverite samples it becomes apparent that it is possible to substitute a slightly higher concentration of Cu(II) than Zn(II) into the B-sites (Table 3.3). These results are similar to those reported by Dutrizac and Dinardo (1983), and Jambor and Dutrizac (1983, 1985). Another important feature of these formulae is that the amount of structural water present from the protonation of the hydroxyl groups is very low in comparison to the other synthesised jarosites. At first glance, these values are small, considering that they are supposedly the artefact of charge balancing the B-site vacancies. For the beaverite structures, however, these values are probably higher than those of other endmembers, due to the mixed substitution of Fe by either Cu(II) or Zn(II). For these two samples, the low amounts of structural water can be explained by a net positive charge at the A-site due to structural hydronium. Therefore, the main mechanism for charge balance of the B-site can be mainly attributed to the hydronium content at the A-site.

Table 3.5. Comparison of the formula of potassium jarosite determined by wet chemistry and analytical SEM.

Technique	Formula
Wet chemistry	$(H_3O)_{0.16}K_{0.84}Fe_{2.46}(SO_4)_2(OH)_{4.38}(H_2O)_{1.62}$
Analytical SEM	$(H_3O)_{0.12}K_{0.88}Fe_{2.50}(SO_4)_2(OH)_{4.50}(H_2O)_{1.50}$

Another method of calculating the atomic percentages required to determine the actual formula of a jarosite is analytical SEM. To appraise this technique the actual formula of synthetic potassium jarosite was determined and compared to the results from wet chemistry. The values are remarkably similar (Table 3.5), but the K and Fe concentrations were higher in the formula calculated by the analytical SEM. A known limitation in EM work, however, is that if a sample contains a large amount of structural water and if the voltage of the electron beam is set too high, some of the water can be lost during the analysis, thereby leading to substantial error in elemental quantification. Considering that the jarosite structure contains significant amounts of structural water, some of which is not strongly bound, all the formulae of the synthetic jarosites for this study were determined by wet chemical analysis. The two natural jarosite samples were instead analysed by analytical SEM, primarily because of the significantly lower amount of structural water anticipated in these highly crystalline compounds. However, if the accelerating voltage and current are too high beam damage will occur even in highly crystalline samples. Figure 3.9 shows SEM images of natural plumbojarosite crystals exhibiting the classic signs of beam burn by an

analytical SEM in the early attempts of quantitative analysis of this compound. Of the two natural jarosites analysed in this study, plumbojarosite showed by far the worst structural damage under the electron beam. Ultimately, these two natural samples would have benefited from wet chemical analysis; unfortunately sample quantity in both instances ruled this out.

Figure 3.9. SEM images of natural plumbojarosite crystals [BM 1966,403] exhibiting the classic effects of electron beam damage.
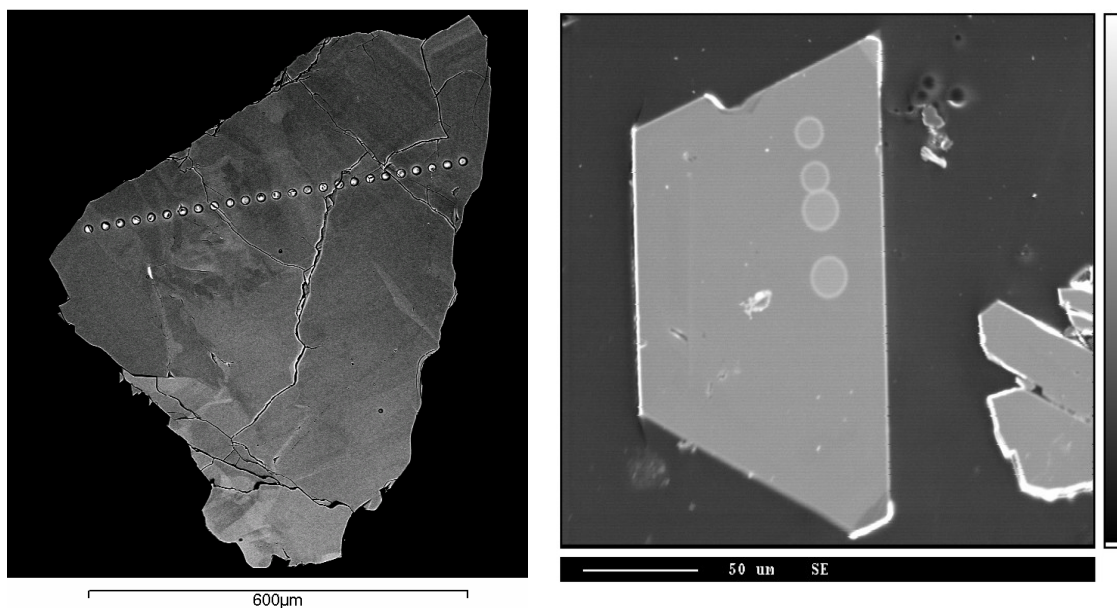
3.2 Thermal analysis

The thermal decomposition of the jarosites synthesised in this study were investigated by thermal gravimetric and differential thermal analysis (TG-DTA) performed under an Ar atmosphere up to $1100^{o}C$. Figures 3.10a-3.14a show the TG and DTA profiles of the jarosites, where weight loss and heat flow are plotted against temperature, respectively. Figures 3.10b-3.14b show the powder X-ray diffraction analyses after heating the samples under Ar to various relevant temperatures selected from the TG-DTA profiles.

3.2.1 Potassium jarosite

The total weight loss over the temperature range is 40.25 % (Figure 3.10a). The TG curve shows that the weight loss occurs over three principal temperature intervals: (1) 1.25 % weight loss between 200 and $320^{o}C$, (2) 13 % weight loss between 350 and $450^{o}C$, and (3) 26 % weight loss between 560 and $800^{o}C$. The DTA curve comprises

three significant endothermic peaks at 425, 694 and 1067°C, and a muted peak at 240°C. There are also two small exothermic peaks at 501 and 612°C.
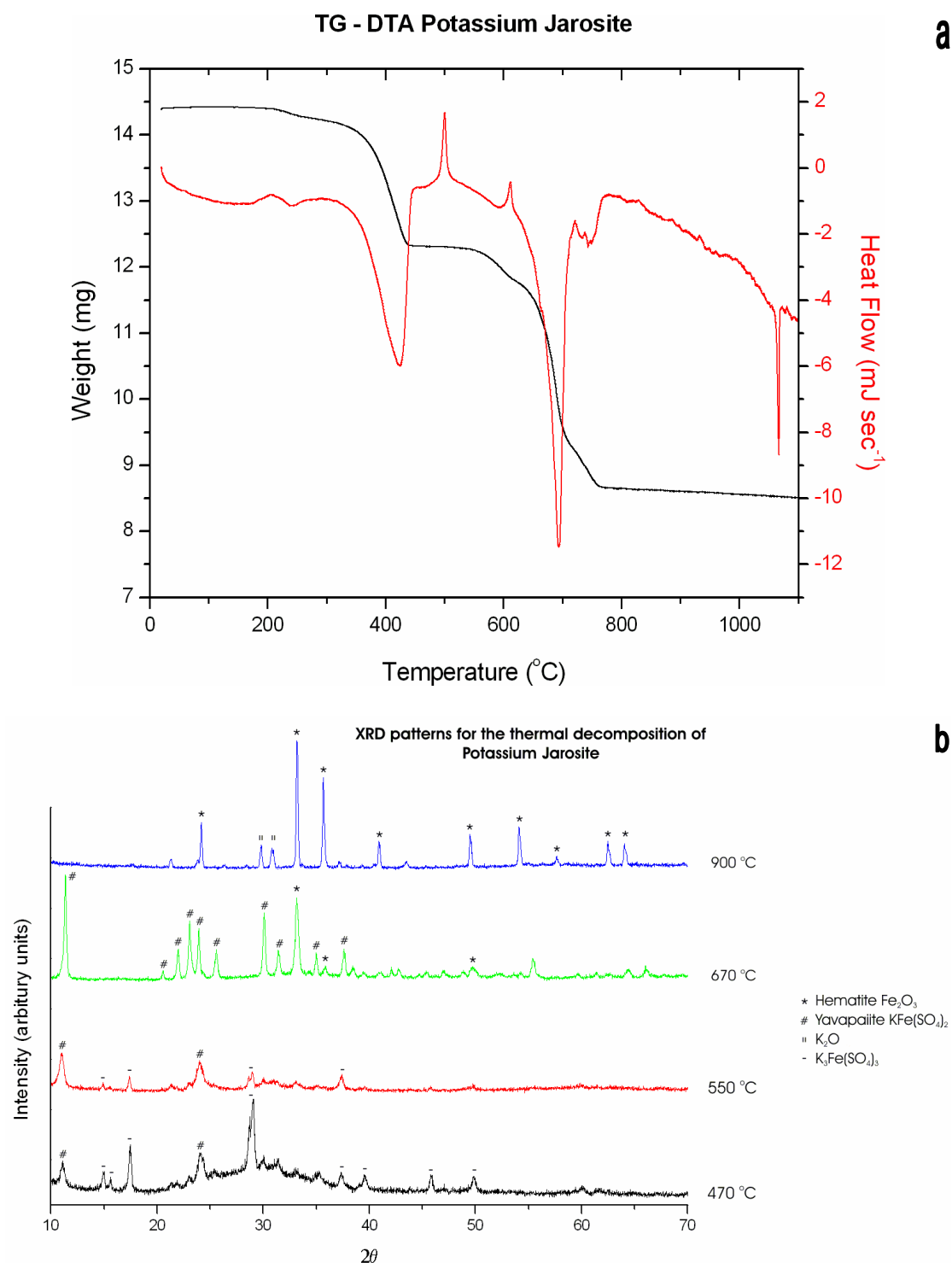
Figure 3.10. (a) Thermal gravimetric and differential thermal analysis (TG-DTA) profiles of synthetic potassium jarosite. The sample was heated from 25 to 1100°C at a rate of 10°C min^{-1}, under an argon atmosphere at a rate of 30 ml min^{-1}. Data were collected every second. (b) Powder X-ray diffraction patterns for the thermal decomposition of synthetic potassium jarosite under argon at 470, 550, 670, and 900°C. The samples were mounted on a Bruker zero background silicon (510) sample holder. Cu Kα radiation (λ = 1.54056 Å) was used, 2-theta range 10-70°, step size 0.020°, step time 18s. Identifiable phases are highlighted.

The weight loss in the interval from 200 to 320°C has usually been attributed to the loss of hydronium (Brophy and Sheridan 1965, Kubisz 1970, Alpers et al. 1989). Baron and Palmer (1996b) and Drouet and Navrotsky (2003) attributed this weight loss to the removal of H_2O molecules referred to as 'additional water'. Baron and Palmer (1996b) put forward this alternative explanation with support from Härtig et al. (1984) for the weight loss, because the resultant amount of hydronium associated with the loss of weight at these temperatures greatly exceeded the quantity of hydronium that had been calculated chemically. For this study, the 1.25 % weight loss would be equivalent to about 5 wt. % of H_2O.

The 13 % weight loss between 350 and 450°C, and an intense endothermic peak at 425°C in the DTA curve, corresponds to the dehydroxylation of the jarosite structure. For potassium jarosite, X-ray diffraction analysis indicate that yavapaiite, $KFe(SO_4)_2$, is the major crystalline phase formed during this process (Figure 3.10b). The dehydroxylation reaction for synthetic potassium jarosite made for this study can be summarised by Eq. 3.1 (Kubisz 1970, Alpers et al. 1989, Baron and Palmer 1996b, Drouet and Navrotsky 2003).

$$(H_3O)_{0.16} K_{0.84} Fe_{2.46} (SO_4)_2 (OH)_{4.38} \rightarrow$$
$$0.84 KFe(SO_4)_2 + 0.81 Fe_2O_3 + 2.43 H_2O_{(g)} + 0.32 SO_{3(g)} \quad (3.1)$$
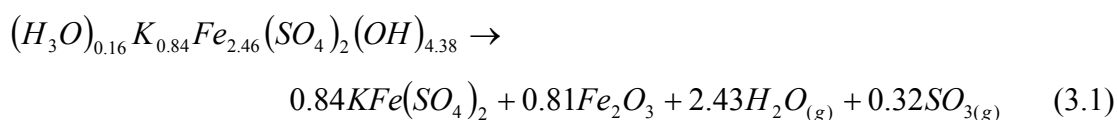
Small exothermic peaks at 501 and 612°C in the DTA curve correspond to specific phase changes (i.e. crystallisation) due to the absence of any weight loss in the TG trace (Alpers et al. 1989). XRD results for 470-550°C show diffraction peaks for hematite, indicating that the two small exothermic peaks can be assigned to the crystallisation of α-Fe_2O_3 (Figure 3.10b) (Kubisz 1971, Drouet and Navrotsky 2003). The observed 13 % weight loss is close to the expected weight loss of 15 %.

The final weight loss of 26 % between 560 and 800°C represents the thermal decomposition of yavapaiite into K_2O and α-Fe_2O_3 and the release of gaseous sulphur dioxide, probably through a reaction similar to Eq. 3.2. The final thermal decomposition phases of K_2O and α-Fe_2O_3 were confirmed by XRD analysis (Figure

3.10b). Once again, the final weight loss of 26 % is quite close to the theoretical weight loss from the stoichiometry of the sample of 28 %.

$$0.84KFe(SO_4)_2 \rightarrow 0.42Fe_2O_3 + 0.42K_2O + 1.68SO_{3(g)} \qquad (3.2)$$

The endothermic peak at 694^oC in the DTA directly relates to the release of SO_3 as observed in the TG. Finally, the sharp endothermic peak at 1067^oC in the DTA trace can be attributed to the melting of the sample.

3.2.2 Plumbojarosite

The total weight loss over the temperature range is 47.5 % (Figure 3.11a). The TG curve shows that the weight loss occurs over three principal temperature intervals: (1) 15 % weight loss between 150 and 500^oC, (2) 31 % weight loss between 500 and 1000^oC, and (3) 1.5 % weight loss between 1000 and 1100^oC. The DTA curve shows both a strong and a weak endothermic peak at 662^oC and 428^oC respectively. A series of small endothermic peaks are present between 150 and 300^oC, which are similar to the peaks reported by Ozacar et al. (2000) for a natural sample of plumbojarosite.

The 15 % weight loss between 150 and 500^oC can be attributed to two specific mechanisms. The first involves the removal of the 'additional' water within the structure, which coincides with a series of small endothermic peaks in the DTA between 150 and 300^oC (Kubisz 1971, Baron and Palmer 1996b, Drouet and Navrotsky 2003). The second, more dramatic mechanism, which contributes to the majority of the 15 % weight loss, is the breakdown of the jarosite structure through its dehydroxylation; the expected value is 14 %. XRD analysis at 490^oC identifies $Fe_2(SO_4)_3$ as the most significant phase after the removal of all the structural water (Figure 3.11b). The dehydroxylation reaction for the synthetic plumbojarosite sample can be summarised by the equation:

$$(H_3O)_{0.74} Pb_{0.13} Fe_{2.92}(SO_4)_2(OH)_{5.76} \rightarrow$$
$$0.13PbSO_4 + 0.623Fe_2(SO_4)_2 + 0.837Fe_2O_3 + 3.99H_2O_{(g)} \qquad (3.3)$$
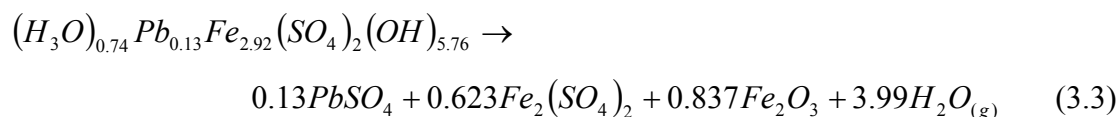
There is a small exothermic peak at 541^oC in the DTA curve, which has no corresponding weight loss. The peak can be associated with the crystallization of hematite (α-Fe_2O_3) (Figure 3.11b) (Drouet and Navrotsky 2003).
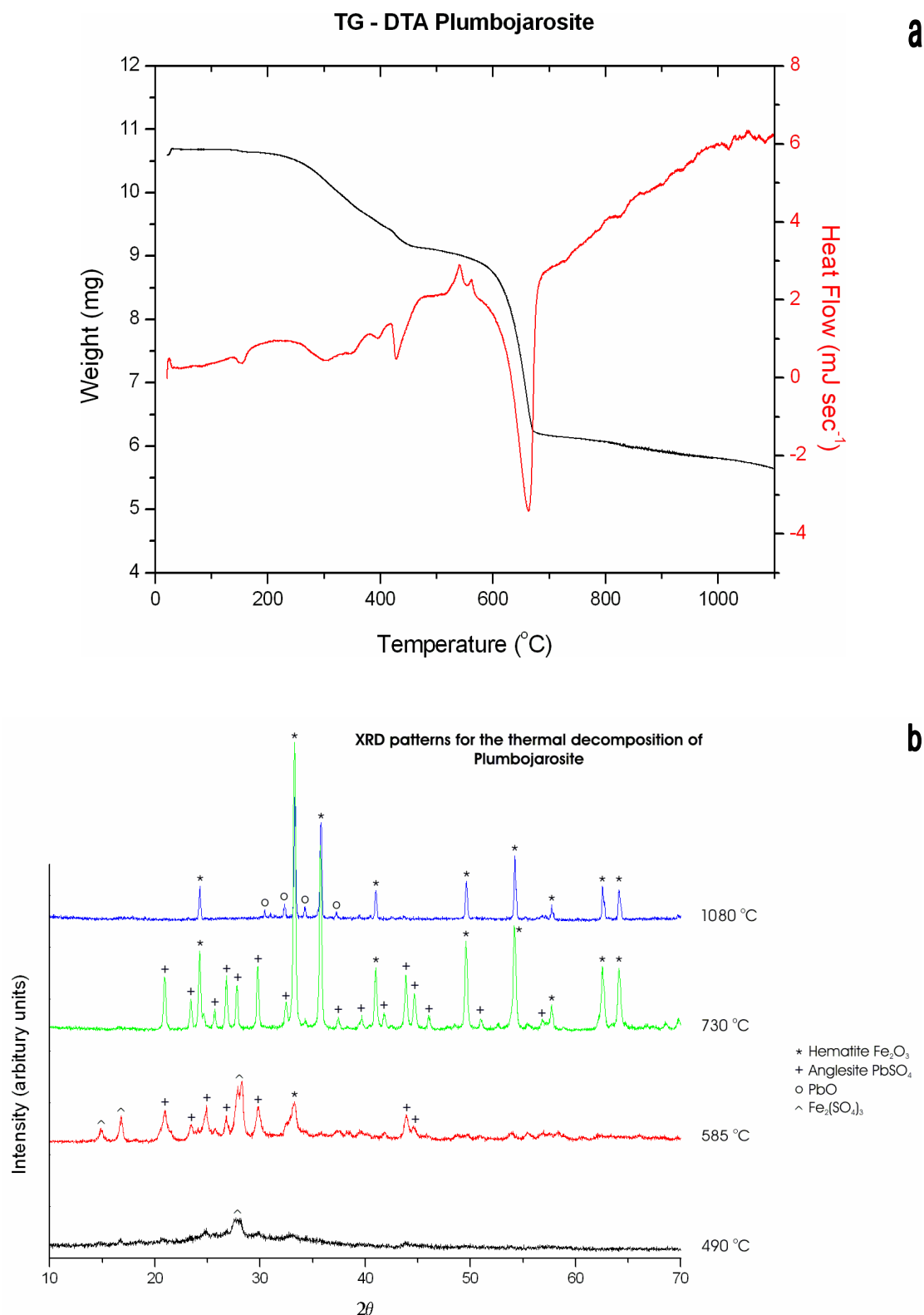
Figure 3.11. (a) Thermal gravimetric and differential thermal analysis (TG-DTA) profiles of synthetic plumbojarosite. The samples were heated from 25 to 1100°C at a rate of 10°C min⁻¹, under an argon atmosphere at a rate of 30 ml min⁻¹. Data were collected every second. (b) Powder X-ray diffraction patterns for the thermal decomposition of synthetic plumbojarosite under argon at 490, 585, 730, and 1080°C. The samples were mounted on a Bruker zero background silicon (510) sample holder. Cu Kα radiation (λ = 1.54056 Å) was used, 2-theta range 10-70°, step size 0.020°, step time 18s. Identifiable phases are highlighted.

The second and most dramatic weight loss (31 %) occurs between 500 and 1000°C; this coincides with the most intense endothermic peak in the DTA curve at 662°C. Both events are attributed to the thermal decomposition of $Fe_2(SO_4)_3$ into crystalline α-Fe_2O_3 and the release of sulphurous gas (Figure 3.11b) (Ozacar et al. 2000). The calculated weight loss for this decomposition was 30 %, and can be expressed through the reaction:

$$0.623Fe_2(SO_4)_2 \rightarrow 0.623Fe_2O_3 + 1.869SO_{3(g)} \qquad (3.4)$$
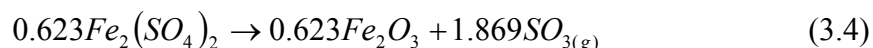
The final weight loss (1.5 %) observed in the TG curve occurs between 1000 and 1100°C. Ozacar et al (2000) proposed that this weight loss was associated with the breakdown of anglesite, $PbSO_4$ to PbO and this study has confirmed this suggestion by XRD analysis at 1080°C (Figure 3.11b) (Eq. 3.5). The expected weight loss for the decomposition of $PbSO_4$ is 2 %.

$$0.13PbSO_4 \rightarrow 0.13PbO + 0.13SO_{3(g)} \qquad (3.5)$$

3.2.3 Beaverite-Cu

The total weight loss over the temperature range is 47 % (Figure 3.12a). The TG curve shows that the weight loss occurs over four principal temperature intervals: (1) 13 % weight loss between 150 and 480°C, (2) 24 % weight loss between 480 and 780°C, (3) 6 % weight loss between 780 and 980°C, and (4) 4 % weight loss between 980 and 1100°C. The DTA curve has two intense endothermic peaks, at 420 and 646°C, and a significant peak at 668°C. At temperatures above 850°C, there is a series of three small endothermic peaks, at 864, 893, and 1040°C. There is also a small exothermic peak at 523°C.

The 13 % weight loss between 150 and 480°C is similar to that of plumbojarosite and potassium jarosite, in that between 150 to 300°C the 'additional' water is removed from within the structure (Drouet and Navrotsky 2003). The mechanism that accounts for the majority of the weight loss is the dehydroxylation. The calculated weight loss for this reaction is 13 % and is expressed as:

$$(H_3O)_{0.67}Pb_{0.33}Fe_{2.71}Cu_{0.25}(SO_4)_2(OH)_{5.96} \rightarrow$$
$$0.33PbSO_4 + 0.25CuSO_4 + 0.473Fe_2(SO_4)_2 + 0.882Fe_2O_3 + 3.984H_2O_{(g)} \qquad (3.6)$$
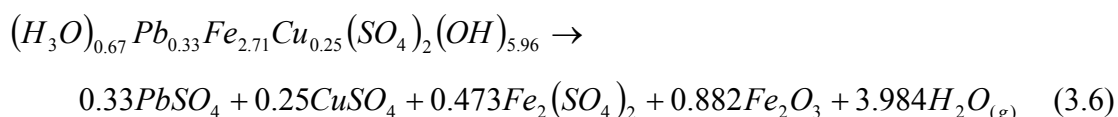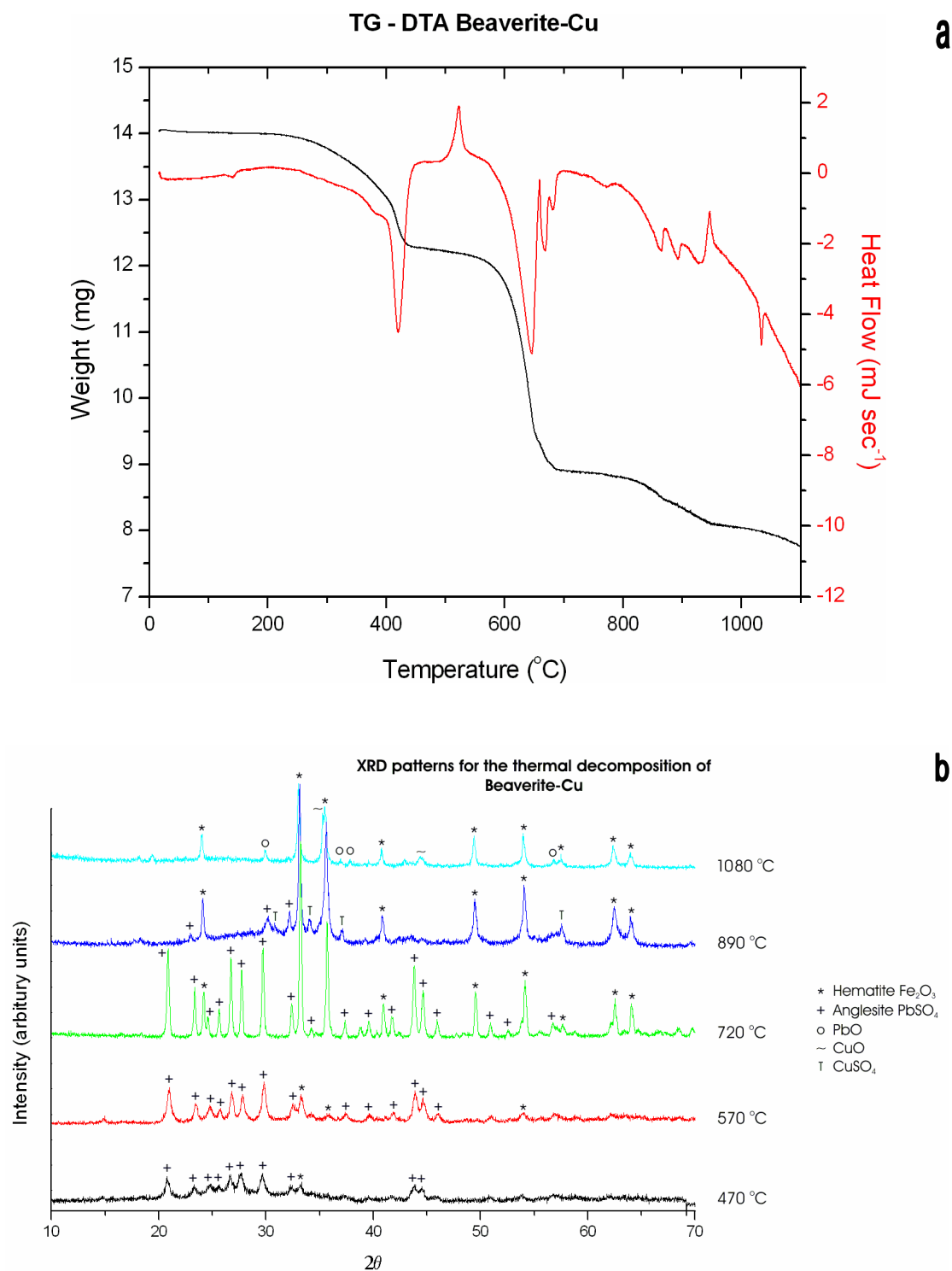
Figure 3.12. (a) Thermal gravimetric and differential thermal analysis (TG-DTA) profiles of synthetic beaverite-Cu. The samples were heated from 25 to 1100°C at a rate of 10°C min^{-1}, under an argon atmosphere at a rate of 30 ml min^{-1}. Data were collected every second. (b) Powder X-ray diffraction patterns for the thermal decomposition of synthetic beaverite-Cu under argon at 470, 570, 720, 890, and 1080°C. The samples were mounted on a Bruker zero background silicon (510) sample holder. Cu Kα radiation (λ = 1.54056 Å) was used, 2-theta range 10-70°, step size 0.020°, step time 18s. Identifiable phases are highlighted.

XRD results for 470-570°C show diffraction peaks for anglesite, $PbSO_4$, the most dominant phase after the dehydroxylation of beaverite-Cu (Figure 3.12b). There is a small exothermic peak at 523°C in the DTA curve, which has no weight loss associated with it. After XRD investigation at 570°C, the peak is assigned to the crystallisation of hematite (Figure 3.12b) (Drouet and Navrotsky 2003).

The second and largest weight loss (24 %) occurs between 480 and 780°C; this matches the most intense endothermic peak in the DTA curve at 646°C. Both events are attributed to the thermal decomposition of $Fe_2(SO_4)_3$, to α-Fe_2O_3 and gaseous SO_3, similar to that seen for plumbojarosite (Figure 3.12b) (Ozacar et al. 2000) (Eq. 3.7). The calculated weight loss from the beaverite-Cu formula is 21 %.

$$0.473Fe_2(SO_4)_2 \rightarrow 0.473Fe_2O_3 + 1.419SO_{3(g)} \qquad (3.7)$$
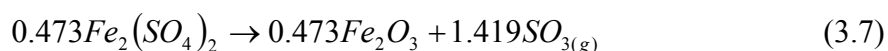
The third weight loss (6 %) occurs between 780 and 980°C, and this coincides with two small endothermic peaks at 864 and 893°C in the DTA. These events can be explained by the decomposition of $CuSO_4$ to its oxide and the subsequent release of sulphurous gas (Eq. 3.8), where the expected weight loss is 4 %. This reaction is confirmed by XRD analysis (Figure 3.12b).

$$0.25CuSO_4 \rightarrow 0.25CuO + 0.25SO_{3(g)} \qquad (3.8)$$

The final weight loss (4 %) observed in the TG trace occurs between 980 and 1100°C, within this temperature window there is a small endothermic peak at 1040°C in the DTA curve. This weight loss is associated with the breakdown of anglesite to PbO (Figure 3.12b) (Eq. 3.9). The expected weight loss for the decomposition of $PbSO_4$ is 5 %.

$$0.33PbSO_4 \rightarrow 0.33PbO + 0.33SO_{3(g)} \qquad (3.9)$$

3.2.4 Beaverite-Zn

The total weight loss over the interval is 43 % (Figure 3.13a). The TG curve shows that the weight loss occurs over three principal temperature intervals: (1) 12 % weight loss between 150 and 460°C, (2) 21 % weight loss between 460 and 800°C, and (3) 10 % weigh loss between 800 and 1100°C. The DTA trace has two intense endothermic peaks at 414 and 626°C. Other noticeable small endothermic peaks occur at 859, 911,
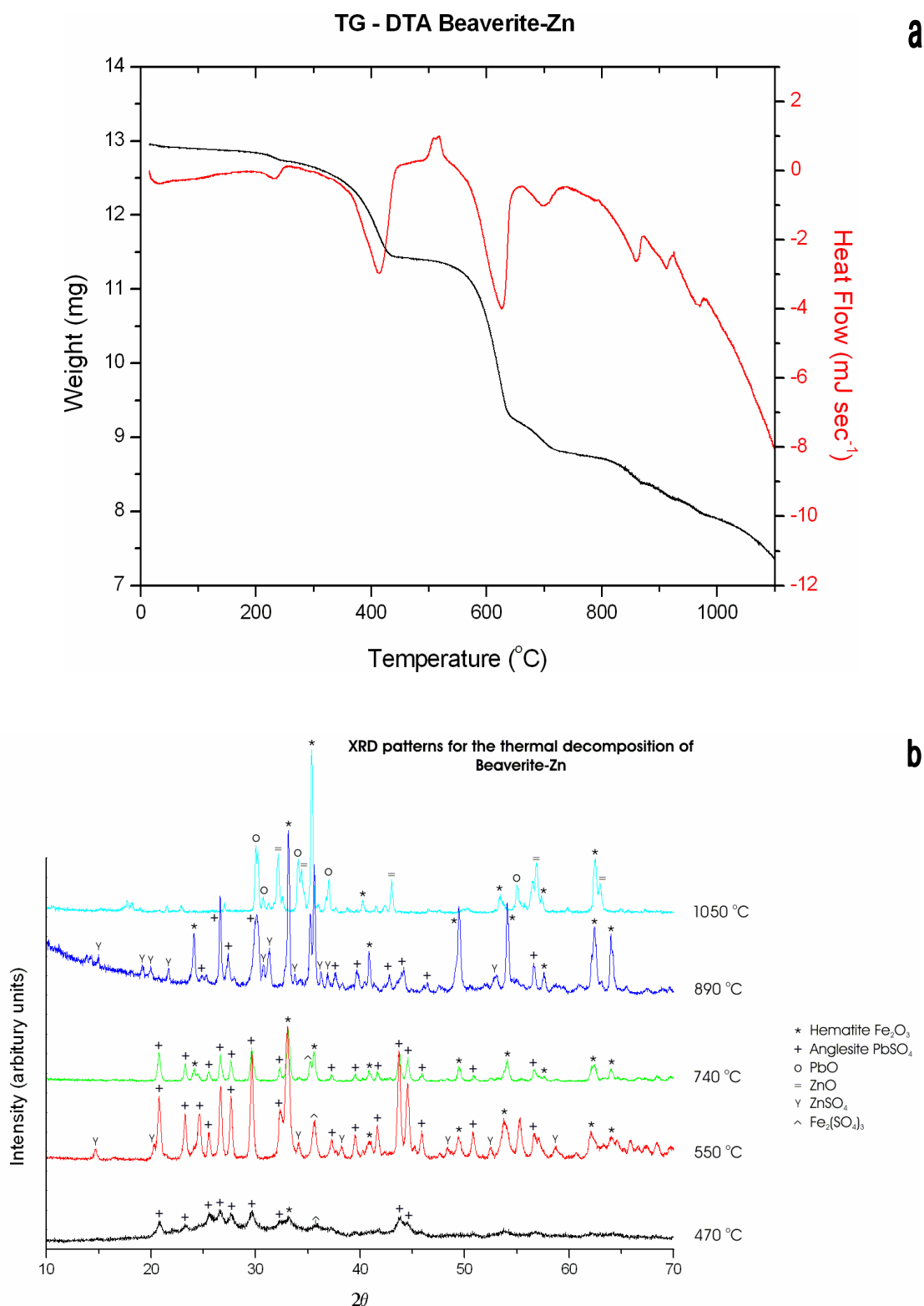
Figure 3.13. (a) Thermal gravimetric and differential thermal analysis (TG-DTA) profiles of synthetic beaverite-Zn. The samples were heated from 25 to 1100°C at a rate of 10°C min^{-1}, under an argon atmosphere at a rate of 30 ml min^{-1}. Data were collected every second. (b) Powder X-ray diffraction patterns for the thermal decomposition of synthetic beaverite-Zn under argon at 470, 550, 740, 890, and 1050°C. The samples were mounted on a Bruker zero background silicon (510) sample holder. Cu Kα radiation (λ = 1.54056 Å) was used, 2-theta range 10-70°, step size 0.020°, step time 18s. Identifiable phases are highlighted.

and 966°C. Between the two intense endothermic peaks, there is a small exothermic peak at 517°C.

The 12 % weight loss seen between 150 and 460°C is very similar to the other synthetic jarosites described earlier. Initially the 'additional' water is removed from the structure around 150 to 300°C, and then the structure undergoes dehydroxylation, where the majority of the weight loss for this interval occurs, the theoretical weight loss is 12 % from the stoichiometry of beaverite-Zn (Drouet and Navrotsky 2003). The dehydroxylation reaction is nearly identical to beaverite-Cu in that the structural lead, and zinc in this sample form sulphates (Figure 3.13b). The reaction can be summarised by the equation:

$$(H_3O)_{0.57}Pb_{0.43}Fe_{2.70}Zn_{0.21}(SO_4)_2(OH)_{5.95} \rightarrow$$
$$0.43PbSO_4 + 0.21ZnSO_4 + 0.453Fe_2(SO_4)_3 + 0.897Fe_2O_3 + 3.829H_2O_{(g)} \quad (3.10)$$
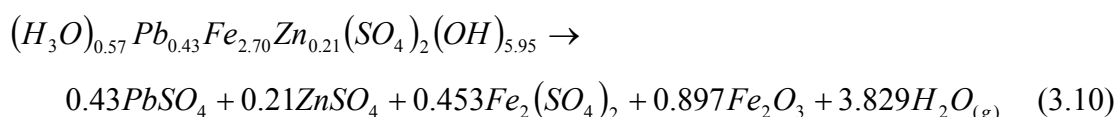
Once again, there is a small exothermic peak, at 517°C between two intense endothermic peaks. This corresponds, like the other synthetic jarosites, to the crystallisation of hematite (Figure 3.13b) (Drouet and Navrotsky 2003).

The second and greatest weight loss (21 %) occurs between 460 and 800°C, which coincides with a very intense endothermic peak at 626°C in the DTA. These events are related to the thermal decomposition of $Fe_2(SO_4)_3$, where the expected weight loss is 19 % from the beaverite-Zn formula (Eq. 3.11) (Figure 3.13b) (Ozacar et al. 2000).

$$0.453Fe_2(SO_4)_3 \rightarrow 0.453Fe_2O_3 + 1.359SO_{3(g)} \quad (3.11)$$
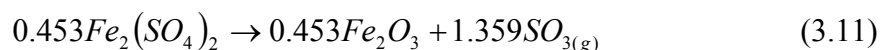
The final weight loss (10 %) occurs between 800 and 1200°C, and this falls in the temperature range where three small endothermic peaks occur: 859, 911, and 966°C. The weight loss can be explained by two specific events, the first being the thermal decomposition of $ZnSO_4$ to zinc oxide and sulphurous gas (Figure 3.13b) (Eq. 3.12) around 859 and 911°C, inferred by the small endothermic peaks in the DTA.

$$0.21ZnSO_4 \rightarrow 0.21ZnO + 0.21SO_{3(g)} \quad (3.12)$$

The second mechanism is the breakdown of anglesite similar to that seen for plumbojarosite and beaverite-Cu to lead oxide and sulphurous gas (Figure 3.13b) (Eq.

3.13). The breakdown probably occurs around 966°C, as inferred by the endothermic peak in the DTA curve.

$$0.43PbSO_4 \rightarrow 0.43PbO + 0.43SO_{3(g)} \qquad (3.13)$$

3.2.5 Beudantite

The weight loss over the interval is 42 % (Figure 3.14a). The TG curve shows that the weight loss occurs over three principal intervals: (1) 13 % weight loss between 150 and 460°C, (2) 24 % weight loss between 460 to 800°C, and (3) 5 % weight loss between 800 and 1100°C. The DTA curve has two strong and two weak endothermic peaks at 454, 656, 744, and 966°C, respectively. At the beginning of the analysis, at low temperature, there are three small endothermic peaks at 327, 368, and 413°C. There is a weak exothermic peak at 560°C.

The 13 % weight loss observed between 150 and 460°C can be accounted for by the removal of 'additional' water and the dehydroxylation of the jarosite structure (Drouet and Navrotsky 2003). The removal of the 'additional' water is evident from the DTA trace as a series of three small endothermic peaks at 327, 368, and 413°C. The process occurs at higher temperatures than the other jarosites, probably due to the partial incorporation and the localised structural effects of the arsenate unit at the T-site, seen through stronger hydrogen bonds to the hydroxyl and protonated hydroxyl groups (i.e. 'additional' water). The Eq. 3.14 illustrates the dehydroxylation reaction for beudantite, where XRD analysis identified anglesite, $PbSO_4$, and scorodite, $FeAsO_4$, as the dominant product phases of the breakdown; the ideal value of weight loss for this reaction is 13 % (Figure 3.14b).

$$(H_3O)_{0.68}Pb_{0.32}Fe_{2.86}(SO_4)_{1.69}(AsO_4)_{0.31}(OH)_{5.59} \rightarrow$$
$$0.32PbSO_4 + 0.31FeAsO_4 + 0.456Fe_2(SO_4)_2 + 0.819Fe_2O_3 + 3.813H_2O_{(g)} \quad (3.14)$$
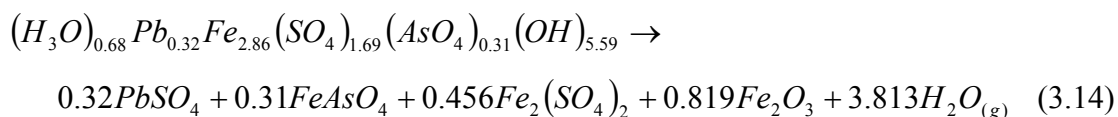
The weak exothermic peak at 560°C corresponds to the crystallisation of Fe_2O_3 to hematite (α-Fe_2O_3) proven by XRD analysis between 580-700°C (Figure 3.14b).

The greatest and second weight loss (24 %) occurs between 460 and 800°C, and coincides with an intense and a significant endothermic peak at 656 and 744°C in the DTA. These events relate to thermal decomposition of $Fe_2(SO_4)_3$ into crystalline
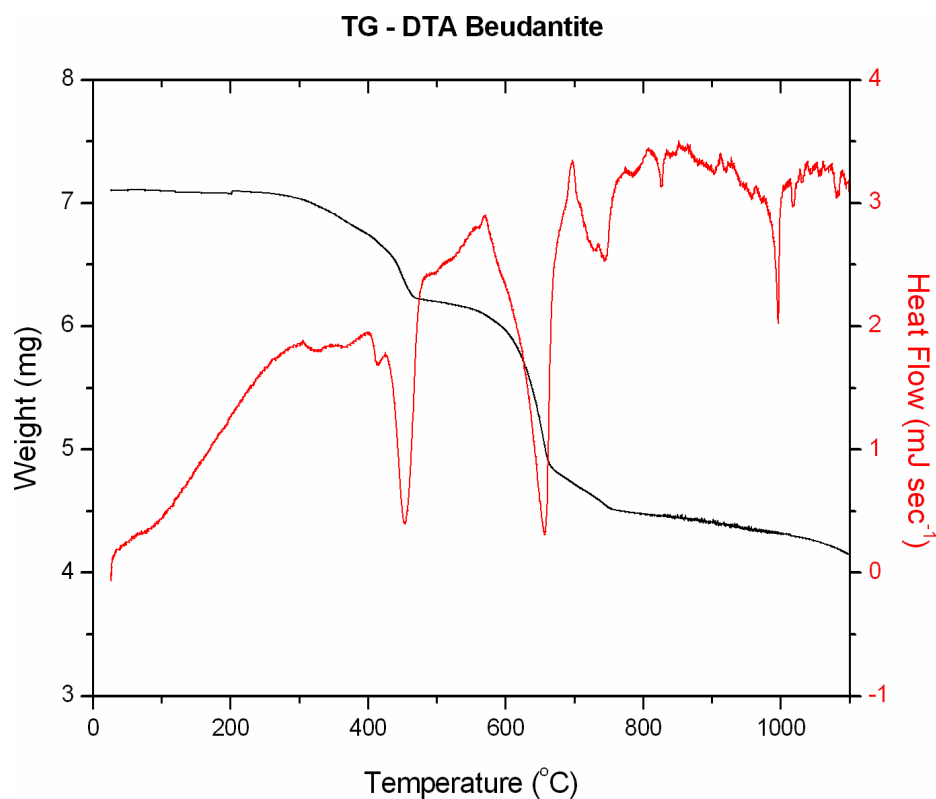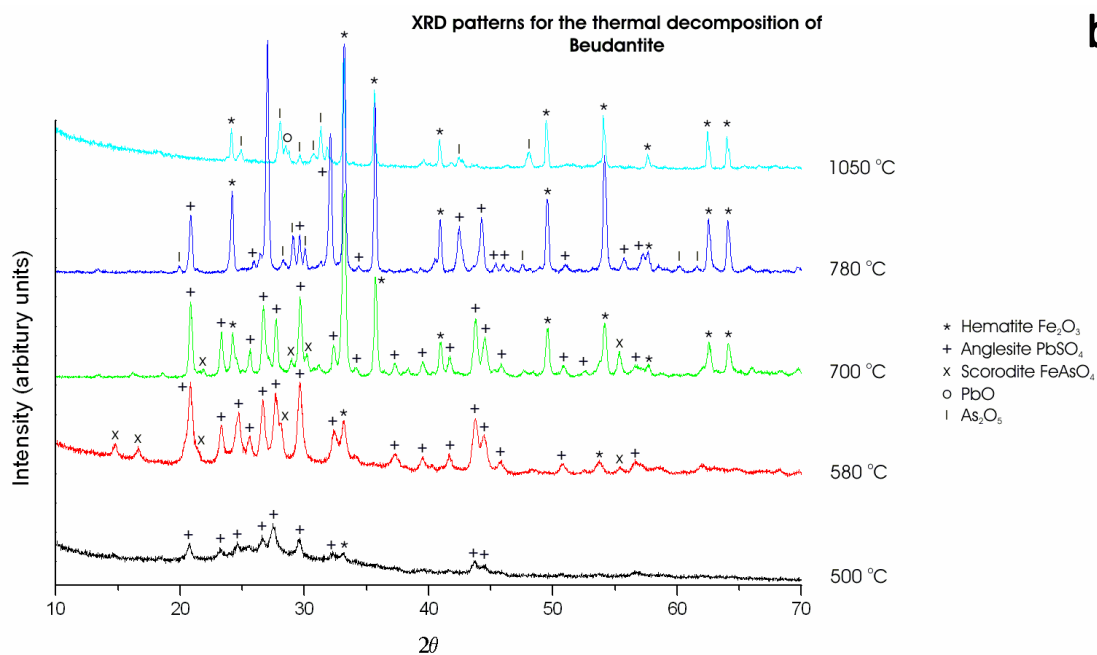
Figure 3.14. (a) Thermal gravimetric and differential thermal analysis (TG-DTA) profiles of synthetic beudantite. The samples were heated from 25 to 1100°C at a rate of 10°C min^{-1}, under an argon atmosphere at a rate of 30 ml min^{-1}. Data were collected every second. (b) Powder X-ray diffraction patterns for the thermal decomposition of synthetic beudantite under argon at 500, 580, 700, 780, and 1050°C. The samples were mounted on a Bruker zero background silicon (510) sample holder. Cu Kα radiation (λ = 1.54056 Å) was used, 2-theta range 10-70°, step size 0.020^{o}, step time 18s. Identifiable phases are highlighted.

α-Fe_2O_3 and the release of sulphurous gas (Eq. 3.15) (Figure 3.14b); the expected weight loss for this breakdown is 21 %.

$$0.456Fe_2(SO_4)_2 \rightarrow 0.456Fe_2O_3 + 1.368SO_{3(g)} \tag{3.15}$$
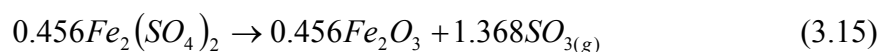
The breakdown of scorodite ($FeAsO_4$), to hematite and As_2O_5 is believed to occur between 700 and 800°C, signified by an endothermic peak at 744°C in the DTA profile, and by XRD evidence (Eq. 3.16) (Figure 3.14b). This additional breakdown might account for the higher than expected weight loss for the decomposition of $Fe_2(SO_4)_3$ around 460 and 800°C (Figure 3.14a).

$$0.31FeAsO_4 \rightarrow 0.155Fe_2O_3 + 0.155As_2O_5 \tag{3.16}$$
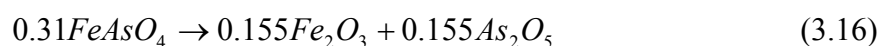
The final weight loss (5 %) observed in the TG trace occurs between 800 and 1200°C, and this occurs around a significant peak at 996°C in the DTA curve. The weight loss is associated with the breakdown of anglesite to PbO and sulphurous gas; the expected weight loss for this reaction from the beudantite formula is 5 % (Eq. 3.17) (Figure 3.14b).

$$0.32PbSO_4 \rightarrow 0.32PbO + 0.32SO_{3(g)} \tag{3.17}$$

3.3 Fourier transform infrared spectroscopy

3.3.1 Synthetic jarosites

The Fourier transform infrared (FTIR) spectra of the five synthetic jarosites are shown in Figures 3.15a,b,c, and 3.16a,b respectively. The assignments of the infrared spectra are given in Table 3.6. The spectra are similar to those previously reported (Powers et al. 1975, Baron and Palmer 1996b, Serna et al. 1986, Sasaki et al. 1998, Drouet and Navrotsky 2003).

The intense absorption observed in the region 2900 to 3700 cm^{-1} (Figures 3.15, 3.16) can be attributed to O-H stretching (v_{OH}). The band shifts towards lower frequencies for the jarosites with lead at the A-site in comparison to the potassium endmember (Table 3.6). The shift is probably due to an increase in energy of hydrogen bonds within the structure (Powers et al. 1975, Drouet and Navrotsky 2003). Sulphate oxygen atoms are located on trigonal axes, parallel to the c-axis of the unit cell and
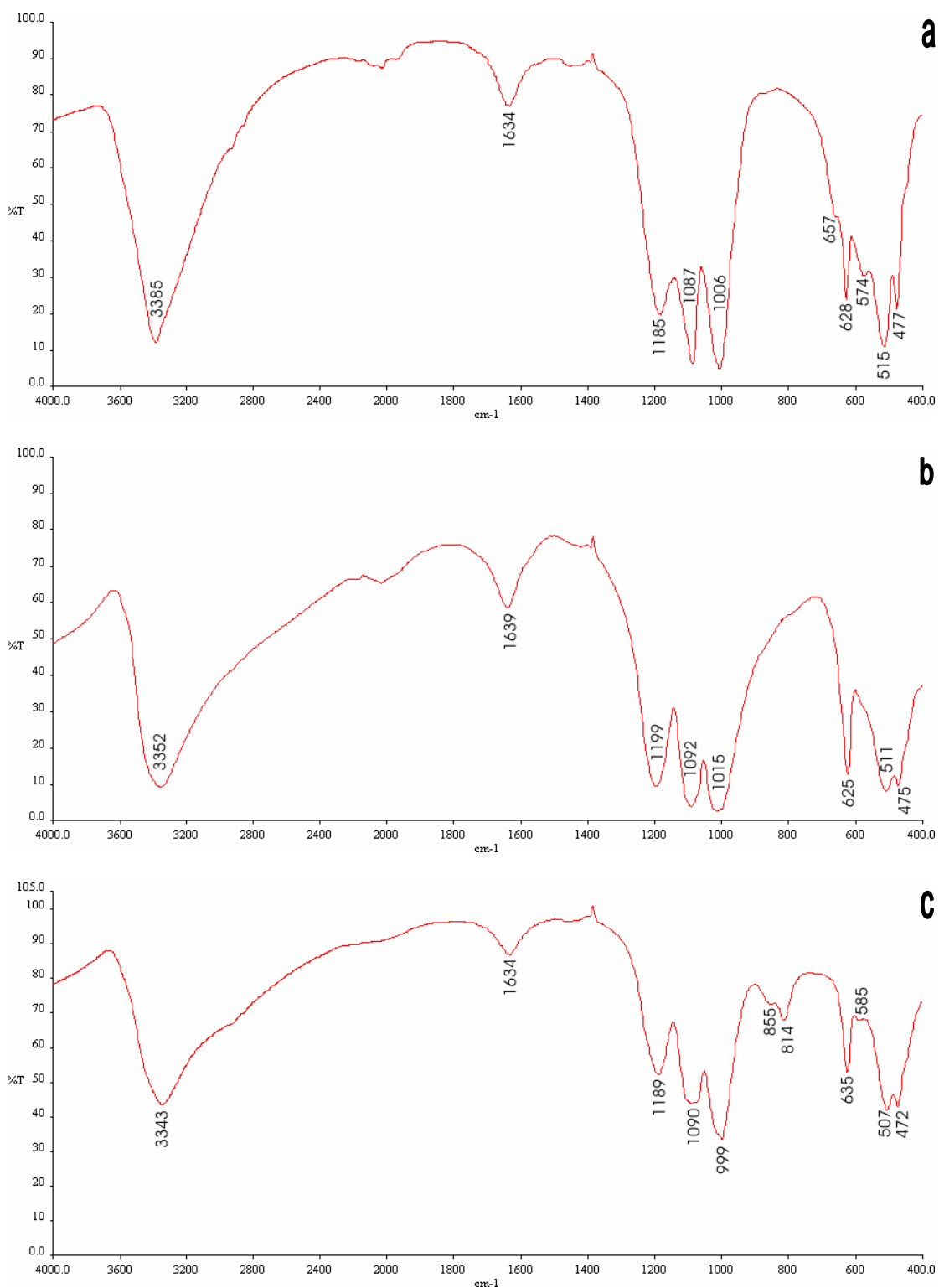
Figure 3.15. Fourier transform infrared spectra (FTIR) of (a) potassium jarosite, (b) plumbojarosite, and (c) beudantite. The range was 400 – 4000 cm^{-1} wavenumbers with a resolution of 4 cm^{-1}, five scans were accumulated. The main vibrational bands in the spectrum are marked.
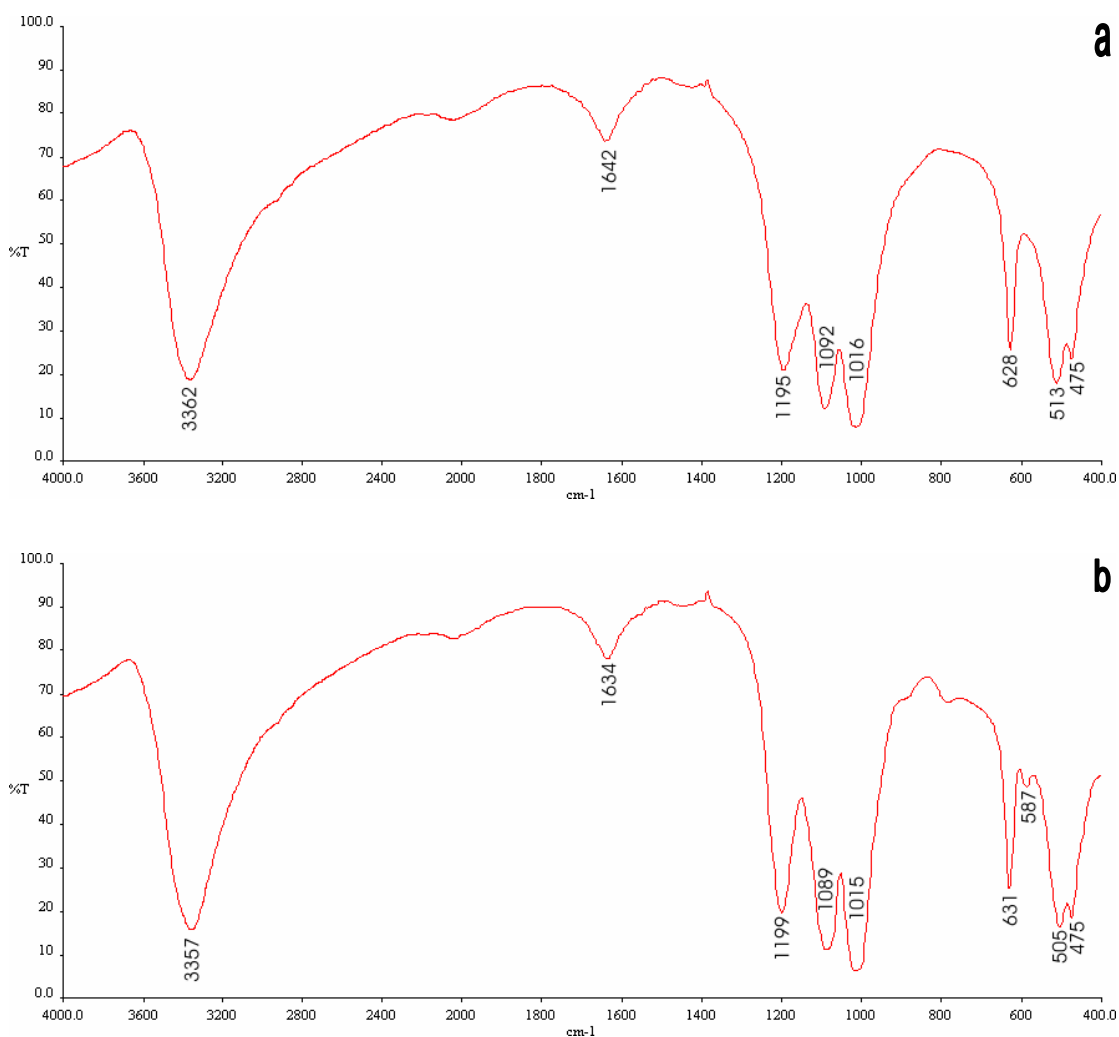
Figure 3.16. Fourier transform infrared spectra (FTIR) of (a) beaverite-Cu and (b) beaverite-Zn. The range was $400 - 4000$ cm^{-1} wavenumbers with a resolution of 4 cm^{-1}, five scans were accumulated. The main vibrational bands in the spectrum are marked.

are surrounded by three hydroxyl groups (Hendricks 1937). Hendricks (1937) suggested that the hydrogen atoms were orientated in such a way as to bind to these oxygen atoms, thus forming OH-OSO$_3$ hydrogen bonds (Figure 3.17). Drouet and Navrotsky (2003) found that there was a direct correlation between lower O-H stretching frequencies and decreases in the c-axis parameter across the K-Na jarosite solid solution, where the a-axis parameter remained almost constant. A-site cations are thought to have little influence on a_o and are theoretically responsible for the main variations in c_o (Jambor and Dutrizac 1983). It is possible to distinguish two vibrational modes around the hydrogen: O-H and H-OSO$_3$. Contractions in the c-axis would result in the decrease of some bond lengths, most probably including the H-OSO$_3$, therefore strengthening the hydrogen bonds, and in turn, weakening the O-H

bond of the hydroxyl groups (Drouet and Navrotsky 2003). The consequence of this is an overall decrease in frequency of the stretching vibration of the band observed at 2900 to 3700 cm^{-1} when lead is present in the A-site over a univalent cation. Potassium jarosite has the longest c-axis parameter and the highest v_{OH} assignment of all the synthetic jarosites (Tables 3.2, 3.6). Similar correlations between the c-axis parameter and v_{OH} assignment are seen for the other lead-rich jarosites, except plumbojarosite (Tables 3.2, 3.6), which is probably related to the unit cell not doubling in the c-axis direction. The lowest v_{OH} vibration out of all five synthetic jarosites is exhibited by beudantite, probably due to the partial substitution of arsenate (AsO$_4^{3-}$) for sulphate in the structure. Arsenic has a lower electronegativity than sulphur; therefore, hydrogen bonds are likely to be stronger in OH-OAsO$_3$ than OH-OSO$_3$, thereby overall increasing the amount of hydrogen bonding in beudantite and reducing the v_{OH} vibration assignment.
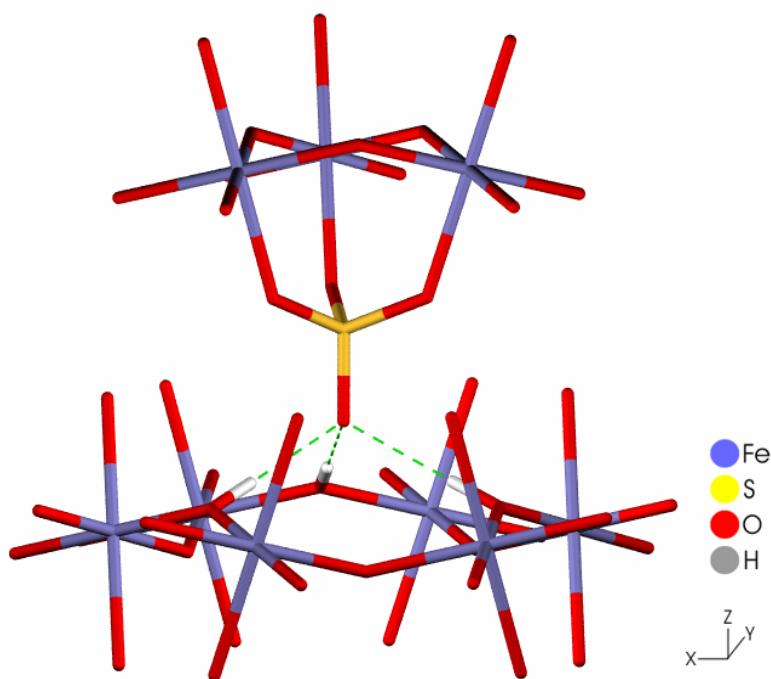
Figure 3.17. A schematic diagram of the jarosite structure, highlighting the presence of OH-OSO$_3$ hydrogen bonds (green dashed lines), formed between the uncoordinated oxygen atom of the sulphate tetrahedra and three hydroxyl groups in the lower T-O-T sheet.

The band observed at 1634 to 1641 cm^{-1} (Figures 3.15, 3.16) is attributed to HOH deformation, in agreement with the results of Powers et al. (1975), Baron and Palmer (1996b) and Drouet and Navrotsky (2003). The HOH deformation mode is directly related to the 'additional' water groups formed from the protonation of the hydroxyl

groups. The identification of hydronium in jarosites by FTIR is generally difficult and often not conclusive (Wilkins et al. 1974, Ripmeester et al. 1986). The only easily identifiable peak associated with hydronium in jarosites lies in the 1535 – 1575 cm^{-1} region as a weak peak on the shoulder of a stronger peak at 1635 - 1640 cm^{-1}, associated with HOH deformation (Kubisz 1972, Wilkins et al. 1974). The hydronium peak is absent in all the synthetic jarosite spectra.

Table 3.6. Assignments of infrared wavenumbers for the synthetic jarosites.

Wavenumbers (cm^{-1})					Assignments
potassium jarosite	plumbojarosite	beaverite -Cu	beaverite -Zn	beudantite	
3384.5	3352.0	3362.2	3356.7	3343.0	ν_{OH}
1634.4	1638.9	1641.8	1634.3	1633.5	HOH
1087.3	1197.7	1194.9	1199.4	1189.0	$\nu_3(SO_4^{2-})$
1184.5	1092.0	1091.7	1088.6	1089.8	$\nu_3(SO_4^{2-})$
1006.0	1014.9	1015.6	1014.7	999.1	$\nu_1(SO_4^{2-})$
				855.4	$\nu_3(AsO_4^{3-})$
				813.5	$\nu_1(AsO_4^{3-})$
			895.7		γ_{OH}
			785.6		γ_{OH}
657.3					$\nu_4(SO_4^{2-})$
628.1	624.6	627.8	630.5	634.9	$\nu_4(SO_4^{2-})$
573.7			586.7	584.8	γ_{OH}
514.5	510.9	512.5	504.7	506.5	O-Fe
477.1	474.6	474.6	474.7	472.2	$\nu_2(SO_4^{2-})$

All spectra (Figures 3.15, 3.16) have three intense absorption bands at 1000 – 1200 cm^{-1} (Table 3.6), assigned to the vibrational modes of $\nu_3(SO_4^{2-})$ (doublet, at the two higher wavenumbers) and $\nu_1(SO_4^{2-})$ (at the lowest wavenumber). Two other vibrational modes of sulphate occur, the $\nu_4(SO_4^{2-})$ around 630 cm^{-1} and as a doublet in potassium jarosite at 657 cm^{-1}, and the $\nu_2(SO_4^{2-})$ near 470 cm^{-1}. The ν_1 and ν_3 are the stretching modes and the ν_2 and ν_4 are the bending modes of sulphate (Figure 3.18) (Sasaki et al. 1998). For the beudantite sample (Figure 3.15c) there are an additional two peaks in the spectra between 810 and 860 cm^{-1}; these correspond to the $\nu_3(AsO_4^{3-})$ and $\nu_1(AsO_4^{3-})$ vibrational modes of arsenate (Table 3.6).

Sasaki et al. (1998) attributed IR bands observed near 580 and 505 cm^{-1} to an O-H bending mode (γ_{OH}) and to an O-Fe vibration within the FeO$_6$ coordination octahedron (Figures 3.15, 3.16) (Table 3.6). O-H bending modes are not present in the spectra of plumbojarosite (Figure 3.15b) and beaverite-Cu (Figure 3.16a).

Additional γ_{OH} vibrations are seen as extremely weak peaks at 786 and 896 cm^{-1} in beaverite-Zn (Figure 3.16b) (Table 3.6).
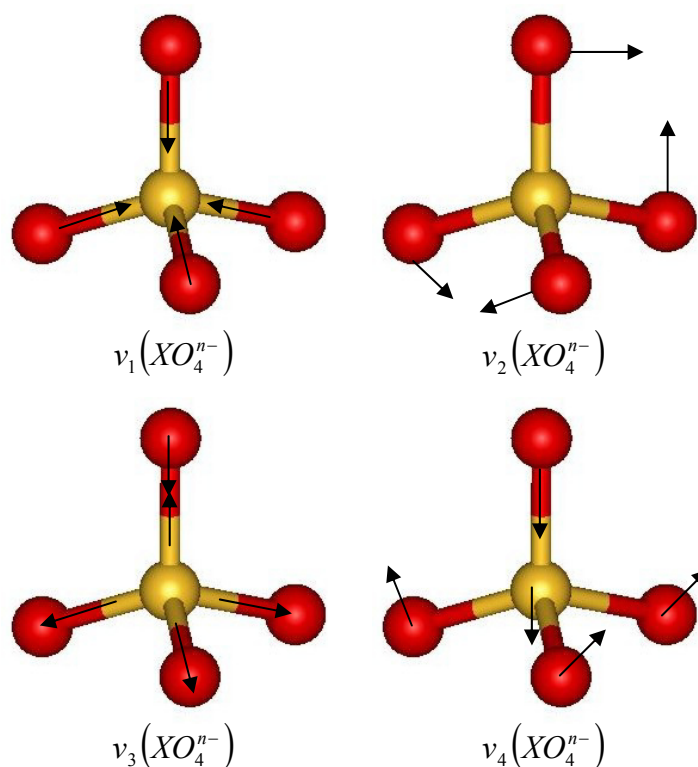
Figure 3.18. The four vibrational modes of a tetrahedral ion XO_4^{n-} (SO_4^{2-} and AsO_4^{3-}).

3.3.2 Natural jarosites

To appraise the vibrational spectroscopy of the synthetic jarosite samples, FTIR spectra of natural crystalline potassium jarosite, Margaritas mine, Mexico, and plumbojarosite, Tintic mine, USA, [BM 1966.403] were collected. These are presented in Figure 3.19, and their assignments are given in Table 3.7. Unfortunately, suitable natural samples could not be found for beaverite or beudantite.

Comparing the two sets of natural and synthetic spectra together for potassium jarosite and plumbojarosite, it can be said the bands in the natural samples are visibly shaper; this can simply be explained by lower concentrations of defects in the natural crystalline samples compared to the synthetic powders made for this study. Even though the disorder is higher in the synthetic samples the main vibrational assignments are extremely close when the numbers are compared for the synthetic and natural samples in Tables 3.6 and 3.7, respectively. It is worth highlighting the
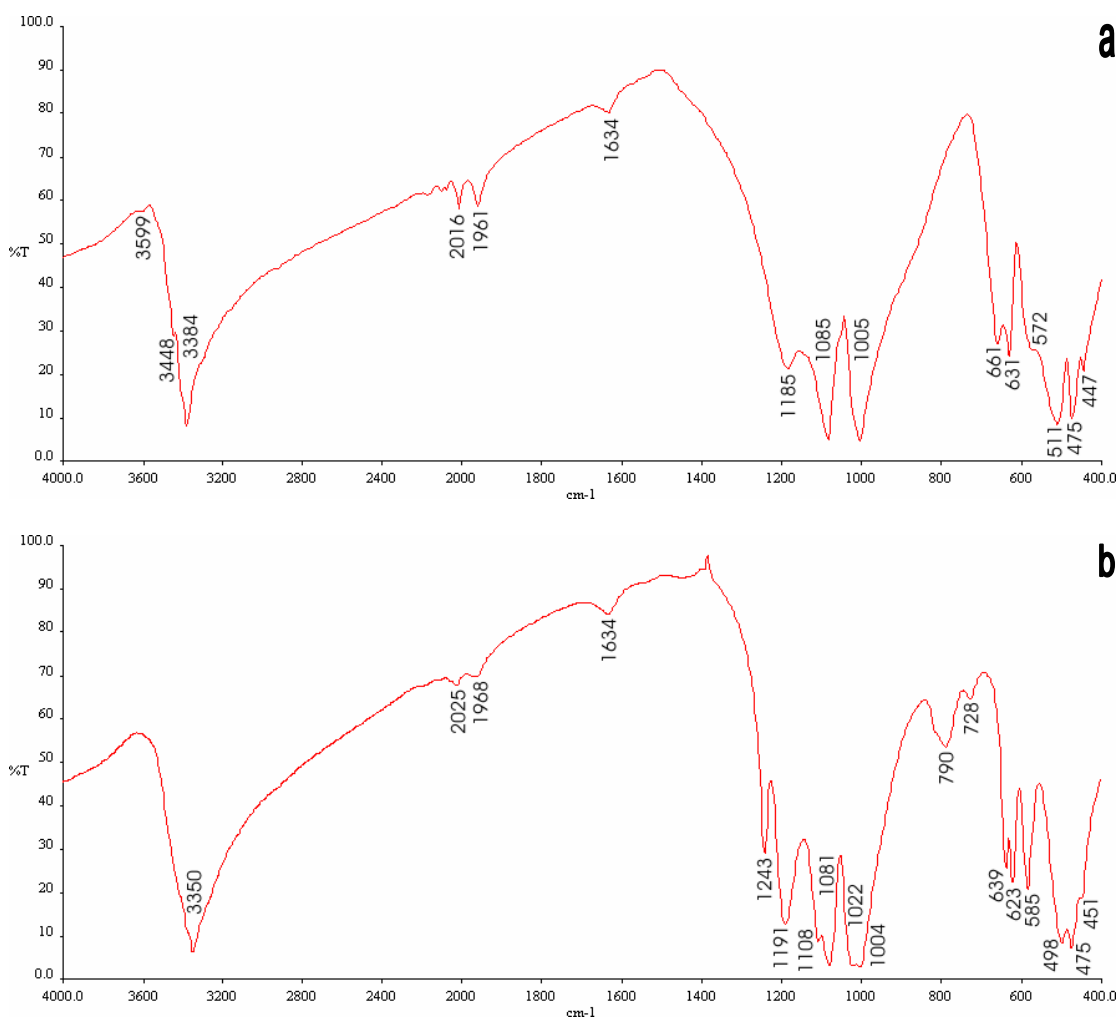
Figure 3.19. Fourier transform infrared spectra (FTIR) of (a) natural potassium jarosite, Margaritas mine, Mexico; (b) natural plumbojarosite, Tintic mine, USA [BM 1966,403]. The range was 400 – 4000 cm^{-1} wavenumbers with a resolution of 4 cm^{-1}, five scans were accumulated. The main vibrational bands in the spectrum are marked.

addition of two extra O-H stretching (v_{OH}) modes in the natural potassium jarosite sample at 3348 and 3599 cm^{-1} (Figure 3.19a, Table 3.7). These modes are predicted from factor analysis of the space group ($R\overline{3}m \equiv D_{3d}^5$) that the general jarosite structure belongs too, though are rarely seen in natural and synthetic powders, and have only really been observed in highly crystalline natural samples (Sasaki et al. 1998). The absence of these two addition v_{OH} modes in the synthetic potassium jarosite sample is generally not that concerning, considering they are only found in the most ideal of samples. An interesting mode to point out is the HOH water deformation mode in the two natural samples around 1634 cm^{-1}; the presence of this vibration relates to the 'additional' water formed by the protonation of the hydroxyl groups as a means to charge balance any Fe deficiencies in the structure (Figure 3.19,

Table 3.7). The presence of the HOH mode is important with respect to the calculated formula of these two natural samples as it implies that even these extremely pure, near ideal, well crystalline samples have Fe structural deficiencies similar to those seen in all the synthetic jarosite structures made for this study (Figure 3.19, Tables 3.3, 3.4, 3.6, 3.7).

Table 3.7. Assignments of infrared wavenumbers for natural samples of potassium jarosite and plumbojarosite.

Wavenumbers (cm^{-1})		Assignments
potassium jarosite, Margaritas Mine, Mexico	plumbojarosite, Tintic Mine, USA [BM 1966,403]	
3599.4		v_{OH}
3348.2		v_{OH}
3383.8	3349.6	v_{OH}
1634.0	1634.0	HOH
1185.4	1242.5	$v_3(SO_4^{2-})$
1085.3	1190.9	$v_3(SO_4^{2-})$
	1107.6	$v_3(SO_4^{2-})$
	1080.6	$v_3(SO_4^{2-})$
1005.0	1021.5	$v_1(SO_4^{2-})$
	1004.0	$v_1(SO_4^{2-})$
	789.6	γ_{OH}
	728.3	γ_{OH}
661.2	638.7	$v_4(SO_4^{2-})$
631.2	623.0	$v_4(SO_4^{2-})$
571.6	584.5	γ_{OH}
511.1	498.3	O-Fe
474.9	475.3	$v_2(SO_4^{2-})$
447.1	451.3	O-Fe

When the FTIR spectra for the synthetic and natural plumbojarosite samples are studied more closely, an interesting relationship concerning the (SO_4^{2-}) modes becomes known (Figure 3.15b, 3.19b). Figure 3.20 is a magnified section of the FTIR spectrums for the natural and synthetic plumbojarosite samples' concentrating on the (SO_4^{2-}) vibrational modes between 800 and 1400 wavenumbers. Factor analysis of the jarosite structure predicts three internal stretching modes for (SO_4^{2-}): this commonly breaks down to a $v_3(SO_4^{2-})$ doublet and a $v_3(SO_4^{2-})$ singlet, where the doublet is at the two higher wavenumbers and the singlet is at the lowest. This relationship between the $v_3(SO_4^{2-})$ doublet and a $v_3(SO_4^{2-})$ singlet is seen very clearly in the synthetic plumbojarosite spectrum in Figure 3.20b. In the natural plumbojarosite sample there appear to be six (SO_4^{2-}) vibrational modes between 800 and 1400 wavenumbers (Figure 3.20a). It is believed that the fundamental $v_3(SO_4^{2-})$ doublet and $v_1(SO_4^{2-})$ singlet are still present in the natural plumbojarosite sample,
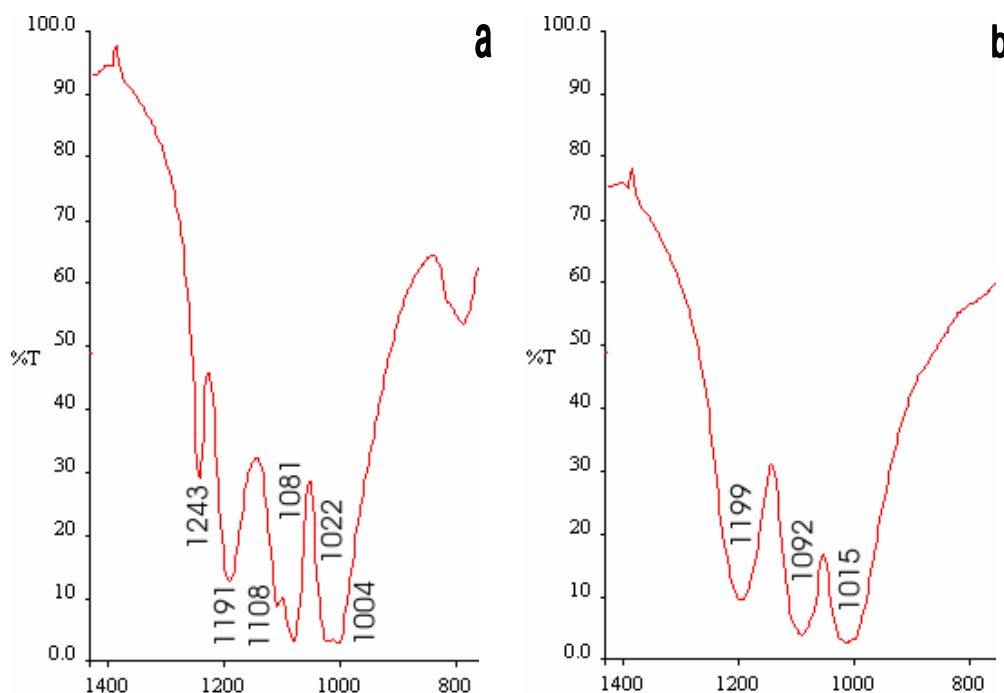
Figure 3.20. FTIR spectra of the sulphate modes in (a) natural plumbojarosite [BM 1966,403] and (b) synthetic plumbojarosite. The range was from 800 – 1400 cm^{-1} wavenumbers. The splitting of the three sulphate modes (2 modes of $v_3(SO_4^{2-})$ and $v_1(SO_4^{2-})$)) are clearly evident in the natural sample. The sulphate modes in the natural sample are seeing both the A-site filled with Pb(II) and a vacancy. No splitting is seen in the synthetic sample. The main sulphate vibrational bands are marked on the spectrums.

though the modes have split further in two. The reason for the splitting of the three modes is the ability of the (SO_4^{2-}) unit to distinguish between an A-site occupied with Pb(II) and a vacancy. Sasaki et al. (1998) proposed that the $v_1(SO_4^{2-})$ and $v_3(SO_4^{2-})$ values assigned to S-O bonds in sulphate adjacent to Pb(II) ions are smaller than those in (SO_4^{2-}) not adjacent to Pb(II) ions. The absence of splitting of the (SO_4^{2-}) stretching modes in the synthetic plumbojarosite sample adds to the further evidence of the lack of ordering between Pb(II) ions and vacancies in the A-site for this sample.

3.4 Morphology and surface area of the precipitates

Figure 3.21 provides a general view of the synthetic jarosite analogues, as observed in powder mounts on the scanning electron microscope (SEM). The synthetic jarosites have a varied range of morphologies, from the globular potassium jarosite (Figure 3.21a) to rhombohedral (pseudocubic) crystals in plumbojarosite (Figure 3.21b). Individual crystals are typically less than 3 μm across. No other crystalline or amorphous phases can be seen in any of the SEM micrographs (Figure 3.21a-e).
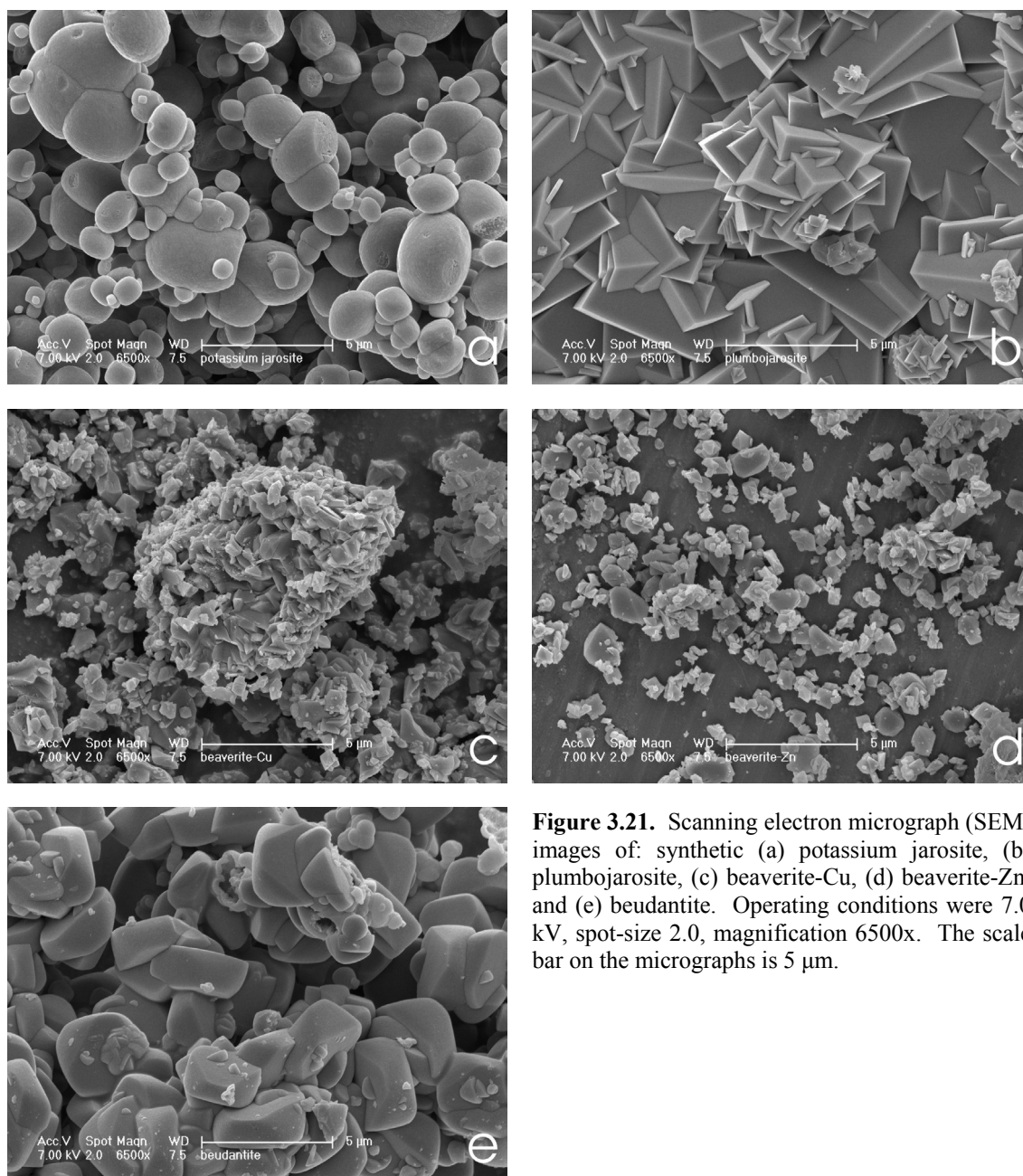
Figure 3.21. Scanning electron micrograph (SEM) images of: synthetic (a) potassium jarosite, (b) plumbojarosite, (c) beaverite-Cu, (d) beaverite-Zn, and (e) beudantite. Operating conditions were 7.0 kV, spot-size 2.0, magnification 6500x. The scale bar on the micrographs is 5 μm.

Many particle morphologies have been reported for the jarosite subgroup, ranging from perfect euhedral to small and irregular (Baron and Palmer 1996b). Sasaki and Konno (2000) investigated the possible mechanisms that might affect particle morphology in synthetic jarosites. Generally, they found that the jarosite-subgroup phases formed by the same technique showed similar morphology, although some differences were observed, depending upon which monovalent cations were involved. Looking at the five jarosite analogues made for this study (Figure 3.21a-e) it becomes evident that the particle morphology of potassium jarosite ($A = K^+$) (Figure 3.21a) is

very different from the other four analogous enriched with lead (A = Pb(II)) (Figure 3.21b-e). The change is probably due to different A-site cations present (Sasaki and Konno 2000). The contrasting morphologies within the lead analogues are probably due to the subtle changes in specific cations on the B- and T-sites (Figures 3.21b-e).

The morphology of potassium jarosite (Figure 3.21a) is irregular and globular in appearance, with various grain sizes, although the majority are between 1-5 μm, and the smallest down to 0.1 μm. A noticeable characteristic is that some of the grains appear to show cleaved sides that may be signs of mechanical abrasion; this is likely due to the stirring during the synthesis. Bigham (1996), Baron and Palmer (1996b), Dutrizac and Jambor (2000) and Sasaki and Konno (2000) have all reported particle morphologies for synthetic potassium jarosite similar to those in this study. Comparing the synthetic and natural morphologies of potassium jarosite in Figure 3.22a,b it becomes immediately apparent that the grain sizes of the natural samples are smaller (1-3 μm) than those in the synthetic sample. However, the morphology of the natural potassium jarosite sample is much closer to the ideal rhombohedral morphology than the irregular and globular appearance of the synthetic sample (Figure 3.22a,b). These morphological differences are probably related to the crystal growth time over which these samples have formed, the natural sample being considerably longer and therefore having crystal faces more attainable towards the ideal.

The synthetic plumbojarosite (Figure 3.21b) exhibits rhombohedral (pseudocubic) morphology characteristic of many jarosite precipitates, particularly lead-bearing ones (Dutrizac and Chen 2003). The synthetic sample consists of numerous intergrown crystals 1-3 μm across. By contrast, plumbojarosite made in an autoclave at elevated temperatures exhibits a euhedral crystal habit (Dutrizac et al. 1980). The near ideal rhombohedral morphology of the synthetic plumbojarosite is similar to that displayed by the natural sample (Figure 3.22c,d).

The crystal morphologies of beaverite-Cu and -Zn (Figure 3.21c and Figure 3.21d respectively) are very similar, in that the precipitates occur as spherical or cauliflower-like aggregates of individual crystals with diameters < 2 μm across. The sizes of individual crystals are so small that individual faces are distinguishable in

some cases only. At higher magnification, it is possible to see that the synthetic crystals have a grossly euhedral type habit, very close and ultimately epitomised by the morphology of natural beaverite (Figure 3.22e,f).
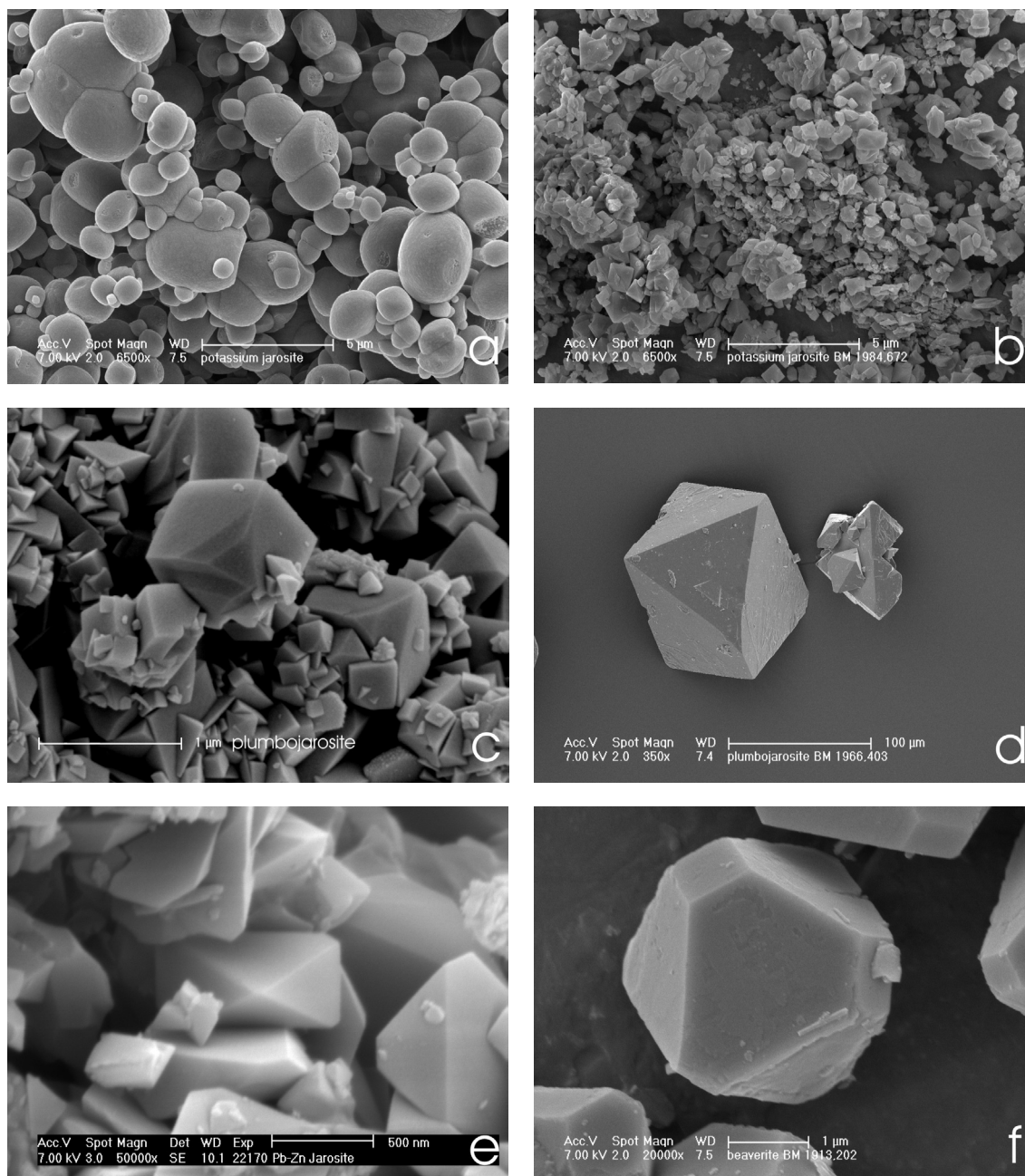
Figure 3.22. Various SEM micrographs comparing the morphologies of natural and synthetic jarosites. (a) Synthetic potassium jarosite, (b) natural potassium jarosite [BM 1984,672], (c) synthetic plumbojarosite, (d) natural plumbojarosite [BM 1966,403], (e) synthetic beaverite-Zn, and (f) natural beaverite [BM 1913,202]. Operating conditions indicated on each micrograph.

For beudantite (Figure 3.18e), the precipitates are intergrown crystals approximately 2-3 μm across, with a slight resemblance to a rhombohedral crystal morphology. Of the four lead-rich synthetic jarosites, the morphology of the beudantite analogue has

the least affinity to the rhombohedral crystal habit, and in some rare cases, is quite similar to the particle shape of potassium jarosite. The major difference between the morphology of beudantite and that of the other three lead jarosites may be explained by the partial substitution of arsenate for sulphate in the jarosite structure.

The surface areas (Table 3.8) of the synthetic jarosites determined by N_2-BET are closely linked to the crystal morphology of the jarosite analogues. Surface area is an important parameter because it is typically rate-determining in processes such as dissolution and adsorption (Drever 1997). Considering that one of the principal objectives of this study is to monitor the rate of release of toxic elements from synthetic jarosites, the surface area data generated by the N_2-BET technique will be crucial in appraising any absorption hypotheses.

Table 3.8. Surface area measurements of the synthetic jarosites.

Compound	$N_2 - $ BET surface area (m^2/g)
potassium jarosite	1.43 ± 0.016
plumbojarosite	1.03 ± 0.023
beaverite-Cu	3.19 ± 0.034
beaverite-Zn	3.67 ± 0.025
beudantite	9.58 ± 0.096

The surface areas for the two beaverite compounds are very similar (3.2-3.6 m^2/g) which is not surprising, considering they are structurally nearly identical and both have similar particle size (Table 3.8) (Figure 3.21c,d). Even though potassium jarosite and plumbojarosite are structurally and morphologically different, their surface area values are also very similar (1.4 and 1.0 m^2/g respectively). For the lead-rich samples, the values vary greatly between 1.0 m^2/g for plumbojarosite to 9.6 m^2/g for beudantite. Sasaki and Konno (2000) reported an N_2-BET surface area value for synthetic potassium jarosite at 4.0 m^2/g, even though they synthesised the jarosite via an autoclave. It has been reported that using an autoclave rather than a reaction vessel synthesis produced jarosites of greater crystallinity (Dutrizac et al. 1980, Dutrizac and Jambor 2000, Dutrizac and Chen 2003). Considering morphology and surface area values are highly correlated, this might shed some light on why there is a difference between Sasaki and Konno (2000)'s value for the surface area and that for potassium jarosite reported in this study. If synthesis conditions are a major contributing factor to the surface area of synthetic jarosites, this could explain the large variations

observed in surface area for the jarosite analogues in this study (Table 3.8). Unfortunately, there are no published surface area data at present for any natural jarosite and no synthetic data on any of the lead-bearing jarosites in the series.

3.5 Conclusions and Summary

All five synthetic jarosites (i.e. potassium jarosite, plumbojarosite, beaverite-Cu and – Zn, beudantite) made in this study could be identified by the comparison of their X-ray diffraction patterns to those reported in the ICDD PDF files and by their individual structural Rietveld refinement. The absence of unidentified peaks in the patterns indicated that no other phases were present at detectable levels. Structural refinement of the lattice parameters of the four lead-rich jarosites (plumbojarosite, beaverite-Cu and –Zn, beudantite) suggested no doubling of the c-axis in these compounds. No 11 Å (003) refection was seen for any of the four lead-bearing jarosites, indicating that the Pb(II) ions and vacancies on the A-site were not ordered. The mineral formulas for the five jarosites were calculated using wet chemical data rather than SEM analytical data, because of the problems of beam damage due to large quantities of structural water present in the jarosite structure. The comparison of the elemental analysis for natural crystalline samples of potassium jarosite and plumbojarosite to their corresponding synthetic analogous was found to be favourable. The respective weight losses seen in the TG-DTA profiles for the five synthetic jarosites corresponded very well with the expected values calculated from the jarosite stoichiometries. The FTIR spectra of the jarosites were very similar to those that have been reported elsewhere. The absence of any splitting of the (SO_4^{2-}) stretching modes in synthetic plumbojarosite, in comparison to that seen in a natural sample, added credence to the lack of any ordering of the Pb(II) ions and vacancies in the A-site in this analogue. The jarosites made in this study exhibited a varied range of morphologies: from globular in potassium jarosite to rhombohedral (pseudocubic) crystals in plumbojarosite. Individual crystals are typically less than 3 μm across. No other crystalline or amorphous phases could be seen in any of the SEM micrographs. The comparison of the morphologies of synthetic potassium jarosite, plumbojarosite, and the two-beaverite endmembers to natural samples was found to be very agreeable. In conclusion all the synthetic potassium jarosite, plumbojarosite, beaverite-Cu and – Zn, and beudantite are phase pure and can be used with confidence as analogues for natural samples in the forthcoming dissolution experiments.

4 Acid dissolution studies

Chapter 4 describes the acid dissolution studies of potassium jarosite, plumbojarosite, and beudantite. The chapter has four sections: dissolution experimental data, residual solid data, discussion and overall summary.

4.1 Dissolution experiments

Acid dissolution studies of potassium jarosite, plumbojarosite, and beudantite were carried out to investigate their stability and breakdown mechanisms under an acidic regime that would mimic an environment affected by acid-rock or -mine drainage (ARD/AMD). Figures 4.1-4.6 show the evolution of the solution composition over time for the dissolution experiments at 20°C and initial pH 2. All experiments were carried out in triplicate. To avoid problems of amalgamating data together, solution profiles of all three bottles used in the dissolution experiments of the three jarosites are presented to prove reproducibility. Final ion concentrations and pH values for the three experiments, and their corresponding molar ratios, are summarised in Tables 4.1 and 4.2, respectively. Calculated equilibrium activities and saturation indices for the dissolutions are presented in Tables 4.3 and 4.4, respectively. All the raw aqueous data and equilibrium activity data can be found in Appendix C.1 and C.4.1, respectively.

4.1.1 Potassium jarosite

In the potassium jarosite experiment, most of the dissolution occurred within the first 500 hrs, with rates declining with time (Figure 4.1). The final K concentration in bottle 1 was 0.2422 mmol L^{-1}, which was higher than the corresponding K values in bottles 2 and 3 of 0.2088 and 0.2044 mmol L^{-1}, respectively (Table 4.1). At the beginning of the experiment, the initial concentration of K in solution in Bottle 1 was approximately 0.05 mmol L^{-1}, in comparison to the other two triplicates where the K concentration was close to zero (Figure 4.1). Bottle 1 was probably slightly contaminated with KCl at the very beginning of the experiment as the pH of the starting solution was being adjusted with HClO$_4$, because KCl was present in the experiment as the electrolyte in the pH probe. Contamination from this source would explain for the higher K ion concentration at the beginning of the experiment in comparison to the other two bottles. The initial contamination of bottle 1 by KCl
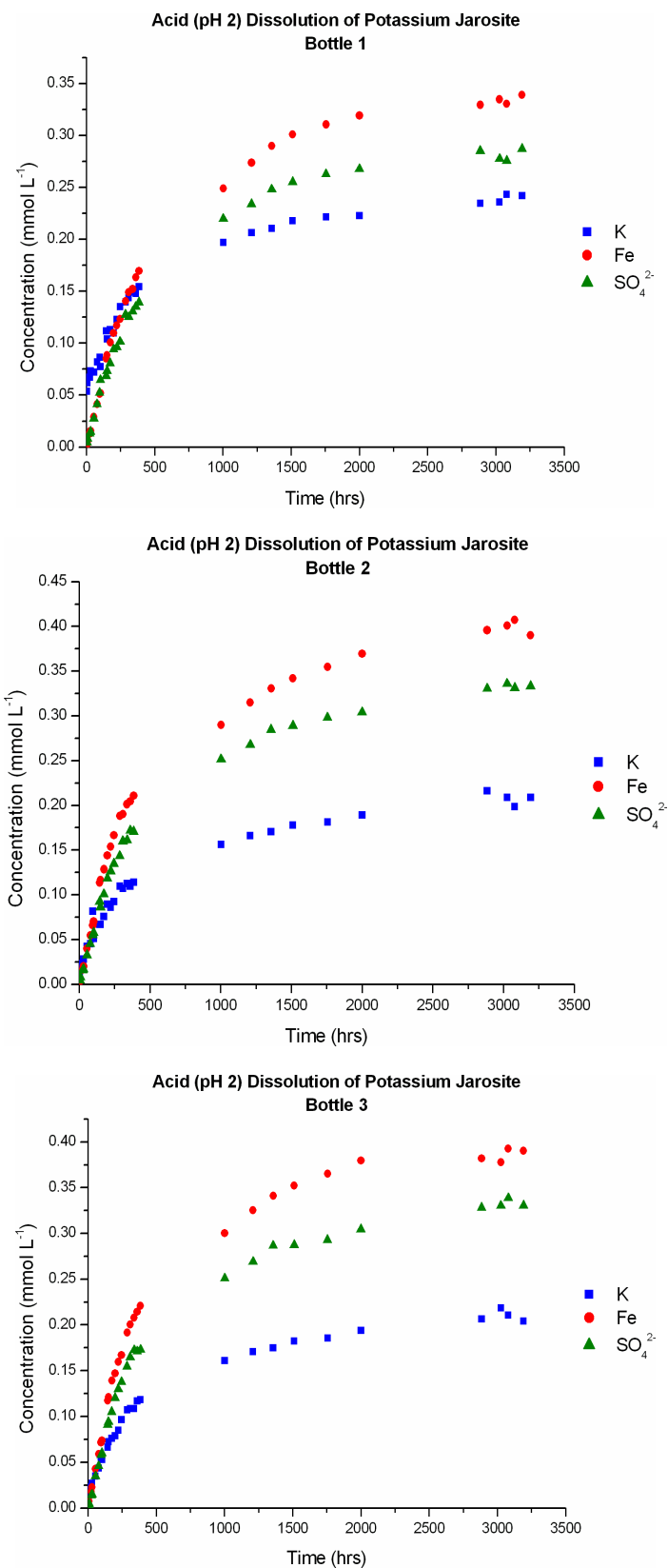
Figure 4.1. Concentrations of K_{tot}, Fe_{tot}, and $SO_4^{2-}{}_{tot}$ in solution for the acid dissolution of potassium jarosite plotted against time, with the initial pH set at 2.00. Solution profiles for all three bottles are presented to prove reproducibility.

appears not to have affected the overall acidic dissolution of potassium jarosite, as the ion profiles are comparable across the three bottles. The 0.04 mmol L^{-1} difference seen in the K ion concentration for bottle 1 when compared to bottles 2 and 3 at the end of the experiment, was nearly identical to the difference between the bottles at the beginning of the experiment (approximately 0.05 mmol L^{-1}) (Figure 4.1). The concentration profiles of K, Fe, and SO$_4^{2-}$ all displayed characteristics commonly attributed to parabolic rate kinetics, where steady state was attained after approximately 3000 hrs (Figure 4.1). The pH of the triplicates remained nearly constant over the duration of the experiment, the final pHs ranged from 2.02 to 2.04, from an initial of 2.00 (Table 4.1). The final total concentrations of K, Fe, and SO$_4^{2-}$ at steady state and their corresponding molar ratios are presented in Table 4.1 and Table 4.2, respectively. The molar ratios of ions in solution were calculated under the pretext that SO$_4^{2-}$ equalled 2, a common assumption frequently used in calculating the formula of jarosite-type structures (Section 1.4.1, Table 3.3). The K ratio in solution varied from 1.24 – 1.25 (when the outlier K value for bottle 1 was excluded) compared to that of the idealised synthetic of 0.84. The Fe ratio in solution varied from 2.34 – 2.36 compared to that of the synthetic solid of 2.46 (Table 3.3).

Table 4.1. Final pH and aqueous ion concentrations for the acid dissolutions.

Compound	pH	K	Pb	Fe	SO$_4^{2-}$	AsO$_4^{3-}$
Potassium jarosite						
Acid Bottle 1	2.04	0.2422	-	0.3391	0.2871	-
Acid Bottle 2	2.02	0.2088	-	0.3900	0.3332	-
Acid Bottle 3	2.03	0.2044	-	0.3904	0.3304	-
Plumbojarosite						
Acid Bottle 1	2.07	-	0.0108	0.2797	0.1973	-
Acid Bottle 2	2.07	-	0.0166	0.4222	0.3011	-
Acid Bottle 3	2.07	-	0.0196	0.4873	0.3487	-
Beudantite						
Acid Bottle 1	2.10	-	0.000059	0.0723	0.0144	0.0404
Acid Bottle 2	2.10	-	0.000039	0.0727	0.0141	0.0406
Acid Bottle 3	2.10	-	0.000034	0.0735	0.0145	0.0416

Aqueous concentration (mmol L^{-1})

Based on the measured steady state pH and concentrations of K$_{tot}$, Fe$_{tot}$, and SO$_4^{2-}$$_{tot}$, equilibrium aqueous activities of K$^+$, Fe^{3+}, and SO$_4^{2-}$ were calculated using the geochemical speciation suite of programs in The Geochemist's Workbench (GWB) version 4.0.2 (Bethke 1996). The activity coefficients were calculated using the extended form of the Debye-Hückel equation described by Helgeson (1969) and the

latest form of the GWB thermodynamic database (based on the 1996 revision of the EQ3/6 database; Wolery 1979, 1996). The corresponding equilibrium aqueous activities for the potassium dissolution can be found in Table 4.3. The charge balance error across the triplicates ranged from 3 to 6 % (Table 4.3). Saturation indices were also calculated for the three bottles in the acid dissolution of potassium jarosite and they are summarised in Table 4.4, only minerals with log Q/K greater than -3 are listed. Positive saturation indices were found for hematite and goethite, whilst that for potassium jarosite was negative (Table 4.4).

Table 4.2. Aqueous molar ratios for the acid dissolutions.

Compound	Aqueous molar ratios				
	K	Pb	Fe	SO_4^{2-}	AsO_4^{3-}
Potassium jarosite					
Acid Bottle 1	1.68	-	2.36	2	-
Acid Bottle 2	1.25	-	2.34	2	-
Acid Bottle 3	1.24	-	2.36	2	-
Plumbojarosite					
Acid Bottle 1	-	0.109	2.83	2	-
Acid Bottle 2	-	0.110	2.80	2	-
Acid Bottle 3	-	0.112	2.79	2	-
Beudantite					
Acid Bottle 1	-	0.0069	8.485	1.69	4.741
Acid Bottle 2	-	0.0046	8.713	1.69	4.866
Acid Bottle 3	-	0.0040	8.567	1.69	4.849

4.1.2 Plumbojarosite

For plumbojarosite, the majority of the reaction occurred within the first 250 hrs, with the dissolution rate declining rapidly afterwards (Figure 4.2). The Pb ion concentration from Figure 4.2 was re-plotted on a more appropriate scale in Figure 4.3 to illustrate the true shape of its concentration profile. All three ions in solution (Pb, Fe, and SO_4^{2-}) conform well to profiles epitomised by parabolic rate kinetics, steady state was judged to have occurred around 1500 hrs (Figures 4.2 and 4.3). As was similar in the previous dissolution, the pH for the acid dissolution of plumbojarosite remained very constant across all three triplicates over the duration of the experiment, the pH changed from an initial value of 2.00 to a final value of 2.07 (a value seen in all three bottles) (Table 4.1). The final total concentrations of Pb, Fe, and SO_4^{2-} and their corresponding molar ratios are presented in Table 4.1 and Table 4.2, respectively. Once again, the molar ratios of the ions in solution were calculated by setting SO_4^{2-} as 2. The Pb molar ratio in solution varied from $0.109 - 0.112$,

Figure 4.2. Concentrations of Pb$_{tot}$, Fe$_{tot}$, and SO$_4^{2-}$$_{tot}$ in solution for the acid dissolution of plumbojarosite plotted against time, with the initial pH set at 2.00. Solution profiles for all three bottles are presented to prove reproducibility.
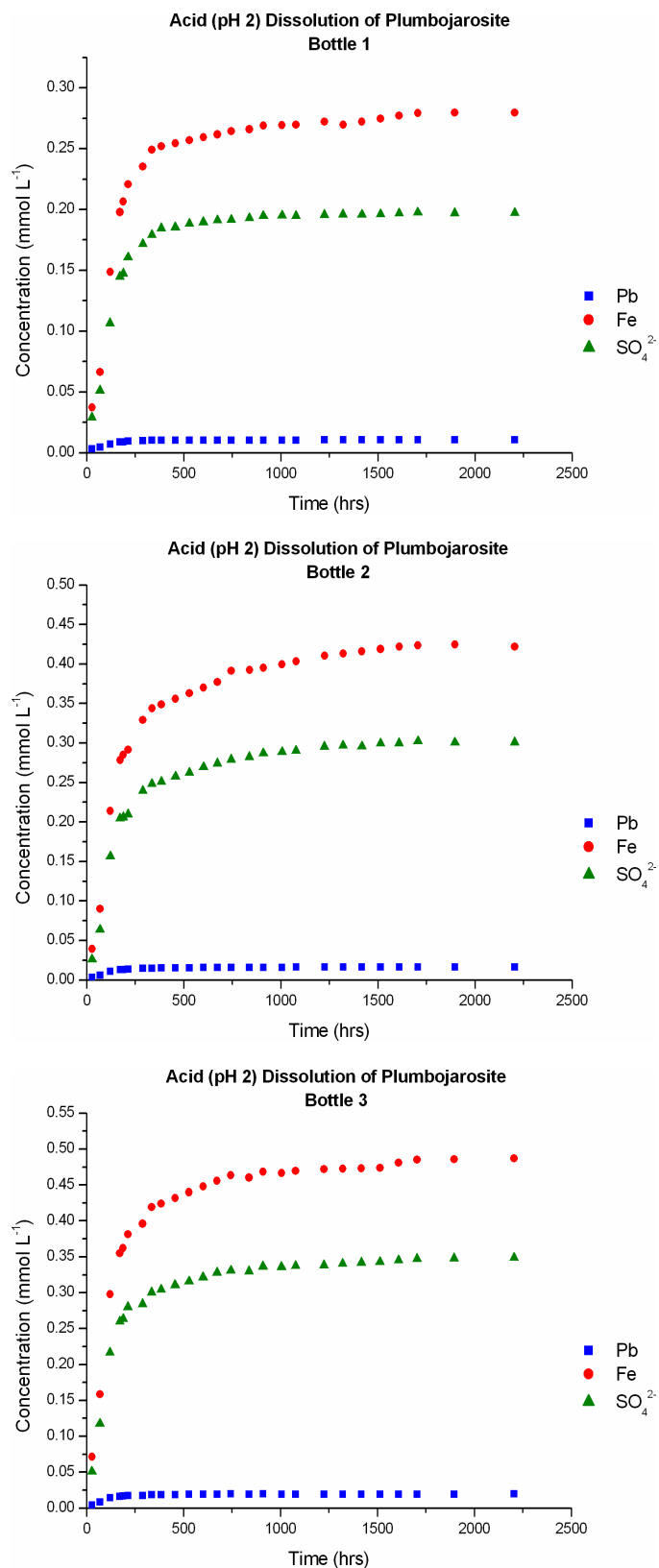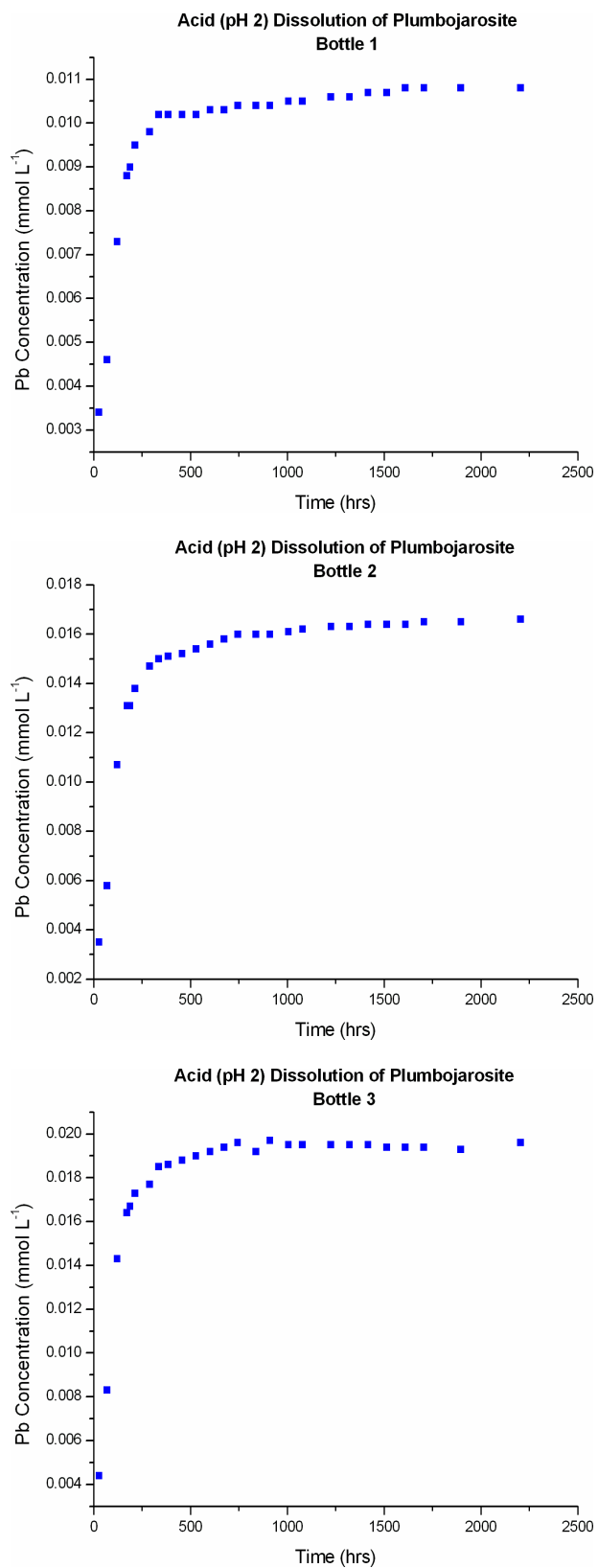
Figure 4.3. Concentrations of Pb_{tot} in solution re-plotted from Figure 4.2 on a more appropriate scale for the acid dissolution of plumbojarosite. Solution profiles for all three bottles are presented to prove reproducibility.

compared to that of synthetic plumbojarosite (0.13), and the Fe ratio in solution varied from 2.79 – 2.83 compared to synthetic value 2.92 (Table 3.3). Equilibrium aqueous activities were calculated using the final pH and Pb_{tot}, Fe_{tot}, and $SO_4^{2-}{}_{tot}$, for Pb^{2+}, $Fe^{3+,}$ and SO_4^{2-}, by GWB (Table 4.3). The charge balance error across the triplicates ranged from 3 to 5 % (Table 4.3). Positive saturation indices were found for hematite and goethite, whilst a negative index was calculated for anglesite (Table 4.4).

Table 4.3. Calculated equilibrium activities for the acid dissolutions.

Compound	pH	Calculated equilibrium activities					Charge balance error (%)	Calculated log IAP
		log $\{SO_4^{2-}\}$	log $\{H_2AsO_4^-\}$	log $\{K^+\}$	log $\{Pb^{2+}\}$	log $\{Fe^{3+}\}$		
Potassium jarosite								
Acid Bottle 1	2.04	-3.95	-	-3.67	-	-4.02	3	-11.36±0.25
Acid Bottle 2	2.02	-3.90	-	-3.73	-	-3.96	6	-11.30±0.25
Acid Bottle 3	2.03	-3.96	-	-3.74	-	-3.96	5	-11.38±0.25
Plumbojarosite								
Acid Bottle 1	2.07	-4.09	-	-	-5.21	-4.10	3	-10.65±0.25
Acid Bottle 2	2.07	-3.91	-	-	-5.03	-3.93	4	-9.68±0.25
Acid Bottle 3	2.07	-3.85	-	-	-4.96	-3.87	5	-9.35±0.25
Beudantite								
Acid Bottle 1	2.10	-5.21	-4.80	-	-7.47	-4.67	5	-
Acid Bottle 2	2.10	-5.21	-4.79	-	-7.64	-4.67	5	-
Acid Bottle 3	2.10	-5.20	-4.78	-	-7.70	-4.67	5	-

4.1.3 Beudantite

The concentration ion profiles from the acid dissolution of beudantite (Figure 4.4) were different to the other acid experiments. The main differences are evident in the Pb and SO_4^{2-} profiles, which have been re-plotted from the original figure on more appropriate scales in Figures 4.5 and 4.6, respectively. The Pb concentration was extremely low, and the SO_4^{2-} concentration in solution was lower than AsO_4^{3-} (Figure 4.4). The lack of data points for Pb in bottles 2 and 3 just before 400 hrs into the experiment indicated that the Pb concentrations in solution were below the detection limits (5 ppb) of the ICP-OES. All three Pb profiles from the triplicates indicated a very sharp drop in concentration in the first 250 – 300 hrs of the experiment. Due to the lack of Pb data for bottles 2 and 3 after 400 hrs, the Pb concentration in bottle 1 had to be relied upon to give an insight into the ion's overall profile during the lifetime of the experiment. After the sharp decrease in Pb concentration in the first 250 to 300 hrs of the experiment in bottle 1, the concentration then slowly reached a plateau around 0.00006 mmol L^{-1}. All the re-plotted SO_4^{2-} profiles (Figure 4.6) from
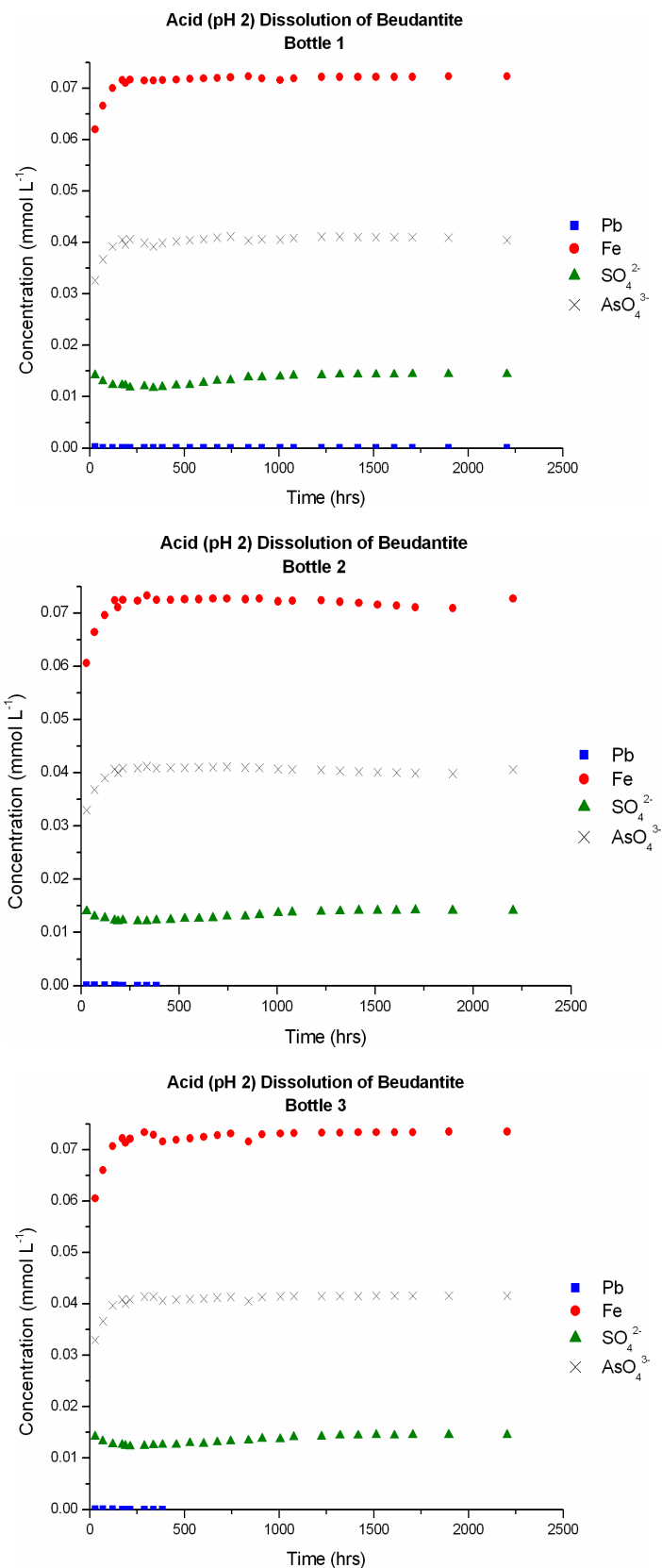
Figure 4.4. Concentrations of Pb_{tot}, Fe_{tot}, $SO_4^{2-}{}_{tot}$, and $AsO_4^{3-}{}_{tot}$ in solution for the acid dissolution of beudantite plotted against time, with the initial pH set at 2.00. Solution profiles for all three bottles are presented to prove reproducibility.
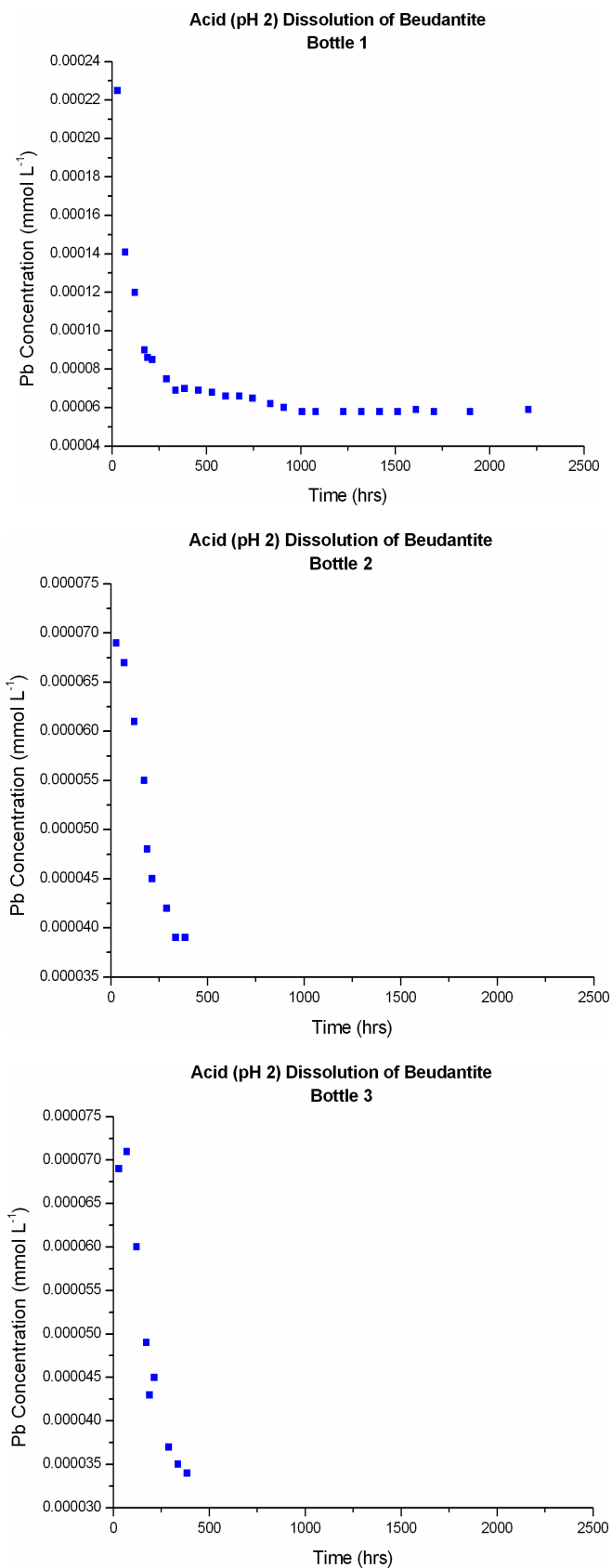
Figure 4.5. Concentrations of Pb_{tot} in solution re-plotted from Figure 4.4 on a more appropriate scale for the acid dissolution of beudantite. Solution profiles for all three bottles are presented to prove reproducibility.
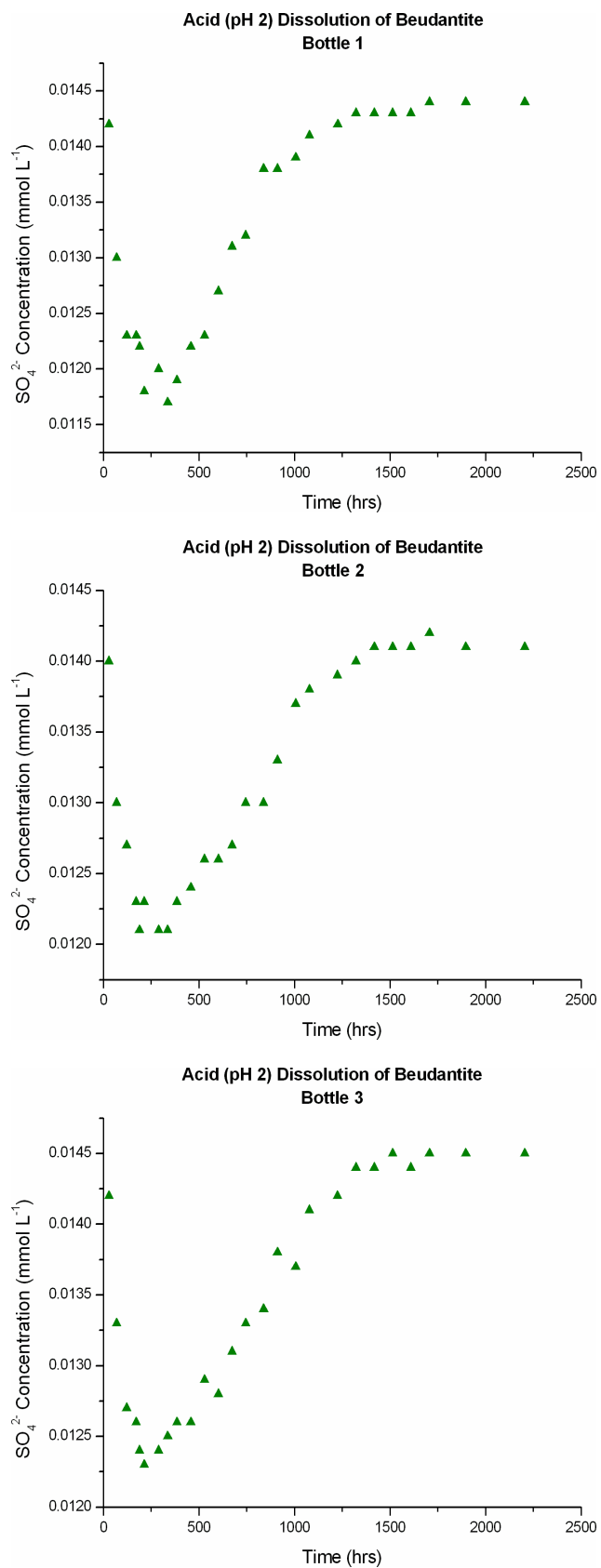
Figure 4.6. Concentrations of $SO_4^{2-}{}_{tot}$ in solution re-plotted from Figure 4.4 on a more appropriate scale for the acid dissolution of beudantite. Solution profiles for all three bottles are presented to prove reproducibility.

the three triplicates had very similar shapes, in that the concentration of the ion decreased sharply to a minimum around 250 to 300 hrs, after which the profiles took on a linear resemblance from approximately 300 to 1250 hrs. The concentration of SO_4^{2-} then became relatively uniform until the end of the experiment. In all three cases, the concentrations of SO_4^{2-} at the beginning of the experiments were relatively close to those at the end (Figure 4.6). The Fe and AsO_4^{3-} concentration profiles were extremely similar across the three bottles, resembling ions that conform to parabolic rate kinetics (Figure 4.4).

Table 4.4. Calculated saturation indices for the alkali dissolutions.

Compound	Saturation Indices (log Q/K)*		
Potassium jarosite			
Acid Bottle 1	Hematite 4.11	Goethite 1.57	Jarosite -1.99
Acid Bottle 2	Hematite 4.07	Goethite 1.55	Jarosite -1.93
Acid Bottle 3	Hematite 4.13	Goethite 1.58	Jarosite -1.88
Plumbojarosite			
Acid Bottle 1	Hematite 4.13	Goethite 1.58	Anglesite -1.45
Acid Bottle 2	Hematite 4.48	Goethite 1.76	Anglesite -1.09
Acid Bottle 3	Hematite 4.59	Goethite 1.82	Anglesite -0.96
Beudantite			
Acid Bottle 1	Hematite 3.12	Goethite 1.08	
Acid Bottle 2	Hematite 3.14	Goethite 1.09	
Acid Bottle 3	Hematite 3.15	Goethite 1.09	

* Only minerals with log Q/K > -3 are listed

Due to the complicated nature of the aqueous ion profiles for the acid dissolution of beudantite, no obvious point in time could be found to class the reaction to have reached steady state; therefore, the experiment was terminated before 2250 hrs. As a result, all ion concentrations and pH values are reported as final rather than steady state concentrations. The final pH once again hardly moved over the duration of the experiment (2.00 to 2.10 across the three bottles; Table 4.1). The final total concentrations of Pb, Fe, SO_4^{2-}, and AsO_4^{3-} and their corresponding molar ratios are presented in Table 4.1 and Table 4.2, respectively. The molar ratios of the ions in solution were calculated by setting SO_4^{2-} equal to 1.69, a value calculated from the characterisation of the synthetic beudantite (Table 3.3). The Pb ratio in solution varied from 0.0040 – 0.0069 compared with that of the synthetic beudantite (0.32); the large variation was likely due the lack of measurable Pb in the in bottles 2 and 3 at the end of the experiment. The Fe ratio in solution varied from 8.485 – 8.713

compared with the synthetic solid (2.86). Finally, the AsO_4^{3-} solution ratio ranged from 4.741 – 4.849, in comparison to 0.31 for synthetic beudantite (Table 3.3).

Equilibrium aqueous activities were calculated using the final pH and Pb_{tot}, Fe_{tot}, $SO_4^{2-}{}_{tot}$, $AsO_4^{3-}{}_{tot}$ for Pb^{2+}, Fe^{3+}, SO_4^{2-}, and $H_2AsO_4^-$, by GWB (Table 4.3). Even though AsO_4^{3-} is a structural unit (T-site) in beudantite, AsO_4^{3-} is not a stable aqueous phase in acidic (pH < 6.2) oxidising conditions (Smedley and Kinniburgh 2002). Under the alkali dissolution conditions for beudantite, the stable aqueous phase of As^{5+} is the arsenic oxyanion, $H_2AsO_4^-$. It is for this reason that the As aqueous contribution for the calculated equilibrium activities is represented by $H_2AsO_4^-$ and not AsO_4^{3-} (Table 4.3) (Smedley and Kinniburgh 2002). The charge balance error across the triplicates was 5 % (Table 4.3). Positive saturation indices were found for hematite and goethite (Table 4.4).

4.2 Residual solids

Varying solution concentrations of K, Pb, Fe, SO_4^{2-}, and AsO_4^{3-} have been found from the three acidic dissolution experiments. This section discusses the characterisation of the remaining solids and the investigations carried out to determine if any new solid phases formed from solution. These are considered important tasks to help to understand the mechanisms of jarosite breakdown.

4.2.1 Chemical analysis of residual solids

Upon completion of the all three experiments the post-acid dissolution solids of potassium jarosite, plumbojarosite, and beudantite were analysed by wet chemistry (ICP-OES) for total concentrations of K, Pb, Fe, SO_4^{2-}, and AsO_4^{3-}, where the SO_4^{2-} and AsO_4^{3-} concentrations were inferred from total S and As values. The residual solid concentrations from the three dissolution experiments and their corresponding molar ratios are summarised in Tables 4.5 and 4.6, respectively. All the raw data corresponding to this section on chemical analysis of the residual solids can be found in Appendix C.3.

Table 4.5. Residual solid concentrations for the acid dissolutions.

Compound	Residual solid concentration (mmol L^{-1})				
	K	Pb	Fe	SO_4^{2-}	AsO_4^{3-}
Potassium jarosite					
Acid Bottle 1	0.1552	-	0.6147	0.4636	-
Acid Bottle 2	0.1582	-	0.6345	0.4713	-
Acid Bottle 3	0.1576	-	0.6266	0.4682	-
Plumbojarosite					
Acid Bottle 1	-	0.0273	0.3628	0.2306	-
Acid Bottle 2	-	0.0273	0.3723	0.2376	-
Acid Bottle 3	-	0.0276	0.3704	0.2358	-
Beudantite					
Acid Bottle 1	-	0.0920	0.6680	0.3607	0.0335
Acid Bottle 2	-	0.0927	0.6754	0.3643	0.0340
Acid Bottle 3	-	0.0920	0.6660	0.3590	0.0341

For the potassium jarosite acid dissolution, the molar ratios of the concentrations of the residual solids were calculated on a similar pretext as to that of the aqueous data, that is, that SO_4^{2-} equalled 2 (Table 4.6). Under these conditions the K ratio in the residual solids varied from $0.669 - 0.673$, whereas the K ratio in the synthetic solid was 0.84. The Fe ratio in the residual solids ranged from $2.652 - 2.692$, where as the corresponding value in the synthetic solid was 2.46 (Table 3.3). The molar ratios for the ions in the residual solids of the plumbojarosite dissolution (Table 4.6) were calculated on the same premise as above, that being SO_4^{2-} also equalled 2. The Pb ratio varied from $0.230 - 0.236$, compared to the synthetic value of 0.13, and the Fe ratio ranged from $3.133 - 3.137$, where the value in synthetic plumbojarosite was 2.92.

Table 4.6. Residual solid molar ratios for the acid dissolutions.

Compound	Residual solid molar ratios				
	K	Pb	Fe	SO_4^{2-}	AsO_4^{3-}
Potassium jarosite					
Acid Bottle 1	0.669	-	2.652	2	-
Acid Bottle 2	0.671	-	2.692	2	-
Acid Bottle 3	0.673	-	2.676	2	-
Plumbojarosite					
Acid Bottle 1	-	0.236	3.147	2	-
Acid Bottle 2	-	0.230	3.133	2	-
Acid Bottle 3	-	0.234	3.141	2	-
Beudantite					
Acid Bottle 1	-	0.431	3.129	1.69	0.157
Acid Bottle 2	-	0.430	3.133	1.69	0.158
Acid Bottle 3	-	0.433	3.135	1.69	0.160

Finally, the molar ratios of the residual solid of beudantite (Table 4.6) were calculated on the basis that the SO_4^{2-} value in the characterised solid was calculated to be 1.69 (Table 3.3). The Pb ratio was found to vary from 0.430 – 0.433, compared to the synthetic of 0.32; the Fe varied from 3.129 – 3.135, whilst in synthetic beudantite the Fe ratio was 2.86. The AsO_4^{3-} value in the residual solid of beudantite ranged from 0.157 – 0.160, compared to the idealised synthetic value of 0.31 (Table 3.3).

4.2.2 Identification of residual solids

X-ray diffraction patterns were attained for the post-acidic dissolution solids of potassium jarosite, plumbojarosite, and beudantite (Figures 4.7-4.9, respectively). The diffraction patterns were then compared with the corresponding ICDD PDF files used to identify the original synthetic endmember jarosites (potassium jarosite 22-0827, plumbojarosite 33-0759, and beudantite 19-0689). All the peaks produced by the residual solids could be identified as those relating to the structure of their corresponding synthetic analogues. The absence of unidentified peaks in the patterns indicated that no new phases were present at detectable levels.
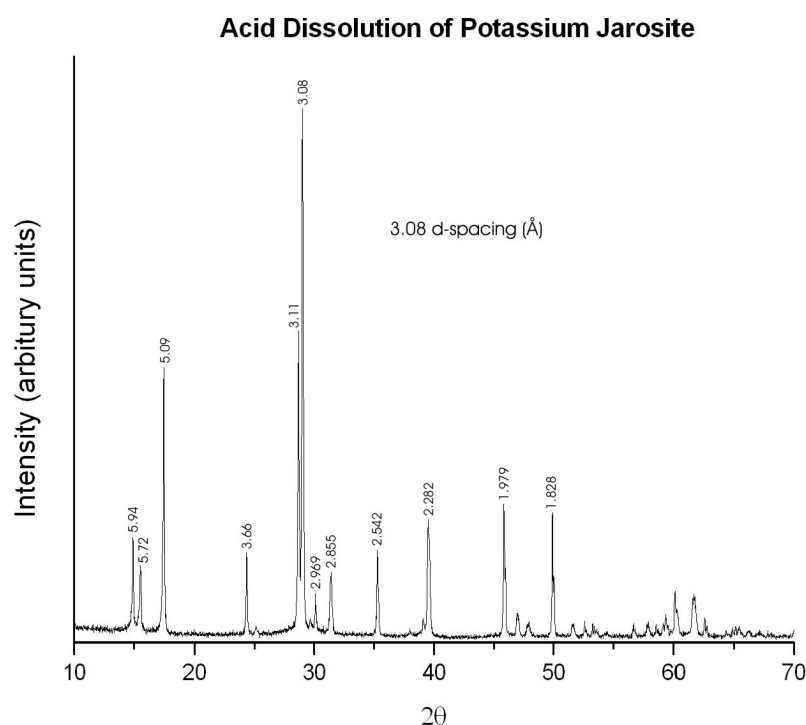
Figure 4.7. Powder X-ray diffraction of the residual solid from the acidic dissolution of potassium jarosite, mounted on a Bruker zero background silicon (510) sample holder; using Cu Kα radiation (λ = 1.54056 Å) source, 2-theta range 10-70°, step size 0.020°, step time 27s. d-spacings have been indicated for the strongest peaks.

Acid Dissolution of Plumbojarosite
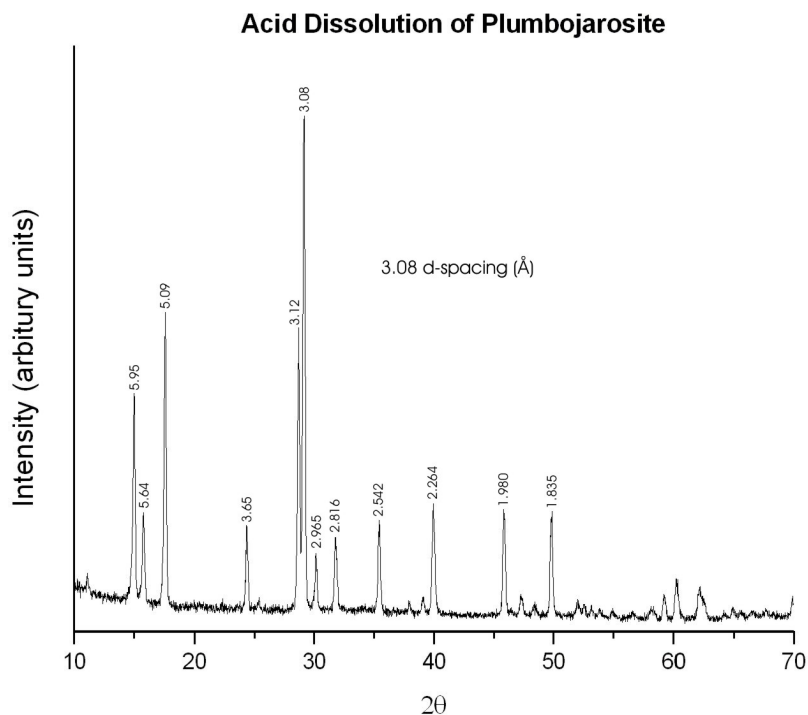
Figure 4.8. Powder X-ray diffraction of the residual solid from the acidic dissolution of plumbojarosite, mounted on a Bruker zero background silicon (510) sample holder; using Cu Kα radiation (λ = 1.54056 Å) source, 2-theta range 10-70°, step size 0.020°, step time 18s. d-spacings have been indicated for the strongest peaks.

Acid Dissolution of Beudantite
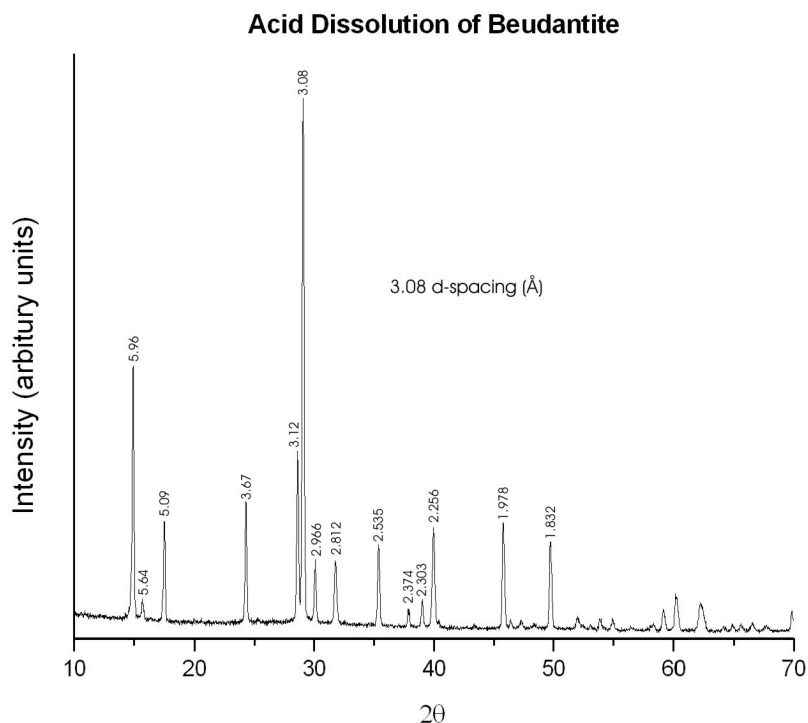
Figure 4.9. Powder X-ray diffraction of the residual solid from the acidic dissolution of beudantite, mounted on a Bruker zero background silicon (510) sample holder; using Cu Kα radiation (λ = 1.54056 Å) source, 2-theta range 10-70°, step size 0.020°, step time 27s. d-spacings have been indicated for the strongest peaks.

Synthetic Anglesite
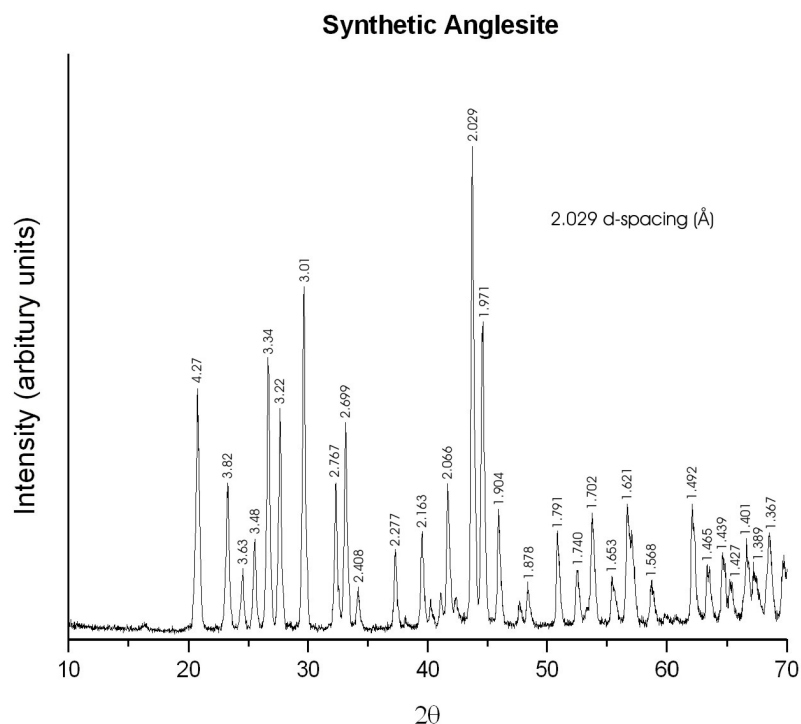
Figure 4.10. Powder X-ray diffraction of synthetic anglesite (PbSO4), mounted on a Bruker zero background silicon (510) sample holder; using Cu Kα radiation (λ = 1.54056 Å) source, 2-theta range 10-70°, step size 0.020°, step time 27s. d-spacings have been indicated for the strongest peaks.

FTIR spectra of the residual solids recovered from the acidic dissolution experiments are shown in Figure 4.11. The spectra are very similar to those of the original synthetic analogues shown in Figure 3.15. No extra bands relating to additional phases could be seen.

All the FTIR spectra contain an intense absorption band in the region 2900 to 3700 cm^{-1} attributed to O-H stretching (v_{OH}). A band at 1634 to 1641 cm^{-1}, assigned to HOH deformation, relating to the presence of 'additional water' groups. Three intense absorption bands at 1000 to 1200 cm^{-1}, credited to two vibrational modes within the sulphate unit $v_3(SO_4^{2-})$ (doublet, at the two higher wavenumbers) and $v_1(SO_4^{2-})$ (at the lowest wavenumber). Two other vibrational modes of sulphate, the $v_4(SO_4^{2-})$ around 630 cm^{-1} and as a doublet in potassium jarosite at 657 cm^{-1} (Figure 4.11a), and the $v_2(SO_4^{2-})$ near 470 cm^{-1}. For the beudantite sample (Figure 4.11c), two additional peaks were seen between 810 and 860 cm^{-1}; these correspond to the $v_3(AsO_4^{3-})$ and $v_1(AsO_4^{3-})$ vibrational modes of arsenate. IR bands near 580 and 505 cm^{-1} correspond to an O-H bending mode (γ_{OH}) and to an O-Fe vibration within the FeO$_6$ coordination octahedron. O-H bending modes were not present in the spectra of

plumbojarosite (Figure 4.11b) (Powers et al. 1975, Baron and Palmer 1996b, Serna et al. 1986, Sasaki et al. 1998, Drouet and Navrotsky 2003).
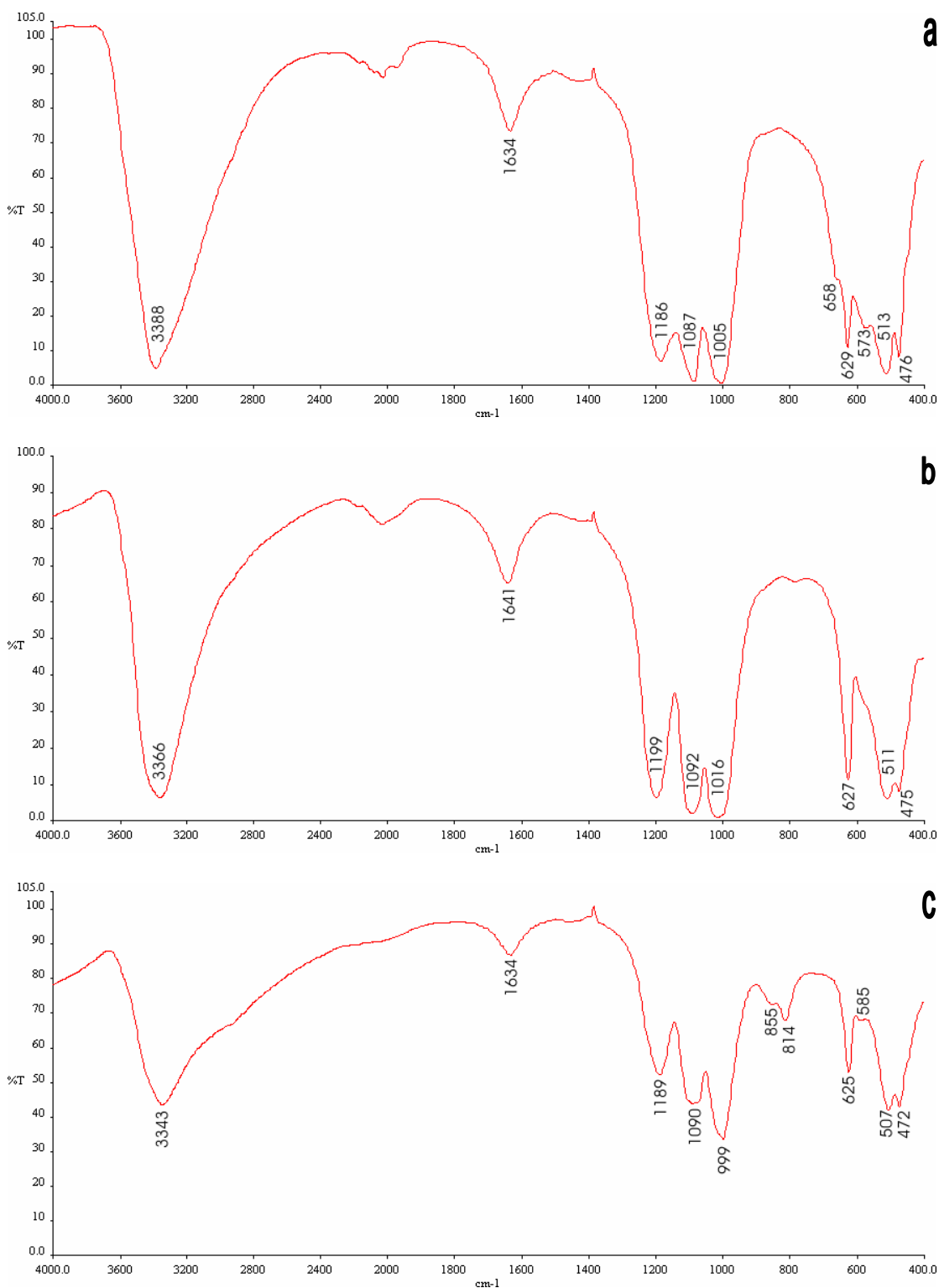
Figure 4.11. Fourier transform infrared spectra (FTIR) of the acidic dissolutions of (a) potassium jarosite, (b) plumbojarosite, and (c) beudantite. The range was 400 – 4000 cm^{-1} wavenumbers with a resolution of 4 cm^{-1}, five scans were accumulated. The main vibrational bands in the spectrum are marked.
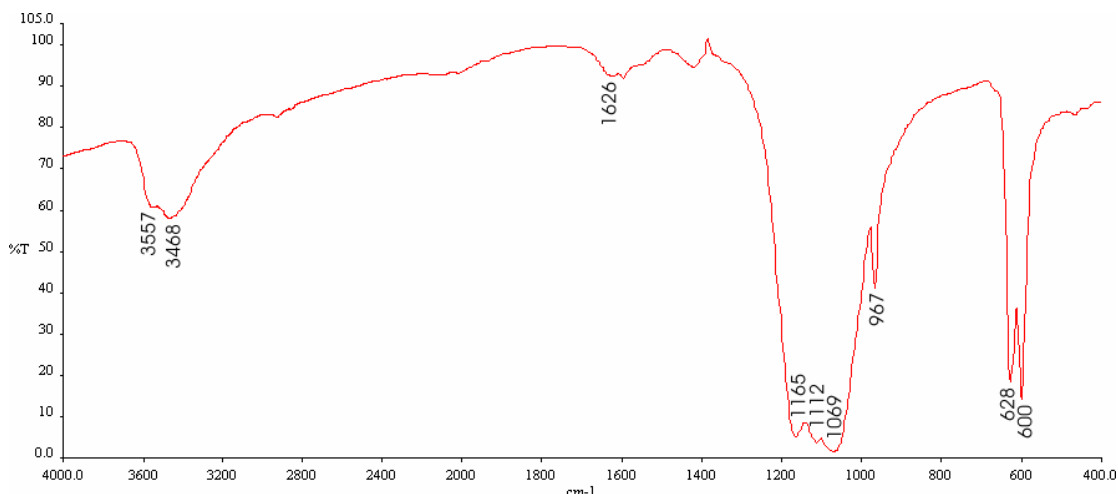
Figure 4.12. Fourier transform infrared spectra (FTIR) of synthetic anglesite (PbSO$_4$). The range was 400 – 4000 cm^{-1} wavenumbers with a resolution of 4 cm^{-1}, five scans were accumulated. The main vibrational bands in the spectrum are marked.

4.2.3 Morphology

Figure 4.13 shows the subtle colour changes between the original synthetic jarosites and the residual solids recovered at the end of the acidic dissolutions. Munsell colours were assigned to the residual solids and are compared to the original synthetic values (Table 3.1). For the dissolution of potassium jarosite, the residual solid had a Munsell colour of 2.5Y 8/8; the solid had a higher yellow component and a higher chroma indicating a purer and lighter colour, compared to the original synthetic potassium jarosite. For plumbojarosite, the residual solid had a Munsell colour of 10YR 7/8 and only a slightly higher chroma than the original solid. The Munsell colour for the residual solid in the acidic dissolution of beudantite was 10YR 7.5/8; the value is slightly less than the original synthetic beudantite, indicating the residual solid is slightly darker in colour.

Figure 4.14a is an overview of the particle morphology of the residual solid from the potassium jarosite dissolution. It is clear in the micrograph that the majority of the grains had a degree of surface roughness and showed extensive pitting on the surface, compared to the very smooth globular grain morphology seen for the original synthetic analogue (Figure 3.21a). At higher magnification (Figure 4.14b), it was possible to see the extent of the surface pitting. The surface roughness appears to arise from the internal structure of the grains being exposed as the smooth surface was
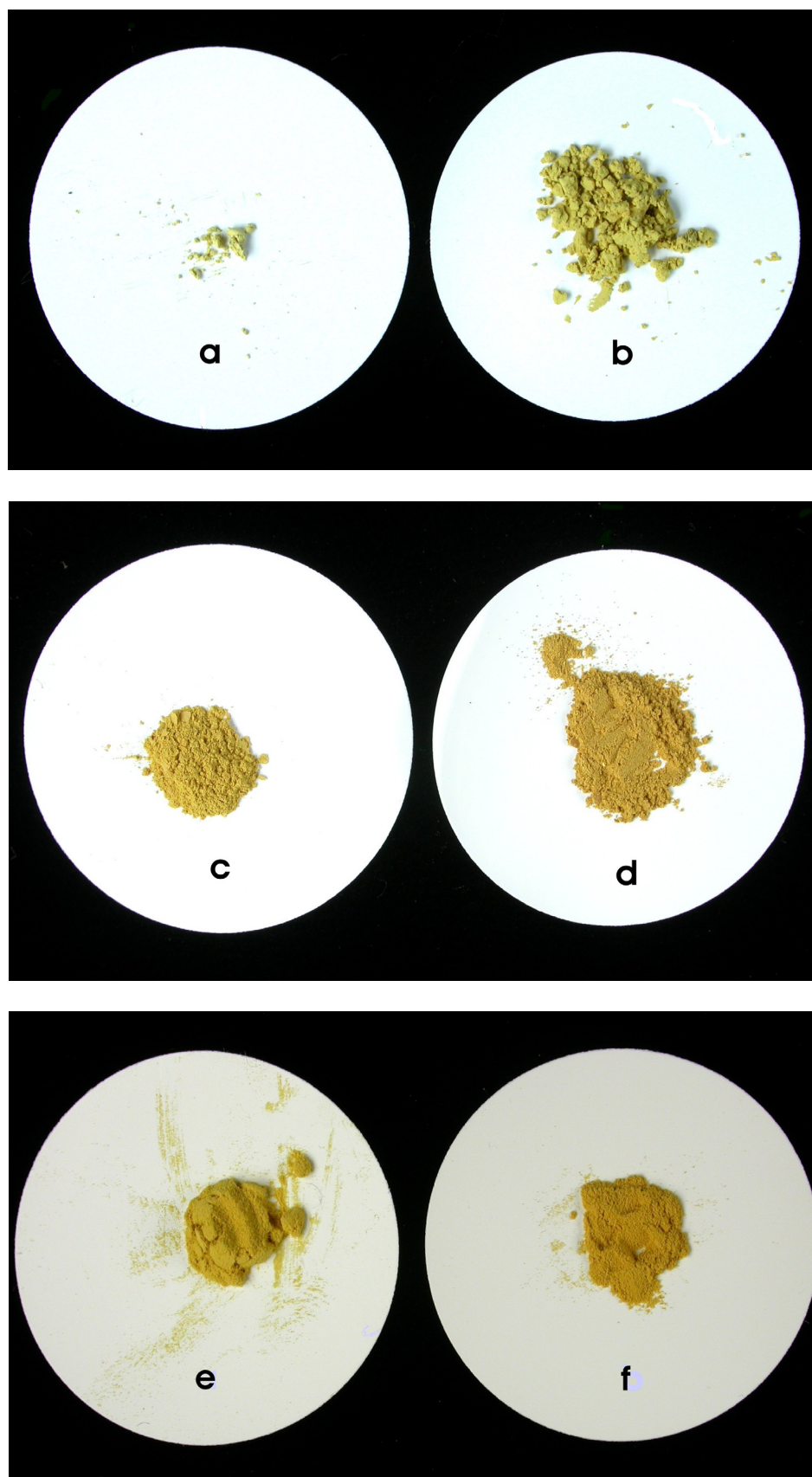
Figure 4.13. Illustrations showing the subtle colour changes between the synthetic jarosites and the residual solids recovered at the end of the acidic dissolutions. Potassium jarosite: (a) residual solid and (b) synthetic. Plumbojarosite: (c) residual solid and (d) synthetic. Beudantite: (e) residual solid and (f) synthetic.

being removed. Neither micrograph in Figure 4.14 showed any evidence of a new phase being present.
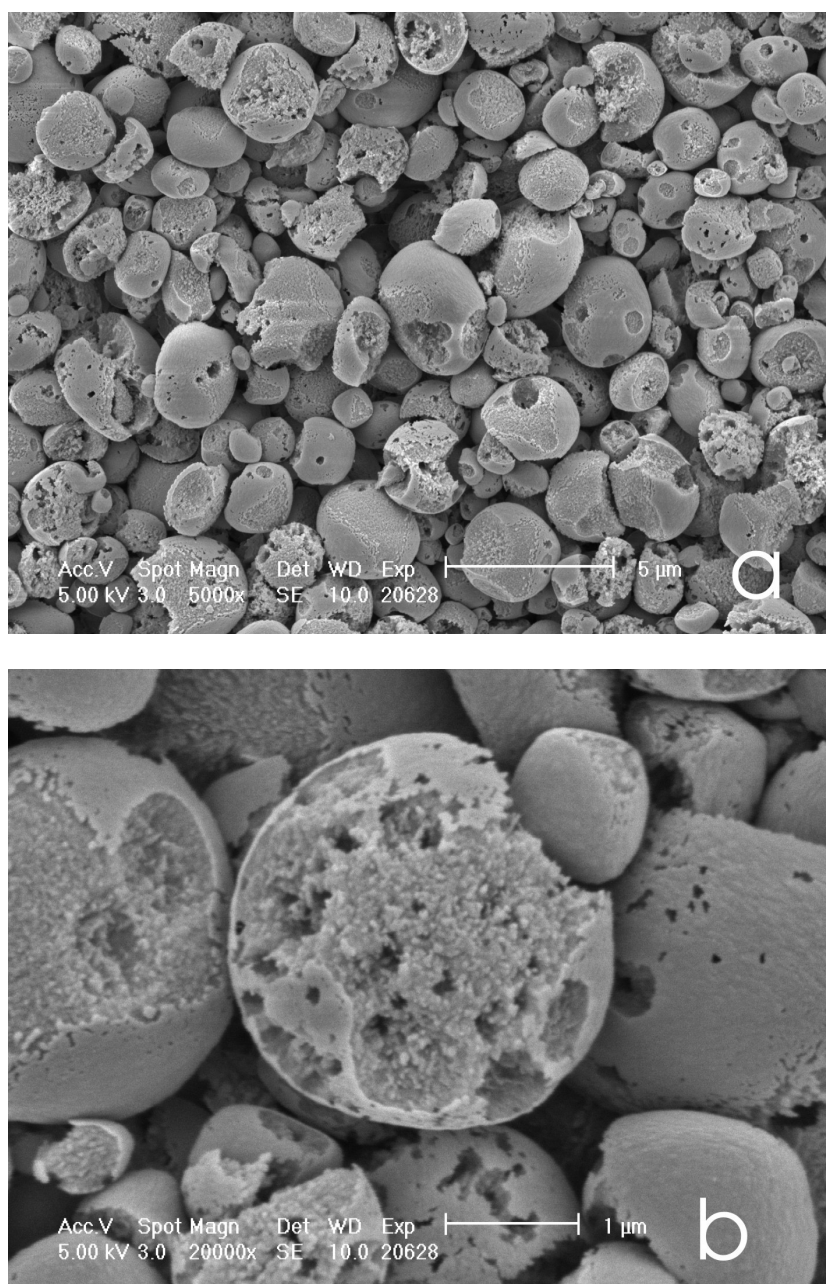
Figure 4.14. Scanning electron micrograph (SEM) images of the residual solid from the acidic dissolution of potassium jarosite. Image (a) is a general overview of the residual solid, extensive pitting of the surface can be observed. Image (b) is a high-resolution micrograph of a single potassium jarosite grain; again, extensive surface weathering and pitting are evident. Operating conditions indicated on each micrograph.

For the plumbojarosite dissolution, the particle morphology of the residual solid (Figure 4.15a) was quite different from that of potassium jarosite (Figure 4.14) in that there appeared to be some selective dissolution occurring at the grain surface. This selective dissolution appeared to follow the crystal habit, so much so that as the
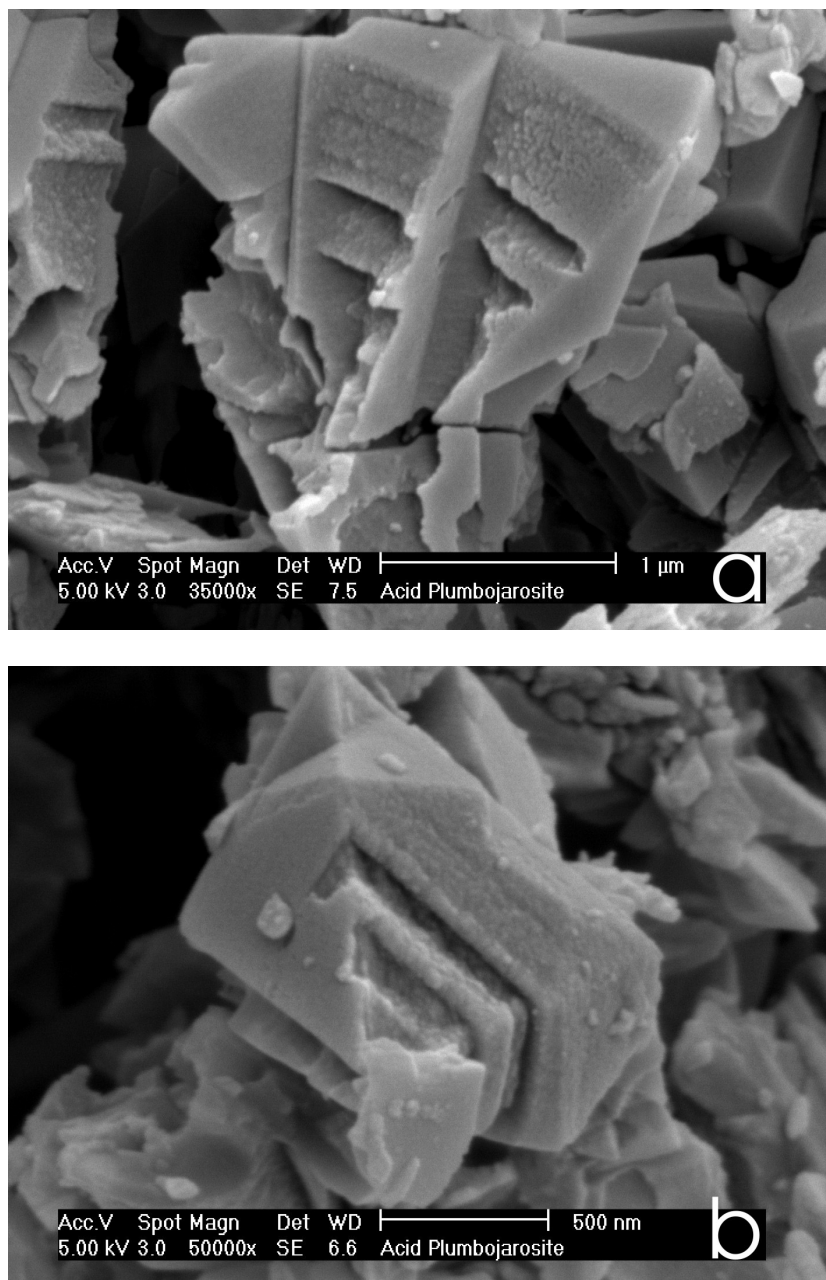
Figure 4.15. Scanning electron micrograph (SEM) images of the residual solid from the acidic dissolution of plumbojarosite. Image (a) highlights common dissolution morphology throughout the plumbojarosite sample. Image (b) is a high-resolution micrograph of a single plumbojarosite grain, selective dissolution at the surface of the grain is clearly visible. Operating conditions indicated on each micrograph.

dissolution occurred across two surfaces of a grain there appeared to be a right angle bend in the dissolution feature (Figure 4.15b). In comparison to the original synthetic plumbojarosite (Figure 3.21b), the morphology of the residual solid exhibited fine dissolution pitting (Figure 4.15a). Once again, neither micrograph in Figure 4.15 showed any evidence of a new phase being present.
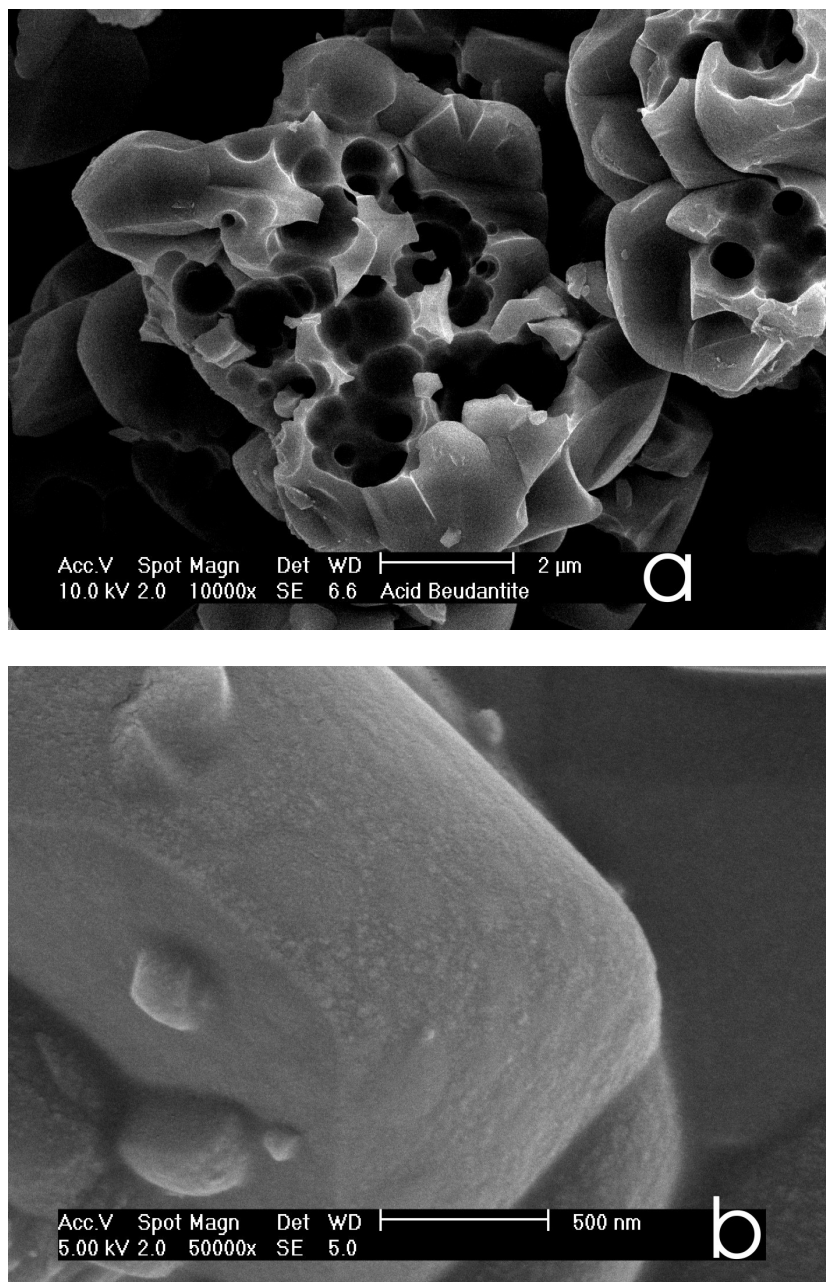
Figure 4.16. Scanning electron micrograph (SEM) images of the residual solid from the acidic dissolution of beudantite. Image (a) is a general overview of the residual solid, extensive pitting of the surface can be observed. Image (b) is a high-resolution micrograph of a single plumbojarosite grain, showing the presence of a very finely dispersed secondary phase, probably amorphous lead sulphate. Operating conditions indicated on each micrograph.

For beudantite (Figure 4.16a), the morphology of the residual solid was different to that in both of the two previous studies. The residual grains showed extensive internal dissolution, resembling smooth tubular or spherical holes, very fine dissolution pitting could be seen on the mineral surface (Figure 3.21e). At higher magnification (Figure 4.16b), a very finely distributed, 1-5 nm diameter secondary phase could be seen covering all the beudantite grains. The presence of this

secondary phase in the acid dissolution of beudantite (Figure 4.16b) is unique, as neither acid dissolution of potassium jarosite or plumbojarosite formed a secondary phase from the ions in solution (Figures 4.14, 4.15).

4.3   Discussion

4.3.1 Acid dissolution of potassium jarosite and plumbojarosite

Some similarities may be drawn between the solution compositions for the acidic dissolutions of potassium jarosite (Figure 4.1) and plumbojarosite (Figure 4.2 and 4.3) plotted over time in that they conformed to parabolic rate kinetics. The beginning of both experiments saw rapid releases of constituent ions that make up both jarosites being eluted into solution. The rate of release then slowly deceased until there was very little change in solution concentration. At the point where the solution concentration for each constituent ion was constant, the dissolution reaction had reacted quasi-steady state. Based on this relative simplistic description of steady state, it is possible to say that the acidic dissolution of plumbojarosite reached steady state more rapidly than did potassium jarosite (~ 1500 hrs compared to 3000 hrs). The jarosite subgroup of minerals are all isostructural and the main structural difference between potassium jarosite and plumbojarosite is the A-site cation (K^+ for potassium jarosite and Pb(II) for plumbojarosite). Both minerals share similar T-O-T sheeting made up from Fe(III) ions and SO_4^{2-} tetrahedra, but the incorporation of Pb(II) at the A-site leads ideally to a doubling of the jarosite unit cell along the c-axes, when the Pb(II) occupancy is high (i.e. > 0.4 formula units, where ideal is 0.5) (Dutrizac et al. 1980). From the powder X-ray diffraction pattern for the synthetic plumbojarosite (Figure 3.3), the absence of an 11 Å (003) reflection indicates that the Pb(II) ions and vacancies were not ordered in the A-site. The added strain of accommodating a Pb(II) ion instead of a K^+ ion in the A-site, shown through the lack of a doubled c-axis and the lack of A-site ordering, would suggest that the plumbojarosite structure was inherently less stable than the potassium jarosite structure. This instability could account for the increased rate of dissolution over the first 500 hrs for plumbojarosite than for potassium jarosite, even though both endmembers have very similar surface areas (Table 3.8).

A comparison of the molar ratios for the aqueous and residual solid data for the acid dissolution of potassium jarosite and those of the characterised formula of the synthetic $((H_3O)_{0.16}K_{0.84}Fe_{2.46}(SO_4)_2(OH)_{4.38}(H_2O)_{1.62}$, Table 3.3) reveals some interesting relationships. The aqueous molar ratios of K and SO_4^{2-} (1.25-1.24:2, Table 4.2; excluding the K data in bottle 1, due to contamination by KCl from the pH probe) suggest that there were excessive K ions in solution compared to SO_4^{2-}, considering the synthetic ratio should be 0.84:2. A similar disparity between K and SO_4^{2-} in the molar ratios of the residual solids is seen. These molar ratios indicate a net deficiency of K in the solid in comparison to SO_4^{2-} (0.669-0.673:2), compared to the synthetic idealised ratio of 0.84:2 (Table 4.5, 3.3). A similar relationship is seen between Fe and SO_4^{2-}, though in this case Fe was found to be deficient in solution in compared to SO_4^{2-} (2.34-2.36:2, compared to 2.46:2) (Table 4.2, 3.3). Once again, the residual solid molar ratio data supports the Fe deficiency in solution by a higher than synthetic Fe: SO_4^{2-} ratio in the residual solid of 2.652-2.676:2 compared to 2.46:2 (Table 4.5, 3.3). To summarise, all three ions show-varying degrees of incongruency with respect to their concentrations in solution at the end of the acidic dissolution of potassium jarosite, where steady state was thought to have been attained. Specifically, K and SO_4^{2-} are in excess compared to Fe, and K is in excess to SO_4^{2-} (Tables 4.2, 4.5, 3.3).

For the plumbojarosite acid dissolution, similar trends to potassium jarosite are seen when the aqueous and residual molar ratios are compared against the synthetic solid $((H_3O)_{0.74}Pb_{0.13}Fe_{2.92}(SO_4)_2(OH)_{5.76}(H_2O)_{0.24}$, Table 3.3). For this experiment the overall residual solid ratios for Pb:SO_4^{2-} (0.230-0.236:2) and Fe:SO_4^{2-} (3.133-3.141:2), compared to the synthetic values of 0.13:2 and 2.92:2, respectively, indicated that the dissolved solid was significantly depleted in SO_4^{2-} (Tables 4.6, 3.3). Higher SO_4^{2-} values in solution would have had an overall effect of reducing the aqueous molar ratios of Pb and Fe. The Pb:SO_4^{2-} aqueous molar ratios ranged from 0.109-0.112:2, just slightly lower than the synthetic of 0.13:2. Similarly, the Fe:SO_4^{2-} aqueous molar ratios ranged from 2.79-2.83:2, compared to the synthetic value of 2.92:2 (Table 4.2, 3.3). All three ions (Pb, Fe, and SO_4^{2-}) in solution displayed similar varying degrees of incongruency (Tables 4.2, 4.5). In contrast to the acidic dissolution of potassium jarosite, where the K concentration exceeded that of SO_4^{2-}, the reverse is seen here between Pb and SO_4^{2-}. The reason for highlighting this discrepancy is that Pb and K occupy the A-sites in potassium jarosite and

plumbojarosite, respectively. In relative percentage terms, K occupied 84 % of the crystallographic A-sites in potassium jarosite, compared to 13 % for Pb in plumbojarosite; the remainder in each case was made up with hydronium (H_3O^+) until 100 % occupancy of the A-sites had been attained (Table 3.3). It is these opposing degrees of A-site occupancy that account for the fact that in the plumbojarosite dissolutions, SO_4^{2-} was always in relative excess to Pb. Overall, Pb and SO_4^{2-} aqueous concentrations exceed those of Fe, and SO_4^{2-} concentrations exceed Pb concentrations (Tables 4.2, 4.5, 3.3).

The aqueous ion concentration profiles for both the acid dissolution of potassium jarosite (Figure 4.1) and plumbojarosite (Figure 4.2-4.3) suggest that a transport-controlled dissolution model governed these experiments (Stumm and Morgan 1996). A general schematic representation of this dissolution model is presented in Figure 1.3a. In transport-controlled dissolution, the concentration immediately adjacent to the mineral reflects the solubility steady state. Dissolution is then limited by the rate at which dissolved dissolution products are transported by diffusion or advection to the bulk of the solution (Stumm and Morgan 1996). The shape of the acid dissolution concentration profiles for potassium jarosite and plumbojarosite (Figures 4.1, 4.2-4.3, respectively) can also be described by a dissolution rate-determining step governed by diffusion of ions from the mineral surface to the bulk solution (Stumm and Morgan 1996). Both acidic dissolutions of potassium jarosite and plumbojarosite are classed as incongruent reactions, not because any secondary phase(s) were identified, but because of the non-ideal dissolution of the parent solids. This is indicated by differing aqueous and solid molar ratios compared to the idealised synthetic molar ratios (Tables 4.2, 4.6, and 3.3).

The X-ray diffraction patterns, FTIR spectra, and SEM micrographs of the residual solids for the acidic dissolutions of potassium jarosite (Figures 4.7, 4.11a, 4.14) and plumbojarosite (Figures 4.8, 4.11b, 4.15) clearly show no new phases present, which may have precipitated from the ions in solution. The lack of any major colour change between the original synthetic endmembers (Figure 3.1, Table 3.1) and the residual solids (Figure 4.13) recovered at the end of the potassium jarosite and plumbojarosite dissolutions confirm the lack of any new phases. The SEM micrographs for potassium jarosite (Figure 4.14b) and plumbojarosite (Figure 4.15b) show extensive

and varied dissolution morphology. The difference in the dissolution structures can be explained broadly by differing degrees of crystallinity: potassium jarosite is quite globular and thus, poorly crystalline and plumbojarosite has smooth rhombohedral (pseudocubic) crystal faces. The higher degree of crystallinity for plumbojarosite was simply the result of a slower more controlled synthesis, to avoid the contamination of the product with $PbSO_4$. The selective surface dissolution seen for plumbojarosite is believed to be due to the discriminatory removal of SO_4^{2-} groups closest to the mineral's surface, which ultimately make up the linear T-O-T sheets with the B-site Fe octahedrons. The surface features in Figure 4.15b show this on a macroscopic scale. The relatively uniform weathering seen for potassium jarosite is most easily explained by its relative poor crystallinity.

In summary, the acidic dissolution of both potassium jarosite and plumbojarosite can be described as being governed by transport-controlled dissolution kinetics. Non-ideal final aqueous concentrations for the parent ions that made up the two-endmember jarosites were recorded suggesting that both dissolutions were incongruent. The acidic dissolutions of potassium jarosite and plumbojarosite can be described by Eq. 4.1 and 4.2, respectively.

$$KFe_3(SO_4)_2(OH)_{6(s)} + H^+_{(aq)} \rightarrow K^+_{(aq)} + Fe^{3+}_{(aq)} + SO^{2-}_{4(aq)} \qquad (4.1)$$

$$Pb_{0.5}Fe_3(SO_4)_2(OH)_{6(s)} + H^+_{(aq)} \rightarrow Pb^{2+}_{(aq)} + Fe^{3+}_{(aq)} + SO^{2-}_{4(aq)} \qquad (4.2)$$
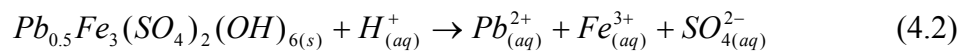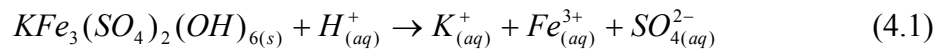
An ion activity product (IAP) was calculated for the acidic dissolution of potassium jarosite and plumbojarosite, using the equilibrium activities and final pH values from the triplicates (Table 4.3). The calculation of the IAP for the dissolution of a mineral is important, because at equilibrium, the IAP is equal to the solubility product, K_{SP}. If the dissolution of potassium jarosite and plumbojarosite were written as in Eq. 4.3 and 4.4, then the IAP for these two reactions would be as in Eq. 4.5 and 4.6, respectively.

$$KFe_3(SO_4)_2(OH)_{6(s)} + 6H^+_{(aq)} \rightarrow K^+_{(aq)} + 3Fe^{3+}_{(aq)} + 2SO^{2-}_{4(aq)} + 6H_2O_{(l)} \qquad (4.3)$$

$$Pb_{0.5}Fe_3(SO_4)_2(OH)_{6(s)} + 6H^+_{(aq)} \rightarrow \frac{1}{2}Pb^{2+}_{(aq)} + 3Fe^{3+}_{(aq)} + 2SO^{2-}_{4(aq)} + 6H_2O_{(l)} \qquad (4.4)$$
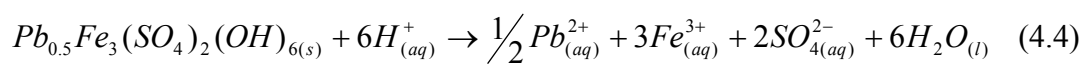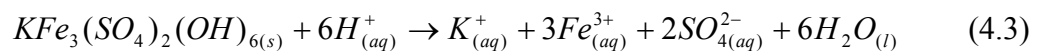
$$\log IAP = \log\{K^+\} + 3\log\{Fe^{3+}\} + 2\log\{SO_4^{2-}\} + 6\log\{H_2O\} + 6pH \qquad (4.5)$$

$$\log IAP = \log \tfrac{1}{2}\{Pb^{2+}\} + 3\log\{Fe^{3+}\} + 2\log\{SO_4^{2-}\} + 6\log\{H_2O\} + 6pH \quad (4.6)$$

A few assumptions are commonly applied when calculating IAP values and solubility products. The first and probably the one most open for questioning is that the dissolution reaction in question has reached perfect equilibrium. The reason for this assumption is that aqueous activities of ions are all calculated and reported on the premise that the initial concentrations used in computer speciation programs like GWB have come from a reaction at equilibrium. The second assumption is that the dissolution has occurred perfectly congruently, that is, the mole fractions for the particular ions in the solid equal those seen in solution (Eq. 4.3 and 4.4).

This study has shown that the acidic dissolution of both potassium jarosite and plumbojarosite are incongruent in that there is non-ideal dissolution with respect to the ions in the solid relative to those seen in solution. For this specific reason, no definitive K_{SP} value could be reported for these two dissolutions. It is, however, worth appraising the calculated IAP values for both dissolutions against published IAP values. The vast majority of the solubility data on jarosites are for potassium jarosite; at present, there are no known data for plumbojarosite. Baron and Palmer (1996b) publish an IAP value of -11.36±0.25 for a near identical experiment to that reported in this study for the dissolution of potassium jarosite. Calculated IAP values for bottles 2 and 3 (that were not contaminated by KCl) in the acidic potassium jarosite dissolution range from -11.30±0.25 to -11.38±0.25 (Table 4.3). These are extremely similar to those reported by Baron and Palmer (1996b), which is surprising considering the incongruency of the potassium jarosite dissolution. The problems of incongruent mineral dissolution can also be seen in the range of calculated IAP values for the acidic dissolution of plumbojarosite (-10.65±0.25 to -9.35±0.25, Table 4.3).

Of the saturation indices that have been calculated for the acid dissolutions of potassium jarosite and plumbojarosite (Table 4.4) by GWB, the indices for potassium jarosite are the only ones that are meaningful. The problem with the plumbojarosite saturation data is that the latest version of the GWB thermodynamic database does not contain any data for the mineral. The lack of any mineral thermodynamic data results in the program assuming that the aqueous ion concentrations determined for the plumbojarosite dissolution were due to the dissolution of anglesite. This can be seen

in Table 4.4 as a series of negative saturation indices for anglesite, where, in fact, the mineral should be plumbojarosite. As the GWB database lacks thermodynamic data on plumbojarosite the calculated positive saturation indices for hematite and goethite are also incorrect. The calculated saturation indices for the acid dissolution of potassium jarosite are similar for the three triplicates (Table 4.4). Speciation modelling of the acid dissolution of potassium jarosite predicts the stability of hematite and goethite in solution (Table 4.4). Hematite is commonly reported as a positive saturation index in nearly all aqueous Fe^{3+} rich oxic environments by programs like GWB, because the mineral is extremely stable in natural environments. The slight positive index for goethite (1.55-1.58), indicates that, probably over a long period, goethite might precipitate out of solution from the acidic dissolution of potassium jarosite. This result is not too surprising as goethite secondary weathering coatings have been observed around potassium jarosite outcrops in ARD/AMD environments (Bigham 1994).

An Eh versus pH diagram (Figure 4.17) was constructed in GWB using the equilibrium activities from Bottle 2 of the triplicates in the acid dissolution of potassium jarosite. Figure 4.17a is an Eh-pH diagram of the acid dissolution, where all the possible minerals are shown; principally this is taken up by hematite. Phase relations computed in Eh-pH space indicate the metastability of potassium jarosite relative to hematite (and any others). In order for potassium jarosite to appear on Eh–pH diagrams, hematite (and goethite etc) had to be "suppressed" (not included) in calculations carried out using Geochemist's Workbench. This indicates that phase assemblages that include potassium jarosite have higher free energies than those including hematite (and goethite etc). When hematite and a series of other minerals are suppressed (FeO, goethite, magnetite, pyrrhotite, and troilite), potassium jarosite occurs as a stable phase in a pH range of 0.5 to 5, similar to the experimental dissolution conditions (Figure 4.17b). The next stable phase is $Fe(OH)_3$, a known meta-stable phase of goethite, a mineral phase predicted to be present in the system by a positive saturation index (Table 4.4).
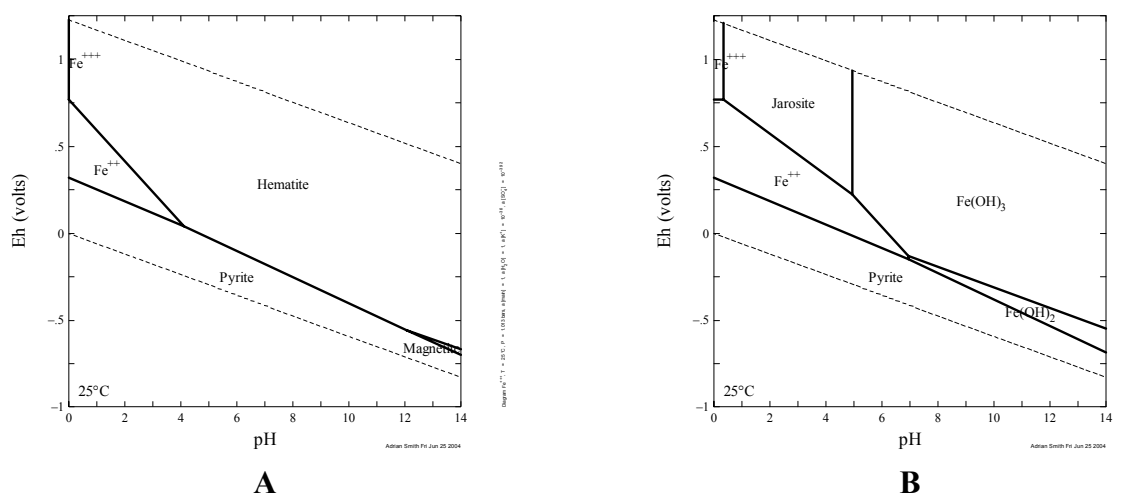
Figure 4.17. Eh-pH diagrams for the acid dissolution of potassium jarosite. Equilibrium aqueous activities were taken from Bottle 2. (a) is an Eh-pH diagram of the dissolution where all possible minerals are shown, (b) is an Eh-pH diagram where hematite and a series of other minerals have been suppressed (FeO, goethite, magnetite, pyrrhotite, and troilite) to simulate more accurately experimental conditions. The experimental conditions were: $f_{O_{2(g)}} = 0.2$, $f_{CO_{2(g)}} = 10^{-3.5}$, $ClO_4^- = 0.01$ molal, pH = 2.02, Eh = 1.09 volts, $K^+ = 0.2088$ ppm, $Fe^{3+} = 0.3900$ ppm, $SO_4^{2-} = 0.3332$ ppm.

4.3.2 Acid dissolution of beudantite

There are some similarities and more importantly, some differences, between the dissolution profiles of beudantite (Figure 4.4-4.6) and those of potassium jarosite (Figure 4.1) and plumbojarosite (Figure 4.2-4.3). In the beudantite acid dissolution, Fe and AsO_4^{3-} show similar concentration profiles to all the constituent ions involved in the potassium jarosite and plumbojarosite reactions, in that they all follow parabolic rate kinetics. The major differences between the beudantite experiment and the dissolution of potassium jarosite and plumbojarosite are the concentration profiles of Pb and SO_4^{2-}, which ultimately will have implications for the overall dissolution mechanism of beudantite in an acidic regime (Figures 4.5 and 4.6, respectively).

Some interesting relationships become obvious when comparing the molar ratios for the aqueous and residual solid together for the acidic dissolution of beudantite (Table 4.2, 4.6) against the formula of the synthetic beudantite $((H_3O)_{0.68}Pb_{0.32}Fe_{2.86}(SO_4)_{1.69}(AsO_4)_{0.31}(OH)_{5.59}(H_2O)_{0.41}$, Table 3.3). There was virtually no measurable Pb in solution for bottles 2 and 3, and a low Pb concentration $(0.000059$ mmol $L^{-1})$ in bottle 1 after 400 hrs (Table 4.1). The corresponding aqueous molar ratios ranged from 0.0040-0.0069:1.69 compared to the idealised value of 0.32:1.69 in synthetic beudantite (Table 3.3, 4.2). The molar ratio of Pb and SO_4^{2-} in

the residual solid ranges from 0.430-0.433:1.69, and importantly is higher than the synthetic beudantite (0.34:1.69; Tables 3.3, 4.6). The implication of this is that a Pb-rich secondary phase is likely to be present. In the first 300 hrs of the experiment, both Pb and SO_4^{2-} aqueous concentrations fell sharply (Figures 4.5, 4.6). In the case of the Pb, the concentration for two of the bottles was that low that it was not measurable and in bottle 1, the Pb concentration started to stabilise out to a relative uniform concentration (Figure 4.5). The SO_4^{2-} ion profiles, after reaching a concentration minimum after 300 hrs, started to rise in a linear fashion, until the concentrations reached a plateau at approximately 1250 hrs (Figure 4.6). It is proposed that the Pb-rich phase is $PbSO_4$, and the majority of the Pb precipitated out of solution as $PbSO_4$ before 400 hrs in bottles 2 and 3. As for bottle 1, it is thought that precipitation of $PbSO_4$ partially inhibited the remainder of the dissolution, thereby significantly reducing the probability of the Pb concentration changing drastically in solution, which is borne out by the relative stable Pb concentration after 1000 hrs (Figure 4.5). It is well known that $PbSO_4$ is a stable phase in these conditions as it is a common impurity in the synthesis of lead-bearing jarosites like beudantite (Dutrizac et al. 1980). The early precipitation of the Pb as $PbSO_4$ in the dissolution experiment would account for the profile of SO_4^{2-} in solution (Figure 4.6). In the synthetic beudantite, SO_4^{2-} exceeds Pb, in the order of 1.69:0.32 (Table 3.3). It is reasonable to suggest that the lower concentrations of SO_4^{2-} seen in the first 300 hrs of the reaction reflect the precipitation of $PbSO_4$. When the Pb has been removed from solution in bottles 2 and 3, and has been stabilised by the precipitation of $PbSO_4$ in bottle 1, the SO_4^{2-} concentration rises by continued dissolution of the parent solid, to a point where the concentration plateaus toward the end of the experiment (Figure 4.6).

The positive identification of $PbSO_4$ is difficult as no evidence could be found by X-ray diffraction (Figure 4.9) or FTIR spectroscopy (Figure 4.11c). The main evidence for this phase being present is a secondary phase in the SEM micrographs of the residual solid of this dissolution (Figure 4.16). It is believed that the $PbSO_4$ phase was quite amorphous as crystalline $PbSO_4$ (anglesite) has quite a distinctive X-ray diffraction pattern (Figure 4.10). As for the identification of the phase by FTIR spectroscopy, there is only one unique weak vibration at 967 cm^{-1} in crystalline synthetic anglesite (Figure 4.12) that may have identified the phase, as all the other

vibrations in this mineral also occur in jarosites (Figure 3.15, 3.16, 4.11). The absence of this 967 cm^{-1} vibrational mode confirms the amorphous nature of the PbSO$_4$ solid. Synthetic anglesite (PbSO$_4$) is pure white in colour, therefore any identification of this phase by changing Munsell colour values from the residual solid to the synthetic is going to be extremely difficult to near impossible to identify (Figure 4.13).

The concentration profiles of Fe and AsO$_4^{3-}$ resemble those of ions that conform to parabolic rate kinetics. Both profiles appeared to plateau at approximately 250 hrs (Figure 4.4), when PbSO$_4$ was being precipitated. The aqueous molar ratio for Fe:SO$_4^{2-}$ ranges from 8.485-8.713:1.69, the residual solids data from 3.129-3.135:1.69, and that for synthetic beudantite is 2.86:1.69 (Table 4.2, 4.6, 3.3). The aqueous AsO$_4^{3-}$:SO$_4^{2-}$ molar ratios range from 4.741-4.866:1.69, that for the residual solids from 0.157-0.160:1.69, and that for synthetic beudantite is 0.31:1.69 (Table 4.2, 4.6, 3.3). The molar ratios in the solids are likely to be artificially low because the total concentration of SO$_4^{2-}$ used to calculate the molar ratio is assumed to belong to beudantite; the total SO$_4^{2-}$ concentration, however, comprises the residual solid and the PbSO$_4$ secondary phase. From the aqueous molar ratios of Fe:SO$_4^{2-}$ and AsO$_4^{3-}$:SO$_4^{2-}$ it is possible to say that Fe and AsO$_4^{3-}$ are significantly in excess compared to the SO$_4^{2-}$ concentration in solution (Table 4.2). The degree to which AsO$_4^{3-}$ is in excess compared to SO$_4^{2-}$ (considering both these units occupy the same T-site in the beudantite structure) is also reflected by the residual solid AsO$_4^{3-}$:SO$_4^{2-}$ ratio (0.157-0.160:1.69), which is nearly half of the synthetic ratio of 0.31:1.69 (Table 4.6, 3.3). Even though the aqueous Fe:SO$_4^{2-}$ ratio is nearly three times higher than the synthetic value, the corresponding residual solid ratio is slightly higher than that in the synthetic beudantite. The reason for this is that the parent residual beudantite solid is still very deficient in SO$_4^{2-}$, especially considering the inherent lower residual solid ratios due to the presence of the PbSO$_4$ secondary phase. If the PbSO$_4$ secondary phase had not formed during the early part of this experiment, it is reasonable to hypothesise that the concentration of SO$_4^{2-}$ and AsO$_4^{3-}$ would have been in excess in solution compared to Pb and Fe. At the end of the experiment, however, Fe and AsO$_4^{3-}$ concentrations were found to be in excess compared to Pb and SO$_4^{2-}$. Moreover, AsO$_4^{3-}$ was found to be in excess compared to Fe, seen by the range in the aqueous molar ratios of Fe:AsO$_4^{3-}$ (0.5547-0.5551:0.31) compared to synthetic value of 2.86:0.31 (Table 3.3). All these

subtleties in non-ideal dissolution of the parent solid, and the precipitation of a secondary phase, broadly classes the acidic dissolution of beudantite as an incongruent reaction.

Due to the complexity of the acidic dissolution of beudantite, it is difficult to describe which type of dissolution model (transport or surface) best describes this dissolution. The slight linearity of the SO_4^{2-} ion concentration profile between 300-1250 hrs (Figure 4.6) suggests that after 300 hrs, the kinetics were governed by a surface-controlled reaction. To complicate matters, the initial Fe and AsO_4^{3-} profiles for the first 250 hrs are parabolic, indicative of a transport-controlled dissolution. The acidic dissolution of beudantite was therefore probably governed by a mixed transport-surface kinetic dissolution reaction, where transport mechanisms dominated the first 250 hrs of the reaction, until the secondary phase was present to such a degree on the residual solids to dominate the dissolution rate-determining step for the remainder of the experiment.

The acidic dissolution of beudantite can be summarised as being governed by mixed transport-surface controlled dissolution kinetics, where surface process superseded transport after approximately 250 to 300 hrs into the experiment. The beudantite experiment varied from the other two acidic dissolutions in that it contained an amorphous $PbSO_4$ secondary phase. The acidic dissolution of beudantite can be described by the reaction in Eq. 4.7.

$$PbFe_3(AsO_4)(SO_4)(OH)_{6(s)} + H_{(aq)}^+ \rightarrow PbSO_{4(gel)} + Fe_{(aq)}^{3+} + SO_{4(aq)}^{2-} + AsO_{4(aq)}^{3-} \quad (4.7)$$

No IAP values could be calculated for any of triplicates for the acidic dissolution of beudantite, as a secondary phase was deemed to be present in all three bottles (Table 4.3). The problem arises from the fact that a true IAP value for dissolution of a mineral assumes that the reaction has reached steady state and no ions have precipitated out of solution. Secondary phase formation in mineral dissolution skews the overall calculated IAP to a lower value than the real experimental value, because lower ion concentrations in solution result in lower equilibrium aqueous activities being reported.

None of the saturation indices that have been calculated for the acidic dissolution of beudantite by GWB are likely to be meaningful (Table 4.4). As mentioned earlier for the plumbojarosite dissolution, the problem lies in the fact that the latest version of the GWB thermodynamic database does not contain any mineral data for beudantite. This results in the program assigning a mineral that it thinks is being dissolved (in the case of plumbojarosite the program thought the parent mineral was anglesite, Table 4.4). As the GWB database lacks data on beudantite, the calculated positive saturation indices for hematite and goethite are also incorrect and therefore meaningless.

4.4   Conclusions and summary

The acidic dissolutions of potassium jarosite, plumbojarosite, and beudantite can be all classed as incongruent dissolution reactions because of the non-ideal dissolution of the parent solids, and for the formation of an amorphous secondary phase of $PbSO_4$ in the beudantite experiment. Both the potassium jarosite and plumbojarosite dissolutions could be described by transport-controlled dissolution kinetics. For the beudantite dissolution, a mixed surface-transport model was found to be the most likely mechanism that could describe the overall dissolution kinetics.

IAP values were calculated for the acidic dissolution of potassium jarosite and plumbojarosite, though no IAP could be calculated for the beudantite dissolution due to the presence of a secondary phase. The accuracy of the IAP values calculated for the potassium jarosite and plumbojarosite in this study and those in the published literature, were all called into question due to the inherit incongruency of jarosite-type minerals. An Eh-pH diagram for the acidic dissolution of potassium jarosite found that the mineral was a stable phase under the conditions of an acidic AMD/ARD environment (pH = 2.02 and Eh = 1.09 volts) (Figure 4.17).

5   Alkali dissolution studies

Chapter 5 describes the alkali dissolution studies of potassium jarosite, plumbojarosite, and beudantite.   The chapter has four sections: dissolution experimental data, residual solid characterisation data, discussion and overall summary.

5.1   Dissolution experiments

Alkali dissolution studies of potassium jarosite, plumbojarosite, and beudantite were carried out to investigate their stability and breakdown mechanisms under an alkali regime that would mimic an AMD/ARD environment recently remediated with slaked lime ($Ca(OH)_2$). Figures 5.1-5.5 show the evolution of the solution compositions over time for the dissolution experiments at 20^oC and initial pH 8. All experiments were conducted in triplicate. To avoid problems of amalgamating data together, solution profiles of all three bottles used in the dissolution experiments of the three jarosites are presented to prove reproducibility. Final ion concentrations and pH values for the three experiments and their corresponding molar ratios are summarised in Tables 5.1 and 5.2, respectively. Calculated equilibrium activities and saturation indices for the dissolutions are presented in Tables 5.3 and 5.4, respectively. All the raw aqueous data and equilibrium activity data can be found in Appendix C.2 and C.4.2, respectively.

5.1.1 Potassium jarosite

In the potassium jarosite experiment the majority of the dissolution occurred within the first 1500 hrs, with rates declining with time (Figure 5.1). The Fe concentration in solution remained extremely low throughout the experiment in all three bottles. By the end of the experiment the Fe concentration in solution varied from 0.0023 – 0.0025 mmol L^{-1} in the three bottles. The concentration profiles of K and SO_4^{2-} displayed characteristics commonly attributed to parabolic rate kinetics. The solution data for bottle 1 was terminated early at approximately 3250 hrs to investigate the possibility of the existence of a secondary phase(s). Steady state was judged to have occurred after approximately 3500 – 4000 hrs, taken based on the solution profiles for bottles 2 and 3. Over the course of the dissolution experiment, the pH across the triplicates changed from initial pHs of 8.0 to final pHs ranging from 3.26 to 3.30.
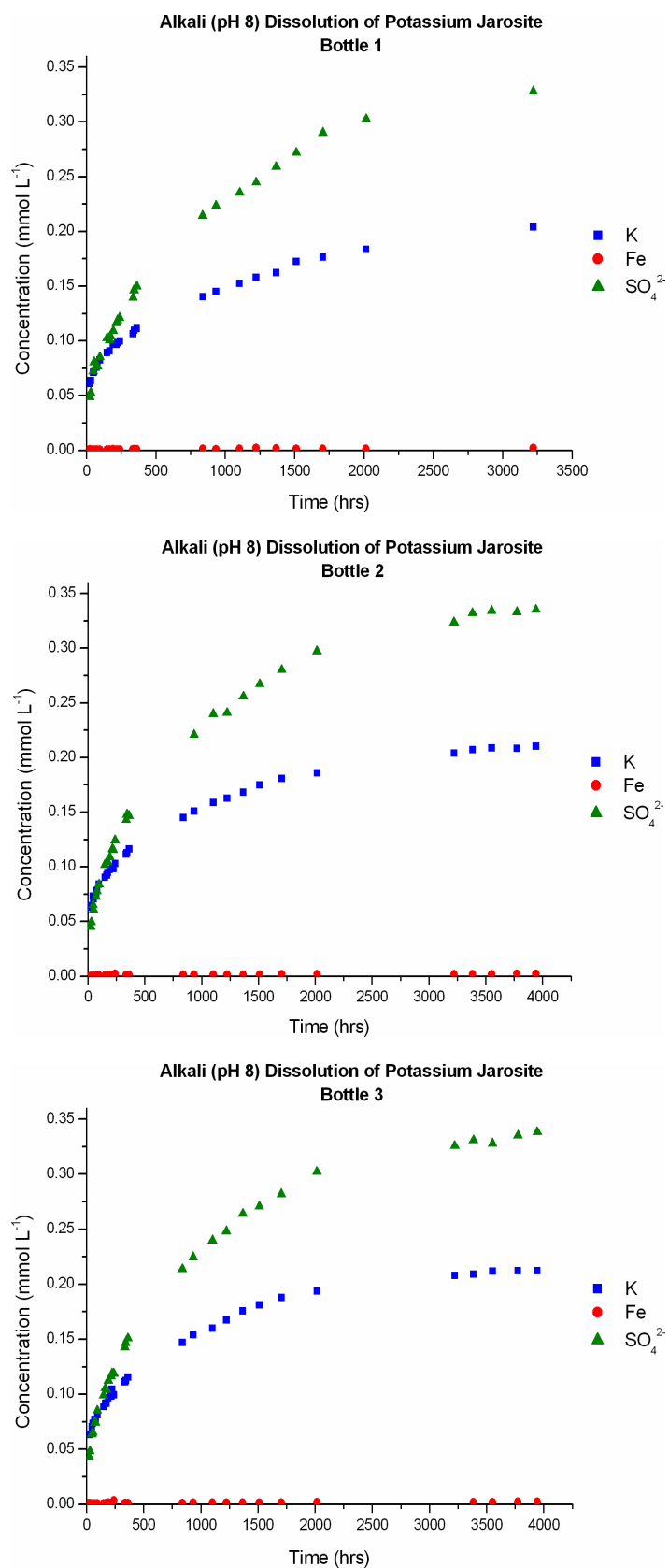
Figure 5.1. Concentrations of K_{tot}, Fe_{tot}, and $SO_4^{2-}{}_{tot}$ in solution for the alkali dissolution of potassium jarosite plotted against time, with the initial pH set at 8.00. Solution profiles for all three bottles are presented to prove reproducibility.

The final total concentrations of K, Fe, and SO_4^{2-} at steady state and their corresponding molar ratios are presented in Table 5.1 and Table 5.2, respectively. The molar ratios of the ions in solution were calculated under the pretext that SO_4^{2-} equalled 2, a common assumption frequently used in calculating the formula of jarosite type structures (Section 1.4.1, Table 3.3). Generally, it was found that the K ratio in solution varied from 1.24 – 1.26 compared to that of the idealised synthetic potassium jarosite of 0.84; and the Fe ratio in solution varied from 0.0136 – 0.0149 compared to that of the synthetic solid of 2.46 (Table 3.3).

Table 5.1. Final pH and aqueous ion concentrations for the alkali dissolutions.

| Compound | pH | Aqueous concentration (mmol L^{-1}) | | | | |
		K	Pb	Fe	SO_4^{2-}	AsO_4^{3-}
Potassium jarosite						
Alkali Bottle 1	3.30	0.2041	-	0.0023	0.3279	-
Alkali Bottle 2	3.28	0.2102	-	0.0025	0.3352	-
Alkali Bottle 3	3.26	0.2123	-	0.0023	0.3383	-
Plumbojarosite						
Alkali Bottle 1	3.54	-	0.0066	0.0004	0.1194	-
Alkali Bottle 2	3.46	-	0.0068	0.0004	0.1226	-
Alkali Bottle 3	3.44	-	0.0071	0.0004	0.1269	-
Beudantite						
Alkali Bottle 1	4.78	-	0.00007	0.000087	0.0151	0.0017
Alkali Bottle 2	4.58	-	-	0.000127	0.0136	0.0015
Alkali Bottle 3	4.62	-	-	0.000098	0.0135	0.0014

Based on the measured steady state pH and concentrations of K_{tot}, Fe_{tot}, and $SO_4^{2-}{}_{tot}$, equilibrium aqueous activities of K^+, Fe^{3+} and SO_4^{2-} were calculated using the geochemical speciation suite of programs in The Geochemist's Workbench (GWB), version 4.0.2 (Bethke 1996). The corresponding equilibrium aqueous activities for the potassium dissolution can be found in Table 5.3. The charge balance error across the triplicates ranged from 7 to 8 % (Table 5.3). Saturation indices were also calculated for the three bottles in the alkali dissolution of potassium jarosite (Table 5.4): only minerals with log Q/K greater than -3 are listed. Positive saturation indices were found for hematite and goethite, whilst potassium jarosite and $Fe(OH)_3$ had negative indices (Table 5.4).

5.1.2 Plumbojarosite

The alkali dissolution of plumbojarosite differs markedly from that of potassium jarosite and the other acidic dissolutions presented in Chapter 4 as none of the ions in solution could be described as following classical parabolic rate kinetics (Figure 5.2). Specifically the SO_4^{2-} ion in all three triplicates displayed a linear style relationship with respect to concentration in solution and time. The concentrations of both Pb and Fe in solution were also very low throughout the duration of the experiment. Plots of these two ions in Figure 5.3 shows that the Pb ion in solution displays a similar linear style relationship with its concentration in solution and time as that of SO_4^{2-} (Figure 5.2), when re-plotted on a more appropriate scale. The Fe concentration (Figure 5.3) in solution remained extremely low throughout the whole experiment, and a similar trend was seen across all three bottles, much like the profile of Fe seen in the alkali dissolution of potassium jarosite (Figure 5.1). At the end of the experiment, the Fe concentration was 0.0004 mmol L^{-1} across the triplicates (Table 5.1). Due to the linear style concentration profiles of Pb and SO_4^{2-} in solution, no obvious point in time could be placed where the experiment may have reached steady state, in comparison to dissolution profiles that fit parabolic kinetics. For this reason of ambiguity around the position of steady state, the reaction was stopped just before 2250 hrs and the final pH of the reaction was found to have changed from an initial 8.0 to one varying from 3.44 – 3.56 across the three bottles (Table 5.1).

Table 5.2. Aqueous molar ratios for the alkali dissolutions.

Compound	Aqueous molar ratios				
	K	Pb	Fe	SO_4^{2-}	AsO_4^{3-}
Potassium jarosite					
Alkali Bottle 1	1.24	-	0.0140	2	-
Alkali Bottle 2	1.25	-	0.0149	2	-
Alkali Bottle 3	1.26	-	0.0136	2	-
Plumbojarosite					
Alkali Bottle 1	-	0.110	0.0067	2	-
Alkali Bottle 2	-	0.116	0.0065	2	-
Alkali Bottle 3	-	0.109	0.0063	2	-
Beudantite					
Alkali Bottle 1	-	0.0078	0.0097	1.69	0.190
Alkali Bottle 2	-	-	0.0157	1.69	0.186
Alkali Bottle 3	-	-	0.0122	1.69	0.175
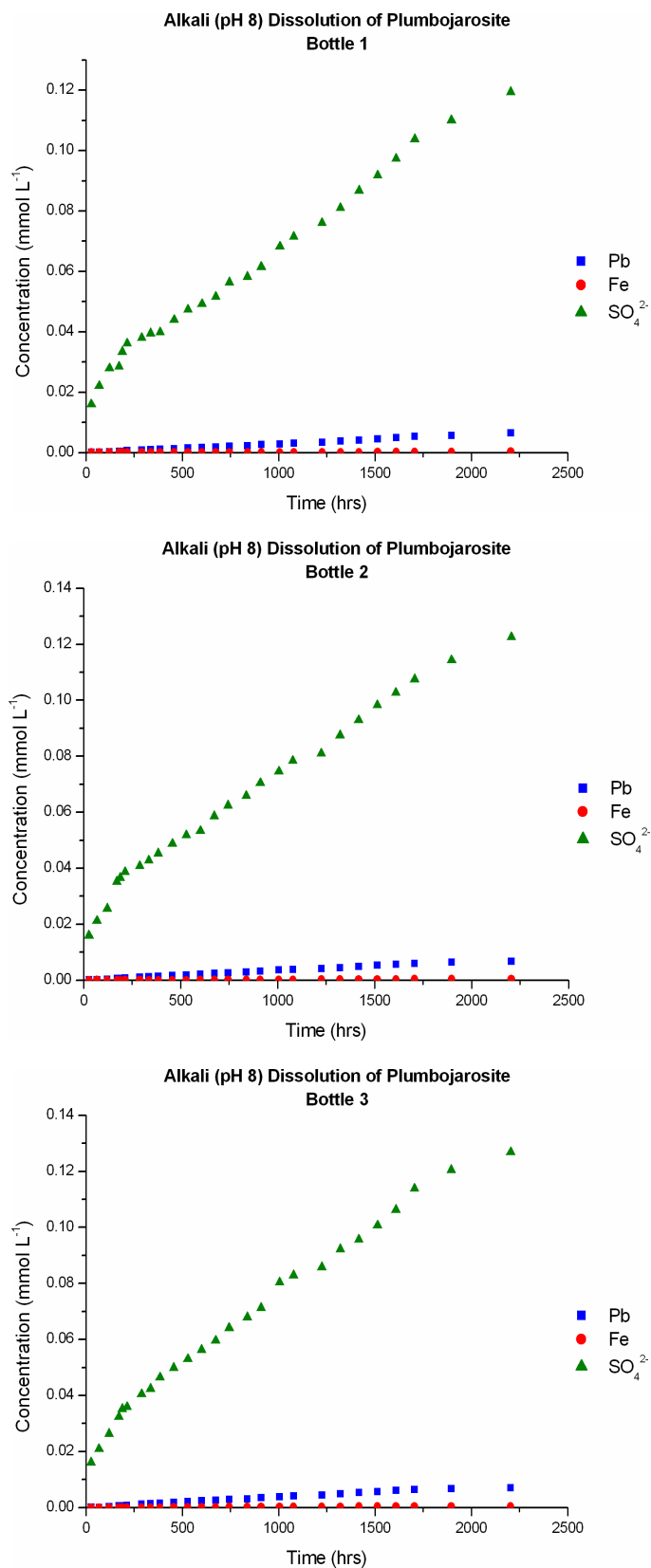
Figure 5.2. Concentrations of Pb_{tot}, Fe_{tot}, and $SO_4^{2-}{}_{tot}$ in solution for the alkali dissolution of plumbojarosite plotted against time, with the initial pH set at 8.00. Solution profiles for all three bottles are presented to prove reproducibility.
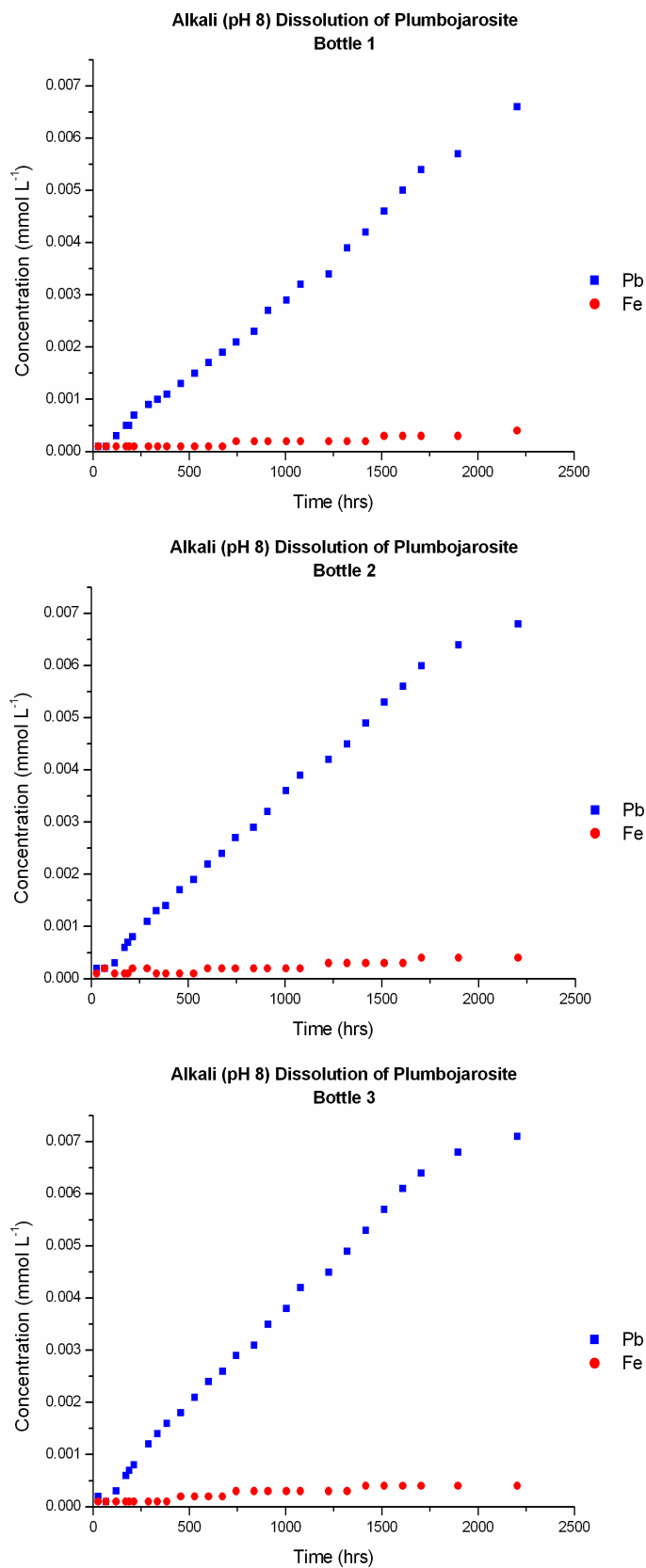
Figure 5.3. Concentrations of Pb$_{tot}$ and Fe$_{tot}$ in solution re-plotted from Figure 5.2 on a more appropriate scale for the alkali dissolution of plumbojarosite. Solution profiles for all three bottles are presented to prove reproducibility.

The final total concentrations of Pb, Fe, and SO_4^{2-} and their corresponding molar ratios are presented in Table 5.1 and Table 5.2, respectively. Once again, the molar ratios of the ions in solution were calculated setting SO_4^{2-} at 2. The Pb ratio in solution varied from 0.109 – 0.116 compared to that of synthetic plumbojarosite of 0.13, and the Fe ratio in solution varied from 0.0063 – 0.0067 compared to the synthetic solid of 2.92 (Table 3.3). Equilibrium aqueous activities were calculated using the final pH and Pb_{tot}, Fe_{tot}, and $SO_4^{2-}{}_{tot}$, for Pb^{2+}, $Fe^{3+,}$ and SO_4^{2-}, by GWB (Table 5.3). The charge balance error across the triplicates ranged from 7 to 9 % (Table 5.3). Positive saturation indices were found for hematite and goethite, whilst that for anglesite was negative (Table 5.4).

5.1.3 Beudantite

The concentration ion profiles from the beudantite alkali dissolution (Figure 5.4) were different to those in the two previous alkali experiments and all the acid dissolutions. The main difference surrounded the SO_4^{2-} profile, which appeared to take on an appearance similar to a sigmoidal curve, and resembled the SO_4^{2-} profile for the acid dissolution of beudantite (Figure 4.6). The AsO_4^{3-} concentration profiles across the triplicates were extremely similar and took on a likeness similar to ions that conform to parabolic rate kinetics; specifically, the AsO_4^{3-} ion profiles appeared to plateau off at approximately 250 hrs. The concentrations of Pb and Fe in solution were extremely low and these two ions were re-plotted on a more appropriate scale in Figure 5.5. What becomes immediately noticeable in Figure 5.5 was the lack of Pb in solution over the three bottles only one Pb concentration point was found above the detection limits (5 ppb) of the ICP-OES and that was the first sampling point in Bottle 1 at approximately 28 hrs at a concentration of 0.00007 mmol L^{-1} (15 ppb). The Fe profile (Figure 5.5) was also significantly different from the two earlier alkali dissolutions (Figure 5.1, 5.3), in that after a minima in the Fe concentration seen in all three bottles around 250 hrs, the concentration then slowly rose throughout the remainder of the experiment, specifically with a linear relationship with regards to concentration and time. In the first 250 hrs of the experiment, the Fe concentration appeared to have dropped fairly sharply to a global minimum, this is seen best in the Fe profiles of Bottles 1 and 2.
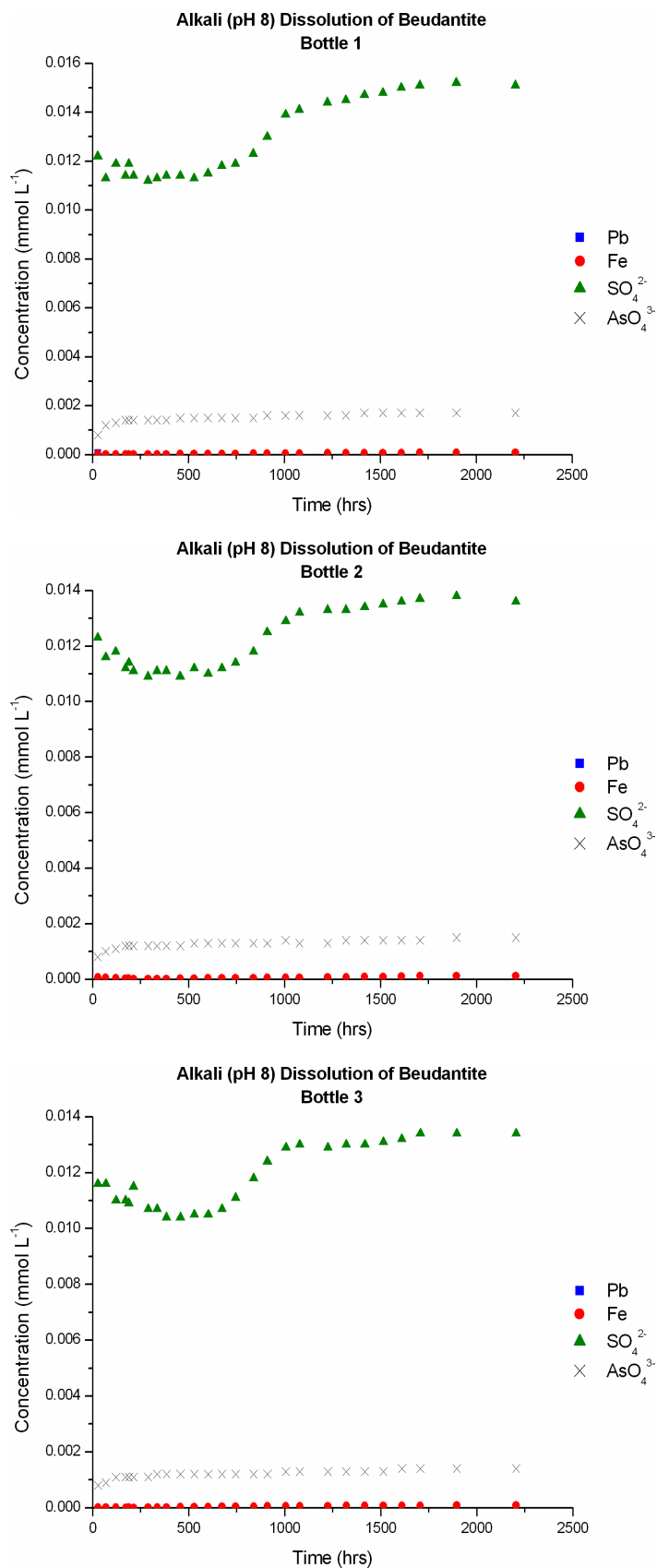
Figure 5.4. Concentrations of Pb_{tot}, Fe_{tot}, $SO_4^{2-}{}_{tot}$, and $AsO_4^{3-}{}_{tot}$ in solution for the alkali dissolution of beudantite plotted against time, with the initial pH set at 8.00. Solution profiles for all three bottles are presented to prove reproducibility.
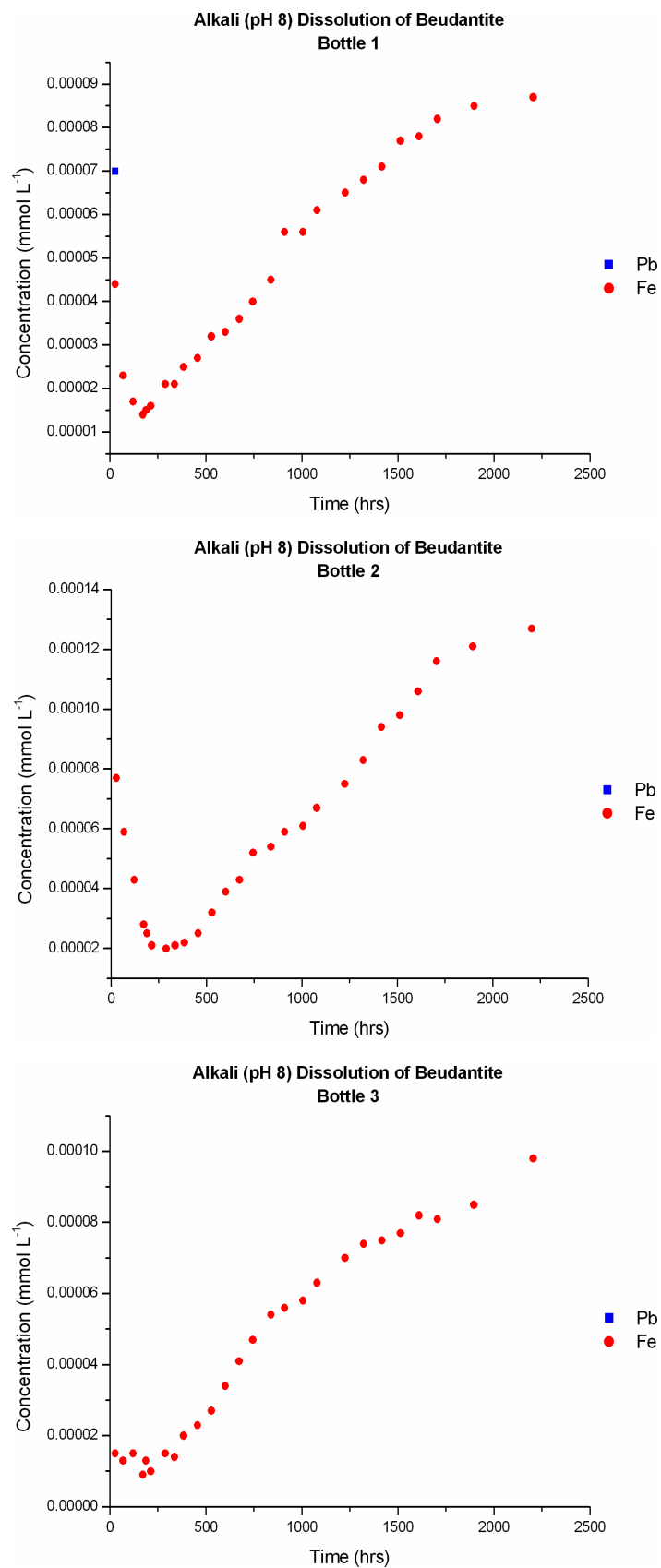
Figure 5.5. Concentrations of Pb$_{tot}$ and Fe$_{tot}$ in solution re-plotted from Figure 5.4 on a more appropriate scale for the alkali dissolution of beudantite. Solution profiles for all three bottles are presented to prove reproducibility.

Due to the complicated nature of the aqueous ion profiles for the alkali dissolution of beudantite, no obvious point in time could be found to class the reaction to have reached a steady state, much like in the alkali dissolution of plumbojarosite; therefore, the experiment was terminated before 2250 hrs. Under these conditions, it was decided to state all the ion concentrations and pH values as final rather than at steady state. The final pH values ranged from 4.58 – 4.78 across the triplicates from an initial value of 8.0 (Table 5.1).

Table 5.3. Calculated equilibrium activities for the alkali dissolutions.

| Compound | pH | Calculated equilibrium activities | | | | | Charge balance error (%) |
		log $\{SO_4^{2-}\}$	log $\{H_2AsO_4^-\}$	log $\{K^+\}$	log $\{Pb^{2+}\}$	log $\{Fe^{3+}\}$	
Potassium jarosite							
Alkali Bottle 1	3.30	-3.57	-	-3.71	-	-7.03	7
Alkali Bottle 2	3.28	-3.56	-	-3.69	-	-6.97	8
Alkali Bottle 3	3.26	-3.55	-	-3.69	-	-6.99	8
Plumbojarosite							
Alkali Bottle 1	3.54	-3.97	-	-	-5.22	-	7
Alkali Bottle 2	3.46	-3.97	-	-	-5.21	-8.01	8
Alkali Bottle 3	3.44	-3.95	-	-	-5.19	-7.92	9
Beudantite							
Alkali Bottle 1	4.78	-4.84	-5.77	-	-7.15	-	9
Alkali Bottle 2	4.58	-4.88	-5.84	-	-7.63	-	9
Alkali Bottle 3	4.62	-4.88	-5.85	-	-7.63	-	6

The final total concentrations of Pb, Fe, SO_4^{2-}, and AsO_4^{3-} and their corresponding molar ratios are presented in Table 5.1 and Table 5.2, respectively. The molar ratios of the ions in solution were calculated with respect that SO_4^{2-} equalled 1.69, a value calculated from the characterisation of the synthetic beudantite (Table 3.3). As only one data point was found for the Pb concentration in the entirety of the experiment (Bottle 1), its value was used to calculate the molar ratio, in this instance the value was 0.0078 compared with that of the synthetic of 0.32. The Fe ratio in solution varied from 0.0097 – 0.0122 compared with the synthetic solid of 2.86; and finally the AsO_4^{3-} solution ratio ranged from 0.175 – 0.190, in comparison to 0.31 in synthetic beudantite (Table 3.3). Equilibrium aqueous activities were calculated using the final pH and Pb_{tot}, Fe_{tot}, $SO_4^{2-}{}_{tot}$, $AsO_4^{3-}{}_{tot}$ for Pb^{2+}, Fe^{3+}, SO_4^{2-}, and $H_2AsO_4^-$, by GWB (Table 5.3). Even through AsO_4^{3-} is a structural unit (T-site) in beudantite, AsO_4^{3-} is not a stable aqueous phase in acidic (pH < 6.2) oxidising conditions (Smedley and Kinniburgh 2002). Under the alkali dissolution conditions for beudantite, the stable aqueous phase of As^{5+} is the arsenic oxyanion, $H_2AsO_4^-$. It is for this reason that the

As aqueous contribution for the calculated equilibrium activities is represented by $H_2AsO_4^-$ and not AsO_4^{3-} in Table 5.3 (Smedley and Kinniburgh 2002). The charge balance error across the triplicates ranged from 6 to 9 % (Table 5.3). Positive saturation indices were found for hematite and goethite, whilst that for $Fe(OH)_3$ was negative (Table 5.4).

Table 5.4. Calculated saturation indices for the alkali dissolutions.

Compound	Saturation Indices (log Q/K)*			
Potassium jarosite				
Alkali Bottle 1	Hematite 5.61	Goethite 2.32	Jarosite -2.78	$Fe(OH)_3$ -2.80
Alkali Bottle 2	Hematite 5.60	Goethite 2.32	Jarosite -2.70	$Fe(OH)_3$ -2.80
Alkali Bottle 3	Hematite 5.50	Goethite 2.27	Jarosite -2.81	$Fe(OH)_3$ -2.85
Plumbojarosite				
Alkali Bottle 1	Hematite 4.92	Goethite 1.98	Anglesite -1.34	
Alkali Bottle 2	Hematite 4.64	Goethite 1.84	Anglesite -1.32	
Alkali Bottle 3	Hematite 4.69	Goethite 1.86	Anglesite -1.29	
Beudantite				
Alkali Bottle 1	Hematite 6.59	Goethite 2.82	$Fe(OH)_3$ -2.31	
Alkali Bottle 2	Hematite 6.51	Goethite 2.77	$Fe(OH)_3$ -2.35	
Alkali Bottle 3	Hematite 6.36	Goethite 2.70	$Fe(OH)_3$ -2.42	

* Only minerals with log Q/K > -3 are listed

5.2   Residual solids

This section discusses the characterisation of the post-dissolution solids and the investigations carried out to determine if any new solid phases formed from solution. These are considered important tasks to help to understand the mechanisms of jarosite breakdown.

5.2.1 Chemical analysis of residual solids

Upon completion of the all three experiments, the post-alkali dissolution solids of potassium jarosite, plumbojarosite, and beudantite were analysed by wet chemistry (ICP-OES) for total concentrations of K, Pb, Fe, S and As. SO_4^{2-} and AsO_4^{3-} concentrations were inferred from total S and As values. The residual solid concentrations from the three dissolution experiments and their corresponding molar ratios are summarised in Tables 5.5 and 5.6, respectively. All the raw data corresponding to this section on chemical analysis of the residual solids can be found in Appendix C.3.

Table 5.5. Residual solid concentrations for the alkali dissolutions.

| Compound | Residual solid concentration (mmol L^{-1}) | | | | |
	K	Pb	Fe	SO_4^{2-}	AsO_4^{3-}
Potassium jarosite					
Alkali Bottle 1	0.1221	-	0.8745	0.3614	-
Alkali Bottle 2	0.1265	-	0.8910	0.3713	-
Alkali Bottle 3	0.1239	-	0.8943	0.3685	-
Plumbojarosite					
Alkali Bottle 1	-	0.0355	0.7267	0.3994	-
Alkali Bottle 2	-	0.0362	0.7309	0.4012	-
Alkali Bottle 3	-	0.0366	0.7323	0.3987	-
Beudantite					
Alkali Bottle 1	-	0.0844	0.6949	0.3458	0.0549
Alkali Bottle 2	-	0.0855	0.7041	0.3497	0.0553
Alkali Bottle 3	-	0.0854	0.7019	0.3476	0.0556

For the potassium jarosite alkali dissolution, the molar ratios of the concentrations of the residual solids were calculated using a similar pretext as to that of the aqueous data; that is, that SO_4^{2-} equalled 2 (Table 5.6). Under these conditions, the K ratio in the residual solids varied from 0.672 – 0.681, compared to the respective K value in the synthetic solid of 0.84. The Fe ratio in the residual solids ranged from 4.799 – 4.853, and the corresponding value in the synthetic was 2.46 (Table 3.3). The molar ratios (Table 5.6) for the ions in the residual solids of the plumbojarosite dissolution were calculated on the same premise as above. In this case the Pb ratio varied from 0.178 – 0.183, compared to an idealised value of 0.13 in the synthetic; and the Fe ratio in the residual solid ranged from 3.639 – 3.673, where the value in synthetic plumbojarosite was 2.92 (Table 3.3). Finally, the molar ratios of the residual solid of beudantite (Table 5.6) were calculated on the basis that the SO_4^{2-} value in the characterised solid was calculated to be 1.69 (Table 3.3). The Pb ratio in the residual solids was found to vary from 0.412 – 0.415, compared to the synthetic of 0.32; the Fe varied from 3.296 – 3.412, whilst in the synthetic the Fe ratio was 2.86. The AsO_4^{3-} value in the residual solid of beudantite ranged from 0.267 – 0.270, compared to the idealised synthetic value of 0.31 (Table 3.3).

Table 5.6. Residual solid molar ratios for the alkali dissolutions.

Compound	Residual solid molar ratios				
	K	Pb	Fe	SO_4^{2-}	AsO_4^{3-}
Potassium jarosite					
Alkali Bottle 1	0.676	-	4.840	2	-
Alkali Bottle 2	0.681	-	4.799	2	-
Alkali Bottle 3	0.672	-	4.853	2	-
Plumbojarosite					
Alkali Bottle 1	-	0.178	3.639	2	-
Alkali Bottle 2	-	0.180	3.643	2	-
Alkali Bottle 3	-	0.183	3.673	2	-
Beudantite					
Alkali Bottle 1	-	0.412	3.396	1.69	0.269
Alkali Bottle 2	-	0.413	3.402	1.69	0.267
Alkali Bottle 3	-	0.415	3.412	1.69	0.270

5.2.2 Identification of residual solids

X-ray diffraction patterns were attained for the residual solids from the alkali dissolution experiments of potassium jarosite, plumbojarosite, and beudantite (Figures 5.6-5.8). The diffraction patterns were then compared with the corresponding ICDD PDF files used to identify the original synthetic endmember jarosites (potassium jarosite 22-0827, plumbojarosite 33-0759, and beudantite 19-0689). All the peaks produced by the plumbojarosite and beudantite residual solids could be identified as those relating to the structure of their corresponding synthetic analogue. The absence of unidentified peaks in the diffraction patterns for plumbojarosite and beudantite indicated that no new phases were present at detectable levels. The alkali dissolution X-ray data for potassium jarosite (Figure 5.6) is much nosier than that for the scan taken under identical conditions for the acid dissolution (Figure 4.7). All major peaks on the alkali diffraction pattern (Figure 5.6) fit to those of potassium jarosite defined by the synthetic ICDD PDF (22-0827) standard but there was an unaccounted-for broad peak at approximately 22° 2-theta. This peak is identified as a reflection belonging to the mineral goethite (ICDD PDF 03-0249, Figure 5.9). The broadness of the ~ 22° 2-theta peak could indicate that the secondary goethite phase could be poorly crystalline and have a very small particle size (Figure 5.6).

Alkali Dissolution of Potassium Jarosite
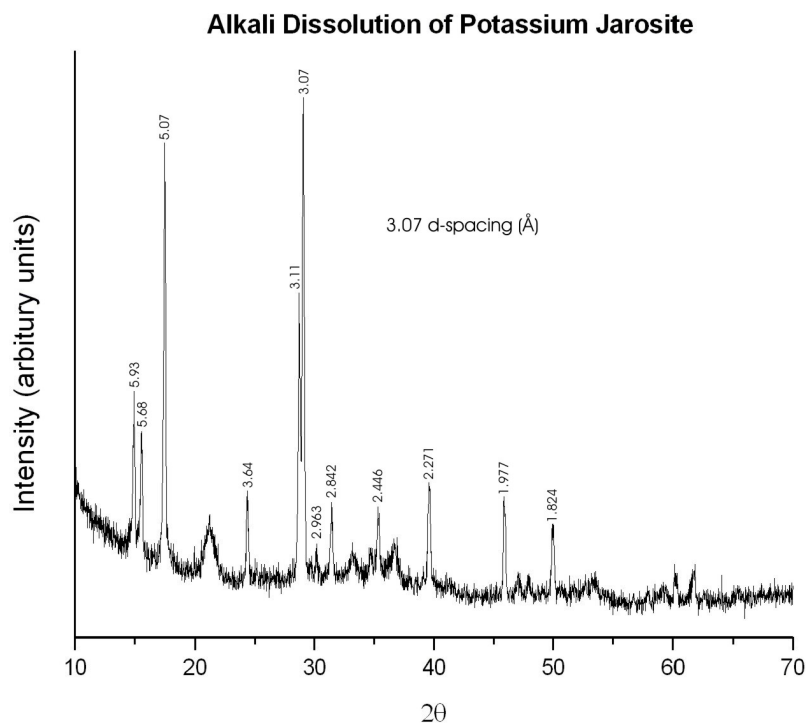
Figure 5.6. Powder X-ray diffraction of the residual solid from the alkali dissolution of potassium jarosite, mounted on a Bruker zero background silicon (510) sample holder; using Cu Kα radiation (λ = 1.54056 Å) source, 2-theta range 10-70°, step size 0.020°, step time 27s. d-spacings have been indicated for the strongest peaks.

Alkali Dissolution of Plumbojarosite
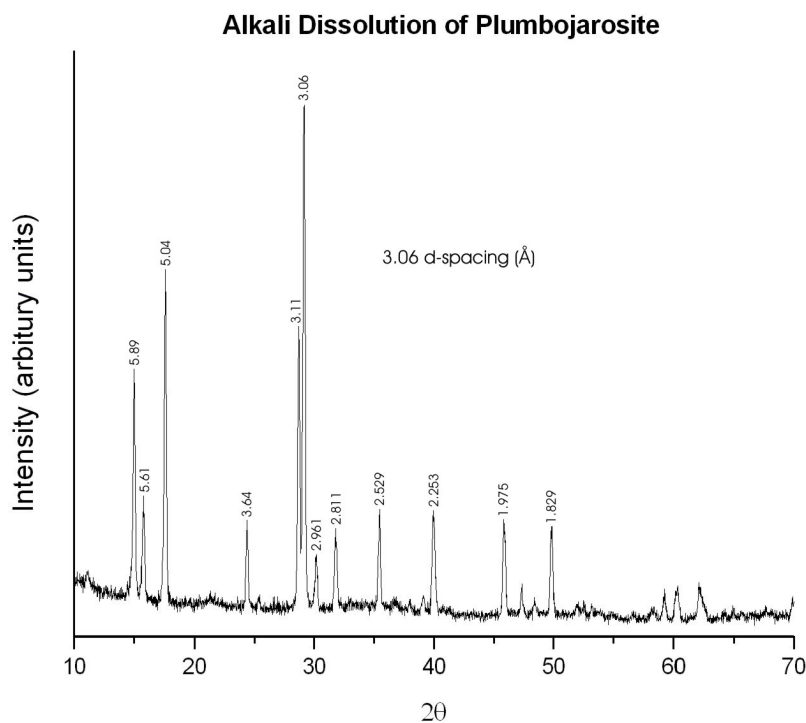
Figure 5.7. Powder X-ray diffraction of the residual solid from the alkali dissolution of plumbojarosite, mounted on a Bruker zero background silicon (510) sample holder; using Cu Kα radiation (λ = 1.54056 Å) source, 2-theta range 10-70°, step size 0.020°, step time 27s. d-spacings have been indicated for the strongest peaks.

Alkali Dissolution of Beudantite
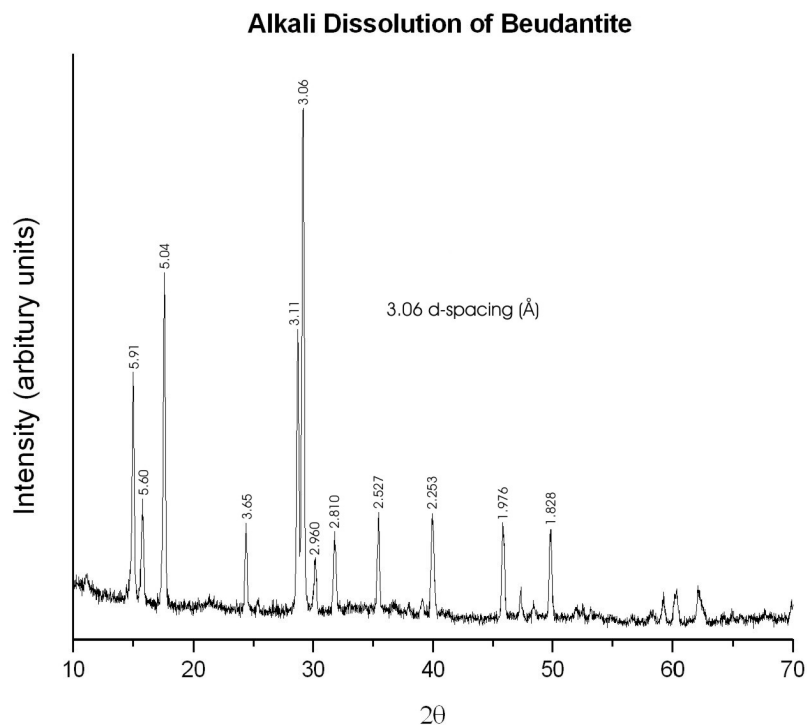
Figure 5.8. Powder X-ray diffraction of the residual solid from the alkali dissolution of beudantite, mounted on a Bruker zero background silicon (510) sample holder; using Cu Kα radiation (λ = 1.54056 Å) source, 2-theta range 10-70°, step size 0.020°, step time 27s. d-spacings have been indicated for the strongest peaks.

Synthetic Goethite
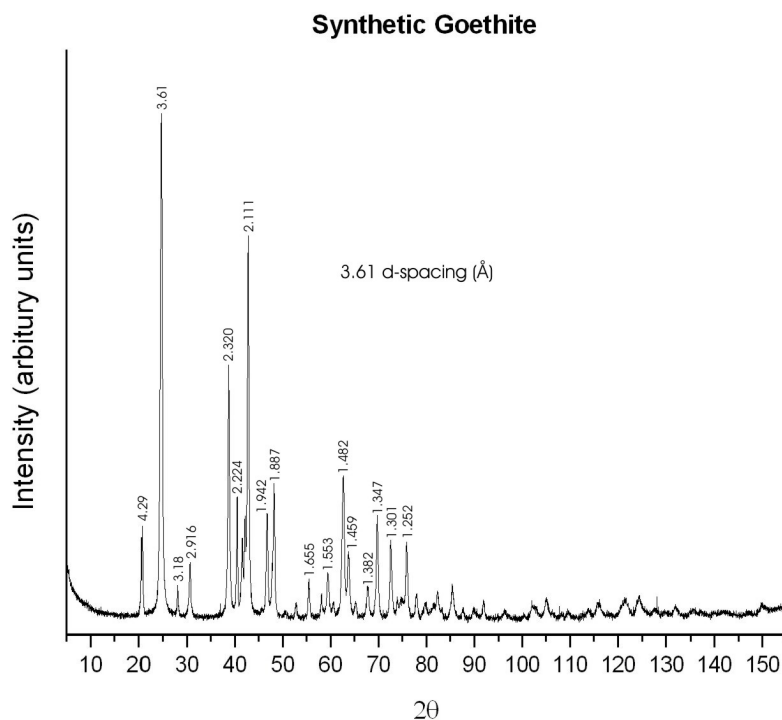
Figure 5.9. Powder X-ray diffraction of synthetic goethite; using Co Kα₁Kα₂ radiation (λα₁ = 1.788965 Å and λα₂ = 1.792850 Å) source, 2-theta range 5-155°, step size 0.025°, step time 10s. d-spacings have been indicated for the strongest peaks.

Synthetic Ferrihydrite
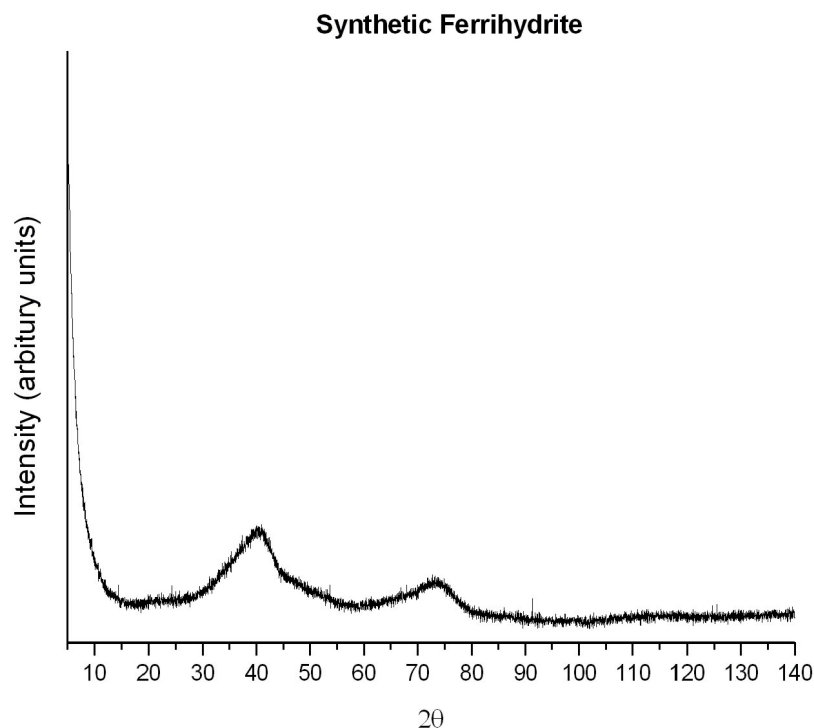
Figure 5.10. Powder X-ray diffraction of synthetic ferrihydrite; using Co $K\alpha_1 K\alpha_2$ radiation ($\lambda\alpha_1$ = 1.788965 Å and $\lambda\alpha_2$ = 1.792850 Å) source, 2-theta range 5-155°, step size 0.025°, step time 10s.

FTIR spectra of the residual solids recovered from the alkali dissolution experiments are shown in Figure 5.11. The spectra are very similar to those of the original analogues shown in Figure 3.15. Two additional bands were observed in the residual solid belonging to potassium jarosite at 888 and 797 cm^{-1}; otherwise no extra bands were found in the residual solids belonging to plumbojarosite and beudantite.

All the spectra contain an intense absorption band in the region 2900 to 3700 cm^{-1} attributed to O-H stretching (v_{OH}). A band also occurs at 1634 to 1641 cm^{-1}, and assigned to HOH deformation relating to the presence of 'additional water' groups. Three intense absorption bands occur at 1000 to 1200 cm^{-1}, and are credited to two vibrational modes within the sulphate unit $v_3(SO_4^{2-})$ (doublet, at the two higher wavenumbers) and $v_1(SO_4^{2-})$ (at the lowest wavenumber). Two other vibrational modes of sulphate, the $v_4(SO_4^{2-})$ at around 630 cm^{-1} and a doublet in potassium jarosite at 658 cm^{-1} (Figure 5.11a), and the $v_2(SO_4^{2-})$ near 470 cm^{-1}. For the beudantite sample (Figure 5.11c), two additional peaks occur between 810 and 860 cm^{-1}; these correspond to the $v_3(AsO_4^{3-})$ and $v_1(AsO_4^{3-})$ vibrational modes of arsenate. IR bands near 580 and 505 cm^{-1} correspond to an O-H bending mode (γ_{OH}) and to an O-Fe vibration within the FeO_6 coordination octahedron. O-H bending modes were

not present in the spectra of plumbojarosite (Figure 4.11b) (Powers et al. 1975, Baron and Palmer 1996b, Serna et al. 1986, Sasaki et al. 1998, Drouet and Navrotsky 2003).
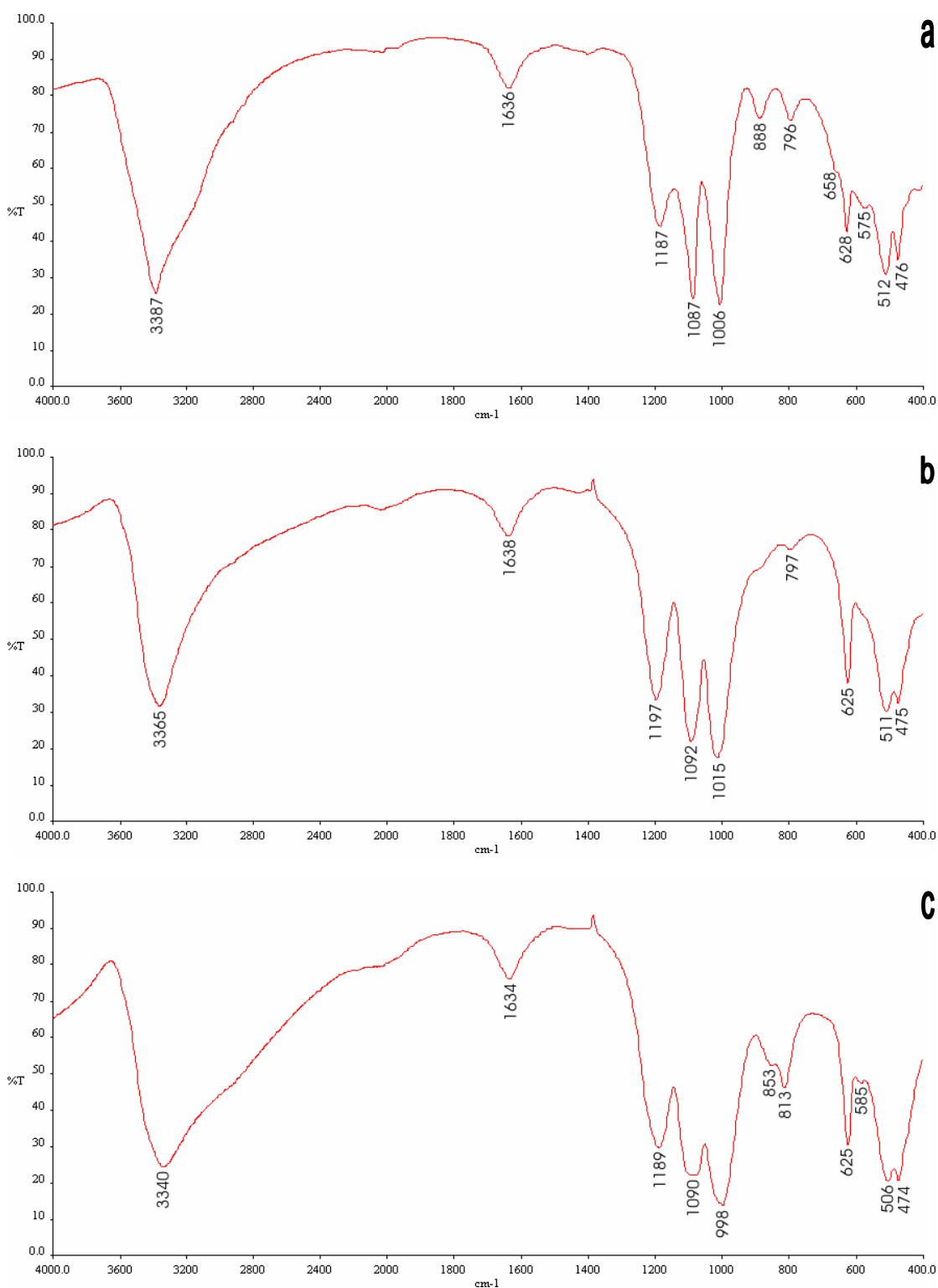
Figure 5.11. Fourier transform infrared spectra (FTIR) of the alkali dissolutions of (a) potassium jarosite, (b) plumbojarosite, and (c) beudantite. The range was 400 – 4000 cm^{-1} wavenumbers with a resolution of 4 cm^{-1}, five scans were accumulated. The main vibrational bands in the spectrum are marked.
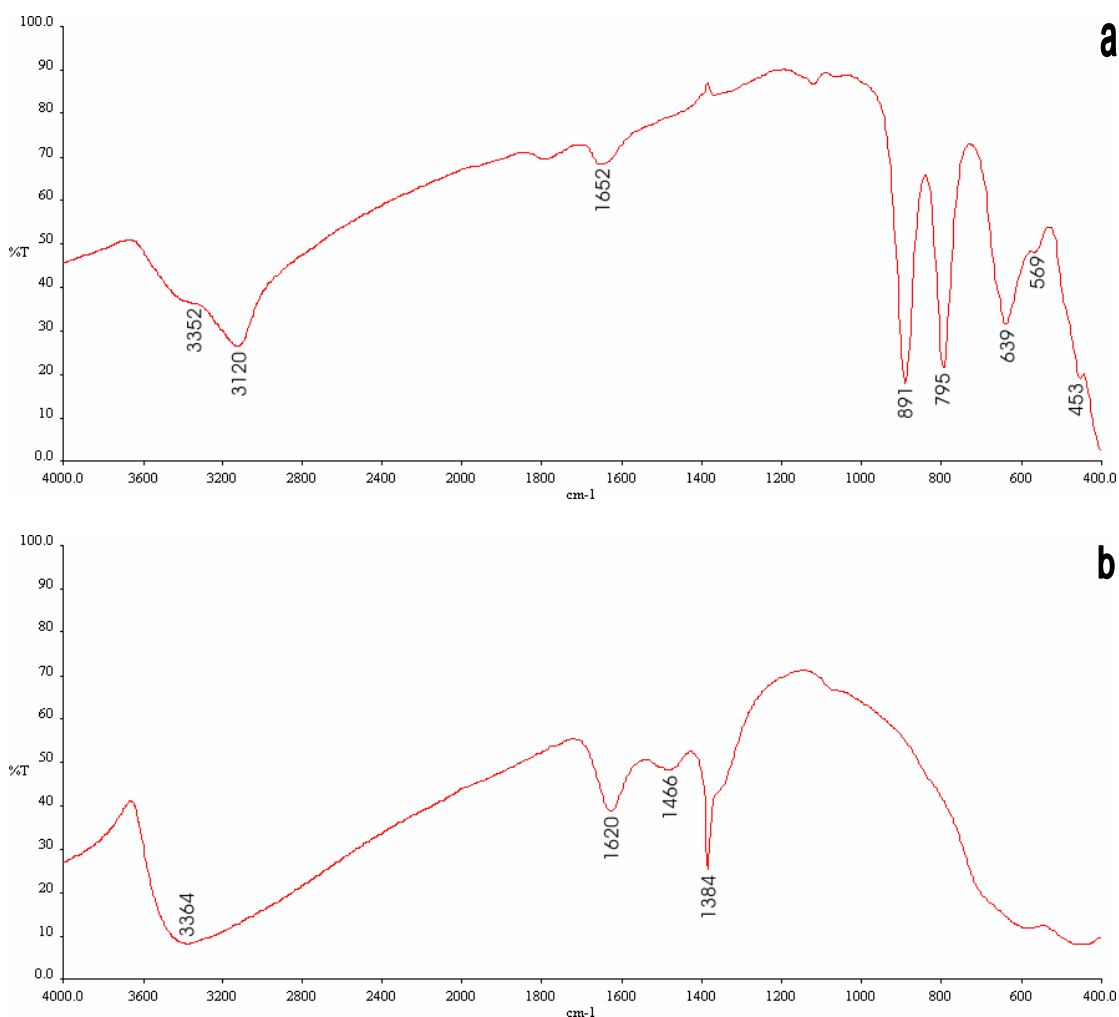
Figure 5.12. Fourier transform infrared spectra (FTIR) of synthetic (a) goethite and (b) ferrihydrite. The range was 400 – 4000 cm^{-1} wavenumbers with a resolution of 4 cm^{-1}, five scans were accumulated. The main vibrational bands in the spectrum are marked.

The two main additional bands in the potassium jarosite spectrum (Figure 5.11a) at 888 and 796 cm^{-1} can be positively identified specifically as O-Fe vibrations belonging to the crystal structure of goethite (α-FeO(OH)). Figure 5.12a illustrates an FTIR spectrum of synthetic goethite, where the very distinctive and individual O-Fe vibrations are found at 891 and 795 cm^{-1}.

5.2.3 Morphology

Figure 5.13 shows the subtle colour changes between the original synthetic jarosites and the residual solids recovered at the end of the alkali dissolutions. Munsell colours were assigned to the residual solids and compared to the idealised solids (Table 3.1). For the dissolution of potassium jarosite, the residual solid had a Munsell colour of 7.5YR 5.5/8; the solid has a higher red component and a lower chroma indicating a
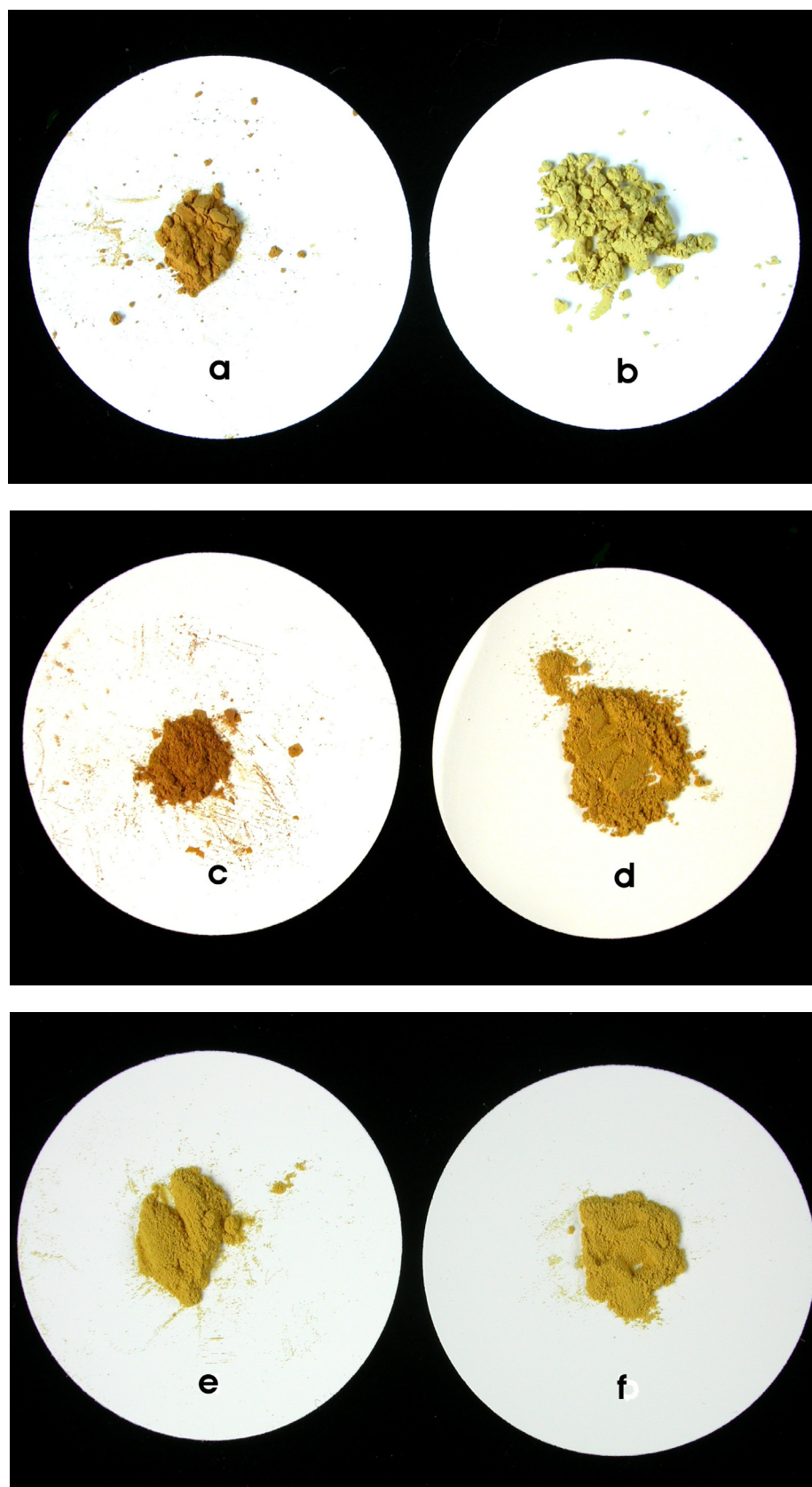
Figure 5.13. Illustrations showing the subtle colour changes between the synthetic jarosites and the residual solids recovered at the end of the alkali dissolutions. Potassium jarosite: (a) residual solid and (b) synthetic. Plumbojarosite: (c) residual solid and (d) synthetic. Beudantite: (e) residual solid and (f) synthetic.

more mixed darker colour in comparison to the original synthetic. Bigham (1994) reported that goethite found in ARD ochres have Munsell colours varying from 7.5YR – 10YR. For plumbojarosite, the residual solid had a Munsell colour of 7.5YR 4.5/7; in comparison to the synthetic, the solid has again been enriched in a higher red component and has a significantly low chroma indicating a far darker colour. The Munsell colour for the residual solid in the alkali dissolution of beudantite was 10YR 6.5/8; the chroma value is less, indicating that the residual solid is darker in colour in comparison to the synthetic analogue. A secondary mineral that is commonly found in ARD environments with a similar composition to what was seen in the alkali dissolution of plumbojarosite is ferrihydrite (5YR – 7.5YR) (Bigham 1994); the red colours seen in the residual solids correspond well to ferrihydrite.

One of the fundamental properties that influences colour in isostructural compounds is particle size and shape. SEM micrographs showing sizes and shapes of the alkali dissolution products of potassium jarosite, plumbojarosite, and beudantite are presented in Figures 5.14, 5.16 and 5.18, respectively.

Figure 5.14a is an overview of the particle morphology of the residual solid from the potassium jarosite dissolution. The most striking feature about this micrograph is that all the grains and nearly all the surfaces have what appear to be a 'frost like' coating; the grains also show varying degrees of pitting, but generally to a much less extent than that seen in the acid experiment (Figure 4.14). At higher magnification (Figure 5.14b), it is possible to see the needle or rod-like morphology of a secondary phase coating the smooth globular surfaces of the synthetic potassium jarosite (Figure 3.21a). The needle crystallites vary in size from approximately 10-100 nm (Figure 5.14b). The crystal morphology of this secondary phase is extremely similar to that of goethite, which is classically described as being made up from short rods (Bigham 1994). Micrographs of synthetic goethite can be seen in Figure 5.15, specifically the needle like morphology of this mineral and the resemblance to the secondary phase seen in the alkali dissolution of potassium jarosite is epitomised by the higher resolution micrograph in Figure 5.15b.
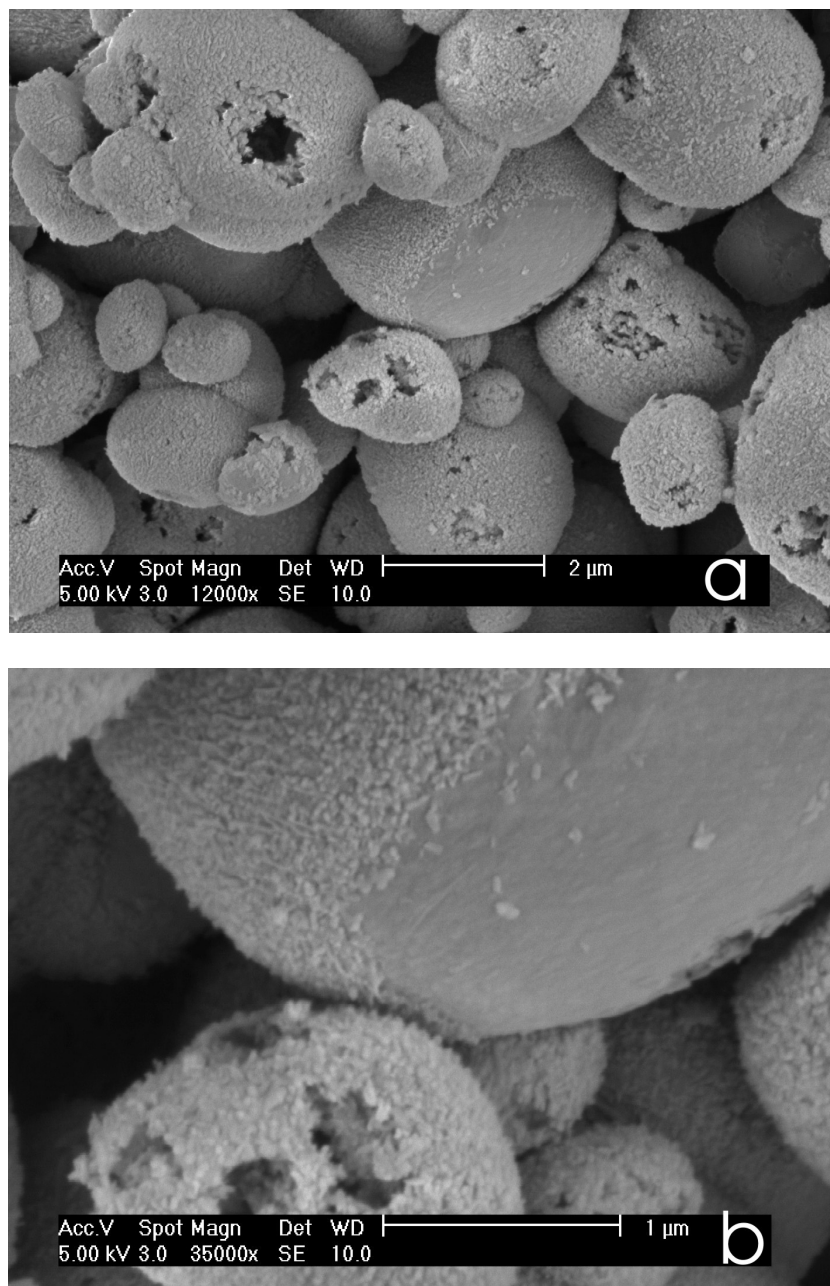
Figure 5.14. Scanning electron micrograph (SEM) images of the residual solid from the alkali dissolution of potassium jarosite. Image (a) is a general overview of the residual solid; a fine crystalline coating can be seen. Image (b) is a high-resolution micrograph of a couple of potassium jarosite grains; a fine needle crystalline coating is evident. Operating conditions indicated on each micrograph.

For the plumbojarosite dissolution, the particle morphology of the residual solid (Figure 5.16a) is similar to that of potassium jarosite (Figure 5.14) in that there appears to be a secondary phase coating the grains. The plumbojarosite dissolution secondary phase is quite globular in appearance, and there was no evidence of any selective surface dissolution in the alkali experiment. The globular morphology of the
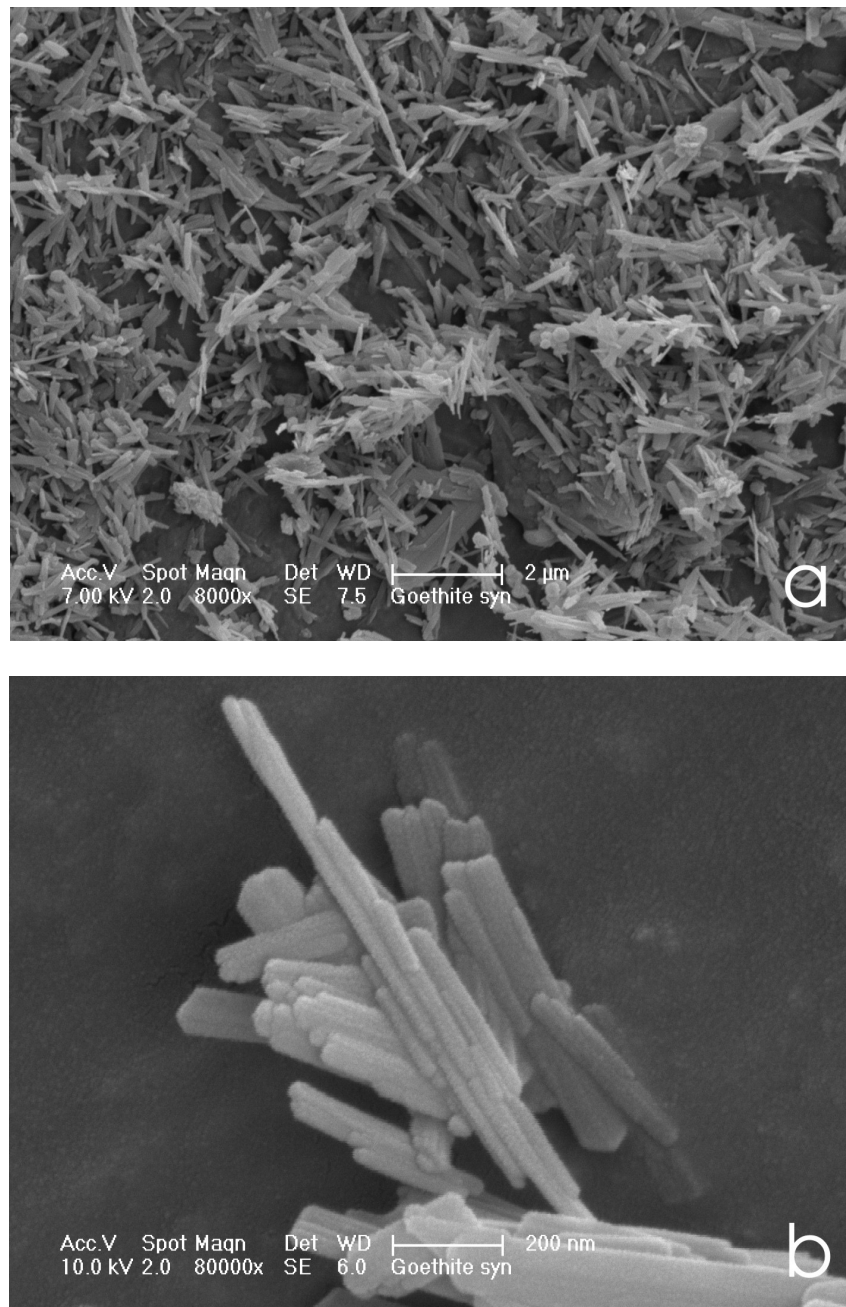
Figure 5.15. Scanning electron micrograph (SEM) images of synthetic goethite. Image (a) is a general overview of fine interlocking rods that are synonymous with the particle morphology of goethite. Image (b) is a high-resolution micrograph of interlocking rods that make up goethite; it is possible to see the macro-structure of the particles, where in particular the rods have intergrown and stacked to make larger particles. Operating conditions indicated on each micrograph.

secondary coating can be seen more clearly in the higher magnification micrograph presented in Figure 5.16b. The average grain size of the secondary phase was between 5 to 20 nm (Figure 5.16b). The morphology of this secondary phase was very comparable to that of poorly crystalline to amorphous ferrihydrite, which is described as having a spherical crystal habit (Bigham 1994).
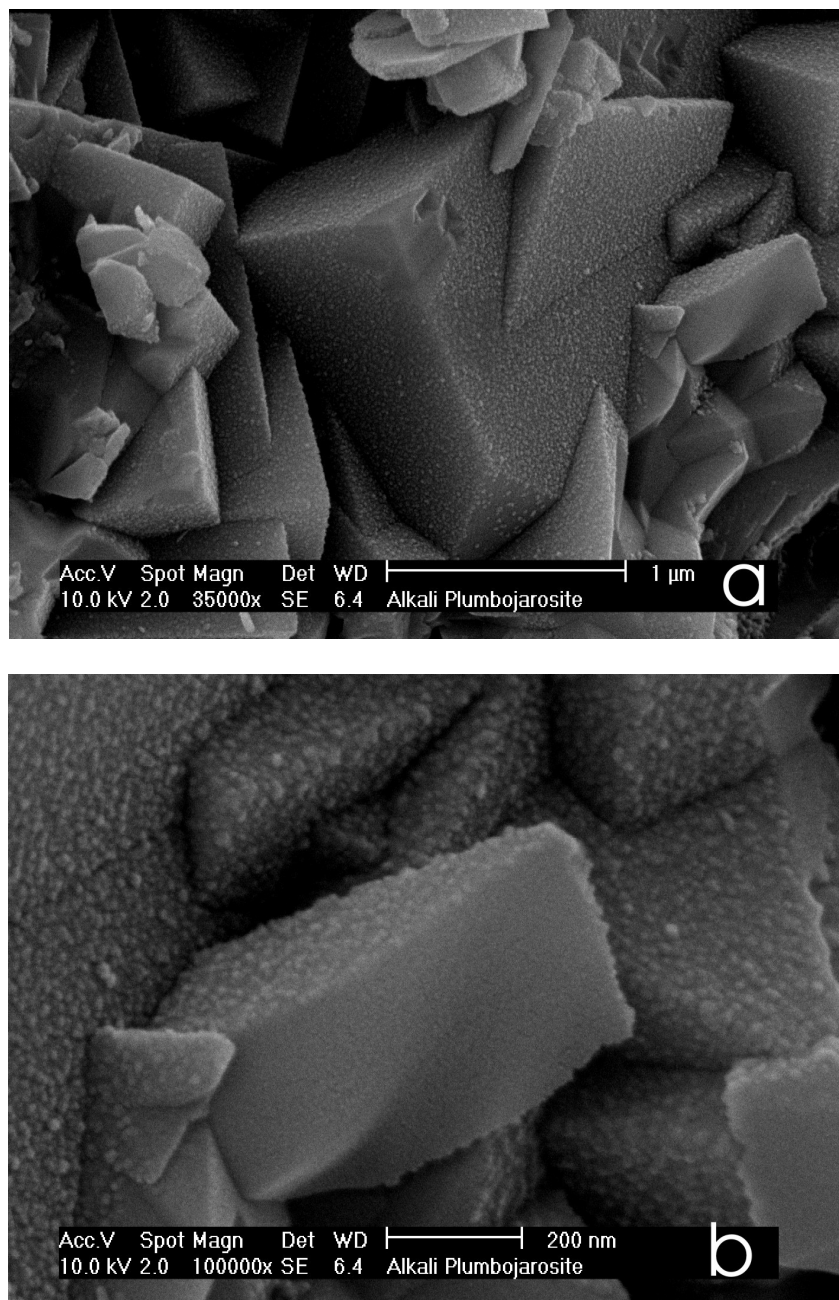
Figure 5.16. Scanning electron micrograph (SEM) images of the residual solid from the alkali dissolution of plumbojarosite. Image (a) highlights a very fine globular coating seen throughout the plumbojarosite sample. Image (b) is a high-resolution micrograph of a couple of plumbojarosite grains; a fine globular coating is clearly visible on the smooth plumbojarosite surfaces. Operating conditions indicated on each micrograph.

SEM micrographs of synthetic ferrihydrite are presented in Figure 5.17, where a resemblance can be seen between the high-resolution micrographs of synthetic ferrihydrite and the secondary phase in the alkali dissolution of plumbojarosite, in Figures 5.17b and 5.16b, respectively.
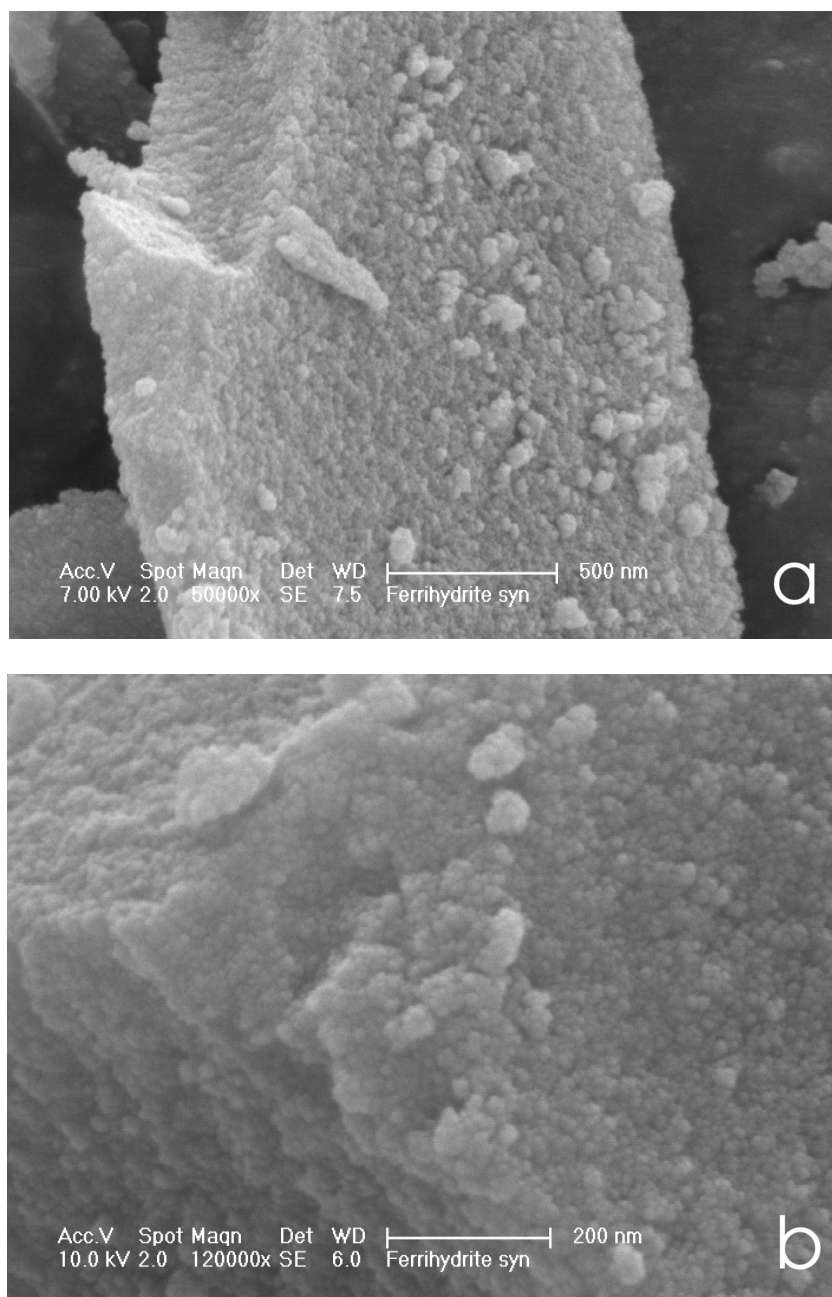
Figure 5.17. Scanning electron micrograph (SEM) images of synthetic ferrihydrite. Image (a) is a general overview of the solid, where it appears to be comprised from aggregates of smaller spherical particles. Image (b) is a high-resolution micrograph of ferrihydrite, the finer globular particles are more pronounced and there is a distinctive lack of any noticeable crystal habit. Operating conditions indicated on each micrograph.

For beudantite (Figure 5.18a), the morphology of the residual solid from the alkali dissolution was broadly similar with the two previous studies in that a secondary phase was found coating the beudantite grains. A general comparison of the morphologies between the acid (Figure 4.16a) and alkali (Figure 5.18a) dissolutions of beudantite highlighted the lack of any slight/moderate internal dissolution

(resembling smooth tubular or spherical holes) in the alkali dissolution. At higher magnification of the beudantite residual solid (Figure 5.18b), the secondary phase appeared to be very finely distributed across all the grains, with a very approximate particle size of 1-5 nm.
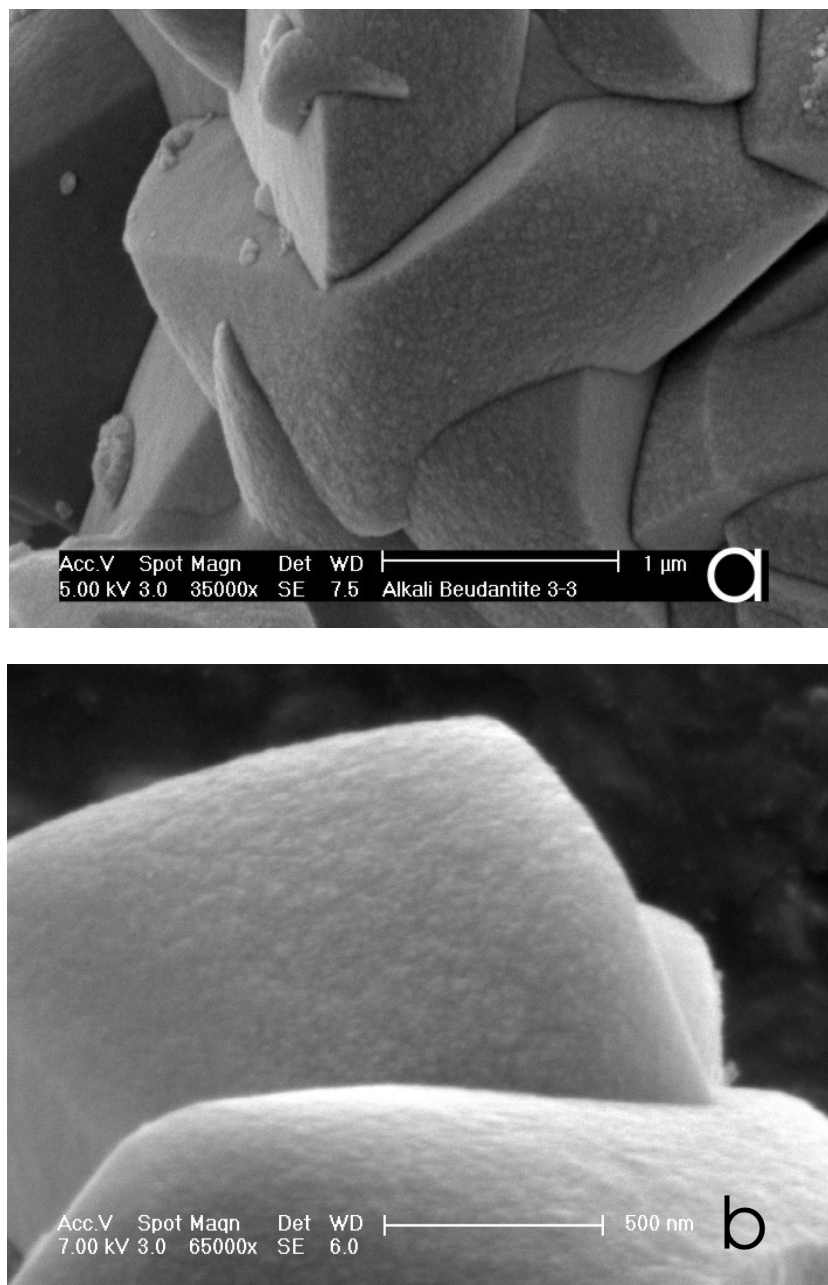
Figure 5.18. Scanning electron micrograph (SEM) images of the residual solid from the alkali dissolution of beudantite. Image (a) is a general overview of the residual solid; a fine globular coating can be observed. Image (b) is a high-resolution micrograph of a beudantite grain, showing again the presence of a very finely dispersed secondary phase. Operating conditions indicated on each micrograph.

5.3 Discussion

5.3.1 Potassium jarosite

A comparison of the molar ratios for the aqueous and residual solid data for the alkali dissolution of potassium jarosite with the characterised formula of the synthetic $((H_3O)_{0.16}K_{0.84}Fe_{2.46}(SO_4)_2(OH)_{4.38}(H_2O)_{1.62}$; Table 3.3) reveals some interesting relationships. The aqueous concentrations of K and SO_4^{2-} greatly exceed that of Fe, to such a degree it could be said that there are nearly negligible concentrations of Fe present in all three triplicates (Tables 5.1, 5.2). Aqueous molar ratios of K and SO_4^{2-} (1.24-1.26:2, Table 5.2) imply that there is an excessive quantity of K ions in solution compared to SO_4^{2-}, considering the idealised ratio should be 0.84:2. This incongruency is also borne out in the residual solid data, where the ratio of K to SO_4^{2-} ranges from 0.672-0.681:2, indicating a net deficiency in K ions in the dissolution solid.

The K and SO_4^{2-} aqueous and residual solid molar ratios for the acid and alkali dissolutions of potassium jarosite are similar (90 % for the aqueous and 80 % for the residual solid) (Tables 4.2, 4.5, 5.2, 5.5). This suggests that no sulphate adsorption to the residual solid had occurred in either the acid or alkali dissolution experiments. The residual solid molar ratios of Fe and SO_4^{2-} ranged from 4.799-4.853:2, nearly double the idealised value of 2.46:2 seen in the synthetic solid. The excessive amount of Fe in the alkali residual solid of potassium jarosite implies that a secondary Fe-rich phase formed during the course of the experiment.

The aqueous ion concentration profiles (Figure 5.1) show good fit to a transport-controlled dissolution model (Stumm and Morgan 1996). This dissolution model was also assigned to the acid dissolution of potassium jarosite (Section 4.3.1). A general schematic representation of this dissolution model is presented in Figure 1.3a. Generally, the alkali dissolution of potassium jarosite is broadly classed as an incongruent reaction for two main reasons; first due to the precipitation of a secondary phase, and second, due to the non-ideal dissolution of K and SO_4^{2-}, observed by differing aqueous and solid molar ratios compared to the idealised synthetic ratios (Tables 3.3, 5.2, 5.5).

The alkali dissolution of potassium jarosite gives the strongest evidence that an Fe-rich secondary phase forms during the experiment. This phase is confirmed to be goethite using a combination of X-ray diffraction (Figure 5.6), FTIR (5.11a), SEM particle morphology (Figures 5.14, 5.15), and Munsell colour data (Figure 5.13; Bigham, 1994).

In summary, the alkali dissolution of potassium jarosite is governed by transport-controlled dissolution kinetics, and is incongruent, with the formation of an Fe-rich goethite secondary phase throughout the experiment. The incongruency of the dissolution is also reflected in the non-ideal concentrations of K and SO_4^{2-} ions in the final solutions. The alkali dissolution of potassium jarosite can be described by the reaction in Eq. 5.1.

$$KFe_3(SO_4)_2(OH)_{6(s)} + OH^-_{(aq)} \rightarrow FeO(OH)_{(s)} + K^+_{(aq)} + SO_4^{2-}_{(aq)} \qquad (5.1)$$

5.3.2 Plumbojarosite

For the plumbojarosite alkali dissolution, similar features to those of potassium jarosite are seen when comparing the aqueous and residual molar ratios to the idealised solid $((H_3O)_{0.74}Pb_{0.13}Fe_{2.92}(SO_4)_2(OH)_{5.76}(H_2O)_{0.24})$. Once again, the concentrations of Pb and SO_4^{2-} in solution greatly exceed that of Fe (Tables 5.1, 5.2). The range of Pb and SO_4^{2-} aqueous molar ratios (0.109-0.116:2, Table 5.2) indicate that SO_4^{2-} is slightly in excess compared to Pb in solution, when considering the synthetic ratio is 0.13:2. The higher molar ratio of Pb to SO_4^{2-} in the residual solids (0.178-0.183:2, Table 5.6), compared to the synthetic of 0.13:2, supports the argument that the solids have a net deficiency of SO_4^{2-}, and to a lesser extent Pb. The reason why the plumbojarosite residual solid maybe very slightly deficient in Pb, but not to the degree shown for K in the potassium jarosite dissolutions, is due to the relative occupancy that these ions have of the A-site. As suggested in Section 4.3.1, a small percentage of the crystallographic A-sites are occupied by Pb in plumbojarosite, in comparison to K in potassium jarosite that nearly has 80% occupancy in the synthetic solid made for this study. It is these opposing degrees of A-site occupancy that account for the fact that in the plumbojarosite dissolutions, SO_4^{2-} is always in relative excess to Pb, compared to K to SO_4^{2-} in potassium jarosite that is vice versa.

The residual solid molar ratios of Fe and SO_4^{2-} ranged from 3.639-3.673:2 nearly one and half times the idealised value of 2.92:2 seen in the synthetic solid. The excessive amount of Fe in the alkali residual solid of plumbojarosite implies that a secondary Fe-rich phase probably formed during the course of the experiment. The acid dissolution concentrations of Pb and SO_4^{2-} in solution are approximately double those of the alkali dissolution (Tables 4.1 and 5.1). The aqueous molar ratios of both experiments are, however, extremely similar, (0.109-0.112:2 and 0.109-0.116:2 for the acid and alkali dissolution respectively; Tables 4.2 and 5.2). This similarity suggests the lack of any significant adsorption of Pb or SO_4^{2-} ions to the Fe-rich secondary phase.

The aqueous dissolution profiles of SO_4^{2-} and Fe for the alkali dissolution of plumbojarosite display linear-style relationships (Figures 5.2 and 5.3, respectively). This suggests that a surface-controlled dissolution model governs the alkali dissolution of plumbojarosite (Stumm and Morgan 1996). A general schematic representation of this dissolution model is presented in Figure 1.3b. Surface-controlled dissolution results when detachment from the mineral surface via surface reactions are so slow that concentrations adjacent to the surface build up to values essentially the same as in the surrounding bulk solution. Dissolution is not affected by increased flow velocities or stirring. The dissolution kinetics follow a zero-order rate law if the steady-state conditions at the surface prevail (Stumm and Morgan 1996). The alkali dissolution of plumbojarosite is also classified as an incongruent reaction due to the precipitation of a secondary phase and the non-ideal dissolution of Pb and SO_4^{2-}, as suggested by differing aqueous and solid molar ratios compared to idealised synthetic ratios (Tables 3.3, 5.2, 5.5).

The existence of an Fe-rich secondary phase in the alkali dissolution of plumbojarosite is difficult to prove, mainly because no secondary phase could be identified by X-ray diffraction (Figure 5.7) or FTIR spectroscopy (Figure 5.11b). The globular morphology of the secondary phase seen in the SEM micrographs of the plumbojarosite residual solid (Figure 5.16), the spherical habit of a sample of synthetic ferrihydrite (Figure 5.17), and the Munsell colour of the residual solid (Figure 5.13; Bigham, 1994) all suggest that the Fe-rich phase is ferrihydrite $(Fe(OH)_3)$. The extremely poor crystallinity of ferrihydrite may have hampered its

identification by X-ray diffraction. To prove how poor and difficult ferrihydrite is to see yet alone identify by XRD, a diffraction pattern of a synthetic sample was collected (Figure 5.10). There are no easily identifiable sharp reflections produced from this synthetic sample. The X-ray amorphous nature of ferrihydrite may explain for the lack of evidence this minor phase in the overall residual solid diffraction pattern of the alkali plumbojarosite dissolution. Similarly, the amorphous nature of ferrihydrite may have prevented a positive identification by FTIR spectroscopy. Figure 5.12b is an FTIR spectrum of the same synthetic ferrihydrite used in the XRD and SEM results. Excluding a peak at 1384 cm^{-1}, which is identified as resulting in a carbonate impurity, there are no unique vibrational mode(s) that are only seen in ferrihydrite and not it any other jarosite-type mineral (Figure 3.15, 3.16, 5.11).

In summary, the alkali dissolution of plumbojarosite is governed by surface-controlled dissolution kinetics, and is incongruent, with the formation of an Fe-rich amorphous ferrihydrite ($Fe(OH)_3$)-like secondary phase throughout the duration of the experiment. The linear aqueous ion profiles of SO_4^{2-} and Pb (Figures 5.2 and 5.3, respectively) suggest that the dissolution is surface-controlled. There is no good evidence for Pb adsorption throughout the duration of this experiment (Tables 4.2 and 5.2, respectively). The alkali dissolution of plumbojarosite can be described by the reaction in Eq. 5.2.

$$Pb_{0.5}Fe_3(SO_4)_2(OH)_{6(s)} + OH^-_{(aq)} \rightarrow Fe(OH)_{3(gel)} + Pb^{2+}_{(aq)} + SO^{2-}_{4(aq)} \qquad (5.2)$$
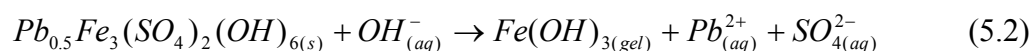
5.3.3 Beudantite

The SO_4^{2-} concentration profile for the alkali dissolution experiment of beudantite (($H_3O)_{0.68}Pb_{0.32}Fe_{2.86}(SO_4)_{1.69}(AsO_4)_{0.31}(OH)_{5.59}(H_2O)_{0.41}$; Table 3.3, Figures 5.4, 5.5) is markedly different to those of potassium jarosite (Figure 5.1) and plumbojarosite (Figure 5.2, 5.3) but does bear some resemblance to that of the acid dissolution of beudantite (Figure 4.6). In two of the triplicates, there was no measurable aqueous Pb, and in the third bottle, the Pb concentration was 0.00007 mmol L^{-1} at ~ 28 hrs into the duration of the experiment. The corresponding aqueous molar ratio of Pb to SO_4^{2-} was 0.0078:1.69 compared to the idealised value of 0.32:1.69 present in the synthetic solid (Table 3.3, 5.2). The residual solid molar ratios of Pb to SO_4^{2-} range from 0.412-0.415:1.69, and importantly, is higher than the synthetic ideal of 0.34:1.69

(Tables 3.3, 5.6). This implies that a Pb-rich secondary phase is likely to be present, similar to the acid dissolution of beudantite. It is proposed that the Pb-rich phase is $PbSO_4$, and the majority of Pb precipitated out of solution as $PbSO_4$ before 1000 hrs. It is well known that $PbSO_4$ is a stable phase in these conditions as it is a common impurity in the synthesis of lead-bearing jarosites such as beudantite (Dutrizac et al. 1980). The early precipitation of the Pb as $PbSO_4$ in the dissolution experiment explains the profile of SO_4^{2-} in solution (Figure 5.4), in that SO_4^{2-} is in excess compared to Pb in the ratio 1.69:0.32 (Table 3.3). In the first 1000 hrs of the reaction, SO_4^{2-} concentrations are low due to the precipitation of $PbSO_4$, and when all the Pb has been removed from solution, the SO_4^{2-} concentration rises by the continuing dissolution of the parent solid, to a point where the concentration plateaus toward the end of the experiment (Figure 5.4).

The beudantite dissolution aqueous molar Fe to SO_4^{2-} ratios range from 0.0097-0.0157:1.69, and the residual solid Fe to SO_4^{2-} ratios from 3.396-3.412:1.69, where ultimately the idealised synthetic ratio is 2.86:1.69 (Table 5.2, 5.6, and 3.3, respectively). These ratios suggest a Fe-rich secondary phase is present in the residual solids. It is worth highlighting that the molar ratios in the solids are likely to be artificially low; this is because the total concentration of SO_4^{2-} used to calculate the molar ratio is assumed to belong to beudantite, whereas in the later stages of the dissolution, the total SO_4^{2-} concentration is made up the residual solid and the $PbSO_4$ secondary phase (see below). Even though the concentrations of Fe in solution are extremely low, when Fe is re-plotted on a more appropriate scale a linear-style relationship emerges after 250 hrs (Figure 5.5). The AsO_4^{3-} and SO_4^{2-} aqueous molar ratios vary from 0.175-0.190:1.69 compared to the synthetic of 0.31:1.69 (Tables 5.2 and 3.3, respectively), indicating a net deficiency of AsO_4^{3-} in solution. The residual solid ratios of AsO_4^{3-} and SO_4^{2-} are 0.267-0.270:1.69, these are again lower than the ideal seen in the synthetic (0.31:1.69), but due to the probable precipitation of $PbSO_4$, the AsO_4^{3-} component of the residual solid molar ratio is likely to be statistically lower than the real value. All of these data suggest that a proportion of the solution AsO_4^{3-} is likely to have adsorbed to either one or both of the secondary phases. The reason why absorption is a likely mechanism for reducing the concentration of AsO_4^{3-} in solution is that the most likely arsenate-rich precipitate is scorodite ($FeAsO_4$), and this mineral phase would have removed all AsO_4^{3-} from solution as Fe is in excess in

the overall system compared to AsO_4^{3-} (Table 3.3). There is a considerable quantity of published literature supporting the affinity of iron (oxy)hydroxides for the absorption of (AsO_4^{3-}) bearing species within the changeable pH window (8 to 4) seen in the alkali dissolution of beudantite (Raven et al. 1998, Jain et al. 1999, Richmond et al. 2004).

The complexity of the alkali dissolution of beudantite, makes it difficult to assign it a dissolution model (transport or surface). The linearity of the Fe ion concentration profile against time (Figure 5.5) suggests that, after 250 hrs into the experiment, the kinetics are governed by a surface-controlled reaction. By contrast, the AsO_4^{3-} profile for the first 250 hrs appears to have a parabolic style profile that is indicative of transport-controlled dissolution. The alkali dissolution of beudantite, therefore, is probably governed by a mixed transport-surface kinetic dissolution reaction, where transport mechanisms dominate the first 250 hrs of the reaction, and the formation of secondary phases on the residual solids dominate the dissolution rate-determining step for the remainder of the experiment.

The aqueous ion profiles (Figures 5.4, 5.5) suggest that two discrete secondary phases were likely to have formed; an Fe-rich phase similar to those already seen in the alkali dissolutions of potassium jarosite and plumbojarosite, and a $PbSO_4$ phase similar to the one found in the acid dissolution of beudantite. The positive identification of either phase is difficult, as no evidence could be found by X-ray diffraction (Figure 5.8) or FTIR spectroscopy (Figure 5.11c). The main evidence for these two phases being present is that of a secondary phase(s) been seen in the SEM micrographs of the residual solid of this dissolution (Figure 5.18). The $PbSO_4$ phase is likely amorphous, since crystalline $PbSO_4$ (anglesite) has quite a distinctive X-ray diffraction pattern and this was not seen in the residual solids (Figure 4.10). Furthermore, the one unique weak FTIR vibration at 967 cm^{-1} in crystalline synthetic anglesite (Figure 4.12) was not seen in the beudantite residual solid. It should be noted that synthetic anglesite ($PbSO_4$) is pure white in colour and is unlikely to be seen using Munsell colour values (Figure 5.13, 4.13). The Fe-rich phase is extremely similar, to the amorphous ferrihydrite-type phase ($Fe(OH)_3$) observed in the plumbojarosite dissolution. As discussed earlier, the identification of this phase is extremely difficult due to the poorly crystalline nature of the material. The lower than ideal aqueous AsO_4^{3-} molar

ratios (Table 5.3) suggest that some of the AsO_4^{3-} was absorbed to the amorphous $Fe(OH)_3$ Fe-rich phase. There is a considerable amount of literature evidence to support this hypothesis of AsO_4^{3-} absorption to high surface area ferrihydrite-type phases ($Fe(OH)_3$) (Raven et al. 1998, Jain et al. 1999, Richmond et al. 2004).

The alkali dissolution of beudantite is governed by mixed transport-surface controlled dissolution kinetics, where surface processes superseded transport after approximately 250 hrs into the experiment. The beudantite experiment differed from the other two alkali dissolutions in that it contained two amorphous secondary phases, $PbSO_4$ and $Fe(OH)_3$. A proportion of the aqueous AsO_4^{3-} adsorbed to the $Fe(OH)_3$ surface. The alkali dissolution of beudantite can be described by the reaction in Eq. 5.3.

$$PbFe_3(AsO_4)(SO_4)(OH)_{6(s)} + OH_{(aq)}^- \rightarrow$$

$$PbSO_{4(gel)} + Fe(OH)_{3(gel)} + AsO_{4(aq)}^{3-} + SO_{4(aq)}^{2-} \quad (5.3)$$
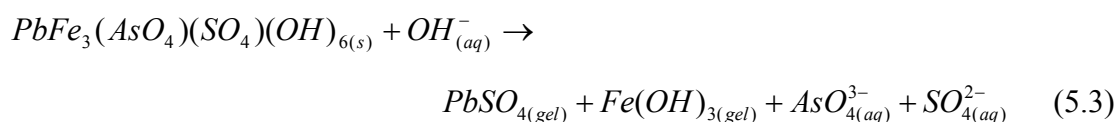
5.3.4 Solubility and Eh-pH

Unfortunately, no IAP values could be calculated for any of triplicates for the alkali dissolution experiment involving potassium jarosite, plumbojarosite, and beudantite. A true IAP value for dissolution of a mineral assumes that the reaction has reached steady state and no ions have precipitated out of solution. Secondary phase formation in mineral dissolution skews the overall calculated IAP to be lower than the real experimental value, because lower ion concentrations in solution result in lower equilibrium aqueous activities being reported. Out of all the acid and alkali dissolution experiments, IAP values could only be calculated for the acid dissolution of potassium jarosite and plumbojarosite (Table 4.3); the remaining four dissolution experiments all contained secondary phases (Table 4.3, 5.3).

Saturation indices were calculated for the alkali dissolutions of potassium jarosite, plumbojarosite, and beudantite (Table 5.4) by GWB, but only the indices for potassium jarosite are meaningful, with similar results for the three triplicates (Table 5.4). Speciation modelling of the alkali dissolution of potassium jarosite predicts the stability of hematite and goethite in solution (Table 5.4). The calculated values are higher than those reported for the same two minerals for the acid dissolution of potassium jarosite. Hematite is commonly reported as a positive saturation index in

nearly all aqueous Fe^{3+} rich oxic environments by programs like GWB, because the mineral is extremely stable in natural environments. The positive indices for goethite give a far greater insight into the reaction pathway for the dissolution of potassium jarosite in an alkali regime, especially since goethite was actually found as an identifiable secondary phase in the dissolution experiments.

An Eh versus pH diagram (Figure 5.19) was also constructed in GWB using the equilibrium activities from Bottle 1 of the triplicates in the alkali dissolution of potassium jarosite. When hematite and a series of other minerals are suppressed (FeO, magnetite, pyrrhotite, and troilite), an Eh-pH diagram (Figure 5.19b) similar to the conditions found in the experimental dissolutions of potassium jarosite is seen. In this case, goethite is the most stable mineral phase and more importantly, it appears potassium jarosite is not stable at all under these conditions.

A   **B**
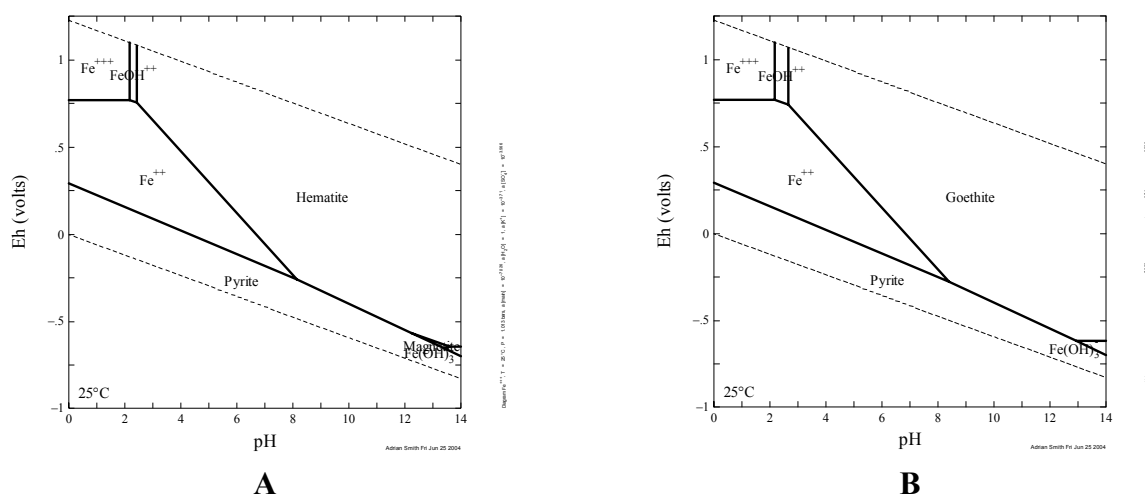
Figure 5.19. Eh-pH diagrams for the alkali dissolution of potassium jarosite. Equilibrium aqueous activities were taken from Bottle 1. (a) is an Eh-pH diagram of the dissolution where all possible minerals are shown, (b) is an Eh-pH diagram where hematite and a series of other minerals have been suppressed (FeO, magnetite, pyrrhotite, and troilite) to simulate more accurately experimental conditions. The experimental conditions were: $f_{O_{2(g)}} = 0.2$, $f_{CO_{2(g)}} = 10^{-3.5}$, $Ca^{2+} = 3.995 \times 10^{-6}$ molal, pH = 3.30, Eh = 1.02 volts, $K^+ = 0.2041$ ppm, $Fe^{3+} = 0.0023$ ppm, $SO_4^{2-} = 0.3279$ ppm.

The problem with the plumbojarosite and beudantite saturation data is that the latest version of the GWB thermodynamic database does not contain any data for these two minerals. This results in GWB assuming incorrectly that the plumbojarosite aqueous data came from the dissolution of anglesite. This is shown in Table 5.4 as a series of negative saturation indices for anglesite, where instead the mineral phase should be plumbojarosite. A similar story is seen for beudantite, where the GWB program

assumes the initial mineral is $Fe(OH)_3$. As the GWB database lacks thermodynamic data on plumbojarosite and beudantite, the calculated positive saturation indices for hematite and goethite are likely incorrect, to what degree it is ultimately hard to say.

5.4   Conclusions and summary

The alkali dissolution reactions of potassium jarosite, plumbojarosite, and beudantite can be broadly classed as incongruent dissolution reactions, where secondary phases form from parent ions in solution. Goethite and amorphous $Fe(OH)_3$ form as a result of the alkali dissolutions of potassium jarosite and plumbojarosite, respectively. Amorphous $PbSO_4$ and $Fe(OH)_3$ form as a result of the alkali dissolution of beudantite. The alkali dissolution of potassium jarosite is described by transport-controlled dissolution kinetics and that of plumbojarosite by surface-controlled kinetics. There was no evidence of Pb adsorption in the plumbojarosite dissolution. For the beudantite dissolution, a mixed surface-transport model is the most likely mechanism that describes the dissolution kinetics. A degree of AsO_4^{3-} absorption was found to have occurred in the alkali dissolution of beudantite, most likely to the high surface area, amorphous $Fe(OH)_3$ secondary phase.

No IAP values for any of the three alkali dissolutions could be calculated due to the presence of secondary phases in all of the dissolution experiments. An Eh-pH diagram for the alkali dissolution of potassium jarosite (calculated from equilibrium activities taken from Bottle 1) confirms that the mineral is not stable under the conditions of an alkali remediation regime (pH = 3.30 and Eh = 1.02 volts) (Figure 5.19).

6   Computational modelling

Chapter 6 describes the computational modelling carried out for this study. The chapter consists of three sections: (i) the creation of a classical model of the potassium jarosite structure, (ii) studies of its stable 2D surfaces, and (iii) the incorporation of toxic elements (e.g. Cu(II), Zn(II)) into the structure. Each of these three sections is divided into subsections of methodology and results. An overall discussion and summary of the computational modelling is given in a fourth and final section.

6.1   Introduction to computational modelling

Over the last two decades, computational modelling has provided a large range of tools for exploring the structures and properties of matter at the atomic level. The range of use is now very broad, encompassing material and surface science, mineralogy, molecular biology and molecule chemistry (Catlow 2003). Computer modelling is a distinctive type of scientific technique that bridges fundamental theory with experimental observation on complex systems (Cormack 1999). Computer simulation studies aim to provide reliable models at the atomistic level that can provide general insight and understanding of the systems simulated. These models can directly assist the interpretation of experimental data and provide accurate numerical data on important parameters, which may be difficult to measure by experiment (Catlow 2003).

Two techniques are available for modelling matter at the atomic level. The first uses interatomic potentials that express the energy of the system and the second uses electronic structure calculations that solve the Schrödinger equation to some level of approximation (Catlow 2003). All of the computation modelling in this study is based on the use of interatomic potential-based methods, often referred to as classical atomistic simulations.

6.2   Theory of classical atomistic simulations

Classical atomistic simulation methods are based on the Born Model of the solid, in which the forces between the ions can be modelled using a potential model. In the Born Model, the solid is considered to be composed of point charges with short-range forces acting between them, in addition to the long-range electrostatic forces

(Cormack 1999). The computer code that was chosen to make the potential model for the potassium jarosite structure was the General Utility Lattice Program (GULP), which was devised by Gale (1997). In the subsequent sections in this chapter, these short and long-range forces will be discussed in more detail with respect to the potentials that ultimately represent them.

6.2.1 Long range potentials

The electrostatic forces in the Born Model are long-range; varying as 1/r, and because of this, the convergence of the Madelung sum for an arbitrary structure is somewhat slow and requires the inclusion of a large number of terms (Cormack 1999). Ewald (1921) developed an alternative approach, based on a separation of the real space Madelung sum into two sums, one of which is in reciprocal space, and the other in real space. The two sums introduced in this approach both converge more rapidly than the direct Madelung sum. The Ewald method is in common use in most computer simulations and has been incorporated into the GULP code (Gale 1997).

6.2.2 Short range potentials

Short-range potentials have their origin in Pauli repulsion and dipolar disperse interactions (Maitland et al. 1981). These potentials are key to a successful simulation and describe the chemistry of the material (Cormack 1999). Three types of short-range interatomic potentials were used to construct a ridged ion model of the potassium jarosite structure in GULP. A ridged ion model is one that does not take into account any polarisability that the ions might naturally exhibit.

6.2.2.1 Two body potentials

Two body potentials represent short-range interactions between two charged clouds, and can be attractive (van der Waals) or repulsive. The interaction has various analytical forms depending upon the type of systems being modelled. All the analytical forms can, however, be classified as bonded or non-bonded interactions (Catlow and Mackrodt 1982).

Buckingham Potential

The Buckingham potential is the most widely used potential to model non-bonded interactions. It contains both repulsive and attractive terms, which take the form:

$$U(r_{ij}) = A_{ij} \exp(\frac{-r_{ij}}{\rho_{ij}}) - \frac{C_{ij}}{r_{ij}^6}$$

(6.1)

where the parameters A_{ij} represents the repulsion between the two ions i and j, ρ_{ij} is related to the size and hardness of the ions and C_{ij} is the term included to model dispersion (Gale 1997). r_{ij} represents the distance between two atoms i and j.

Morse Potential

The Morse potential is used for covalent bonding when distances vary from the equilibrium bond distance. It takes the form:

$$U(r_{ij}) = D_{ij}(\{1 - \exp[-\beta_{ij}(r_{ij} - r_0)]\}^2)$$

(6.2)

where D_{ij} is the bond dissociation energy, r_o is the equilibrium bond distance and β_{ij} is a function of the slope of the potential energy well that can be obtained from spectroscopic data (Catlow and Mackrodt 1982).

6.2.2.2 Multi body potentials

All of the potential functions discussed in the previous section are radial in nature and do not take into account directionality in bonding. When simulating systems in which covalency is important, many body interactions are commonly employed to confer directionality on the two body bonds (Catlow and Mackrodt 1982).

Three Body Interactions

A three body bond bending interaction potential function is represented by:

$$U(r_{ij}, r_{jk}) = \frac{1}{2} k_{ijk} (\theta - \theta_0)^2$$

(6.3)

where k_{ijk} is the force constant and θ_o is the equilibrium bond angle. This type of bonding is between a central ion, i, and two bonded ions, j and k, making a bond angle of θ.

6.2.3 Fitting of interatomic potentials

Before any calculation runs can be performed with an interatomic potential program it is essential to obtain the necessary potential parameters that can represent the system. Typically, the parameters that are published in the literature are not always applicable to the majority of structures; therefore, a certain degree of potential fitting has to be carried out. Potential derivation by fitting can be split into either empirical or non-empirical methods. Non-empirical methods seek to determine the parameters by attempting to fit data from a higher calculation (such as an *ab initio* calculation) by trying to reproduce an energy surface. Empirical methods, by comparison, attempt to derive empirical potentials by aiming to reproduce experimental data (Cormack 1999). The GULP code has a fitting facility that accommodates both these methods (Gale 1997).

Regardless of which method of fitting is used, the key quantity is the 'sum of squares' which measures how good the fit is. Ideally, this should be zero at the end of the fit, but in practice, this will only happen for a small number of cases (Gale 1997). The sum of squares, F, is defined as:

$$F = \sum_{all-observables} w.(f_{calc} - f_{obs})^2 \qquad (6.4)$$

where f_{calc} and f_{obs} are the calculated and observed quantities and w is an appropriate weighting factor (Catlow and Mackrodt 1982). Unique fits do not exist, as there are an infinite number of possible fits depending upon the choice of the weighting factor. The choice of the weighting factor for each of the variables depends on several factors such as the relative magnitude of the quantities and the reliability of the data. A crystal structure, for instance, will generally be more reliable than an elastic constant measurement (Cormack 1999).

The aim of a fit is to minimise the sum of squares by varying the potential parameters. There are several standard techniques for resolving least squares problems. GULP uses a Newton-Raphson functional minimisation approach (Gale 1997), as described below.

6.2.4 Energy minimisation

Energy minimisation is central to many aspects of computer simulation. As its name suggests, the total energy of the system is minimised with respect to certain structural variables (usually the atomic positions) and the unit cell parameters. Given a starting configuration, a structure may be refined, or equilibrated to its minimum energy configuration (Catlow and Mackrodt 1982).

Several types of standard minimisations are available in GULP, the most commonly used optimise at constant pressure, in which all internal and cell variables are included, or at constant volume, where the unit cell remains frozen (Gale 1997). The jarosite structure was optimised at constant pressure for this study.

The most efficient minimisers are those based on the Newton-Raphson method, in which the Hessian or some approximation is used. The minimisation search direction, x, is then given by

$$x = -H^{-1}g$$

(6.5)

where H is the Hessian matrix and g is the corresponding gradient vector (Cormack 1999). The default minimiser in GULP uses the exact second-derivative matrix, calculated analytically, to initialise the Hessian for the minimisation variables, and then subsequently updates it using the Broyden-Fletcher-Goldfarb-Shanno (BFGS) algorithm (Gale 1997).

6.2.5 Lattice energy

Within the framework of the Born Model, one may write the Lattice Energy as:

$$E_{Lattice} = \frac{1}{2} \sum_{i,j} \frac{q_i q_j}{r_{ij}} + V_{ij}(r_{ij}) + U_{ijk}(r_{ij}, r_{jk})$$

(6.6)

where the first term describes the electrostatic contribution, the second term describes the pair-wise short-range potential (Buckingham) energy and the third term describes three-body interactions (Cormack 1999). The third term is often included for materials that display a large degree of covalent bonding character, because it allows

for bond angles that are not linear; in potassium jarosite, this would maintain the sulphate tetrahedral units.

6.3 Classical potential model of potassium jarosite

A rigid ion potential model of potassium jarosite (Figure 6.1) was created through GULP version 1.3 (Gale 1997), where the crystallographic lattice positions were taken from single crystal data in Menchetti and Sabelli (1976) (Table 6.1). Three types of interatomic potentials were used to create the model (Buckingham, Morse and Three-body; Table 6.2).

To understand the stability of jarosite surfaces and why this mineral subgroup can host large amounts of contaminant elements an understanding of its crystallography is essential. Jarosites are members of the alunite supergroup (Jambor 1999) consisting of isostructural minerals described by the general formula $AB_3(TO_4)_2(OH)_6$. The general jarosite structure has $R\overline{3}m$ symmetry and contains metal ions (B) located in slightly distorted octahedra. Each octahedron has four bridging hydroxyl groups (oxygen in hydroxyl groups referred to as O3 in Tables 6.1 and 6.2) in a plane, and sulphate oxygen atoms (O2) at the apices. Three of the tetrahedral oxygen atoms (O2) are coordinated to metal ions, and the symmetry of the $(TO_4)^{2-}$ tetrahedra is reduced from T_d to C_{3v}. The metal ions are joined by these $(TO_4)^{2-}$ tetrahedra and by the network of di-hydroxyl bridges to form sheets separated by the uncoordinated sulphate oxygen atoms (O1) and the alkali A-site cations (Jambor 1999, Becker and Gasharova 2001). Figure 6.2 illustrates the above key relationships in the potassium jarosite structure.

Table 6.1. Atomic fractional co-ordinates of the jarosite structure taken from single crystal data (Menchetti and Sabelli 1976).

Atom	x	y	z
K	0.00000	0.00000	0.00000
S	0.00000	0.00000	0.30880
Fe	0.00000	0.50000	0.50000
O1	0.00000	0.00000	0.39360
O2	0.22340	-0.22340	-0.05450
O3	0.12680	-0.12680	0.13570
H	0.16900	-0.16900	0.10600
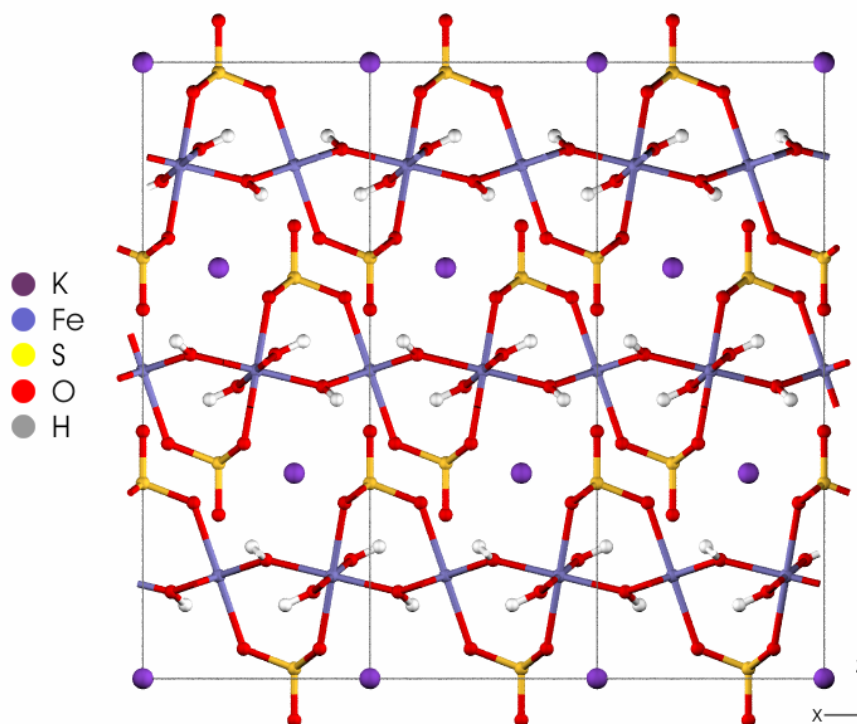
Figure 6.1. X – Z axes cut through a rigid ion potential model of potassium jarosite. The structure is made up of FeO_6 octahedrons bonded to sulphate tetrahedra making a tetrahedral-octahedral-tetrahedral (T-O-T) sheet like structure. Potassium ions are located in 12-fold coordination between the T-O-T sheets.
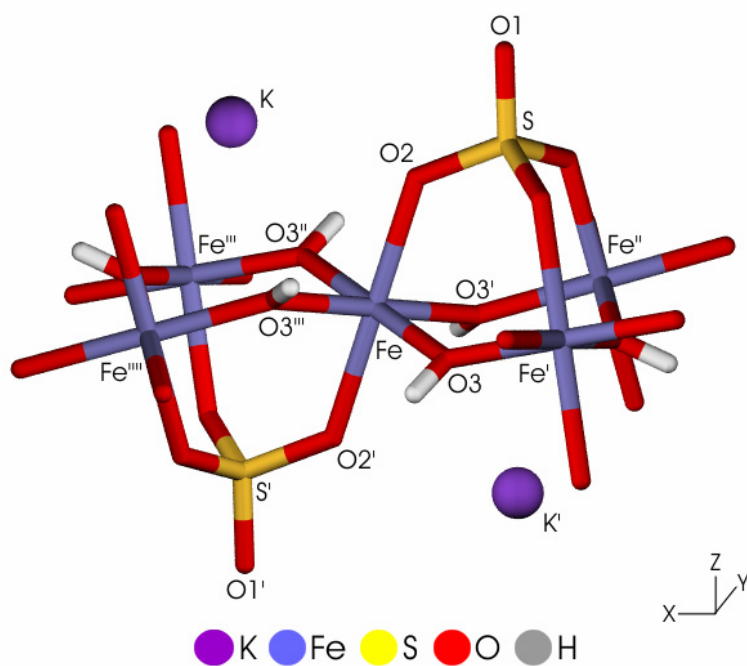
Figure 6.2. High-resolution schematic diagram of the key T-O-T building blocks and the 12-fold coordinated A-site in the potassium jarosite structure. Specific atomistic structural positions are labelled with respect to the central Fe atom.

Table 6.2. Potential parameters for the model of the potassium jarosite structure.

Two-body short range interaction				
Buckingham	A/eV	ρ/Å	C/eV Å^6	Reference
$K^+ - O1^{0.84-}$	987.570	0.3000	0.00	a
$K^+ - O3^{1.426-}$	1587.570	0.3000	0.00	a
$Fe^{3+} - O1^{0.84-}$	3219.335	0.2641	0.00	b
$Fe^{3+} - O3^{1.426-}$	3219.335	0.2641	0.00	b
$O1^{0.84-} - O1^{0.84-}$	103585.02	0.2000	25.98	c
$O1^{0.84-} - O3^{1.426-}$	103585.02	0.2000	25.98	c
$O3^{1.426-} - O3^{1.426-}$	103585.02	0.2000	25.98	c
$Cd^{2+} - O1^{0.84-}$	364.686	0.3500	0.00	b
$Cd^{2+} - O3^{1.426-}$	619.0979	0.3500	0.00	b
$Zn^{2+} - O1^{0.84-}$	294.126	0.3372	0.00	b
$Zn^{2+} - O3^{1.426-}$	499.3139	0.3372	0.00	b
$Cu^{2+} - O1^{0.84-}$	700.1988	0.3000	0.00	d
$Cu^{2+} - O3^{1.426-}$	1188.67	0.3000	0.00	d
Morse	D_e/eV	β/Å^{-1}	r_o/Å	
$S^{1.36+} - O1^{0.84-}$	5.0000	1.2000	1.4650	a
$O3^{1.426-} - H^{0.426+}$	7.0525	2.1986	0.9685	e
Three-body interaction	k_3/eV rad^{-2}	θ/°		
$O1^{0.84-} - S^{1.36+} - O1^{0.84-}$	15.0	109.47		c

The short range potential cut-off was set to 10 Å

[a] fitted from Allan et al. (1993)
[b] fitted from Lewis and Catlow (1985)
[c] Allan et al. (1993)
[d] fitted from Woodley et al. (1999)
[e] Saul et al. (1985)

The potential ion model of potassium jarosite was created using the sulphate potential from Allen et al. (1993) in conjunction with the Morse potential from Saul et al. (1985). Series of other potentials were used to make up the structure from literature values (Table 6.2). The interatomic potentials used to describe the sulphate oxygen atoms O1 and O2 did not discriminate between their individual lattice positions, therefore the sulphate oxygen atoms in the potentials are represented collectively as O1 (Table 6.2). The ridged-ion model of the potassium jarosite structure has two discrete oxygen environments: the sulphate oxygen atoms, (represented by O1 in the potentials) and the oxygen attached to the hydroxyl group (O3). The charges on these oxygen atoms in the two environments are -0.84 and -1.426 respectively. In the case where different oxygen atoms have different charges and where the oxygen atoms have similar metal (A or B) – O interactions it is normal for a scaling factor to be applied (Schroder et al. 1992). In this case, the A-parameter in the Buckingham potentials (Table 6.2) were initially scaled according to the appropriate charges and

then subsequently modified by fitting them to the jarosite structure. Buckingham parameters for $Cu^{2+} - O^{2-}$, $Cd^{2+} - O^{2-}$, and $Zn^{2+} - O^{2-}$ were taken from Lewis and Catlow (1986) and Woodley et al. (1999) and scaled in a similar manner to take account of the lower charges on the O1 and O3 oxygen atoms.

Table 6.3. Summary of the key properties of the five models of the potassium jarosite structure.

Model	Key Properties
Structure 1	Scaled K – O3 Buckingham potential
Structure 2	Scaled K – O3 and Fe – O3 Buckingham potential
Structure 3	Scaled K – O3 and Fe – O3, and an O3 – O3 Buckingham potential
Structure 4	Scaled K – O3, and an O3 – O3 Buckingham potential
Structure 5	An O3 – O3 Buckingham potential

In total, five separate models of the potassium jarosite structure were made by varying certain interatomic potential parameters to produce the most realistic structure that was comparable to experimental results. Table 6.3 briefly summarises the main constituent parts of the five model structures. The main differences between structures 1 and 2 and 3, 4 and 5 is the addition of an O3 – O3 Buckingham interaction to the latter three models to help improve the hydroxyl bridging contributions to the Fe octahedra. Structures 2 and 3 investigated the influence of scaled charges on the Fe – O3 Buckingham potential. Structure 5 solely looked at the influence of the O3 – O3 Buckingham interatomic potential. Unit cell parameters and interatomic distances and angles for the five optimised structures are compared to single crystal data from Menchetti and Sabelli (1976) in Table 6.4, where the a/c axis ratio was used to evaluate the reproducibility of the potassium jarosite unit cell. The total optimised lattice energies of the five structures are also included in Table 6.4. All the interatomic distances and angles were measured used Accelrys Cerius^2 software. Looking initially at the optimised unit cell parameters for all five structures in comparison to the experimental data from Menchetti and Sabelli (1976), it is immediately apparent that all the computer models have longer crystallographic axes. When the unit cell data are viewed by the relative ratio of the a- to c-axes, it appears that all our models compare favourably to those determined by experiment. Out of all five of the models, structures 4 and 1 are most favourable with a/c ratios of 0.4254 and 0.4208, respectively, as compared to 0.4247 from the single crystal data from Menchetti and Sabelli (1976). Structures, 1 and 4 had less than 2 % difference in their unit cell parameters compared to the Menchetti and Sabelli (1976) data.

Table 6.4. Summary of unit cell parameters and interatomic distances and angles for the model potassium jarosite structures in comparison to single crystal experimental data of Menchetti and Sabelli (1976). All distances are in units of angstroms (Å) unless stated otherwise.

	Menchetti & Sabelli (1976)	Structure 1	Structure 2	Structure 3	Structure 4	Structure 5
a	7.315	7.380	7.957	7.965	7.443	7.448
b	7.315	7.380	7.957	7.965	7.443	7.448
c	17.224	17.537	17.419	17.392	17.497	17.189
Vol ($Å^3$)	798.17	827.21	955.21	955.64	839.40	825.79
a/c	0.4247	0.4208	0.4568	0.4580	0.4254	0.4333
Difference (%)						
a		0.89	8.78	8.89	1.75	1.82
b		0.89	8.78	8.89	1.75	1.82
c		1.81	1.13	0.98	1.58	-0.20
Vol ($Å^3$)		3.64	19.68	19.73	5.17	3.46
Energy (eV)		-357.68	-348.07	-348.21	-357.37	-357.59
S-O1	1.465	1.469	1.449	1.449	1.466	1.463
S-O2 x3	1.481	1.542	1.547	1.547	1.543	1.541
K-O3 x6	2.828	2.942	2.845	2.856	2.941	2.886
K-O2 x6	2.978	2.944	3.295	3.299	2.981	2.973
Fe-O2 x2	2.058	2.202	2.132	2.130	2.192	2.186
Fe-O3 x4	1.975	1.966	2.152	2.157	1.988	1.990
O3-O2'	2.886	2.954	3.043	3.048	2.965	2.957
O3-O2	2.828	2.950	3.016	3.015	2.955	2.956
O3-O3'	2.769	2.738	2.930	2.961	2.785	2.776
O3-O3'''	2.857	2.822	3.153	3.137	2.838	2.853
O3-Fe-O2'	91.2°	90.08°	90.52°	90.62°	90.19°	90.03°
O3-Fe-O2	88.8°	89.92°	89.48°	89.38°	89.81°	89.97°
O3-Fe-O3'	88.8°	88.27°	86.79°	86.70°	88.92°	88.42°
O3-Fe-O3'''	91.2°	91.73°	94.21°	93.30°	91.08°	91.58°
Fe-O3-Fe'	135°	139.60°	135.14°	134.78°	138.73°	138.64°
O3-H	0.750	0.883	0.877	0.877	0.882	0.882
O3-H...O1	2.220	2.090	2.277	2.262	2.096	2.061
O3-H...O2	2.942	2.963	3.025	3.040	2.939	2.938

In terms of the interatomic distances and angles of the five structures, the scaled charges on the Fe – O3 Buckingham potential for structures 2 and 3 appear to have improved some of the angles in the FeO_6 octahedra in comparison to the other three structures. The addition of the O3 – O3 Buckingham potential has made the hydroxyl

bridging around the three Fe octahedrons more comparable to Menchetti and Sabelli (1976), shown clearest in structure 4 and 5.   Structure 4 appears to be more representative of the single crystal experimental data than structure 5 in terms of both the unit cell characteristics and interatomic distances and angles.   Even though structure 3 has the scaled charges on the Fe – O3 Buckingham potential, and the benefits that brings with it in comparison to structure 4, the overall a/c ratio and interatomic distances and angles are more comparable.   Both structure 1 and structure 4 have very favourable unit cell proportions as seen by the a/c ratio, but the addition of the O3 – O3 Buckingham potential in structure 4 has greatly improved the hydroxyl bridging around the three FeO_6 octahedra.   In terms of the optimised lattice energies of the five structures, structures 2 and 3 are the worst, with the scaled charges on the Fe – O3 Buckingham potential.   Out of the remaining three structures, the lattice energies were very similar at around -357 eV.   Overall structure 4 was deemed the most representative model of the potassium jarosite structure.   The interatomic potentials in Table 6.2 are therefore those of structure 4.   Table 6.5 summarises the lattice parameters of the single crystal jarosite data from Menchetti and Sabelli (1976) and the optimised positions from structure 4.

Table 6.5. Structural parameters of potassium jarosite.   Experimental data are from Menchetti and Sabelli (1976) and the calculated parameters are of the structure 4 model.

	Experimental			Calculated		
a, b	7.315			7.443		
c	17.224			17.497		
K	0.00000	0.00000	0.00000	0.00000	0.00000	0.00000
S	0.00000	0.00000	0.30880	0.00000	0.00000	0.31719
Fe	0.00000	0.50000	0.50000	0.00000	0.50000	0.50000
O1	0.00000	0.00000	0.39360	0.00000	0.00000	0.40096
O2	0.22340	-0.22340	-0.05450	0.22181	0.77819	0.95187
O3	0.12680	-0.12680	0.13570	0.12474	0.87526	0.14073
H	0.16900	-0.16900	0.10600	0.18668	0.81332	0.11932

Currently the only published classical potential model of potassium jarosite is that of Becker and Gasharova (2001). The Becker and Gasharova model was created using the GULP code and used the same Allan et al. (1993) interatomic potential set as starting parameters as used in our favourable structure 4 model.   Unfortunately, a direct comparison of the unit cell parameters and interatomic distance and angles could not be accomplished because the model of Becker and Gasharova (2001) did not use the same initial experimental structural parameters of Menchetti and Sabelli

(1976); their structural parameters came from a synthesised potassium jarosite sample analysed by single-crystal XRD refinement. The Becker and Gasharova model also contains an additional coulomb term to exclude the electrostatic interaction between the oxygen atoms of the sulphate (the O1 – O1 Buckingham interaction), and lacks an O3 – O3 Buckingham; this ultimately affects its ability to correctly represent the structural bonding between the Fe octahedrons and the bridging sulphate groups. In the Becker and Gasharova (2001) model, the potentials and the cut-offs used constrained the model very heavily to the structure to which it was fitted.

6.4 Theory of simulating the structures and energetics of two-dimensional (2D) surfaces

There are two approaches to the computer modelling of solid surfaces, that is, employing either a two-dimensional (classical atomistic) or a three-dimensional (electronic structure and classical atomistic) simulation cell (Gay and Rohl 1995). Periodic boundary conditions (PBC) are typically used in both 2D and 3D simulation cells to limit the computer time required to model a system of realistic size. PBC allow a finite number of particles to generate realistic behaviour by mimicking an infinite system in such a way that when a particle leaves the simulation box, an image rejoins the box on the opposite side. The box of particles is therefore surrounded by images of itself, producing an infinite repeat of the simulation cell in either two or three dimensions (de Leeuw et al. 2003). All of the computer simulations of the surfaces of the potassium jarosite structure were 2D classical calculations using the Minimisation and Relaxation of Vacancies and Interstials for Neutral Surfaces (MARVIN) code devised by Gay and Rohl (1995).

The classical atomistic simulations of surfaces of ionic solids was pioneered by Tasker (1979) and Mackrodt and Stewart (1979). The majority of the initial work was confined to modelling planar surfaces of the cubic rock salt oxides MgO, CaO and NiO (Colbourn et al. 1983, Tasker and Duffy 1984, Tasker et al. 1985). Soon after, more complicated materials such as Cr_2O_3 (Lawrence et al. 1987), Al_2O_3 (Mackrodt 1989), and Fe_3O_4 (Davis et al. 1994) were studied. Further complexity arrived when models of oxyanions such as SO_4^{2-} and CO_3^{2-} were studied in surface simulations of $BaSO_4$ (Gay and Rohl 1995) and $CaCO_3$ (de Leeuw and Parker 1997).
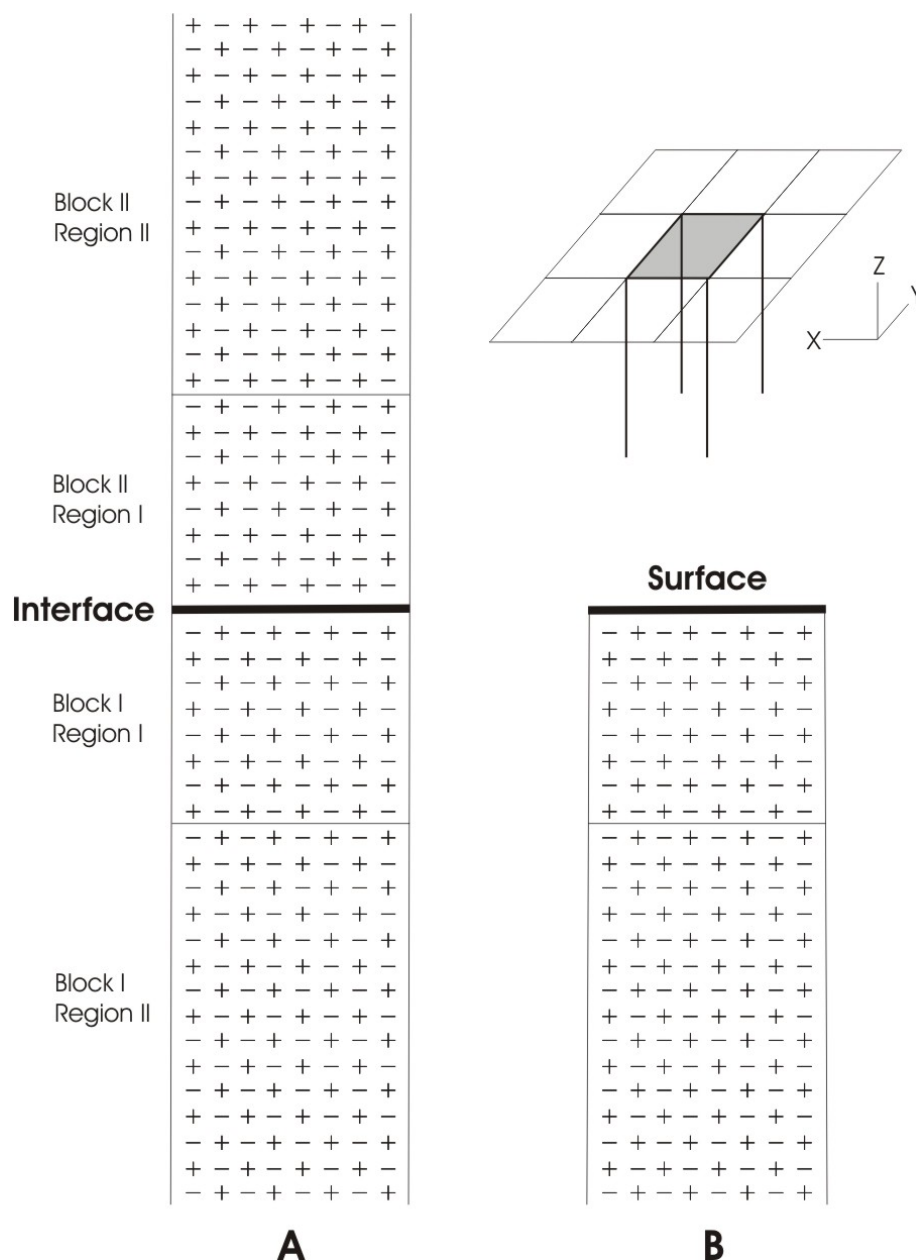
Figure 6.3. The two-region approach used in MARVIN, (a) the complete crystal and (b) half a crystal, exposing a surface, periodic in two dimensions (from de Leeuw et al. 2003).

6.4.1 Two-dimensional simulations

In the MARVIN computer code, the crystal is considered either to consist of a series of charged or neutral planes parallel to the surface and periodic in two dimensions (Gay and Rohl 1995). The crystal is then divided into two blocks, each of which is divided into two regions, region I and region II (Figure 6.3a) (de Leeuw et al. 2003). The ions in region I are allowed to relax explicitly until there is zero force in each of them, whilst those in region II are fixed at their bulk equilibrium positions. The two

region IIs are allowed to move relative to each other (Gay and Rohl 1995). It is necessary to include region II to ensure that the potential of an ion at the bottom of region I is modelled correctly (Tasker 1979). A surface is created when block II is removed with the top of region I as the free surface (Gay and Rohl 1995).

The energy of the crystal is made up of two parts (de Leeuw et al. 2003):

$$U_{latt} = U_1 + U_2 \qquad (6.7)$$

where U_1 and U_2 are the energies of the combined ions in region I and region II respectively. The energy of region I is (de Leeuw et al. 2003):

$$U_1 = \sum_{\substack{i \in I \\ j \in I}} \sum_{1} \Psi_{ij} \left(\left| r_{ij} - r_1 \right| \right) + \frac{1}{2} \sum_{\substack{i \in I \\ j \in II}} \sum_{1} \Psi_{ij} \left(\left| r_{ij} - r_1 \right| \right) \qquad (6.8)$$

where ψ_{ij} is some pair potential (i.e. Buckingham, Morse, and Three-Body). The first term includes interactions between the ions in region I only and the second term describes the interactions between the ions in region I and those in region II, which is referred to as the boundary interaction energy. The energy of region II consists only of this boundary interaction energy because the ions are kept fixed and hence the interaction between the ions in region II itself is unchanged and can therefore be ignored (Gay and Rohl 1995). The energy contribution is (de Leeuw et al. 2003):

$$U_2 = \frac{1}{2} \sum_{\substack{i \in I \\ j \in II}} \Psi_{ij} \left(\left| r_{ij} - r_1 \right| \right) \qquad (6.9)$$

6.4.2 Types of surfaces

In the MARVIN code, the crystal is considered to consist of a series of planes parallel to the surface; Tasker (1979) identified three different types of surfaces. In a type I surface each plane has overall zero charge as it consists of both anions and cations in stoichiometric ratio (Figure 6.4a).
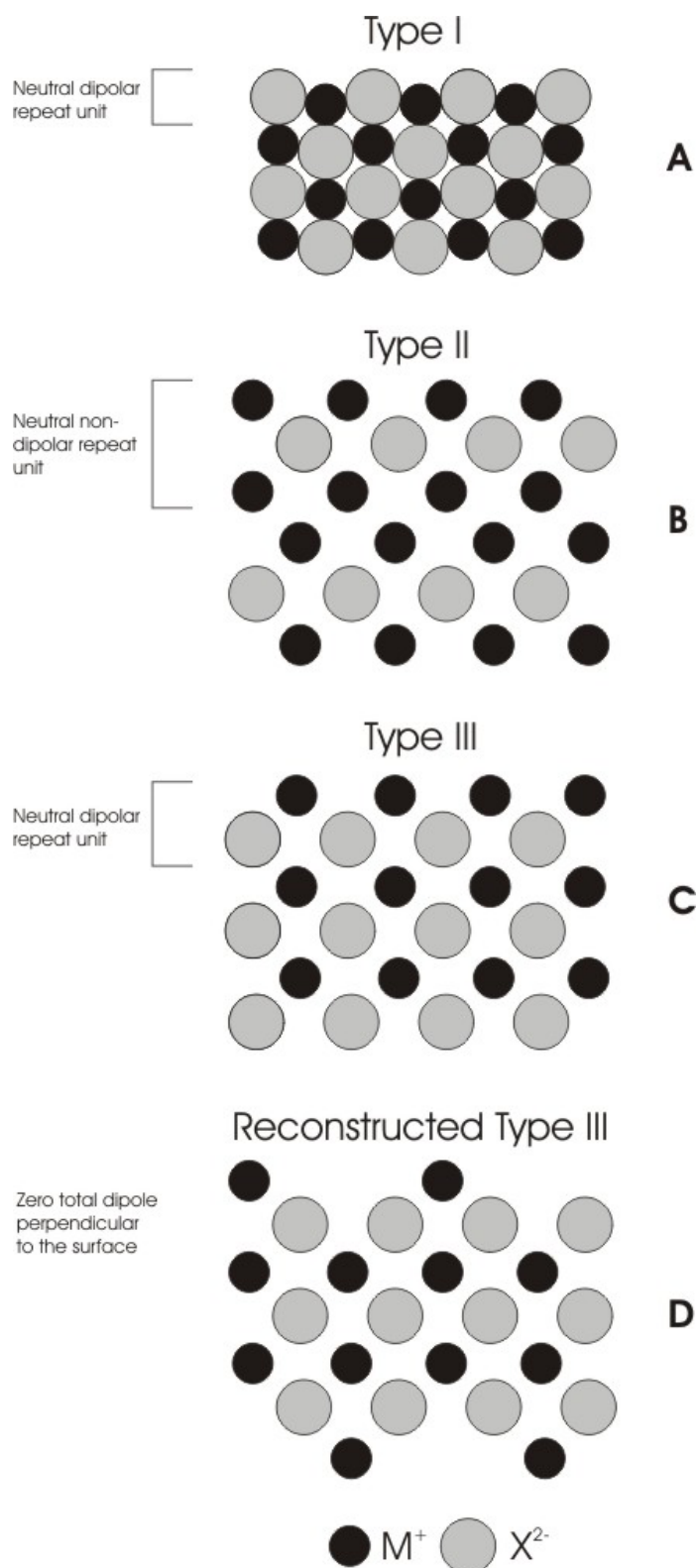
Figure 6.4. Idealised stacking sequences for the three types of crystal surfaces identified under the Tasker notation. (a) Type I surfaces consist of charge neutral layers of positive and negative ions, and (b) type II surfaces consist of positively and negatively charged planes but with a charge neutral and non-dipolar repeat unit. (c) Type III surfaces consist of alternating layers of positive and negative ions giving rise to a dipolar repeat unit, and a reconstructed type III surface (d) where half the surface ions have been shifted to the bottom of the unit cell, which has removed the dipole in the repeat unit (from de Leeuw et al. 2003).

A type II surface has a stacking sequence of charged planes but the repeat unit consists of several planes in a symmetrical configuration and as a result, there is a zero dipole moment perpendicular to the surface (Figure 6.4b). Consequently, type I and type II surfaces have a zero dipole moment perpendicular to the surface (de Leeuw et al. 2003).

The third type of surface (type III) is made up of a stack of alternately charged planes (Figure 6.4c), producing a dipole moment perpendicular to the surface. Bertaut (1958) showed that when such a dipole moment is present in the unit cell, the surface energy diverges and is infinite (de Leeuw et al. 2003). To study this type of surface the dipole needs to be removed, typically through some process of surface reconstruction. One way of achieving this is to remove half the ions from the surface layer at the top of the repeat unit and transfer them to the bottom (Figure 6.4d). Once a surface is generated that has no dipole moment perpendicular to the surface, the surface energy can be calculated (de Leeuw et al. 2003).

6.5   Surface study of potassium jarosite

Experimental SEM and AFM morphology studies of synthetic potassium jarosite show that the crystals are predominantly terminated by the most stable {012} faces. Triangular (001) faces are seen but most of them disappear in favour of the {012} faces in larger crystals (Becker and Gasharova 2001). Two-dimensional simulations of the potassium jarosite surfaces were made through the MARVIN code (version 2.00 beta 3) using the optimised structure 4 model of the potassium jarosite described earlier.

The work of Becker and Gasharova (2001) on simulating potassium jarosite surfaces found that zero net dipoles were present on both the {012} and (001) faces, however, this study found no dipoles for two surface terminations in the {012} faces. All possible terminations on the (001) face required surface reconstruction to remove a dipole. Therefore in this study, the investigation of the surfaces of potassium jarosite will be limited to these two terminations in the {012} faces.
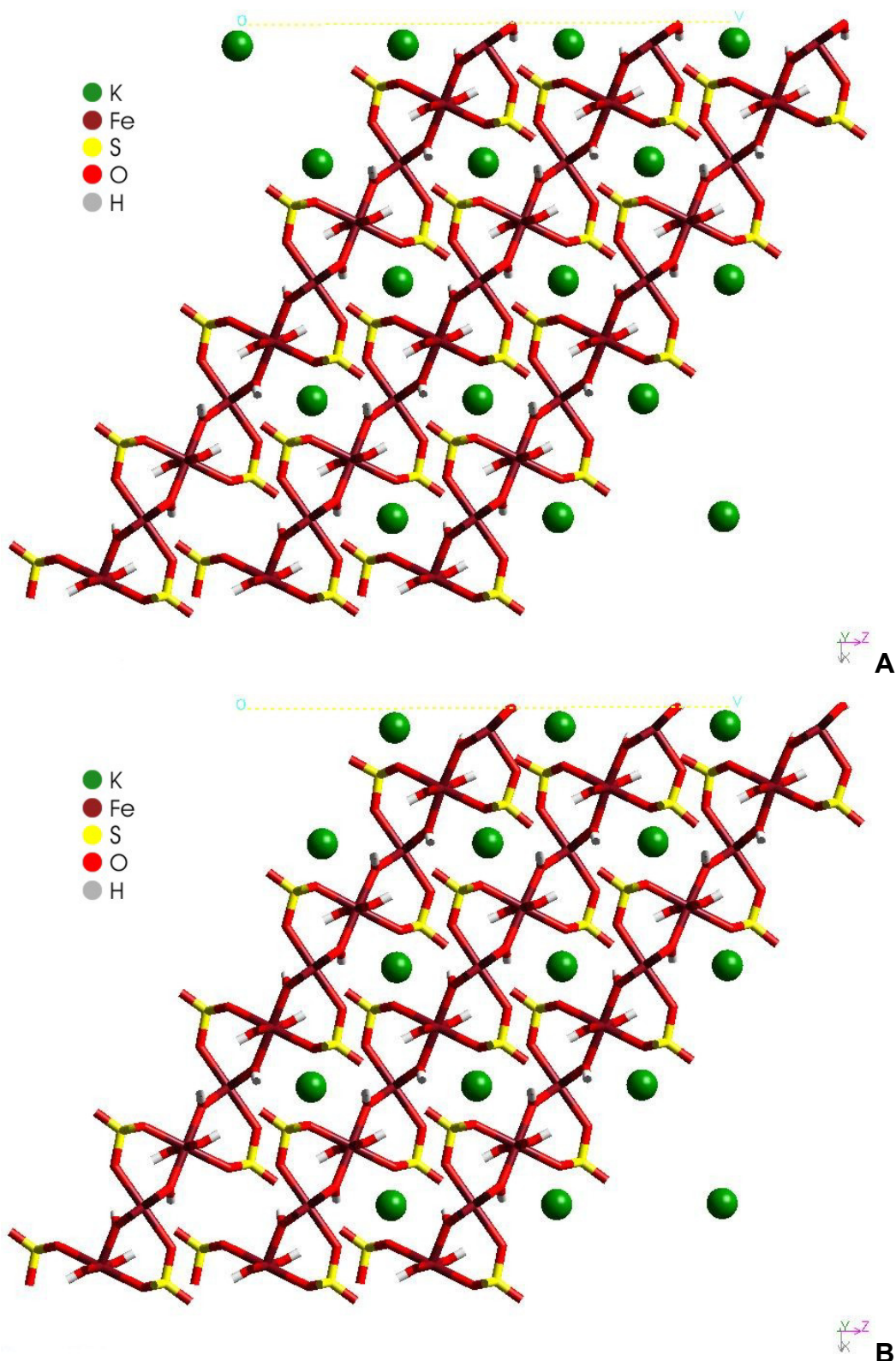
Figure 6.5. X – Z axes cut of the face 1 termination of {012} group of faces of potassium jarosite. The surface comprises of neutral sub-layers with the composition of $[KFe(OH)_4]^0$. Before relaxation (a) the surface is terminated by the O3 oxygens of the hydroxyl group and the K-ions in the A-site. Face 1 experiences a degree of rotation of the T-O-T during surface relaxation (b). The resulting rotation upon relaxation results in face 1 being terminated by K-ions and the hydrogen ions of the hydroxyl group.
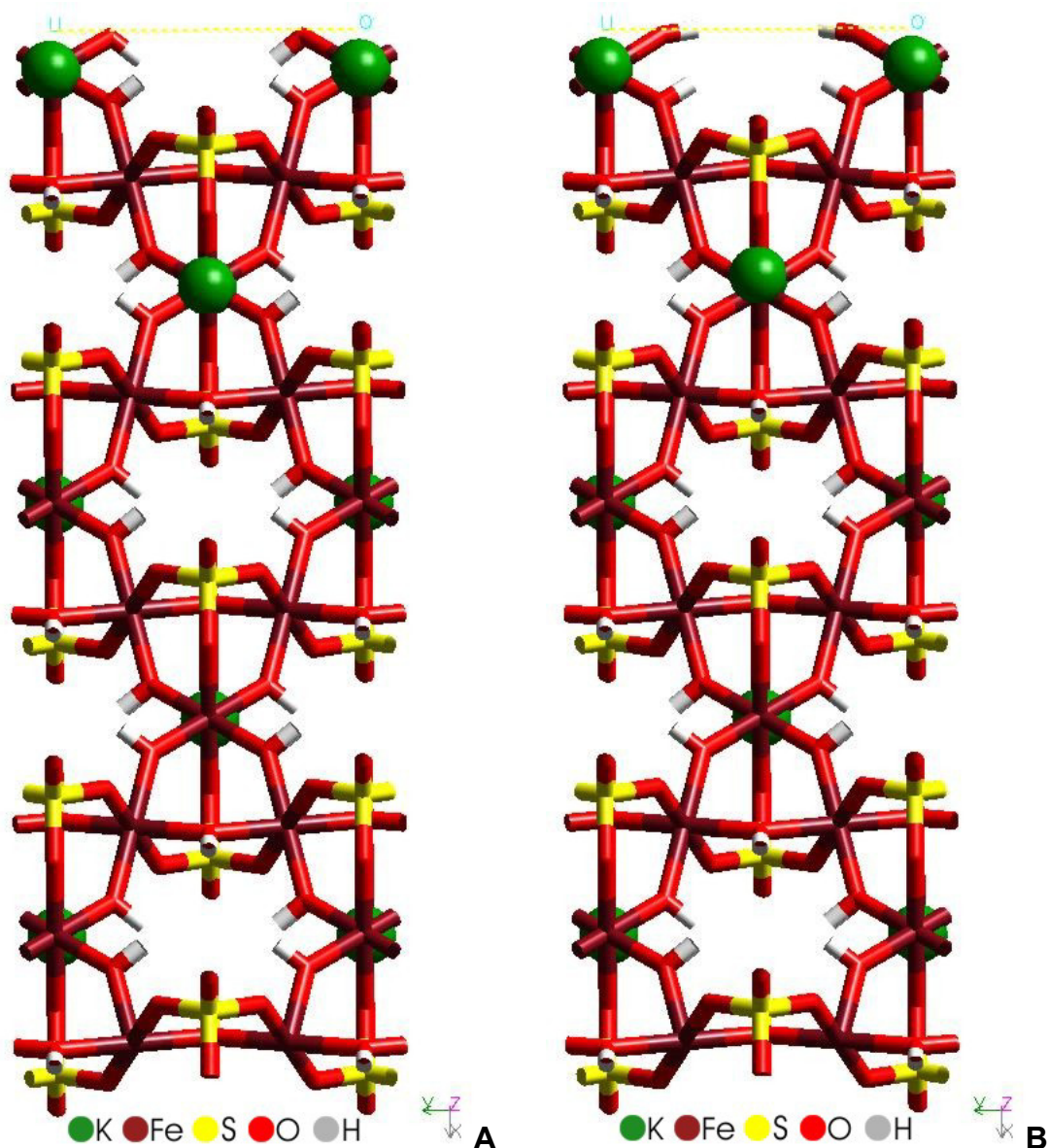
Figure 6.6. X – Y axes cut of the face 1 termination of {012} group of faces of potassium jarosite. The surface comprises of neutral sub-layers with the composition of $[KFe(OH)_4]^0$. The un-relaxed surface (a) is terminated by the O3 oxygens of the hydroxyl group and the K-ions in the A-site. Face 1 experiences a degree of rotation of the T-O-T during surface relaxation (b). After relaxation the hydroxyl group rotates upwards causing the relaxation surface of face 1 being terminated by the hydrogen ions of the hydroxyl group and the K-ions.

The two surfaces were created by the MARVIN code simulated under vacuum at absolute zero, where region I and region II were 2 and 5 unit cells, respectively. Face 1 and face 2, as they will be referred to henceforth, are both classed as type II surfaces under the Tasker notation (Figure 6.4b). The two surfaces are comprised of neutral sub-layers with compositions of $[KFe(OH)_4]^0$ (face 1) and $[Fe_2(SO_4)_2(OH)_2]^0$ (face 2), respectively. As each of the sub-layers had no dipole moment perpendicular to the surface, there was no dipole moment across either slab normal to surface.
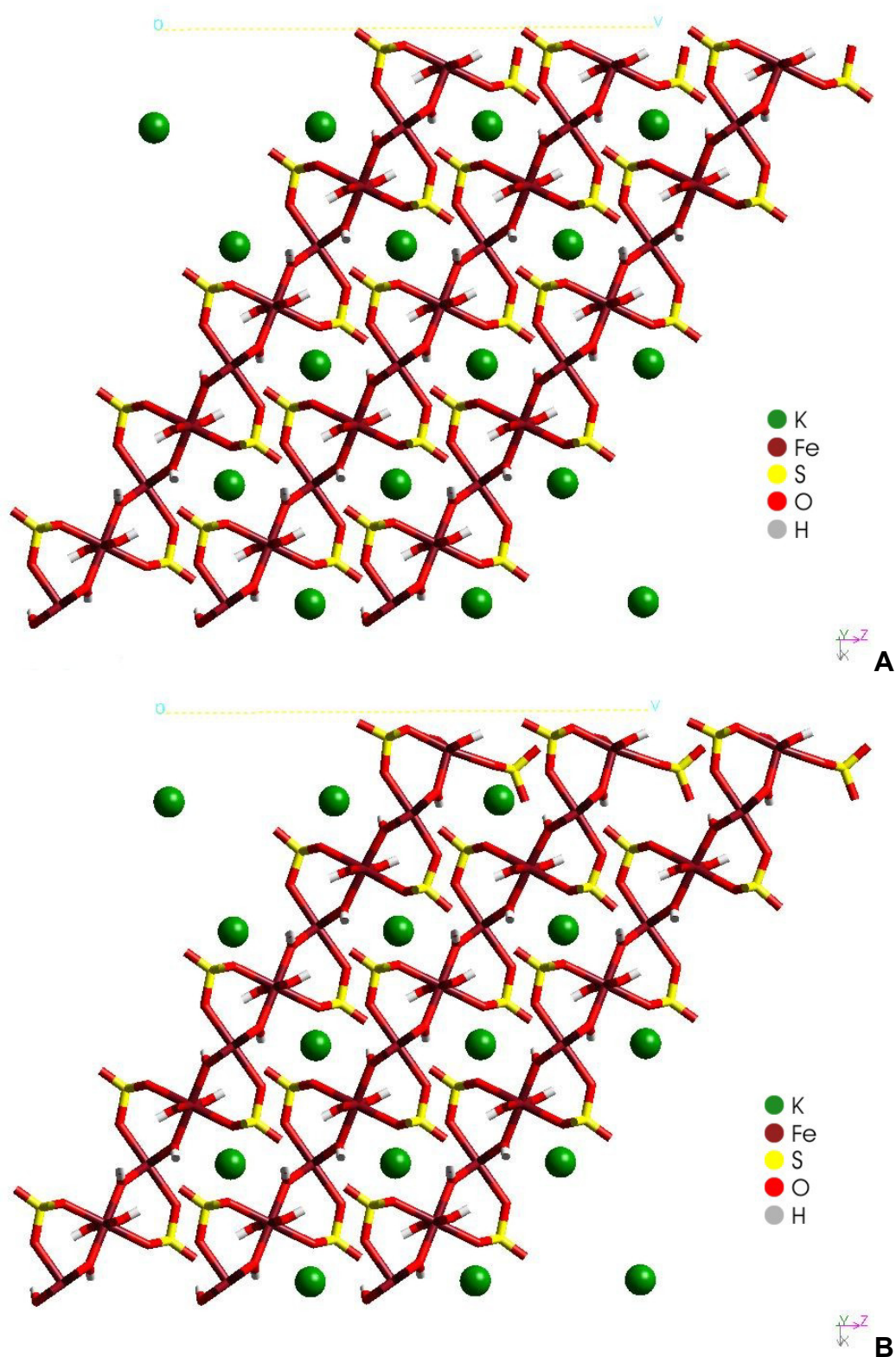
Figure 6.7. X – Z axes cut of the face 2 termination of {012} group of faces of potassium jarosite. The surface comprises of neutral sub-layers with the composition of $[Fe_2(SO_4)_2(OH)_2]^0$. Before relaxation (a) the surface is terminated by the O1 oxygens of the sulphate group. Face 2 experiences a degree of rotation of the T-O-T during surface relaxation (b). The resulting rotation upon relaxation results in the sulphate tetrahedra being rotated inwards into the slab resulting in the O1 oxygens lying just below the termination surface of face 2.
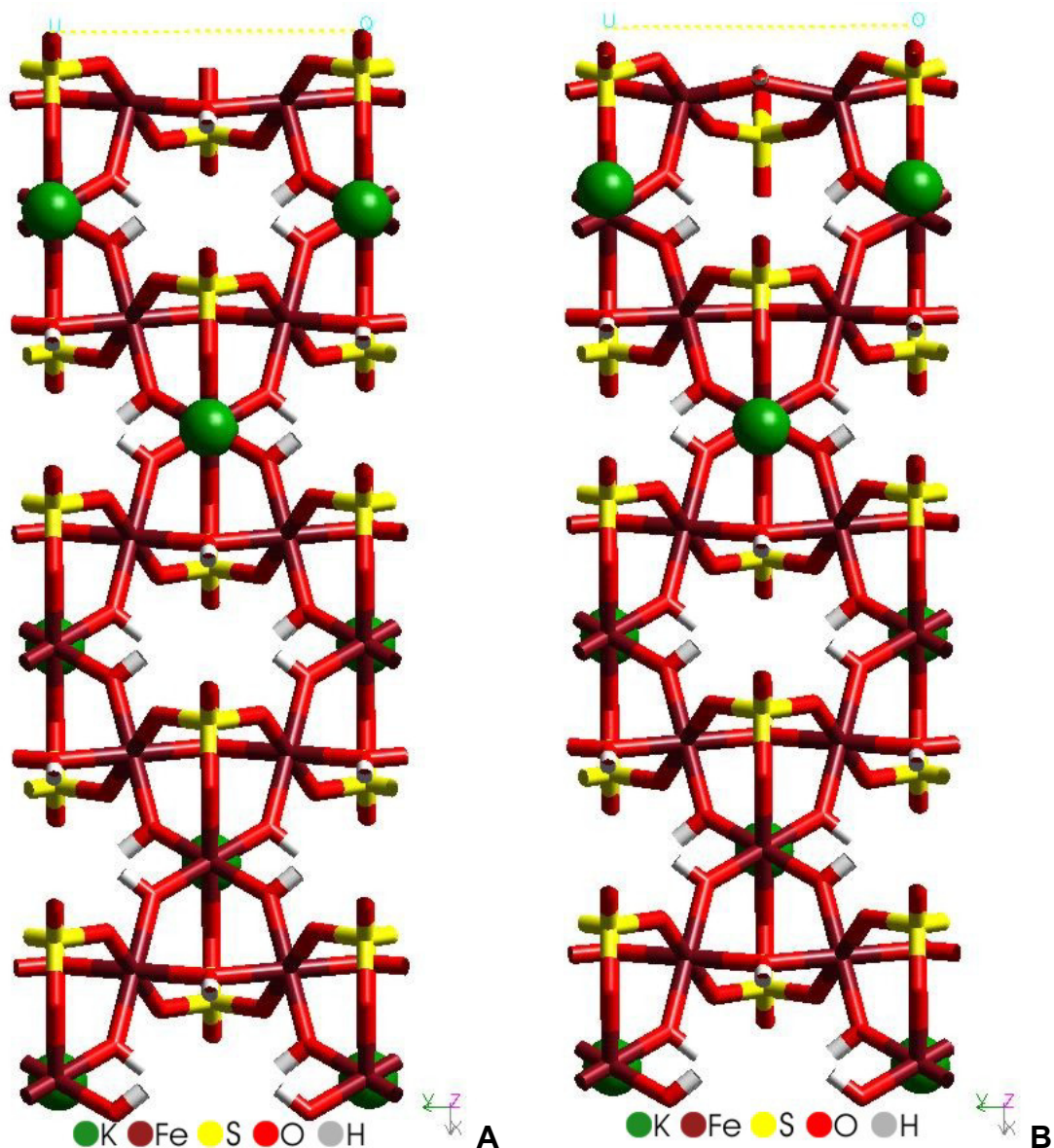
Figure 6.8. X – Y axes cut of the face 2 termination of {012} group of faces of potassium jarosite. The surface comprises of neutral sub-layers with the composition of $[Fe_2(SO_4)_2(OH)_2]^0$. The un-relaxed surface (a) is terminated by the O1 oxygens of the sulphate group. Face 2 experiences a degree of rotation of the T-O-T during surface relaxation (b). The resulting rotation upon relaxation results in the sulphate tetrahedra being rotated resulting in the O1 oxygens lying just below the termination surface of face 2.

The unrelaxed (bulk-like) surfaces of face 1 and 2 can be seen in Figures 6.5a, 6.6a and 6.7a, 6.8a,.

During surface relaxation, the upper and lower sub-layers in both slabs (faces 1 and 2) are mainly affected by rotation (Figures 6.5b, 6.6b, and 6.7b, 6.8b). Before the slab was relaxed in face 1, the surface was terminated by the O3 oxygen atoms of the hydroxyl group and the K-ions in the A-site, where the hydrogen ions of the OH

group were pointing down into the plane; this is shown clearest in Figure 6.5a. During relaxation of the face 1 slab, the hydrogen ions of the hydroxyl group rotated upwards out towards the surface (Figure 6.6b). The resulting rotation during relaxation resulted in the face 1 surface being initially terminated by K-ions and O3 oxygen atoms, and terminated again by K-ions, but more significantly, by hydrogen ions of the hydroxyl group. As for face 2, before slab relaxation the O1 oxygens belonging to the sulphate group terminated the surface (Figures 6.7a and 6.8a). After the surface was relaxed, the sulphate tetrahedra rotated inwards into the slab, resulting in the O1 oxygens lying just below the surface (Figure 6.7b). Also affected by this rotation were the central hydroxyl groups (seen most clearly in Figures 6.8a,b); here the OH groups rotated upwards towards the surface. In the slab of face 2 the K-ions were well embedded in the bulk structure between the first and second sub-layers in region 1, quite far away in comparison to face 1.

Table 6.6. Unrelaxed and relaxed surface energies of the two stable surfaces in the {012} group of faces for potassium jarosite.

Surface	Unrelaxed [eV/Å]	Relaxed [eV/Å]
Face 1	2.07	1.22
Face 2	2.07	1.37

In terms of the energetics of the two surfaces before and after relaxation (Table 6.6), the un-relaxed values for faces 1 and 2 were the same at 2.07 eV/Å. After relaxation, the surface energies of face 1 and face 2 were 1.22 and 1.37 eV/Å, respectively. As both of the relaxed surface energies were similar, either face in the {012} group of faces could be favourable, with the possibility of a slight bias towards the termination in face 1 (K-ions and hydrogen ions belonging to the bridging hydroxyl groups).

6.6   Theory of modelling defect calculations

Many aspects of the physical properties of materials depend on the behaviour of point defects present in the material. These defects may be classed as vacancies, interstitials, or substitutional ions (Catlow 1999). The properties of point defects, which may be readily calculated, are their structure and energetics (formation energy, migration activation energy and association energy; Cormack 1999).

There are two widely used approaches for performing defect calculations on solids, the supercell, and the cluster methods, with or without embedding in the latter case

(Gale and Rohl 2003, Wright 2003). The supercell method is based on the extension of a bulk calculation. All the defect calculations for this study were bulk simulations, modelled in GULP, which uses a technique referred to as the Mott-Littleton method (Mott and Littleton 1938), after the authors of the pioneering work in the field (Gale and Rohl 2003).
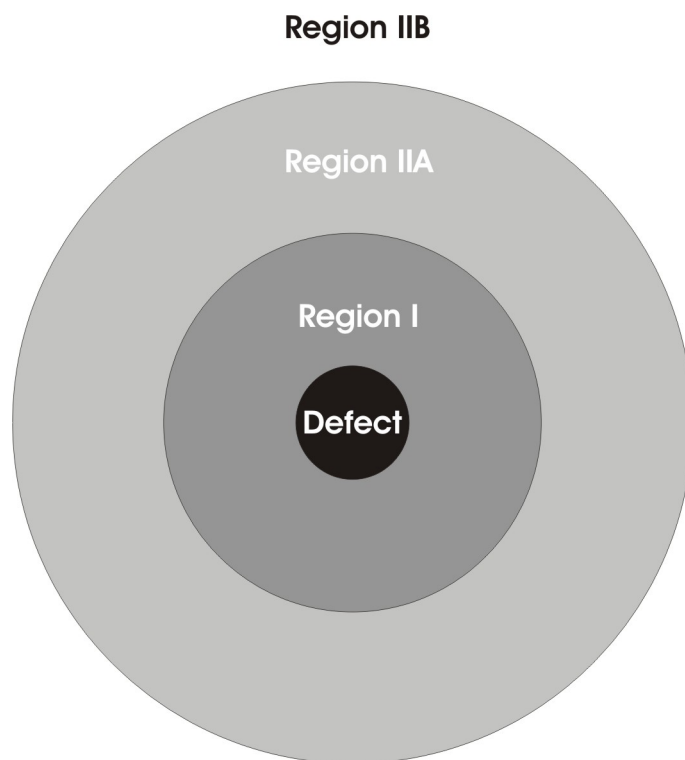
Figure 6.9. Schematic representation of the embedded regions used in the Mott-Littleton approach to defect calculations.

6.6.1 Mott-Littleton Method

In the Mott-Littleton method, the crystal around the defect centre is divided into two spherical regions, with the inner sphere labelled region I, and the outer sphere region IIa. Atoms outside of these spheres belong to region IIb that extends to infinity (Gale and Rohl 2003, Wright 2003) (Figure 6.9). In region I, which contains the defect at its centre, all interactions are treated exactly at an atomistic level and the ions are explicitly allowed to relax in response to the defect. Experience has shown that region I ought to contain 200-300 ions (Cormack 1999). In region IIa the ions are assumed to be situated in a harmonic well and they subsequently respond to the force of the defect accordingly (Catlow and Mackrodt 1982). This approximation is only valid for small perturbations and requires that the bulk lattice has been optimised prior

to the defect calculation. For region IIa individual ion displacements are still considered, whereas for region IIb only the polarisation of sub-lattices, rather than specific ions, are considered (Gale 1997). Region IIb is assumed to be sufficiently far from the defects that the ions only respond by polarising according to the electric field resulting from the total defect charge placed at the centre of region I.

Defect energetics are principally evaluated by performing a calculation on the perfect lattice, which may be equilibrated to either constant volume or pressure. The lattice energy, $E_{PERFECT}$, is then compared with the value, E_{DEFECT}, obtained under the same conditions for the defective lattice. Thus the defect formation energy, E_D, is simply written as (Catlow 2003):

$$E_D = E_{DEFECT} - E_{PERFECT} \qquad (6.10)$$

Within the Mott-Littleton scheme, it is possible to express the total energy for the formation of a defect (E_D), in a two-region system as the sum of contributions from the energies within the regions and between them given by (Wright et al. 1996, Gale et al. 2003):

$$E_D = E_1(x) + E_2(x, y) + E_3(y) \qquad (6.11)$$

where x and y are the coordinates of ions in region 1 and the displacements of ions in region 2 respectively. Parameter E_1 is the energy of the interaction of atoms in region 1, E_3 the energy of the ions in region 2, while E_2 describes the interaction between the regions. When y is small, as is usually assumed, E_3 can be expressed by the harmonic approximation (Wright et al. 1996):

$$E_3 = \frac{1}{2} y^T A y \qquad (6.12)$$

where A is the force constant matrix. At equilibrium we have (Wright et al. 1996):

$$dE_2 \frac{(x, y)}{dy} x = -Ay \qquad (6.13)$$

Thus, E_D can be expressed in terms of E_1 and E_2, and its derivates. The resulting defect energy is then a measure of the perturbation, by the defect, of the static lattice energy of the crystal (Wright et al. 1996).

6.6.2 Schottky and Frenkel defects

The nature of point defects in complex mineral structures is not well understood, and most of our basic ideas come from studies in simpler compounds such as halides, e.g. NaCl, AgCl (Putnis 1992). The simplest type of point defect is one in which a vacant cation in a structure is balanced by a vacant anion site to maintain charge neutrality. Such a pair of vacancies is called a Schottky defect, although the two vacancies are not necessarily directly associated with each other in any way (Catlow 1999). Figure 6.10a shows what a Schottky defect would look like schematically in a NaCl crystal. Another possible type of point defect occurs when an atom moves from a site, leaving a vacancy, and is placed in an alternative interstitial site that is normally unoccupied. This is a Frenkel defect and again leaves the overall charge balance and stoichiometry unaffected (Catlow 1999). Figure 6.10b shows a schematic diagram of a Frenkel defect in NaCl. For most close packed solids, Schottky defects have lower energy.

A   **B**
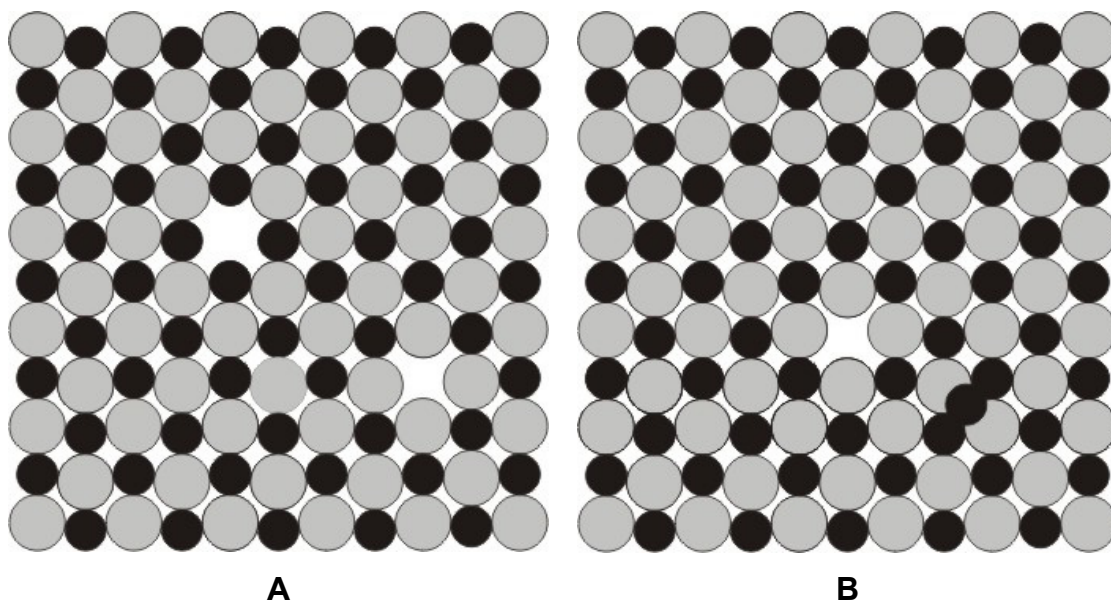
Figure 6.10. Schottky and Frenkel defects in NaCl. A Schottky defect (a) in NaCl consists of one cation and one anion vacancy. A Frenkel defect (b) in NaCl consists of a vacant cation site, with Na^+ ions occupying an interstial position in the ideal structure (from Putnis 1999).

Schottky and Frenkel defects are referred to as intrinsic defects as their numbers are controlled by intrinsic properties of the structure related to the size of the interatomic forces. The presence of impurities, variations in oxidation state for example, also

constitute defects, which are extrinsic and can vary from one crystal to another (Putnis 1992). All intrinsic and extrinsic defects in this study were described using the standard Kröger-Venk notation, Table 6.7 summarises the notation used with respect to the potassium jarosite structure (Kröger 1972).

Table 6.7. Kröger-Venk notation for defects in potassium jarosite [KFe$_3$(SO$_4$)$_2$(OH)$_6$] (Kröger 1972).

Intrinsic defects	
Fe vacancy with effective 3- charge	$V_{Fe}^{'''}$
O vacancy with effective 2+ charge	$V_O^{\bullet\bullet}$
K interstitial with effective 1+ charge	$K_i^{\bullet}$
Extrinsic defects	
Impurity (*e.g.* Cd) at interstitial site	$Cd_i^{\bullet\bullet}$
Neutral substitution. *e.g.* Na$^+$ at K$^+$ site	Na_K^X
Charged substitution *e.g.* Cd^{2+} at Fe^{3+} site	$Cd_{Fe}^{'}$
Charged substitution *e.g.* Cd^{2+} at K$^+$ site	$Cd_K^{\bullet}$

For Schottky and Frenkel disorder, charge neutrality and stoichiometry need to be maintained explicitly; in this study, series of partial Schottky defects are also considered by the use of charge neutral defect clusters. Schottky and Frenkel defects in NaCl are described using the standard Kröger-Venk notation in Eq. 6.14 and 6.15, respectively.

$$Na_{Na}^X + Cl_{Cl}^X \rightarrow V_{Na}^{'} + V_{Cl}^{\bullet} + NaCl_{(s)} \tag{6.14}$$

$$Na_{Na}^X \rightarrow V_{Na}^{'} + Na_i^{\bullet}$$
$$Cl_{Cl}^X \rightarrow V_{Cl}^{\bullet} + Cl_i^{'} \tag{6.15}$$
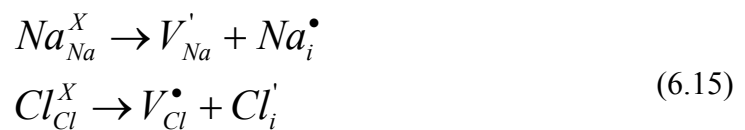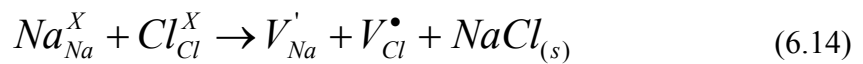
The defect formation energy of a Schottky defect is defined as:

$$E_{Schottky} = E_{V_1} + E_{V_2} + \dots E_{V_n} + U_L \tag{6.16}$$

where E$_V$ is the vacancy energy of a species, and U$_L$ corresponds to the lattice energy of the phase removed. The defect formation energy of a Frenkel defect is given in Eq. 6.17, where E$_V$ is the vacancy energy of the species, and E$_I$ is the interstial energy of the species.

$$E_{Frenkel} = E_V + E_I \qquad (6.17)$$

6.6.3 Impurity atoms and atomic substitutions

Minerals are never pure compounds and may contain a wide variety of substituted atoms. It is possible to treat these substitutions in much the same way as defects, in that there will be an equilibrium concentration of impurity atoms, which will depend upon the enthalpy and entropy associated with the substitution. Some minerals only allow small deviations from their pure endmember compositions, while in others there is a continuous solid solution between two extreme compositions (Putnis 1992).

6.7   Defect calculations in potassium jarosite

Two types of defects were considered and appraised for this study, intrinsic and extrinsic. Extrinsic defects were limited to three 2+ cations commonly observed in the structure and seen in ARD environments: Cd(II), Zn(II), and Cu(II) (Dutrizac 1984, Alpers et al. 1992, Dutrizac et al. 1996).

Table 6.8. Calculated vacancy formation and impurity substitution energies in potassium jarosite.

Intrinsic defects		Extrinsic defects	
Defect	Defect energy (eV)	Defect	Defect energy (eV)
$V_K^{'}$	4.76	$Cd_K^{\bullet}$	-10.92
$V_{Fe}^{'''}$	50.37	$Zn_K^{\bullet}$	-11.63
$V_S^{''''''}$	39.65	$Cu_K^{\bullet}$	-11.79
$V_O^{\bullet\bullet}$	24.47	$Cd_{Fe}^{'}$	26.40
$V_{OH}^{\bullet}$	28.34	$Zn_{Fe}^{'}$	23.73
$V_H^{'}$	12.17	$Cu_{Fe}^{'}$	24.25
$K_i^{\bullet}$	2.64	$Cd_i^{\bullet\bullet}$	-6.33
		$Zn_i^{\bullet\bullet}$	-7.59
		$Cu_i^{\bullet\bullet}$	-3.01

All the defect calculations for this study were bulk simulations, modelled using the Mott-Littleton approximation in GULP (version 1.3). Table 6.8 summarises the vacancy formation and impurity substitution energies within potassium jarosite, where these numbers were calculated using the potentials in Table 6.2. The lattice energies for the various compounds involved in the intrinsic and extrinsic defects are described

in Table 6.9, where their values were calculated using the potentials in Table 6.10. The impurities chosen for this study (Cd(II), Zn(II), and Cu(II)), all initially took the form of minerals commonly seen in ARD environments, notably oxides or sulphates (Alpers et al. 1992). Unfortunately, it was not possible to determine the lattice energies for these three cations as either all oxides or sulphates (Table 6.9). The six compounds labelled as products in Table 6.9 were chosen to represent various neutral vacancy defect clusters in the calculation of partial Schottky energies (Table 6.11), and as potential products of extrinsic defect reaction pathways (Tables 6.13-6.15). The product compounds in Table 6.9 either have been identified in ARD environments (e.g. goethite, Chapter 5) or have been associated with the thermal decomposition of the potassium jarosite structure (TG-DTA analysis, Chapter 3).

Table 6.9. Lattice energies of various reactants and products involved in the intrinsic and extrinsic defect reactions.

Compound	Lattice energy (eV)
Reactants	
CdO	-36.54
ZnO	-39.66
CuO	-40.65
$ZnSO_4$	-65.57
$CuSO_4$	-66.07
Products	
$KFe_3(SO_4)_2(OH)_6$	-357.37
$KFe(SO_4)_2$	-137.06
$FeO(OH)$	-82.14
Fe_2O_3	-152.37
K_2SO_4	-55.82
K_2O	-23.19

Altogether, the vacancy formation and impurity substitution energies combined with the lattice energies of numerous compounds were used to calculate a variety of Schottky energies (Table 6.11), and to study the various impurity substitution pathways in potassium jarosite (Tables 6.13-6.15).

6.7.1 Intrinsic defect reactions

As mentioned earlier, intrinsic defects can be broadly classed into either Schottky or Frenkel style defects. In this study, only Schottky defects or neutral vacancy defect clusters are considered, as no stable interstial sites for Fe or S could be found.

Table 6.10. Potential parameters for the various reactants and products involved in the intrinsic and extrinsic defect reactions.

Two-body short range interaction					
Buckingham	A/eV	ρ/Å	C/eV Å^6	Compound	Reference
$K^+ - O^{0.84-}$	987.570	0.3000	0.00	1, 2	a
$K^+ - O^{2-}$	987.570	0.3000	0.00	3	b
$Fe^{3+} - O^{0.84-}$	3219.335	0.2641	0.00	1	c
$Fe^{3+} - O^{2-}$	3219.335	0.2641	0.00	4, 5	d
$Fe^{3+} - O^{1.426-}$	2297.684	0.2641	0.00	5	b
$Cd^{2+} - O^{2-}$	868.3	0.3500	0.00	6	e
$Zn^{2+} - O^{0.84-}$	294.126	0.3372	0.00	8	c
$Zn^{2+} - O^{2-}$	499.6	0.3595	0.00	7	d
$Cu^{2+} - O^{0.84-}$	700.1988	0.3000	0.00	10	b
$Cu^{2+} - O^{2-}$	923.0467	0.3000	0.00	9	b
$O^{0.84-} - O^{0.84-}$	103585.02	0.2000	25.98	1, 2, 8, 10	f
$O^{2-} - O^{2-}$	103585.02	0.2000	25.98	3	b
$O^{2-} - O^{2-}$	22764.0	0.1490	27.88	5, 6, 7	d
$O^{2-} - O^{2-}$	25.410	0.6932	32.32	4, 9	d
$H^{0.426+} - O^{2-}$	511.0	0.2500	0.00	5	g
$H^{0.426+} - O^{1.426-}$	511.0	0.2500	0.00	5	g
Morse	D_e/eV	β/Å^{-1}	r_o/Å		
$S^{1.36+} - O^{0.84-}$	5.0000	1.2000	1.4650	1, 2, 8, 10	a
$O^{1.426-} - H^{0.426+}$	7.0525	2.1986	0.9685	5	h
Three-body interaction	k_3/eV rad^{-2}	θ/°			
$O^{0.84-} - S^{1.36+} - O^{0.84-}$	15.0	109.47		1, 2, 8, 10	f

The short range potential cut-off was set to 10 Å

[a] fitted from Allan et al. (1993)
[b] fitted from Woodley et al. (1999)
[c] fitted from Lewis and Catlow (1985)
[d] Woodley et al. (1999)
[e] Lewis and Catlow (1985)
[f] Allan et al. (1993)
[g] Steele et al. (2002)
[h] fitted Saul et al. (1985)

Compound			
1	$KFe(SO_4)_2$	6	CdO
2	K_2SO_4	7	ZnO
3	K_2O	8	$ZnSO_4$
4	Fe_2O_3	9	CuO
5	FeO(OH)	10	$CuSO_4$

Using the vacancy formation energies (Table 6.8) coupled with the lattice energies of various strategic compounds (Table 6.9), the energetics of various intrinsic defect configurations were calculated. The results are given in Table 6.11. The dominant defect will be that with the lowest energy per point defect. The calculated formation energy of the stoichiometric $KFe_3(SO_4)_2(OH)_6$ Schottky defect was found to be 243.6 eV (9.37 eV per defect). The formation energies of neutral K_2O, Fe_2O_3, FeO(OH), K_2SO_4, and $KFe(SO_4)_2$ vacancy clusters that can form in a non-stoichiometric phase are also presented in Table 6.11. The lowest energy defect is the K_2O partial Schottky with a formation energy of 10.8 eV (3.6 eV per defect). This was close to the value of the K Frenkel defect energy of 7.4 eV (3.7 per defect). Studying the formation energies (and per defect value) for the five neutral vacancy defect clusters together in

Table 6.11, some interesting relationships begin to emerge. Firstly, defects were more likely on the K sublattice than on the Fe sublattice, while those involving the $(SO_4)^{2-}$ molecular ions were unfavourable. For Fe, the oxide complex had a lower formation energy per defect than the corresponding hydroxide by 0.9 eV. In general, all intrinsic defect formation energies were high, which meant that they would not be present in any appreciable amounts at ambient conditions. At high temperature, potassium jarosite breaks down to form K_2O (+700°C) and Fe_2O_3 (+900°C) (TG-DTA, Chapter 3), so that at high temperatures, such defects could be present. At low temperatures, it is more probable that extrinsic processes will form the majority of defects in potassium jarosite, where the charge imbalance introduced by impurities is compensated by the formation of vacancies or interstials.

Table 6.11. Schottky defect formation energies in potassium jarosite (the number in the brackets is the per defect value).

Schottky		ΔE (eV)
K_2O	$2E_{V_K} + E_{V_O} + U_{K_2O}$	10.8 (3.6)
Fe_2O_3	$2E_{V_{Fe}} + 3E_{V_O} + U_{Fe_2O_3}$	21.78 (4.36)
$FeO(OH)$	$E_{V_{Fe}} + E_{V_O} + E_{V_{OH}} + U_{FeO(OH)}$	21.04 (5.26)
K_2SO_4	$2E_{V_K} + E_{V_S} + 4E_{V_O} + U_{K_2SO_4}$	91.23 (13.03)
$KFe(SO_4)_2$	$E_{V_K} + E_{V_{Fe}} + 2E_{V_S} + 8E_{V_O} + U_{KFe(SO_4)_2}$	193.13 (16.09)
$KFe_3(SO_4)_2(OH)_6$	$E_{V_K} + 3E_{V_{Fe}} + 2E_{V_S} + 8E_{V_O} + 6E_{V_{OH}} + U_{KFe_3(SO_4)_2(OH)_6}$	243.60 (9.37)

No energetics were calculated for possible breakdown reactions (e.g. Eq. 6.18) of the potassium jarosite structure as there was a lack of data on the energetics of important aqueous species (e.g. $(OH)^-_{(aq)}$, $K^+_{(aq)}$, $SO_4^{2-}_{(aq)}$) (see Chapter 8: Conclusions and Recommendations for further work).

$$KFe_3(SO_4)_2(OH)_{6(s)} \rightarrow K^+_{(aq)} + 3Fe^{3+}_{(aq)} + 2SO_4^{2-}_{(aq)}$$
$$KFe_3(SO_4)_2(OH)_{6(s)} \rightarrow 2FeO(OH)_{(s)} + KFe(SO_4)_{2(s)} + 6(OH)^-_{aq}$$

(6.18)
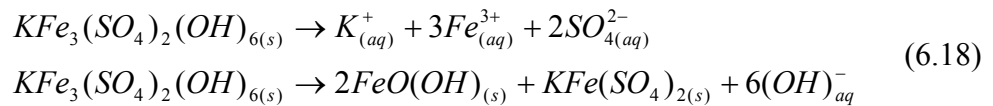
6.7.2 Extrinsic defect reactions

The three impurity cations were introduced in the form of solid oxide or sulphate reactants, specifically CdO, ZnO, CuO, $ZnSO_4$, and $CuSO_4$. The corresponding impurity substitution energies and lattice energies of the various reactants and

products are given in Tables 6.8 and 6.9, respectively. There are three locations for extrinsic defects in the potassium jarosite structure: the A- and B-site and interstial sites between the linear T-O-T sheets and the A-sites.

The impurity substitution energies for the three sites in Table 6.8 have been used to determine the energies of coupled substitution and reactions in the extrinsic regime. Coupled substitutions involving the three impurity cations at the A- and B-sites are given in Table 6.12, where the overall energy is reported per substitution. The results from the coupled substitutions in Table 6.12 suggest that Zn(II) is the most energetically favourable impurity substitution, followed closely behind by Cu(II), and finally Cd(II). This favourability of Zn(II) and Cu(II) is supported by experimental synthesis results, where Cu(II) is favoured over Zn(II) for higher % wt. incorporation in the generic jarosite structure (Dutrizac and Jambor 2000).

Table 6.12. Coupled substitution energies in potassium jarosite (the number in the brackets is the per substitution value).

Coupled Substitution		ΔE (eV)
$Cd_K^{\bullet} + Cd_{Fe}^{'}$	$E_{Cd_K^{\bullet}} + E_{Cd_{Fe}^{'}}$	15.48 (7.74)
$Zn_K^{\bullet} + Zn_{Fe}^{'}$	$E_{Zn_K^{\bullet}} + E_{Zn_{Fe}^{'}}$	12.1 (6.05)
$Cu_K^{\bullet} + Cu_{Fe}^{'}$	$E_{Cu_K^{\bullet}} + E_{Cu_{Fe}^{'}}$	12.46 (6.23)

It is possible to improve upon the information gathered from the coupled substitutions by considering the energetics of full mass and charge balance defect reactions. Such reactions are presented in Tables 6.13-6.15; Table 6.13 also includes a worked example upon how to calculate the overall defect energy of an extrinsic reaction. Initially it was not possible to calculate any defect reactions involving $CdSO_4$ as a reactant as no suitable lattice energy for this compound could be calculated. When all the extrinsic reaction pathways are compared across Tables 6.13-6.15 it is apparent that there are more reactions involving oxide phases than sulphate ones by just over a factor of two. The apparent lack of reactions for the sulphate reactants can be explained simply by the inherent requirement of either, or sometimes both, Fe and S interstials. As mentioned earlier with respect to the lack of any Frenkel defect reactions, interstials of these two critical ions in the T-O-T structure of potassium jarosite are extremely unfavourable and, therefore, unlikely. The problem with the lack of Fe and S interstials also accounts for the incomplete 'suite' of five reaction

pathways for extrinsic defects at the Fe-site, compared to defects at the K-site and as an interstial, when ultimately the defect reactant is in the form of an oxide (Tables 6.13-6.15).

Table 6.13. Reaction energies for series of Cd(II) extrinsic defects; the most significant energy reaction pathways are highlighted in bold. A worked example is also included.

Worked example for calculating the energy of an extrinsic defect reaction:

$$K_K^X + Fe_{Fe}^X + 2S_S^X + 7O_O^X + CdO_{(s)} \rightarrow Cd_K^{\bullet} + V_{Fe}^{'''} + 2V_S^{'''''} + 7V_O^{\bullet\bullet} + KFe(SO_4)_{2(s)}$$

$$\Delta E_{react} = E\ Cd_K^{\bullet} + E\ V_{Fe}^{'''} + E\ 2V_S^{'''''} + E\ 7V_O^{\bullet\bullet} + U_{KFe(SO_4)_{2(s)}} - U_{CdO_{(s)}}$$
$$\Delta E_{react} = (-10.92) + 50.37 + (2 \times 39.65) + (7 \times 24.47) + (-137.06) - (-36.54)$$
$$\Delta E_{react} = 189.52 eV$$

Defect	Reaction	ΔE_{react} (eV)
$Cd_K^{\bullet}$	$K_K^X + Fe_{Fe}^X + 2S_S^X + 7O_O^X + CdO_{(s)} \rightarrow Cd_K^{\bullet} + V_{Fe}^{'''} + 2V_S^{'''''} + 7V_O^{\bullet\bullet} + KFe(SO_4)_{2(s)}$	189.52
	$K_K^X + Fe_{Fe}^X + OH_{OH}^X + CdO_{(s)} \rightarrow Cd_K^{\bullet} + K_i^{\bullet} + V_{Fe}^{'''} + V_{OH}^{\bullet} + FeO(OH)_{(s)}$	26.95
	$2K_K^X + S_S^X + 3O_O^X + CdO_{(s)} \rightarrow Cd_K^{\bullet} + V_K^{'} + V_S^{'''''} + 3V_O^{\bullet\bullet} + K_2SO_{4(s)}$	**87.62**
	$2Fe_{Fe}^X + 2O_O^X + CdO_{(s)} \rightarrow Cd_K^{\bullet} + K_i^{\bullet} + 2V_{Fe}^{'''} + 2V_O^{\bullet\bullet} + Fe_2O_{3(s)}$	25.57
	$2K_K^X + CdO_{(s)} \rightarrow Cd_K^{\bullet} + V_K^{'} + K_2O_{(s)}$	**7.19**
$Cd_{Fe}^{'}$	$K_K^X + Fe_{Fe}^X + 2S_S^X + 7O_O^X + CdO_{(s)} \rightarrow Cd_{Fe}^{'} + V_K^{'} + 2V_S^{'''''} + 7V_O^{\bullet\bullet} + KFe(SO_4)_{2(s)}$	**181.23**
	$Fe_{Fe}^X + OH_{OH}^X + CdO_{(s)} \rightarrow Cd_{Fe}^{'} + V_{OH}^{\bullet} + FeO(OH)_{(s)}$	**9.14**
	$2Fe_{Fe}^X + O_O^X + 2CdO_{(s)} \rightarrow 2Cd_{Fe}^{'} + V_O^{\bullet\bullet} + Fe_2O_{3(s)}$	**-2.02**
$Cd_i^{\bullet\bullet}$	$K_K^X + Fe_{Fe}^X + 2S_S^X + 7O_O^X + CdO_{(s)} \rightarrow Cd_i^{\bullet\bullet} + V_K^{'} + V_{Fe}^{'''} + 2V_S^{'''''} + 7V_O^{\bullet\bullet} + KFe(SO_4)_{2(s)}$	198.87
	$Fe_{Fe}^X + OH_{OH}^X + CdO_{(s)} \rightarrow Cd_i^{\bullet\bullet} + V_{Fe}^{'''} + V_{OH}^{\bullet} + FeO(OH)_{(s)}$	26.78
	$2K_K^X + S_S^X + 3O_O^X + CdO_{(s)} \rightarrow Cd_i^{\bullet\bullet} + 2V_K^{'} + V_S^{'''''} + 3V_O^{\bullet\bullet} + K_2SO_{4(s)}$	96.97
	$2Fe_{Fe}^X + 2O_O^X + CdO_{(s)} \rightarrow Cd_i^{\bullet\bullet} + 2V_{Fe}^{'''} + 2V_O^{\bullet\bullet} + Fe_2O_{3(s)}$	27.52
	$2K_K^X + CdO_{(s)} \rightarrow Cd_i^{\bullet\bullet} + 2V_K^{'} + K_2O_{(s)}$	16.54

When comparing all the defect reactions for Cd(II), Zn(II), and Cu(II) together, presented in Tables 6.13-6.15, respectively, some general trends appear; where the most significant reaction energies are highlighted in bold. Reactions with all three divalent impurity cations, Cd(II), Zn(II), Cu(II), were most favourable when these cations replaced Fe and were charge balanced with an O vacancy. In all cases, reactions with mixed K/Fe vacancy pairs had the highest energies; seen in reactions that had KFe(SO$_4$)$_2$ as a product.

Table 6.14. Reaction energies for series of Zn(II) extrinsic defects; the most significant energy reaction pathways are highlighted in bold.

Defect	Reaction	ΔE_{react} (eV)
$Zn_K^\bullet$	$K_K^X + Fe_{Fe}^X + 2S_S^X + 7O_O^X + ZnO_{(s)} \rightarrow Zn_K^\bullet + V_{Fe}''' + 2V_S''''' + 7V_O^{\bullet\bullet} + KFe(SO_4)_{2(s)}$	191.63
	$K_K^X + Fe_{Fe}^X + OH_{OH}^X + ZnO_{(s)} \rightarrow Zn_K^\bullet + K_i^\bullet + V_{Fe}''' + V_{OH}^\bullet + FeO(OH)_{(s)}$	27.24
	$2K_K^X + S_S^X + 3O_O^X + ZnO_{(s)} \rightarrow Zn_K^\bullet + V_K' + V_S''''' + 3V_O^{\bullet\bullet} + K_2SO_{4(s)}$	90.03
	$2Fe_{Fe}^X + 2O_O^X + ZnO_{(s)} \rightarrow Zn_K^\bullet + K_i^\bullet + 2V_{Fe}''' + 2V_O^{\bullet\bullet} + Fe_2O_{3(s)}$	27.98
	$2K_K^X + ZnO_{(s)} \rightarrow Zn_K^\bullet + V_K' + K_2O_{(s)}$	**9.60**
Zn_{Fe}'	$K_K^X + Fe_{Fe}^X + 2S_S^X + 7O_O^X + ZnO_{(s)} \rightarrow Zn_{Fe}' + V_K' + 2V_S''''' + 7V_O^{\bullet\bullet} + KFe(SO_4)_{2(s)}$	181.68
	$Fe_{Fe}^X + OH_{OH}^X + ZnO_{(s)} \rightarrow Zn_{Fe}' + V_{OH}^\bullet + FeO(OH)_{(s)}$	**9.59**
	$2Fe_{Fe}^X + O_O^X + 2ZnO_{(s)} \rightarrow 2Zn_{Fe}' + V_O^{\bullet\bullet} + Fe_2O_{3(s)}$	**-1.12**
$Zn_i^{\bullet\bullet}$	$K_K^X + Fe_{Fe}^X + 2S_S^X + 7O_O^X + ZnO_{(s)} \rightarrow Zn_i^{\bullet\bullet} + V_K' + V_{Fe}''' + 2V_S''''' + 7V_O^{\bullet\bullet} + KFe(SO_4)_{2(s)}$	200.73
	$Fe_{Fe}^X + OH_{OH}^X + ZnO_{(s)} \rightarrow Zn_i^{\bullet\bullet} + V_{Fe}''' + V_{OH}^\bullet + FeO(OH)_{(s)}$	28.64
	$2K_K^X + S_S^X + 3O_O^X + ZnO_{(s)} \rightarrow Zn_i^{\bullet\bullet} + 2V_K' + V_S''''' + 3V_O^{\bullet\bullet} + K_2SO_{4(s)}$	98.38
	$2Fe_{Fe}^X + 2O_O^X + ZnO_{(s)} \rightarrow Zn_i^{\bullet\bullet} + 2V_{Fe}''' + 2V_O^{\bullet\bullet} + Fe_2O_{3(s)}$	29.38
	$2K_K^X + ZnO_{(s)} \rightarrow Zn_i^{\bullet\bullet} + 2V_K' + K_2O_{(s)}$	18.40
$Zn_K^\bullet$	$K_K^X + Fe_{Fe}^X + S_S^X + 4O_O^X + ZnSO_{4(s)} \rightarrow Zn_K^\bullet + V_{Fe}''' + V_S''''' + 4V_O^{\bullet\bullet} + KFe(SO_4)_{2(s)}$	104.78
	$2K_K^X + ZnSO_{4(s)} \rightarrow Zn_K^\bullet + V_K' + K_2SO_{4(s)}$	**2.88**
Zn_{Fe}'	$2K_K^X + Fe_{Fe}^X + S_S^X + 4O_O^X + ZnSO_{4(s)} \rightarrow Zn_{Fe}' + K_i^\bullet + 2V_K' + V_S''''' + 4V_O^{\bullet\bullet} + KFe(SO_4)_{2(s)}$	101.93
$Zn_i^{\bullet\bullet}$	$K_K^X + Fe_{Fe}^X + 2ZnSO_{4(s)} \rightarrow 2Zn_i^{\bullet\bullet} + V_K' + V_{Fe}''' + KFe(SO_4)_{2(s)}$	**34.03**
	$2K_K^X + ZnSO_{4(s)} \rightarrow Zn_i^{\bullet\bullet} + 2V_K' + K_2SO_{4(s)}$	11.68

The data in Tables 6.13-6.15, specifically regarding the Fe site defect would suggest that Cd(II) was the most energetically favourable impurity substitution, followed by Zn(II) and then Cu(II). This order where Cd(II) was the most favourable of the three cations is the compete opposite to what was seen for the coupled substitutional data earlier and more importantly to what is seen in nature and in the laboratory (Dutrizac and Jambor 2000). A specific reason for this trend is unclear at present, though will probably be related to the partial rather than total occupancy these impurity cations have at the Fe-site in natural and synthetic samples. When the Zn(II) and Cu(II) cations were introduced in the form of sulphates it appeared that the most

energetically favourable pathways were ones where sulphate rich products were formed (i.e $KFe(SO_4)_2$ and K_2SO_4) (Table 6.14-6.15). Specifically, the Zn(II) and Cu(II) cations in the form of sulphate reactants were found to favour defects at the K site coupled with another K vacancy rather than O vacancies (Table 6.14-6.15).

Table 6.15. Reaction energies for series of Cu(II) extrinsic defects; the most significant energy reaction pathways are highlighted in bold.

Defect	Reaction	ΔE_{react} (eV)
$Cu_K^\bullet$	$K_K^X + Fe_{Fe}^X + 2S_S^X + 7O_O^X + CuO_{(s)} \rightarrow Cu_K^\bullet + V_{Fe}^{'''} + 2V_S^{''''''} + 7V_O^{\bullet\bullet} + KFe(SO_4)_{2(s)}$	192.76
	$K_K^X + Fe_{Fe}^X + OH_{OH}^X + CuO_{(s)} \rightarrow Cu_K^\bullet + K_i^\bullet + V_{Fe}^{'''} + V_{OH}^\bullet + FeO(OH)_{(s)}$	28.07
	$2K_K^X + S_S^X + 3O_O^X + CuO_{(s)} \rightarrow Cu_K^\bullet + V_K^{'} + V_S^{''''''} + 3V_O^{\bullet\bullet} + K_2SO_{4(s)}$	90.86
	$2Fe_{Fe}^X + 2O_O^X + CuO_{(s)} \rightarrow Cu_K^\bullet + K_i^\bullet + 2V_{Fe}^{'''} + 2V_O^{\bullet\bullet} + Fe_2O_{3(s)}$	28.81
	$2K_K^X + CuO_{(s)} \rightarrow Cu_K^\bullet + V_K^{'} + K_2O_{(s)}$	**10.43**
$Cu_{Fe}^{'}$	$K_K^X + Fe_{Fe}^X + 2S_S^X + 7O_O^X + CuO_{(s)} \rightarrow Cu_{Fe}^{'} + V_K^{'} + 2V_S^{''''''} + 7V_O^{\bullet\bullet} + KFe(SO_4)_{2(s)}$	183.19
	$Fe_{Fe}^X + OH_{OH}^X + CuO_{(s)} \rightarrow Cu_{Fe}^{'} + V_{OH}^\bullet + FeO(OH)_{(s)}$	**11.10**
	$2Fe_{Fe}^X + O_O^X + 2CuO_{(s)} \rightarrow 2Cu_{Fe}^{'} + V_O^{\bullet\bullet} + Fe_2O_{3(s)}$	**1.90**
$Cu_i^{\bullet\bullet}$	$K_K^X + Fe_{Fe}^X + 2S_S^X + 7O_O^X + CuO_{(s)} \rightarrow Cu_i^{\bullet\bullet} + V_K^{'} + V_{Fe}^{'''} + 2V_S^{''''''} + 7V_O^{\bullet\bullet} + KFe(SO_4)_{2(s)}$	206.30
	$Fe_{Fe}^X + OH_{OH}^X + CuO_{(s)} \rightarrow Cu_i^{\bullet\bullet} + V_{Fe}^{'''} + V_{OH}^\bullet + FeO(OH)_{(s)}$	34.21
	$2K_K^X + S_S^X + 3O_O^X + CuO_{(s)} \rightarrow Cu_i^{\bullet\bullet} + 2V_K^{'} + V_S^{''''''} + 3V_O^{\bullet\bullet} + K_2SO_{4(s)}$	104.40
	$2Fe_{Fe}^X + 2O_O^X + CuO_{(s)} \rightarrow Cu_i^{\bullet\bullet} + 2V_{Fe}^{'''} + 2V_O^{\bullet\bullet} + Fe_2O_{3(s)}$	34.95
	$2K_K^X + CuO_{(s)} \rightarrow Cu_i^{\bullet\bullet} + 2V_K^{'} + K_2O_{(s)}$	23.97
$Cu_K^\bullet$	$K_K^X + Fe_{Fe}^X + S_S^X + 4O_O^X + CuSO_{4(s)} \rightarrow Cu_K^\bullet + V_{Fe}^{'''} + V_S^{''''''} + 4V_O^{\bullet\bullet} + KFe(SO_4)_{2(s)}$	105.12
	$2K_K^X + CuSO_{4(s)} \rightarrow Cu_K^\bullet + V_K^{'} + K_2SO_{4(s)}$	**3.22**
$Cu_{Fe}^{'}$	$2K_K^X + Fe_{Fe}^X + S_S^X + 4O_O^X + CuSO_{4(s)} \rightarrow Cu_{Fe}^{'} + K_i^\bullet + 2V_K^{'} + V_S^{''''''} + 4V_O^{\bullet\bullet} + KFe(SO_4)_{2(s)}$	102.95
$Cu_i^{\bullet\bullet}$	$K_K^X + Fe_{Fe}^X + 2CuSO_{4(s)} \rightarrow 2Cu_i^{\bullet\bullet} + V_K^{'} + V_{Fe}^{'''} + KFe(SO_4)_{2(s)}$	**44.19**
	$2K_K^X + CuSO_{4(s)} \rightarrow Cu_i^{\bullet\bullet} + 2V_K^{'} + K_2SO_{4(s)}$	16.76

The inference that 2+ impurity cations are theoretically more energetically favourable when occupying the octahedral 3+ B-site is extremely important, and fundamental, as this is the relationship that supports experimental data (Dutrizac 1984, Dutrizac et al. 1996) and in the natural environment in areas affected by ARD where jarosites are found (Dutrizac 1982, Dutrizac and Jambor 2000). Looking more closely at the

individual impurity substitution energies (Table 6.8) it becomes apparent that all the 2+ impurity ions chosen for this study do appear to be more energetically favourable in the K-site, than in the Fe-site. Though it is not until the correct mass and charge balance defect reactions (Tables 6.13-6.15) are made and calculated does the true picture start to develop, that is of the B-site (Fe-site) being more favourable to locate 2+ impurity cations in the general jarosite structure, seen through the potassium jarosite example in this study. Furthermore, the extrinsic defect reactions in Tables 6.13-6.15, combined with the knowledge that potassium jarosite has inherent Fe vacancies in its structure (the defect energy of such a vacancy is 50.37 eV, Table 6.8), may explain why natural or synthetic jarosites with compositions similar to $Cu_{0.5}Fe_3(SO_4)_2(OH)_6$ have not been found or synthesised (Dutrizac 1984). The answer is that these 2+ impurity cations will probably locate at the B-site in the structure to reduce the overall lattice energy.

6.8   Discussion and Summary

A very good classical potential model of potassium jarosite has been created through the structure 4 model, but there have been crucial limitations. Unfortunately it has not been possible to model any jarosites that incorporate Pb(II) into their structure, so the plumbojarosite, the beaverite compounds and beudantite investigated experimentally in this study could not be modelled. The reason is that it is quite difficult to create a Buckingham interatomic potential for Pb(II) due to the presence of a lone pair of electrons. Another problem that has been encountered is the lack of any hydronium (H_3O^+) representation in the potassium jarosite model; this is simply because at present, there is no widely available classical potential to represent this ion. Considering that hydronium is such an important species in the general jarosite structure in its ability to charge balance the A-site, the lack of any account of this species in any theoretical model is untoward when trying to relate the model of the structure to experimental and natural examples. Finally, it has not been possible to model and therefore fully appraise ferrihydrite, a poorly-ordered iron rich secondary phase that is common in ARD environments and that was found in the alkali dissolution of plumbojarosite and beudantite (Chapter 5). It is due to the amorphous nature of ferrihydrite that the problem has occurred; there are no reliable crystallographic lattice positions for this mineral.

One of the most important findings in relation to creating a classical potential model of potassium jarosite (structure 4) that is comparable to experimental results (Menchetti and Sabelli 1976) is the inclusion of an O3 – O3 Buckingham potential (Table 6.2). The addition of this potential helps to describe the oxygen interactions between adjacent and opposing hydroxyl groups that make up the hydroxyl bridging that bond the FeO_6 octahedrons to the T-O-T sheet (Figure 6.2). Becker and Gasharova (2001), the only workers who have published a model of the potassium jarosite structure, did not incorporate this additional O3 – O3 Buckingham potential and, the potentials and the cut-offs they used constrained their model very heavily to the structure to which it was fitted.

The 2D modelling of the potassium jarosite surfaces revealed two stable terminations that had no net dipoles belonging to the {012} group of faces. Both terminations could be described as type II surfaces under the Tasker notation (Figure 6.4b). The two terminations comprised of neutral sub-layers with compositions of $[KFe(OH)_4]^0$ (Figure 6.5a, 6.6a) and $[Fe_2(SO_4)_2(OH)_2]^0$ (Figure 6.7a, and 6.8a), respectively. During surface relaxation, the upper and lower sub-layers in both surfaces were mainly affected by rotation. After the surfaces were relaxed the $[KFe(OH)_4]^0$ surface was terminated by K-ions and the hydrogen ions of the hydroxyl groups (Figure 6.5b, 6.6b). The $[Fe_2(SO_4)_2(OH)_2]^0$ surface was terminated by the O1 oxygens of the sulphate tetrahedra lying just below the plane and an upwardly rotated hydroxyl group after relaxation (Figure 6.7b, and 6.8b). The implications for these rotations is that they could be prone to selective dissolution by polar water due to the high surface coverage of bonded and non-bonded oxygen atoms. Furthermore, due to their inherent structure selective dissolution of K-ions and sulphate groups near the surface could be cleaved easier during dissolution relative to stable FeO_6 octahedrons of the T-O-T sheet. Evidence of the selective dissolution of SO_4^{2-} groups can be seen in the SEM morphology micrograph for the acidic dissolution of plumbojarosite (Figure 4.15). Gasharova et al. (2001) have also reported similar selective dissolution of K-ions and sulphate groups on a potassium jarosite surface.

As mentioned earlier it was not possible to calculate Frenkel defects within the potassium jarosite structure due to the profound difficulties of calculating reliable interstials, especially for Fe and S ions, hence, this study primarily concentrated on

Schottky intrinsic defects. The formation energies for series of partial Schottky reactions indicated that defects were more likely on the K sublattice than on the Fe sublattice, while those involving the $(SO_4)^{2-}$ molecular ion were unfavourable (Table 6.11). Even though these three impurity cations had favourable point defect energies for potassium A-site substitutions, it emerged through mass and charge balance calculations that these 2+ cations were more likely to be most energetically favourable in substituting in the iron B-site (Tables 6.8, 6.13-6.15). Overall the presence of Fe vacancies in natural and experimental structures, and the system's ability to reduce the overall lattice energy by 2+ cations occupying the B-site may help to explain the non-existence of endmember jarosites such as $Cu_{0.5}Fe_3(SO_4)_2(OH)_6$.

7   Discussion

Chapter 7 provides an overall discussion, integrating results from the experimental and computational studies. The chapter has three broad sections: (i) appraisal of the fundamental properties of the jarosite structure, (ii) insights from the acid and alkali dissolution experiments, and (iii) the implications of jarosite breakdown mechanisms and products on the natural environment.

7.1   Appraisal of the fundamental properties of the jarosite structure

Jarosites are members of the alunite supergroup consisting of isostructural minerals described by the general formula $AB_3(TO_4)_2(OH)_6$ (Jambor 1999). The most fundamental parts of the jarosite structure are the linear tetrahedral-octahedral-tetrahedral (T-O-T) sheets, made up from slightly distorted BO_6 octahedrons and TO_4 tetrahedrons. The B ions are usually Fe(III), the A-site ions are commonly univalent cations (e.g. K^+, Na^+, H_3O^+), though the jarosite structure can accommodate divalent cations [Pb(II) or Hg(II)] in this site too. The TO_4^{2-} unit is usually SO_4^{2-} or in some cases AsO_4^{3-} (e.g. beudantite). Each octahedron has four bridging hydroxyl groups in a plane, and sulphate oxygen atoms at the apices. Three of the tetrahedra oxygen atoms are coordinated to metals ions (B), and the symmetry of the TO_4^{2-} tetrahedra is reduced from T_d to C_{3v}. The metal ions are joined by these TO_4^{2-} tetrahedra and by the network of di-hydroxyl bridges to form sheets separated by the uncoordinated sulphate oxygen atom and the alkali A-site cations (Jambor 1999, Becker and Gasharova 2001). The key relationships in the jarosite structure can be seen in Figures 1.2, 6.1, and 6.2.

Well-documented structural anomalies present within both synthetic and natural jarosites are Fe(III) vacancies. The degree of Fe deficiency within the lattice can be determined through the $Fe:SO_4$ molar ratio, where the ideal stoichiometry is 3:2 (Kubisz 1970, Alpers et al. 1989). Typically, the $Fe:SO_4$ molar ratio is significantly lower than the ideal, with values as low as 2.33:2 (Ripmeester et al. 1986) and 2.20:2 to 2.57:2 (Härtig et al. 1984) reported. Computational results show that an Fe vacancy has an extremely large positive vacancy formation energy (50.37 eV, Table 6.8), which might explain why no natural or synthetic jarosites of composition similar

to $Cu_{0.5}Fe_3(SO_4)_2(OH)_6$ have ever been found or made before (Dutrizac, 1984). The results from the computer modelling of the potassium jarosite structure suggest that 2+ impurity ions such as Cu or Zn will quite happily locate in the A-site of the general jarosite structure energetically, but jarosites reduce the overall unfavourable lattice energy resultant from the inherent Fe vacancies by occupying these 2+ metal cations in distorted octahedral B-sites

It has not been possible to computationally model any jarosites that incorporate Pb(II) The reason is that it is not possible to create a Buckingham interatomic potential for Pb(II) due to its lone pair of electrons. Another problem that has been encountered is the lack of any hydronium (H_3O^+) representation in the potassium jarosite model. Considering that hydronium is such an important species in the jarosite structure due to its ability to charge balance the A-site, the lack of this species in any theoretical model is unfortunate when attempting to relate the model of the structure to experimental and natural examples.

All the synthetic jarosites prepared for this study were found to be phase pure, where all their reflections matched those of the ICDD PDF standards. The absence of unidentified peaks in the five patterns indicated that no other phases were present at detectable levels. The five jarosites can be broadly divided into two groups. The first group solely contains potassium jarosite; in this structure, univalent K ions occupy the A-site. The second group contains four Pb(II)-bearing jarosites, plumbojarosite, beaverite-Cu and –Zn and beudantite. In the second group, the A-site is occupied with divalent Pb(II) ions. A common substitution in both natural and synthetic jarosites is hydronium (H_3O^+) replacing the A-site cation (Brophy and Sheridan 1965, Kubisz 1970, Dutrizac and Kaiman 1976). The degree of hydronium present within any jarosite sample is calculated indirectly: for a synthetic potassium jarosite, the process is relatively straightforward: the potassium concentration is determined and the molar abundance is subsequently calculated for the A-site. This is typically expressed as $[H_3O^+_{1-x} K_x]$ (see Section 1.4.1 for a more comprehensive explanation).

One of the major differences between plumbojarosite and the other four synthetic jarosites is that in natural samples and occasionally in synthetics samples, the size of the c-axis doubles from approximately 17 to 34 Å (Jambor and Dutrizac 1983). There was no evidence that the plumbojarosite sample made for this study had a doubled

unit cell (Table 3.2). Although the A-site ions are generally thought to have little effect on a_o, they are theoretically responsible for the main variations in c_o (Jambor and Dutrizac 1983). Jambor and Dutrizac (1985) investigated this assumption by comparing the c_o values for plumbojarosite, beaverite and hydronium jarosite endmembers, and found that there was no relationships between c_o and Pb(II) content. Jambor and Dutrizac (1985) concluded that this might arise simply because additional Pb(II) ions can be accommodated in A-site vacancies without disturbing the structure. In plumbojarosite, only half the available A-sites are filled, but the synthetic jarosite compositions show that the structure can readily tolerate additional Pb(II), $(H_3O)^+$ or additional vacancies (Jambor and Dutrizac 1985). Jambor and Dutrizac (1985) found that less than a third of the A-sites needed to be filled by Pb(II) to attain a 34 Å c-axis.

A few authors have reported an 11 Å (003) reflection, mainly from natural lead-rich jarosites (Jambor and Dutrizac 1983, 1985; Dutrizac and Chen 2003). For synthetic analogues, the peak is commonly extremely weak or absent. None of the XRD patterns for the Pb-bearing synthetic jarosites reveal an 11 Å reflection. A natural sample of plumbojarosite from Tintic mine, Dividend, Juab County, Utah, USA [BM 1966,403] was analysed by X-ray diffraction (Figure 3.8), and an 11 Å reflection is clearly evident. Jambor and Dutrizac (1983) synthesised two solid solutions of both beaverite endmembers and studied the relative intensity of the 11 Å reflection as they increased the lead content, from plumbojarosite to the two-beaverite endmembers. They found that the presence or absence of the 11 Å line was not predictable from the bulk composition of the jarosite sample, and suggested that the 11 Å reflection was independent of the total lead content in the jarosite structure. Dutrizac and Chen (2003) proposed that the 11 Å reflection indicates a high degree of ordering of Pb(II) ions and vacancies. The absence of an 11 Å reflection in any of the synthetic lead-rich jarosites made for this study would infer poor internal ordering of the Pb(II) ions and vacancies within their structures.

Further evidence of the lack of ordering between Pb(II) ions and vacancies in the A-site of the synthetic plumbojarosite sample is seen when its FTIR spectrum (Figure 3.15b) is compared to that of the natural plumbojarosite from Tintic mine, Utah [BM 1966,403] (Figure 3.19b). The contrast is seen in the intense absorption bands between 900 to 1300 cm^{-1}, assigned to the vibrational modes of $v_3(SO_4^{2-})$ and $v_1(SO_4^{2-}$

). Typically, in synthetic jarosite samples and natural samples that contain univalent cations at the A-site there are only three vibrational modes of the SO_4^{2-} tetrahedra in this mid-IR region. These include a $v_3(SO_4^{2-})$ doublet at the two higher wavenumbers and a $v_1(SO_4^{2-})$ mode at the lowest wavenumber (Figure 3.15b, 3.20b, Table 3.6). In the natural sample from the Tintic mine, however, there are six bands over the same wavenumber window, 900 to 1300 cm^{-1} (Figure 3.19b, 3.20a, Table 3.7). These six bands are likely a result of splitting of the $v_3(SO_4^{2-})$ doublet and $v_1(SO_4^{2-})$ singlet due to the ability of the (SO_4^{2-}) unit to distinguish between an A-site occupied with Pb(II) and a vacancy.

The jarosite subgroups particle morphologies range from perfect euhedral to small and irregular (Baron and Palmer 1996b). Sasaki and Konno (2000) investigated the possible mechanisms that might affect particle morphology in synthetic jarosites, and found that jarosite subgroup phases synthesised by the same technique showed similar morphologies (although some differences were observed) depending upon which monovalent cations were involved. The particle morphology of potassium jarosite (A = K^+) (Figure 3.21a) is very different from that of the other four analogous enriched with lead (A = Pb(II)) (Figure 3.21 b-e); this is probably due to their different A-site cations (Sasaki and Konno 2000). Contrasting morphologies within the lead analogues (Figures 3.21 b-e) are probably due to subtle changes in specific cations in the B- and T-sites.

Becker and Gasharova (2001) proposed a spiral triangular growth island model to account for the varying jarosite particle morphologies. A triangular growth island was created from the most stable steps of the {012} surface for the potassium jarosite structure. The basis for their experiments was that if crystal growth was faster than the time required to develop an equilibrium triangular shape for a new layer, the transition from one-step to the next would appear rounded. The relationship between particle rounding and the non-equilibrium rate of particle growth may partly account for the globular morphology of the synthetic potassium jarosite in this study. The reason that the potassium jarosite synthesis was more rapid than any of the lead-rich jarosites is that all the reactants were together at the very beginning of the reaction, and K was very much in excess to avoid unfavourable hydronium incorporation at the A-site. By contrast the four lead-rich jarosites underwent a very slow synthesis

reaction where $PbSO_4$ was added extremely slowly to the reaction mixture to avoid possible $PbSO_4$ contamination at the end of the synthesis. If the triangular growth island model proposed by Becker and Gasharova (2001) has any credibility it should be possible to make synthetic potassium jarosite with a similar pseudocubic morphology to plumbojarosite. This would be achieved by introducing the A-site cation to the reaction mixture slowly, thereby attaining a reaction rate closer to equilibrium growth.

7.2 Insights from the acid and alkali dissolution experiments

Due to time constraints, it was not possible to conduct acid and alkali dissolution experiments of either beaverite-Cu or beaverite-Zn. The results from these dissolutions would have been enlightening, as they would have supplied information on the effects of incorporating divalent metal cations (Cu(II), Zn(II)) into the trivalent octahedral B-site that is usually occupied with Fe(III) in jarosites. Specifically these dissolutions would have proved insight into the increased disorder in the B-sites and its overall effects on the very stable T-O-T sheets in the jarosite structure.

The acid and alkali dissolution experiments of potassium jarosite, plumbojarosite, and beudantite were all classed as incongruent dissolution reactions because of the non-ideal dissolution of the parent solids, as shown by differences in the aqueous and residual solid molar ratios compared to idealised values (Table 3.3, 4.2, 4.5, 5.2, 5.5). Throughout the majority of the dissolution experiments, it was found that ions located in the A- and T-sites (K and Pb(II), and SO_4^{2-} and AsO_4^{3-}, respectively) were subject to selective dissolution in preference to the B-site (Fe(III)), located deep within the T-O-T structure. Further evidence of this selective dissolution of SO_4^{2-} groups can be seen in the SEM morphology micrograph for the acidic dissolution of plumbojarosite (Figure 4.15). Gasharova et al. (2001) have reported similar selective dissolution of K^+ and SO_4^{2-} groups on a potassium jarosite surface.

Computer modelling of the potassium jarosite surfaces gives further insight into the selective dissolution of the A- and T-sites (see Section 6.5). The modelling revealed two stable terminations that had no net dipoles belonging to the {012} group of faces. The two terminations comprised of neutral sub-layers with compositions of $[KFe(OH)_4]^0$ (Figure 6.5a, 6.6a) and $[Fe_2(SO_4)_2(OH)_2]^0$ (Figure 6.7a, and 6.8a),

respectively. During surface relaxation, the upper and lower sub-layers in both surfaces were mainly affected by rotation. After the surfaces were relaxed, the $[KFe(OH)_4]^0$ surface was terminated by K-ions and hydrogen ions of the hydroxyl groups (Figure 6.5b, 6.6b). The $[Fe_2(SO_4)_2(OH)_2]^0$ surface was terminated by the uncoordinated oxygen atoms of the sulphate tetrahedra lying just below the plane and an upwardly rotated hydroxyl group after relaxation (Figure 6.7b, and 6.8b). The implications for the rotations of these two neutral sub-layer compositions is that they could be vulnerable to selective dissolution by polar water due to the high surface coverage of bonded and non-bonded oxygen atoms. Furthermore, due to the structure of these two surfaces, K^+ and SO_4^{2-} groups near the surface could be cleaved easier during dissolution relative to stable FeO_6 octahedrons of the T-O-T sheet.

The aqueous ion concentration profiles for the acid dissolution of potassium jarosite and plumbojarosite (Figures 4.1 and 4.2-4.3) and the alkali dissolution of potassium jarosite (Figure 5.1) suggest that a transport-controlled dissolution model governed these dissolution experiments (Stumm and Morgan 1996). The aqueous dissolution profiles of SO_4^{2-} and Fe for the alkali dissolution of plumbojarosite took on the form of linear style relationships with ion concentration in solution versus time (Figures 5.2 and 5.3). The linearity of the SO_4^{2-} and Fe profiles suggests that a surface-controlled dissolution model governed the alkali dissolution of plumbojarosite (Stumm and Morgan 1996). Due to the complexity of the acid and alkali dissolution of beudantite, it is difficult to determine which type of dissolution model (transport or surface) best describes these dissolutions. The degree of linearity of the Fe and SO_4^{2-} ion concentration after 250 hrs and between 300-1250 hrs would indicate that after 250 hrs and 300 hrs for the alkali and acid dissolution experiments respectively, the kinetics were governed by surface-controlled reactions (Figures 5.5, 4.6). To complicate matters, the AsO_4^{3-} profiles for both acid and alkali experiments, as well as the Fe concentration profile for the acid experiment appear to have parabolic profiles in the first 250 hrs, indicative of a transport-controlled dissolution (Figures 4.4, 5.4). To summarise, the acid and alkali dissolutions of beudantite were probably governed by a mixed transport-surface kinetic dissolution reaction, where transport mechanisms dominated the first 250 hrs of both reactions until secondary phases were present to such a degree on the residual solids to dominate the dissolution rate-determining step for the remainder of the experiment.

During the acid and alkali dissolutions of beudantite and the alkali dissolutions of potassium jarosite and plumbojarosite, secondary phase(s) formed from the constituent ions in solution. Specifically, alkali dissolutions of potassium jarosite and plumbojarosite formed goethite and amorphous $Fe(OH)_3$, respectively. For both the beudantite acid and alkaline dissolutions secondary amorphous $PbSO_4$ formed and amorphous $Fe(OH)_3$ formed during the alkali dissolution. Concentrating on the Fe-rich phases an obvious question is: why did crystalline goethite (α-FeO(OH)) form only during the alkali dissolution of potassium jarosite. The formation of amorphous $Fe(OH)_3$ in both alkali dissolution of plumbojarosite and beudantite resulted in the overall dissolution reactions being surface controlled, whilst the alkali potassium dissolution was transport-controlled. The amorphous $Fe(OH)_3$ phases probably inhibited the alkali dissolutions of plumbojarosite and beudantite to such a degree than the concentration of Fe in solution was not great enough to form α-FeO(OH) directly. However, over a longer period it is highly probable that the amorphous $Fe(OH)_3$ would slowly crystallise into the more stable Fe(III) oxyhydroxide phase of goethite (Bigham 1994).

The other interesting result of the acid and alkali experiments was the formation of amorphous $PbSO_4$ in the acid and alkali dissolutions of beudantite but not in any of the plumbojarosite dissolutions. Structurally plumbojarosite and beudantite differ only by the partial incorporation of AsO_4^{3-} at the T-site in the latter. It is hypothesised that the AsO_4^{3-} anion in either or both the residual solid and solution is skewing the thermodynamic equilibria of the system to favour $PbSO_4$ precipitation. A test of this would be to see if $PbSO_4$ were a secondary phase in either acid or alkali dissolutions of beaverite-Cu or –Zn.

It was not possible to calculate IAP values for the acidic dissolution of beudantite or any of the three alkali dissolutions due to the formation of secondary phase(s) (Table 4.3, 5.3). The problem arises from the fact that to calculate a true IAP value, the reaction must have reached steady state and no ions should have precipitated out of solution. Secondary phase formation in mineral dissolution skews the overall calculated IAP to a lower value than the real value, because lower ion concentrations in solution result in lower equilibrium aqueous activities being reported. Similarly, no

definitive K_{SP} values could be calculated for the dissolutions that did not have secondary phases present (acidic dissolutions of potassium jarosite and plumbojarosite) because these were incongruent in that there was non-ideal dissolution with respect to solid:solution ion ratios. The vast majority of the solubility data on jarosites are for potassium jarosite; at present, there are no known data for plumbojarosite. Baron and Palmer (1996b) publish an IAP value of -11.36±0.25 for a near identical experiment to that reported in this study for the dissolution of potassium jarosite. Calculated IAP values for the bottles 2 and 3 (that were not contaminated by KCl) in the acidic potassium jarosite dissolution range from -11.30±0.25 to -11.38±0.25 (Table 4.3). These are extremely similar to those reported by Baron and Palmer (1996), which is surprising considering the incongruency of the potassium jarosite dissolution. Although Baron and Palmer (1996b) used their final aqueous concentrations to calculate IAP and ultimately K_{SP} for potassium jarosite, these values are suspect and likely incorrect due to the incongruency of the potassium jarosite dissolution.

7.3 The implications of jarosite breakdown mechanisms and products on the natural environment

Toxic elements can occupy a variety of locations within the jarosite structure ($AB_3(TO_4)_2(OH)_6$). Pb(II) commonly occupies the A-site (with hydronium, H_3O^+) to varying degrees depending upon the specific jarosite endmember (plumbojarosite $Pb_{0.5}Fe_3(SO_4)_2(OH)_6$ or beudantite $PbFe_3(AsO_4)(SO_4)(OH)_6$). Divalent metal cations such as Cu(II) or Zn (II) partially occupy B-sites at the expense of Fe(III) (e.g. beaverite-Cu $Pb(Fe,Cu)_3(SO_4)_2(OH)_6$ and beaverite-Zn $Pb(Fe,Zn)_3(SO_4)_2(OH)_6$). Another common toxic element found in the highly oxic AMD/ARD environments is As in the +5 oxidation state and commonly in form of the AsO_4^{3-} oxyanion. This oxyanion can occur in the jarosite structure at the T-site, usually at the partial expense of SO_4^{2-}, in the beudantite endmember ($PbFe_3(AsO_4)(SO_4)(OH)_6$).

As mentioned earlier, due to time constraints, it was not possible to complete the acid and alkali dissolution experiments of either beaverite-Cu or –Zn. As a consequence, it is difficult to predict the breakdown pathways that involve these two toxic elements (Cu(II) and Zn(II)) specifically, and probably more importantly gauge the dissolution pathways of jarosite structures that have structural disorder in the T-O-T sheeting, due

to the incorporation of divalent metal cations in trivalent octahedral sites. It is a reasonable hypothesis that due to the increased disorder within the usually very stable T-O-T structure from the partial substitution of divalent ions in the B-site, the two beaverite endmembers may breakdown and release their toxic elements (Pb(II), Cu(II), Zn(II)) more rapidly than the three other endmembers that have ideal trivalent Fe(III) octahedral occupancy.

The selective dissolution of the A- and T-sites in plumbojarosite and beudantite structures have important implications for the toxic element pathways of Pb(II) and AsO_4^{3-} in the natural environment, because Pb(II) occurs at the A-site in plumbojarosite and Pb(II) and AsO_4^{3-} occur at the A- and T-sites, respectively, in beudantite. The breakdown of beudantite is worth highlighting, as it appears in both acid and alkali dissolutions that the Pb(II) in solution was removed by the precipitation of an amorphous $PbSO_4$ phase. The removal of Pb(II) from solution for the dissolution of beudantite is important, as there appears to be a 'natural' sink for this toxic element in this system. Both these jarosite structures contain these toxic elements in significant quantities ($\sim$ 3-5 wt. %).

During the acidic dissolutions of, potassium jarosite, plumbojarosite, and beudantite approximately 20-25 % of the original solid dissolved (beudantite was slightly less due to the secondary formation of $PbSO_4$). During the alkali dissolutions, approximately 10-15 % of the original solid dissolved over the course of the experiment. This is shown quite clearly in Table 7.1, a summary of the total ions released from the solid into solution at the end of the experiments, where the values are in the form of percentages. Unsurprisingly, the acidic dissolutions in which no secondary phase formed (potassium jarosite and plumbojarosite) had the highest proportions of ions in solution at the end of the experiments. The selective dissolution of the A-sites, especially in the acid dissolution of potassium jarosite, is evident. Of the alkali dissolutions, all the experiments contained secondary phases, which probably contributed as inhibitors towards these reactions, thereby limiting the release of ions migrating from the dissolving solids in to the bulk solutions. The effects of these secondary phases on the potential release of toxic elements is seen nowhere more clearly than in the alkali dissolution of beudantite, that has less than 1 % of the available toxic cations from the solid in solution (Table 7.1).

Table 7.1. Percentage values of ions released from the dissolved solid in solution.

| Compound | % values of ions released from the solid in solution | | | | |
	K	Pb	Fe	SO_4^{2-}	AsO_4^{3-}
Potassium jarosite					
Acid Bottle 1	13.52	-	6.47	6.73	-
Acid Bottle 2	11.66	-	7.44	7.81	-
Acid Bottle 3	11.41	-	7.44	7.75	-
Alkali Bottle 1	11.40	-	< 1	7.69	-
Alkali Bottle 2	11.74	-	< 1	7.86	-
Alkali Bottle 3	11.85	-	< 1	7.93	-
Plumbojarosite					
Acid Bottle 1	-	4.14	4.77	4.92	-
Acid Bottle 2	-	6.37	7.21	7.50	-
Acid Bottle 3	-	7.52	8.32	8.69	-
Alkali Bottle 1	-	2.53	< 1	2.98	-
Alkali Bottle 2	-	2.61	< 1	3.06	-
Alkali Bottle 3	-	2.72	< 1	3.16	-
Beudantite					
Acid Bottle 1	-	< 1	1.38	< 1	7.13
Acid Bottle 2	-	< 1	1.39	< 1	7.16
Acid Bottle 3	-	< 1	1.41	< 1	7.34
Alkali Bottle 1	-	< 1	< 1	< 1	< 1
Alkali Bottle 2	-	-	< 1	< 1	< 1
Alkali Bottle 3	-	-	< 1	< 1	< 1

All the acid and alkali dissolution reactions were of a batch reactor design, and more importantly were closed systems. The natural environment, however, is very much an open type system, where important parameters such as solution concentration, pH and temperature can change quickly and markedly. In future, these results could be improved and substantiated if these acid and alkali dissolution experiments were repeated using a more complicated and unfortunately more costly flow-through reactor, that better simulates natural ARD environments (David Richards, Principal Advisor, Environment, Rio Tinto. per comm. 2004).

An Eh-pH diagram was constructed from the steady state aqueous activities of bottle 2 of the acid dissolution of potassium jarosite to judge the minerals phase stability in an environment affected by ARD (Figure 4.17b). Although potassium jarosite partially dissolved in our experiments, it was predicted as being a stable phase in an oxic environment in a pH range of 0.5 to 5. It was not possible to calculate meaningful

Eh-pH diagrams for the acid dissolution of plumbojarosite and beudantite due to the lack of reliable thermodynamic solubility data.

Alkali dissolution studies of potassium jarosite, plumbojarosite, and beudantite were carried out to investigate their stability and breakdown mechanisms under an alkali regime that would mimic an AMD/ARD environment recently remediated with slaked lime ($Ca(OH)_2$). A current industry example of the use of lime-rich material for long-term ARD control comes from the Grasberg Mine in Indonesia. The Grasberg operation is a large copper and gold open pit mine operated by PT Freeport Indonesia (Miller et al. 2003). Specifically, lime-rich material and the potentially acid-forming overburden associated with mining the ore body are blended together to reduce and therefore hopefully control the overall net acid generation (NAG) of the waste overburden (Miller et al. 2003). The results from this study, especially regarding the alkali dissolution of potassium jarosite would signify that this mineral is inherently unstable in this alkali regime. This is shown more clearly by the absence of a stable potassium jarosite phase in the Eh-pH diagram created from the steady state activities from one of the triplicates (Figure 5.19b). Once again, it is very hard to appraise the phase stabilities of plumbojarosite and beudantite under these alkali conditions due to the lack of reliable thermodynamic solubility data. The alkali dissolutions of potassium jarosite, plumbojarosite and beudantite suggested that all the free Fe(III) in solution would precipitate out to form secondary phases, specifically, goethite (α-$FeO(OH)$) from potassium jarosite, and amorphous $Fe(OH)_3$ from both plumbojarosite and beudantite. The presence of amorphous $Fe(OH)_3$ is important in the alkali dissolution of beudantite, as it appeared that AsO_4^{3-} adsorbed to its surface, thereby, reducing the concentration of this toxic element. As mentioned earlier, Pb(II) was removed from solution by the formation of amorphous $PbSO_4$ in the alkali beudantite experiment. To summarise, the alkali dissolution experiments have shown that remediation of AMD/ARD environments by lime-rich material where jarosite-type compounds, containing significant concentrations of toxic elements (Pb(II), As(V)) are present maybe risky as these structures are not stable under these alkali regimes. The breakdown products might mask the full implications of the potential toxic element release, where new phase(s) might either adsorb or co-precipitate with them.

8 Conclusions and Recommendations for further work

Chapter 8 concentrates on the conclusions from this study, where the original aims and objectives are restated and ultimately answered. Recommendations for future research are given in a separate and final section.

8.1 Conclusions

The aims of this study were to determine the mechanisms and products of jarosite breakdown, and the amount of potentially hazardous toxic elements released because of this breakdown. These are critical in understanding and modelling geo-chemical reactions in these acid environments.

The objectives of this project were to:

(1) monitor the rate of release of toxic elements (e.g., Pb(II), As(V), Cu(II), Zn(II)) from synthetic jarosites using dissolution batch experiments;

(2) characterise the new phases formed as a result of these dissolution experiments using a number of different surface- and whole-mineralogical techniques; and

(3) model how toxic elements maybe incorporated within and released from the jarosite structure.

To address the first objective it was imperative to first synthesise five jarosite analogues. These synthetic minerals were: potassium jarosite [$KFe_3(SO_4)_2(OH)_6$], plumbojarosite [$Pb_{0.5}Fe_3(SO_4)_2(OH)_6$], beaverite-Cu [$Pb(Fe,Cu)_3(SO_4)_2(OH)_6$], beaverite-Zn [$Pb(Fe,Zn)_3(SO_4)_2(OH)_6$] and beudantite [$PbFe_3(AsO_4)(SO_4)(OH)_6$]. Six distinctive experimental methods were used to characterise the five synthetic jarosite analogous: XRD, elemental analysis, TG-DTA, FTIR, SEM, and BET. To appraise the suitability of these synthetic analogues to represent samples in the natural environment, a variety of crystalline natural jarosite samples from the UK Natural History Museum mineral collection were also characterised. The results suggested that the synthetic jarosites were good analogues for natural jarosites.

Objective 1 was completed after successful acid and alkali dissolution batch experiments on potassium jarosite, plumbojarosite, and beudantite. Due to time constraints it was not possible to conduct the dissolution experiments for beaverite-Cu and –Zn. The acid dissolution was created to mimic an environment affected by ARD/AMD, and the alkali dissolution an AMD/ARD environment recently remediated with slaked lime (calcium hydroxide $Ca(OH)_2$). All the acid and alkali dissolution experiments were classed as incongruent dissolution reactions because of the non-ideal dissolution of the parent solids. Both the acid and alkali dissolution experiments of potassium jarosite and the acid dissolution of plumbojarosite were found to be governed by transport-controlled reaction kinetics. The alkali dissolution of plumbojarosite was constrained by surface-controlled kinetics. Finally, the acid and alkali dissolution of beudantite were found to be ordered by a mixed transport-surface kinetic reaction. In addition, secondary phases were present following the acid and alkali dissolution of beudantite, and the alkali dissolutions of potassium jarosite and plumbojarosite. Due to the presence of these secondary phases, IAP values were only calculated for the acid dissolution of potassium jarosite and plumbojarosite. The accuracy of the IAP values calculated in this study and those of published K_{SP} values were all questionable due to the incongruent dissolution of jarosite-type minerals. Eh-pH diagrams could only be created for the acid and alkali dissolutions of potassium jarosite, due to the lack of thermodynamic solubility data for plumbojarosite and beudantite. Calculated acid and alkali phase diagrams for potassium jarosite indicated that the mineral was a stable phase in an acid environment (highly oxic and within a pH range of 0.5 to 5), and perhaps more importantly, not stable in an alkali remediation environment.

The second objective of this study was fulfilled when the secondary phases found in the experiments described above were characterised by XRD, elemental analysis, FTIR, and SEM. The secondary phases in the alkali potassium jarosite and plumbojarosite dissolutions were identified as goethite (α-FeO(OH)) and amorphous $Fe(OH)_3$, respectively. The acid and alkali beudantite dissolutions products both contained amorphous $PbSO_4$; the alkali dissolution also contained amorphous $Fe(OH)_3$.

In the acid experiments, the selective dissolutions of the A- and T-sites relative to the Fe(III) rich B-site have important implications as some of the main toxic elements of interest in this study, Pb(II) and AsO_4^{3-}, can be incorporated in these two sites. In the acidic dissolution of potassium jarosite and plumbojarosite, all the parent ions of the solids were eluted into solution. For beudantite, the vast majority of the Pb(II) was removed from solution in the form of $PbSO_4$, whilst the remainder of the ions (Fe(III), AsO_4^{3-}, and SO_4^{2-}) making up the solid diffused into solution. The removal of Pb(II) from solution in the dissolution of beudantite is important, as $PbSO_4$ appears to be a 'natural' sink for this toxic element in this system. The presence of amorphous $Fe(OH)_3$ is important in the alkali dissolution of beudantite, as it appeared AsO_4^{3-} partially adsorbed to its surface, thereby reducing the concentration of this toxic element in solution. Pb(II) was also removed from solution by the formation of amorphous $PbSO_4$ in the alkali beudantite experiment. To summarise, the alkali dissolution experiments have shown that remediation of AMD/ARD environments by lime-rich material where jarosite-type compounds, containing significant concentrations of toxic elements (Pb(II), As(V)) are present may be risky as these structures are not stable in these alkali regimes. Favourable breakdown products might, however, mask the full implications of the potential toxic element release, where new phase(s) might either adsorb or co-precipitate with them.

The third and final objective of this study was met by the initial creation of a very good classical potential model of potassium jarosite; the model was then used for subsequent defect calculations and surface studies of the potassium jarosite structure. It was not possible to model any jarosites that incorporate Pb(II) into their structure (plumbojarosite, the beaverite compounds and beudantite). The reason was that it was quite difficult to create a Buckingham interatomic potential for Pb(II), due to the presence of a lone pair of electrons. Another problem that was encountered was the lack of any hydronium (H_3O^+) representation in the potassium jarosite model; this was simply because, at present, there is no widely available classical potential to represent this ion.

The 2D modelling of the potassium jarosite surfaces revealed two stable terminations that had no net dipoles belonging to the {012} group of faces. Both terminations could be described as type II surfaces under the Tasker notation. The two

terminations comprised of neutral sub-layers with compositions of $[KFe(OH)_4]^0$ and $[Fe_2(SO_4)_2(OH)_2]^0$. During surface relaxation, the upper and lower sub-layers in both surfaces were mainly affected by rotation. The implications for the rotations of these two neutral sub-layer compositions was that they could be prone to selective dissolution by polar water due to the high surface coverage of bonded and non-bonded oxygen atoms. Evidence of this selective dissolution of SO_4^{2-} groups could be seen in the SEM morphology micrograph for the acidic dissolution of plumbojarosite.

Both intrinsic and extrinsic defects were considered and appraised for this study. Extrinsic defects were limited to three 2+ cations commonly observed in jarosite structures and seen in ARD environments, namely Cd(II), Zn(II), and Cu(II). In this study, only Schottky defects or neutral vacancy defect clusters were considered, as no stable interstial sites for Fe or S could be found. The formation energies for series of partial Schottky's indicated that defects were more likely on the K sublattice than on the Fe sublattice, while those involving the $(SO_4)^{2-}$ molecular ion were unfavourable. Even though these three impurity cations had favourable point defect energies for potassium A-site substitutions, it emerged through mass and charge balance calculations that these 2+ cations were more likely to be most energetically favourable in substituting in the iron B-site. Overall the presence of Fe vacancies in natural and experimental structures, and the system's ability to reduce the overall lattice energy by 2+ cations occupying the B-site may help to explain the non existence of endmember jarosites such as $Cu_{0.5}Fe_3(SO_4)_2(OH)_6$.

8.2   Recommendations for future work

In the near future, it would be advantageous if similar acid and alkali dissolution experiments were conducted on beaverite-Cu and beaverite-Zn. This would reveal how the disorder of substituting 2+ cations in the octahedral B-site influences the stability of the T-O-T sheeting in the general jarosite structure. A question to be answered is: does either beaverite-Cu or –Zn breakdown more rapidly during dissolution conditions as compared to the isostructurally similar plumbojarosite structure? Another important question would be: is $PbSO_4$ a secondary phase in either acid or alkali dissolution? If not, then a follow up question would be: why does $PbSO_4$ precipitate in both the acid and alkali dissolutions of beudantite, a structure that uniquely contains the AsO_4^{3-} oxyanion?

This study has highlighted the serious lack of any published thermodynamic solubility data on plumbojarosite, beaverite-Cu and −Zn, and beudantite, jarosite minerals that contain significant quantities of toxic elements. Thermodynamic data such as these underpin aqueous geochemical modelling databases (e.g. PHREEQC, Geochemist's Workbench) that are used extensively by academics and environmental professionals for ARD predictive modelling. Without these data, these models are likely to be significantly inaccurate.

The classical computational modelling of the jarosite structure has been hampered by the lack of Pb(II) and hydronium (H_3O^+) incorporation, hopefully this maybe overcome in the future through more advanced electronic structure type models. In the future, it would be advantageous if the current defect calculations from this study could be supplemented with data from relevant aqueous species that have been identified experimentally.

References

Abdel-Samad, H. and P. R. Watson (1998). "An XPS study of the adsorption of lead on goethite (alpha- FeOOH)." Applied Surface Science **136**(1-2): 46-54.

Alcobe, X., J. Bassas, et al. (2001). Structural characterization of synthetic Beudantite-type phases by Rietveld refinement. Epdic 7: European Powder Diffraction, Pts 1 and 2. **378-3:** 671-676.

Allan, N. L., A. L. Rohl, et al. (1993). "Calculated Bulk and Surface-Properties of Sulfates." Faraday Discussions(95): 273-280.

Allison, J. D., Brown, D.S., Novo-Gradac, K.J. (1990). MINTEQA2/PRODEFA2, A Geochemical Assessment Model for Environmental Systems: Version 3.0. Athens, GA, U.S. Environmental Protection Agency.

Alpers, C. N., D. K. Nordstrom, et al. (1989). "Solubility of jarosite solid solutions precipitated from acid mine waters, Iron Mountain, California, USA." Scientific Geology Bulletin **42**: 281-298.

Alpers, C. N., R. O. Rye, et al. (1992). "Chemical, Crystallographic and Stable Isotopic Properties of Alunite and Jarosite from Acid Hypersaline Australian Lakes." Chemical Geology **96**(1-2): 203-226.

Amacher, M. C. (1991). Methods of Obtaining and Analysing Kinetic Data. Rates of Soil Chemical Processes. D. L. Sparks, Suarez, D.L. Wisconsin, SSSA. **27**.

Atkins, P. W. (1992). The Elements of Physical Chemistry, Oxford University Press.

Banbcan, J. (1971). "Synthesis of jarosite, KFe3(SO4)2(OH)6." Geol. Zb. **22**: 299-304.

Banfield, J. F. and S. A. Nealson (1997). Geomicrobiology: Interactions between Microbes and Minerals, Mineralogical Society of America, USA.

Banfield, J. F. and S. A. Welch (2000). Microbial controls on the mineralogy of the environment. Environmental Mineralogy. D. J. Vaughan and R. A. Wogelius, EMU. **2:** 173-196.

Baron, D. and C. D. Palmer (1996). "Solubility of jarosite at 4-35 degrees C." Geochimica Et Cosmochimica Acta **60**(2): 185-195.

Baron, D. and C. D. Palmer (1996). "Solubility of KFe3(CrO4)(2)(OH)(6) at 4 to 35 degrees C." Geochimica Et Cosmochimica Acta **60**(20): 3815-3824.

Baron, D. and C. D. Palmer (2002). "Solid-solution aqueous-solution reactions between jarosite (KFe3(SO4)(2)(OH)(6)) and its chromate analog." Geochimica Et Cosmochimica Acta **66**(16): 2841-2853.

Becker, U. and B. Gasharova (2001). "AFM observations and simulations of jarosite growth at the molecular scale: probing the basis for the incorporation of foreign ions into jarosite as a storage mineral." Physics and Chemistry of Minerals **28**(8): 545-556.

Berg, D., Borve, K. (1996). The disposal of iron residue at Norzink and its impact on the environment. Iron Control and Disposal. J. E. a. H. Dutrizac, G.B. Montreal, Canadian Institute Mining Metallurgy and Petroleum.

Bertaut, F. (1958). Compt. Rendu. **246**: 3447.

Bethke, C. M. (1996). Geochemical Reaction Modeling, Oxford University Press, Oxford.

Bigham, J. M. (1994). Mineralogy of Ochre Deposits Formed by Sulfide Oxidation. Short course handbook on Environmental Geochemistry of sulfide mine-wastes. J. L. Jambor, D.W. Blowes, Mineralogical Association of Canada.

Bigham, J. M. and D. K. Nordstrom (2000). Iron and aluminum hydroxysulfates from acid sulfate waters. Sulfate Minerals - Crystallography, Geochemistry and Environmental Significance. **40:** 351-403.

Bigham, J. M., U. Schwertmann, et al. (1990). "A Poorly Crystallized Oxyhydroxysulfate of Iron Formed by Bacterial Oxidation of Fe(Ii) in Acid-Mine Waters." Geochimica Et Cosmochimica Acta **54**(10): 2743-2758.

Bigham, J. M., U. Schwertmann, et al. (1996). "Schwertmannite and the chemical modeling of iron in acid sulfate waters." Geochimica Et Cosmochimica Acta **60**(12): 2111-2121.

Bladh, K. W. (1982). "The Formation of Goethite, Jarosite, and Alunite During the Weathering of Sulfide-Bearing Felsic Rocks." Economic Geology **77**(1): 176-184.

Blesa, M., Morando, B.J., Regazzoni, A.E. (1994). Dissolution of Metal Oxides, CRC Press.

Brady, K. S., J. M. Bigham, et al. (1986). "Influence of Sulfate on Fe-Oxide Formation - Comparisons with a Stream Receiving Acid-Mine Drainage." Clays and Clay Minerals **34**(3): 266-274.

Breithaupt, A. (1852). Breg- und hüttenmänn. Ztg. **6**: 68.

Brophy, G. P., Scott, E.S., Snellgrove, R.A. (1962). "Solid solution between alunite and jarosite." American Mineralogist **47**: 112-126.

Brophy, G. P. and M. F. Sheridan (1965). "Sulphate studies. IV. The jarosite-natrojarosite-hydronium jarosite solid solution series." American Mineralogist **50**: 112-126.

Brown, J. B. (1970). "A chemical study of some synthetic potassium-hydronium jarosites." Canadian Mineralogist **10**: 696-703.

Brown, J. B. (1971). "Jarosite-goethite stabilities at 25oC, 1 atm." Mineralium Deposita **6**: 245-252.

Brunauer, S., Emmett, P.H., Teller, E. (1938). Journal of American Chemical Society **60**: 309.

Butler, B. S. (1913). "The occurrence of complex and little known sulphates and sulpharsenates as ore minerals in Utah." Economic Geology **8**: 311-322.

Carlson, L. and U. Schwertmann (1981). "Natural Ferrihydrites in Surface Deposits from Finland and Their Association with Silica." Geochimica Et Cosmochimica Acta **45**(3): 421-429.

Catlow, C. R. A. (1999). Disorder of defects in solids. Microscopic Properties and Processes in Minerals. K. V. Wright and C. R. A. Catlow. Netherlands, NATO Science series, Kluwer Academic Publishers. **543**.

Catlow, C. R. A. (2003). Computer Modelling of Materials: an Introduction. Computational Materials Science. C. R. A. Catlow, Kotomin, E., NATO Science Series, IOS Press.

Catlow, C. R. A. and W. C. Mackrodt (1982). Computer Simulation of Solids, Lecture Notes in Physics, Vol 166.

Chapman, B. M., D. R. Jones, et al. (1983). "Processes Controlling Metal-Ion Attenuation in Acid-Mine Drainage Streams." Geochimica Et Cosmochimica Acta **47**(11): 1957-1973.

Colbourn, E. A., W. C. Mackrodt, et al. (1983). "The Segregation of Calcium-Ions at the Surface of Magnesium- Oxide - Theory and Calculation." Journal of Materials Science **18**(7): 1917-1924.

Cormack, A. N. (1999). Classical computer simulations. Microscopic Properties and Processes in Minerals. K. V. Wright and C. R. A. Catlow. Netherlands, NATO Science series, Kluwer Academic Publishers. **543**.

Cotton, F. A. and G. Wilkinson (1962). Advanced Inorganic Chemistry. New York, Wiley Interscience.

Davies, M. J., S. C. Parker, et al. (1994). "Atomistic Simulation of the Surface-Structure of Spinel." Journal of Materials Chemistry **4**(6): 813-816.

de Leeuw, N. H., Cooper, T.G., Nelson, C.J., Mkhonto, D., and Ngoepe, P.E. (2003). Computer Simulation of Surfaces of Metals and Metal-Oxide Materials. Computational Materials Science. C. R. A. Catlow, Kotomin, E., NATO Science Series, IOP Press.

de Leeuw, N. H. and S. C. Parker (1997). "Atomistic simulation of the effect of molecular adsorption of water on the surface structure and energies of calcite surfaces." Journal of the Chemical Society-Faraday Transactions **93**(3): 467-475.

DeNicola, D. M. and M. G. Stapleton (2002). "Impact of acid mine drainage on benthic communities in streams: the relative roles of substratum vs. aqueous effects." Environmental Pollution **119**(3): 303-315.

Drever, J. I. (1997). The Geochemistry of Natural Waters. New York, Wiley Interscience.

Drouet, C., D. Baron, et al. (2003). "On the thermochemistry of the solid solution between jarosite and its chromate analog." American Mineralogist **88**(11-12): 1949-1954.

Drouet, C. and A. Navrotsky (2003). "Synthesis, characterization, and thermochemistry of K-Na-H3O jarosites." Geochimica Et Cosmochimica Acta **67**(11): 2063-2076.

Dudas, M. J. (1984). "Enriched levels of arsenic inpost-active acid sulphate soils in Alberta." Soil Science Society of America Journal **48**: 1451-1452.

Dudas, M. J. (1987). "Accumulation of Native Arsenic in Acid Sulfate Soils in Alberta." Canadian Journal of Soil Science **67**(2): 317-331.

Dutrizac, J. E., Dinardo, O., Kaiman, S. (1980). "Factors affecting lead jarosite formation." Hydrometallurgy **5**: 305-324.

Dutrizac, J. E. (1982). "Jarosite-Type Compounds and Their Application in the Metallurgical Industry." Journal of Metals **35**(12): A70-A70.

Dutrizac, J. E. (1983). "Factors Affecting Alkali Jarosite Precipitation." Metallurgical Transactions B-Process Metallurgy **14**(4): 531-539.

Dutrizac, J. E. (1984). The behaviour of impurities during jarosite precipitation. Hydrometallurgical Process Fundementals. R. G. Bautista. New York, Plenum Press**:** 125-169.

Dutrizac, J. E. (1996). "The effect of seeding on the rate of precipitation of ammonium jarosite and sodium jarosite." Hydrometallurgy **42**(3): 293-312.

Dutrizac, J. E. and T. T. Chen (1981). "The Synthesis of Mercury Jarosite and the Mercury Concentration in Jarosite-Family Minerals." Canadian Mineralogist **19**(4): 559-569.

Dutrizac, J. E. and T. T. Chen (2000). "The behaviour of gallium during jarosite precipitation." Canadian Metallurgical Quarterly **39**(1): 1-14.

Dutrizac, J. E. and T. T. Chen (2003). "Synthesis and properties of V3+ analogues of jarosite-group minerals." Canadian Mineralogist **41**: 479-488.

Dutrizac, J. E. and O. Dinardo (1983). "The Co-Precipitation of Copper and Zinc with Lead Jarosite." Hydrometallurgy **11**(1): 61-78.

Dutrizac, J. E. and O. Dinardo (1983). "An Overview of Iron Precipitation Technologies and the Incorporation of Divalent Ions in Jarosite-Type Compounds." Journal of Metals **35**(12): 96-97.

Dutrizac, J. E., D. J. Hardy, et al. (1996). "The behaviour of cadmium during jarosite precipitation." Hydrometallurgy **41**(2-3): 269-285.

Dutrizac, J. E. and J. L. Jambor (1984). Formation and characterisation of argentojarosite and plumbojarosite and their relavence to metallurical processing. Applied Mineralogy, Metallurgical Society AIME (American Institute of Mining, Metallurgy and Petroleum Engineers). W. C. Park, H. D.M. and R. D. Hagni. Warrendale, Pennsylvania**:** 507-530.

Dutrizac, J. E. and J. L. Jambor (1987). "The Behavior of Arsenic During Jarosite Precipitation - Arsenic Precipitation at 97-Degrees-C from Sulfate or Chloride Media." Canadian Metallurgical Quarterly **26**(2): 91-101.

Dutrizac, J. E. and J. L. Jambor (1987). "Behavior of Cesium and Lithium During the Precipitation of Jarosite-Type Compounds." Hydrometallurgy **17**(2): 251-265.

Dutrizac, J. E. and J. L. Jambor (1987). "Behavior of Silver During Jarosite Precipitation." Transactions of the Institution of Mining and Metallurgy Section C-Mineral Processing and Extractive Metallurgy **96**: C206-C218.

Dutrizac, J. E. and J. L. Jambor (2000). Jarosites and their application in hydrometallurgy. Sulfate Minerals - Crystallography, Geochemistry and Environmental Significance. **40:** 405-452.

Dutrizac, J. E., J. L. Jambor, et al. (1987). "The Behavior of Arsenic During Jarosite Precipitation - Reactions at 150-Degrees-C and the Mechanism of Arsenic Precipitation." Canadian Metallurgical Quarterly **26**(2): 103-115.

Dutrizac, J. E. and S. Kaiman (1975). "Rubidium jarosite and thallium jarosite - new synthetic jarosite-type compounds and their structures." Hydrometallurgy **1**: 51-59.

Dutrizac, J. E. and S. Kaiman (1976). "Synthesis and properties of jarosite-type compounds." Canadian Mineralogist **14**: 151-158.

Dutrizac, J. E., Mingmin, D (1993). The behaviour of indium during jarosite precipitation. World Zinc '93. I. G. Matthew, Australasian Inst Mining Metall. **1:** 51-59.

Ewald, P. P. (1921). Ann. Physilk. **64**: 253.

Fairchild, J. G. (1933). "Artificial jarosite - the separation of potassium from cesium." American Mineralogist **18**: 543-545.

Farmer, V. C. (1974). The layer silicates. The infrared spectra of minerals. V. C. Farmer. London, Mineralogical Society.

Fukushi, K., T. Sato, et al. (2003). "Solid-solution reactions in As(V) sorption by schwertmannite." Environmental Science & Technology **37**(16): 3581-3586.

Gale, J. D. (1997). "GULP: A computer program for the symmetry-adapted simulation of solids." Journal of the Chemical Society-Faraday Transactions **93**(4): 629-637.

Gale, J. D. and A. L. Rohl (2003). "The General Utility Lattice Program (GULP)." Molecular Simulation **29**(5): 291-341.

Gasharova, B., Becker, U. (2001). Molecular Simulations and AFM Observations of Jarosite Growth at the Molecular Scale. Goldschmidt Conference, Hot Springs, Virginia, USA.

Gay, D. H. and A. L. Rohl (1995). "Marvin - a New Computer Code for Studying Surfaces and Interfaces and Its Application to Calculating the Crystal Morphologies of Corundum and Zircon." Journal of the Chemical Society-Faraday Transactions **91**(5): 925-936.

Gerhardt, A., L. J. de Bisthoven, et al. (2004). "Macroinvertebrate response to acid mine drainage: community metrics and on-line behavioural toxicity bioassay." Environmental Pollution **130**(2): 263-274.

Gill, R. (1997). Electron beam methods. Modern analytical geochemistry. R. Gill, Longman**:** 206-214.

Giuseppetti, G., Tadini, C. (1980). "The crystal structure of osarizawaite." Neues Jahrbuch Fur Mineralogie-Monatshefte: 401-407.

Gregg, S. J., Sing, K.S.W (1982). Absorption, surface area and porosity. London, Academic Press.

Haddad, P. R., Jackson, P.E. (1990). Ion Chromatography: principals and applications. New York, Elsevier.

Haigh, C. J. (1967). "The hydrolysis of iron in acid solutions." Proc. Australasian Inst. Mining Metall. **233**: 49-56.

Haines, P. J. (2002). Principals of thermal analysis and calorimetry. Cambridge, Royal Society of Chemistry.

Hartig, C., P. Brand, et al. (1984). "Fe-Al-Isomorphism and Structural Water in Crystals of Jarosite- Alunite-Type." Zeitschrift Fur Anorganische Und Allgemeine Chemie **508**(1): 159-164.

Hawthorne, F. C., S. V. Krivovichev, et al. (2000). The crystal chemistry of sulfate minerals. Sulfate Minerals - Crystallography, Geochemistry and Environmental Significance. **40:** 1-112.

Heal, G. R. (2002). Thermogravimetry and Derivative Thermogravimetry. Principals of thermal analysis and calorimetry. P. J. Haines. Cambridge, Royal Society of Chemistry.

Helgeson, H. C. (1969). "Thermodynamics of hydrothermal systems at elevated temperatures and pressures." American Journal of Science **267**: 729-804.

Hendricks, S. B. (1937). "The crystal structure of alunite and the jarosites." American Mineralogist **22**: 773-784.

Hudson-Edwards, K. A., C. Schell, et al. (1999). "Mineralogy and geochemistry of alluvium contaminated by metal mining in the Rio Tinto area, southwest Spain." Applied Geochemistry **14**(8): 1015-1030.

Hyashi, H. (1994). "Mineralogy and chemsity of jarosite and acid sulphate soils." Nendo Kagaku **34**(3): 118-124.

ILO (1983). Encyclopedia of Occupational Health and Safety. Geneva, International Labour Organization.

Ivarson, K. C. (1973). "Microbiological formation of basic ferric sulpahtes." Canadian Journal of Soil Science **53**: 393-406.

Ivarson, K. C., R. O. Hallberg, et al. (1976). "The pyritization of basic sulphates in acid sulphate soils: a microbiological interpretation." Canadian Journal of Soil Science **56**: 393-406.

Jain, A., K. P. Raven, et al. (1999). "Arsenite and arsenate adsorption on ferrihydrite: Surface charge reduction and net OH- release stoichiometry." Environmental Science & Technology **33**(8): 1179-1184.

Jambor, J. L. (1998). Theory and applications of mineralogy in environmental studies of sulphate-bearing mine wastes. Modern Approaches to Ore and Environmental Mineralogy. L. J. Cabri and D. J. Vaughan, Mineral. Assoc. Can. Short Course. **27:** 367-401.

Jambor, J. L. (1999). "Nomenclature of the alunite supergroup." Canadian Mineralogist **37**: 1323-1341.

Jambor, J. L. and D. W. Blowes (2000). Mineralogy of mine wastes and strategies for remediation. Environmental Mineralogy. D. J. Vaughan and R. A. Wogelius, EMU. **2:** 255-290.

Jambor, J. L. and J. E. Dutrizac (1983). "Beaverite Plumbojarosite Solid-Solutions." Canadian Mineralogist **21**(FEB): 101-113.

Jambor, J. L. and J. E. Dutrizac (1985). "The Synthesis of Beaverite." Canadian Mineralogist **23**(FEB): 47-51.

Jarvis, K. E. (1997). Inductively coupled plasma-mass spectrometry. Modern analytical geochemistry. R. Gill, Longman**:** 171-187.

Johansson, G. (1963). "On the crystal structure of a basic gallium sulphate related to alunite." Arkiv for kemi **20**: 343-352.

Johnston, C. T., Aochi, Y.O. (1996). Fourier Transform Infrared and Raman Spectroscopy. Methods of Soil Analysis Part 3 Chemical Methods. D. L. Sparks, SSSA**:** 269-321.

Kashkay, C. M., Borovskaya, Y.B., Badazade, M.A. (1975). "Determination of the free energy of formation of synthetic jarosite and its sulfate analogues." Geochem. Intl. **12**: 115-121.

Keith, W. J., L. Calk, et al. (1979). Crystals of coexisting alunite and jarosite, Goldfield, Nevada. USGS Shorter Contributions to Mineralogy and Petrology. **C1-C5**.

Khlybov, V. V. (1976). "Jarosite from the oxidation zone of pyritised rocks of the western Pritimanye." Trudy- Geologicheskii Institut Kirgizskogo Filiala Akademii Nauk SSSR **20**: 65-71.

Kingsbury, A. W. G. (1952). "New occurrences of rare copper and other minerals." Transactions of the Royal Geological Society- Cornwall **18**: 386-410.

Kingsbury, A. W. G. and J. Hartley (1957). "Beaverite from the Lake District." Mineralogical Magazine **31**: 700-702.

Klein, C., Hurlbut, C.S. (1993). Manual of Mineralogy. New York, Wiley.

Kolitsch, U., P. G. Slade, et al. (1999). "The structure of antimonian dussertite and the role of antimony in oxysalt minerals." Mineralogical Magazine **63**(1): 17-26.

Kröger, F. A. (1972). The Chemistry of Imperfect Crystal (Volume I), North. Amsterdam, Holland.

Kubisz, J. (1964). "A study of minerals in the alunite-jarosite group." Prace Geologiczne- Polska Akademia Nauk Komisja Nauk Geologicznych **22**: 1-93.

Kubisz, J. (1970). "Studies on synthetic alkali-hydronium jarosite. I. Synthesis of jarosite and natrojarosite." Mineralogia Polonica **1**: 47-57.

Kubisz, J. (1971). "Studies on synthetic alkali-hydronium jarosites. II:Thermal investigations." Mineralogia Polonica **2**: 51-59.

Kubisz, J. (1972). "Studies on synthetic alkali-hydronium jarosite. III: Infrared absorption study." Mineralogia Polonica **3**: 23-37.

Langmuir, I. (1916). Journal of American Chemical Society **38**: 2221.

Larson, A. C. and R. B. Von Dreele (1998). General Structure Analysis System (GSAS). Los Alamos National Laboratories, Report LAUR 86-748, 2000.

Lawrence, P. J., S. C. Parker, et al. (1988). "Computer-Simulation Studies of Perfect and Defective Surfaces in Cr2o3." Journal of the American Ceramic Society **71**(8): C389-C391.

Laye, P. G. (2002). Differential Thermal Analysis and Differential Scanning Calorimetry. Principals of thermal analysis and calorimetry. P. J. Haines. Cambridge, Royal Society of Chemistry.

Le Bail, A., Duroy, H., Fourquet, J.L. (1988). Materials Research Bulletin **23**: 447-452.

Lewis, G. V. and C. R. A. Catlow (1985). "Potential Models for Ionic Oxides." Journal of Physics C-Solid State Physics **18**(6): 1149-1161.

Long, D. A. (1977). Raman spectroscopy. New York, McGraw-Hill.

Long, D. T., N. E. Fegan, et al. (1992). "Formation of Alunite, Jarosite and Hydrous Iron-Oxides in a Hypersaline System - Lake Tyrrell, Victoria, Australia." Chemical Geology **96**(1-2): 183-202.

Lottermoser, B. G. (1990). "Rare-Earth Element Mineralization within the Mt-Weld Carbonatite Laterite, Western-Australia." Lithos **24**(2): 151-167.

Mackrodt, W. C. (1989). "Atomistic Simulation of the Surfaces of Oxides." Journal of the Chemical Society-Faraday Transactions Ii **85**: 541-554.

Mackrodt, W. C., Stewart, R.F. (1979). Journal of Chemical Physics C: Solid State Physics **12**: 431.

Maitland, G. C., M. Rigby, et al. (1981). Intermolecular Forces, Oxford University Press.

May, A., J. J. Sjoberg, et al. (1973). "Synthetic argentojarosite: physical properties and thermal behaviour." American Mineralogist **58**: 936-941.

McKie, D., McKie, C. (1986). Essentials of Crystallography. Oxford, Blackwell Scientific.

McMillan, P. F., Hofmeister, A.M. (1988). Infrared and Raman Spectroscopy. Spectroscopic Methods in Mineralogy and Geology. F. C. Hawthorne, Mineralogical Society of America.

Menchetti, S. and C. Sabelli (1976). "Crystal chemistry of the alunite series: crystal structure refinement of alunite and synthetic jarosite." Neues Jahrbuch Fur Mineralogie-Monatshefte **9**: 406-417.

Mermut, A. R. and M. A. Arshad (1987). "Significance of Sulfide Oxidation in Soil Salinization in Southeastern Saskatchewan, Canada." Soil Science Society of America Journal **51**(1): 247-251.

Miller, S., Smart, R., Andrina, J., Neale, A., Richards, D. (2003). Evaluation of Limestone Covers and Blends for Long-Term Acid Rock Drainage Control at the Grasberg Mine, Papua Province, Indonesia. 6th International Conference on Acid Rock Drainage, Cairns, Australia.

Morimoto, T., M. Nishiyama, et al. (2003). "Magnetization of new kagome lattice antiferromagnets: Cr- jarosites, $ACr(3)(OH)(6)(SO4)(2)$ A = Na, K, Rb, NH4." Journal of the Physical Society of Japan **72**(8): 2085-2090.

Mott, N. F. and M. J. Littleton (1938). Transactions of the Faraday Society **34**: 485.

Mumme, W. G. and T. R. Scott (1966). "The relationship between basic ferric sulphate and plumbojarosite." American Mineralogist **51**: 443-453.

Nordstrum, D. K. and C. N. Alpers (1999). Geochemistry of acid mine waters. The Environmental Geochemistry of Mineral Deposits: Part A. Processes, Methods, and Health Issues. G. S. Plumlee and M. J. Logsdon. **6A:** 133-160.

Oborn, I. and D. Berggren (1995). "Characterization of Jarosite-Natrojarosite in 2 Northern Scandinavian Soils." Geoderma **66**(3-4): 213-225.

Ozacar, M., A. Alp, et al. (2000). "Kinetics of thermal decomposition of plumbo-jarosite." Journal of Thermal Analysis and Calorimetry **59**(3): 869-875.

Park, Y. H., Park, P.C. (1978). "A study of iron precipitation as jarosite." Taehan Kumsok Hakhoe Chi **16**: 495-502.

Peacock, C. L. and D. M. Sherman (2004). "Copper(II) sorption onto goethite, hematite and lepidocrocite: A surface complexation model based on ab initio molecular geometries and EXAFS spectroscopy." Geochimica Et Cosmochimica Acta **68**(12): 2623-2637.

Potts, P. J. (1987). A Handbook of Silicate Rock Analysis, Blackie.

Powers, D. A., G. A. Rossman, et al. (1975). "Magnetic behaviour and infrared spectra of jarosite, basic iron sulphate, and their chromate analogs." Journal of Solid State Chemistry **13**: 213-225.

Putnis, A. (1992). Introduction to Mineral Sciences, Cambridge University Press, UK.

Raven, K. P., A. Jain, et al. (1998). "Arsenite and arsenate adsorption on ferrihydrite: Kinetics, equilibrium, and adsorption envelopes." Environmental Science & Technology **32**(3): 344-349.

Richmond, W. R., M. Loan, et al. (2004). "Arsenic removal from aqueous solution via ferrihydrite crystallization control." Environmental Science & Technology **38**(8): 2368-2372.

Ripmeester, J. A., C. I. Ratcliffe, et al. (1986). "Hydronium Ion in the Alunite - Jarosite Group." Canadian Mineralogist **24**: 435-447.

Ripp, G. S., Kanakin, S.V., Shcherbakova, M.N. (1998). "Phosphate mineralization in metamorphosed high-alumina rocks of the Ichetoyskoye ore occurrence." Zap Vseross Mineral Obshch **127**(6): 98-108.

Roca, A., J. V. M. Arranz, et al. (1999). "Characterization and alkaline decomposition/cyanidation of beudantite-jarosite materials from Rio Tinto gossan ores." Canadian Metallurgical Quarterly **38**(2): 93-103.

Sasaki, K. and H. Konno (2000). "Morphology of jarosite-group compounds precipitated from biologically and chemically oxidized Fe ions." Canadian Mineralogist **38**: 45-56.

Sasaki, K., O. Tanaike, et al. (1998). "Distinction of jarosite-group compounds by Raman spectroscopy." Canadian Mineralogist **36**: 1225-1235.

Saul, P., C. R. A. Catlow, et al. (1985). "Theoretical-Studies of Protons in Sodium-Hydroxide." Philosophical Magazine B-Physics of Condensed Matter Statistical Mechanics Electronic Optical and Magnetic Properties **51**(2): 107-117.

Savage, K. S., T. N. Tingle, et al. (2000). "Arsenic speciation in pyrite and secondary weathering phases, Mother Lode Gold District, Tuolumne County, California." Applied Geochemistry **15**(8): 1219-1244.

Schempp, C. A. (1925). "Argento-jarosite: a new silver mineral." American Journal of Science **6**: 73-74.

Schnoor, J. L. (1990). Kinetics of Chemical Weathering: A Comparison of Laboratory and Field Weathering Rates. Aquatic Chemical Kinetics. W. Stumm. New York, Wiley-Interscience.

Schroder, K. P., J. Sauer, et al. (1992). "Bridging Hydroxyl-Groups in Zeolitic Catalysts - a Computer- Simulation of Their Structure, Vibrational Properties and Acidity in Protonated Faujasites (H-Y Zeolites)." Chemical Physics Letters **188**(3-4): 320-325.

Schwertmann, U. (1961). "The occurrence and origin of jarosite (maibolt) in marshy soil." Naturwissenschaften **48**: 159-160.

Schwertmann, U., Fitzpatrick, R.W. (1992). Iron minerals in surface environments. Biomineralisation Processes of Iron and Manganese-Modern and Ancient Environments. H. C. W. Skinner, R.W. Fitzpatrick. Catena Verlag, Cremlingen-Destedt, Germany**:** 7-30.

Schwertmann, U., Taylor, R.M. (1989). Iron Oxides. Minerals in Soil Environments. J. B. Dixon, S.B. Weed, Soil Science Society of America**:** 379-438.

Scott, K. M. (1987). "Solid-Solution in, and Classification of, Gossan-Derived Members of the Alunite-Jarosite Family, Northwest Queensland, Australia." American Mineralogist **72**(1-2): 178-187.

Serna, C. J., C. P. Cortina, et al. (1986). "Infrared and Raman-Study of Alunite Jarosite Compounds." Spectrochimica Acta Part a-Molecular and Biomolecular Spectroscopy **42**(6): 729-734.

Sherman, D. M. and S. R. Randall (2003). "Surface complexation of arsenie(V) to iron(III) (hydr)oxides: Structural mechanism from ab initio molecular geometries and EXAFS spectroscopy." Geochimica Et Cosmochimica Acta **67**(22): 4223-4230.

Sigg, L. and W. Stumm (1981). "The Interaction of Anions and Weak Acids with the Hydrous Goethite (Alpha-Feooh) Surface." Colloids and Surfaces **2**(2): 101-117.

Simons, F. S., Mapes, V.E. (1956). "Geology and ore deposits of the Zimapan mining district, State of Hidalgo, Mexico." US Geol Survey Prof Paper **284**.

Small, H. (1989). Ion Chromatography. New York, Plenum Press.

Smedley, P. L. and D. G. Kinniburgh (2002). "A review of the source, behaviour and distribution of arsenic in natural waters." Applied Geochemistry **17**(5): 517-568.

Steele, H. M., K. Wright, et al. (2002). "Modelling the adsorption of uranyl on the surface of goethite." Geochimica Et Cosmochimica Acta **66**(8): 1305-1310.

Steintveit, G. (1970). "Iron precipitation as jarosite and its application in the hydrometallurgy of zinc." Erzmetall **23**: 532-539.

Stoffregen, R. E. (1993). "Stability Relations of Jarosite and Natrojarosite at 150-250-Degrees-C." Geochimica Et Cosmochimica Acta **57**(11): 2417-2429.

Stoffregen, R. E., C. N. Alpers, et al. (2000). Alunite-jarosite crystallography, thermodynamics, and geochronology. Sulfate Minerals - Crystallography, Geochemistry and Environmental Significance. **40:** 453-479.

Stoffregen, R. E. and R. O. Rye (1992). "Jarosite-Water O-18 and D-Fractionations." Abstracts of Papers of the American Chemical Society **204**: 86-GEOC.

Stumm, W., Morgan, J.W (1996). Aquatic Chemistry. New York, Wiley-Interscience.

Swedlund, P. J. and J. G. Webster (2001). "Cu and Zn ternary surface complex formation with SO4 on ferrihydrite and schwertmannite." Applied Geochemistry **16**(5): 503-511.

Swedlund, P. J., J. G. Webster, et al. (2003). "The effect of SO4 on the ferrihydrite adsorption of Co, Pb and Cd: ternary complexes and site heterogeneity." Applied Geochemistry **18**(11): 1671-1689.

Tananaev, I. V., N. K. Bol'shakova, et al. (1967). "Potassium gallium alum and its hydrolysis products." Russian Journal of Inorganic Chemistry **12**: 185-188.

Tananaev, I. V., V. G. Kuznetsov, et al. (1967). "Basic gallium salts of the alunite type." Russian Journal of Inorganic Chemistry **12**(28-30).

Tasker, P. W. (1979). Journal of Chemical Physics C: Solid State Physics **12**: 4977.

Tasker, P. W., E. A. Colbourn, et al. (1985). "Segregation of Isovalent Impurity Cations at the Surfaces of Mgo and Cao." Journal of the American Ceramic Society **68**(2): 74-80.

Tasker, P. W. and D. M. Duffy (1984). "The Structure and Properties of the Stepped Surfaces of Mgo and Nio." Surface Science **137**(1): 91-102.

Turrell, G. (1972). Infrared and Raman spectra of crystals. London, Academic Press.

Van Breemen, N. (1973). Soil forming processes in acid sulphate soils. Acid Sulfate Soils; Proceedings of the International Symposium on Acid Sulphate Soils. D. Dost, Publ.18 ILRI. **I:** 66-130.

Vasilevskaya, G. B. (1970). "Minerals in the oxidation zone of the Shamyrasai complex ore deposits." Nauch Trudy Tashkent Gosudarst Univ **358**(131-134).

Walenta, K., M. Zwiener, et al. (1982). "Philipsbornite, a New Mineral of the Crandallite Series from Dundas, Tasmania." Neues Jahrbuch Fur Mineralogie-Monatshefte(1): 1-5.

Walsh, J. N. (1997). Inductively coupled plasma-atomic emission spectrometry. Modern analytical geochemistry. R. Gill, Longman**:** 41-66.

Wang, R., W. F. Bradley, et al. (1965). "The crystal structure of Alunite." Acta Crystallographica **18**: 249-252.

Wangkarn, S. and S. A. Pergantis (2000). "High-speed separation of arsenic compounds using narrow-bore high-performance liquid chromatography on-line with inductively coupled plasma mass spectrometry." Journal of Analytical Atomic Spectrometry **15**(6): 627-633.

Warshaw, C. M. (1956). "The occurrence of Jarosite in underclays." American Mineralogist **41**: 288-296.

Webster, J. G., P. J. Swedlund, et al. (1998). "Trace metal adsorption onto an acid mine drainage iron(III) oxy hydroxy sulfate." Environmental Science & Technology **32**(10): 1361-1368.

West, R. A. (1991). Basic Solid State Chemistry, Wiley.

Wilkins, R. W. T., A. Mateen, et al. (1974). "The spectroscopic study of oxonium in minerals." American Mineralogist **59**: 811-819.

Wills, A. S. (2001). "Long-range ordering and representational analysis of the jarosites." Physical Review B **6305**(6): art. no.-064430.

Wills, A. S., A. Harrison, et al. (2000). "Magnetic properties of pure and diamagnetically doped jarosites: Model kagome antiferromagnets with variable coverage of the magnetic lattice." Physical Review B **61**(9): 6156-6169.

Wilson, E. B., Decius, J.C., Cross, P.C. (1955). Molecular vibrations: The theory of infrared and Raman vibrational spectra. New York, Dover Publ. Inc.

Wolery, T. (1979). Calculation of equilibrium between aqueous solution and minerals: the EQ3/6 software package, Lawrence Livermore National Laboratory, UCRL-52658.

Wolery, T. (1996). EQ3/6 Database, Lawrence Livermore National Laboratory, USA.

Woodley, S. M., P. D. Battle, et al. (1999). "The prediction of inorganic crystal structures using a genetic algorithm and energy minimisation." Physical Chemistry Chemical Physics **1**(10): 2535-2542.

Wright, K., R. Freer, et al. (1996). "Water-related defects and oxygen diffusion in albite: A computer simulation study." Contributions to Mineralogy and Petrology **125**(2-3): 161-166.

Wright, K. V. (2003). Modelling of Point Defects and Diffusion in Earth Materials. Computational Materials Science. C. R. A. Catlow, Kotomin, E., NATO Science Series, IOP Press.

Yaroslavtsev, A. S., L. S. Getskin, et al. (1975). "Behaviour of impurities when precipitating iron from sulphate zinc solutions." Tsvetn. Metall. **16**: 41-42.

Young, R. A. (1995). Introduction to the Rietveld Method. The Rietveld Method. R. A. Young. Oxford, Oxford University Press.

Appendix A: Theory of physical and chemical analytical techniques

Appendix A describes the general background theory behind the physical and chemical experimental techniques used in this study. The techniques covered are powder X-ray diffraction, electron beam methods, inductively coupled plasma techniques, ion chromatography, Fourier-transform infrared spectroscopy, thermal gravimetric and differential thermal analysis, and surface area analysis.

A.1 Powder X-ray diffraction

X-ray powder diffraction was used to determine the phase purity of the five synthetic jarosites. Wilhelm Conrad Roentgen discovered X-rays accidentally in 1895, it was not until 1912, 17 years later that Max von Laue suggested that X-rays should be used to study crystals (Klein and Hurlbut 1993). Unlike visible light the wavelength of X-rays are similar to the atomic spacing between the constituent atoms in solids and are therefore susceptible to diffraction. The degree to which the X-rays are diffracted is both a function of the interplaner lattice spacings and element composition, and in this respect, is unique for every solid (West 1991).

Laue proposed that diffraction is the interference phenomenon caused by an object in the path of the X-ray waves. The X-ray waves that are reflected from the lattice planes but remain in phase, interfere constructively and produce a cooperative scattering effect known as diffraction. Strong signals or 'peaks' on a diffraction pattern are indicative of this. For the same reason X-rays that are reflected out of phase will result in weak or non-existent signals because of destructive interference (Klein and Hurlbut 1993). Laue created an elegant yet difficult to manipulate set of equations for the treatment of diffraction of X-rays by crystals. A major break through in X-ray diffraction came when W.L. Bragg in 1912 proposed a simple mathematical formula (Eq. A.1) to explain the diffraction phenomenon as a function of incident X-ray angle and separation between the lattice planes (McKie and McKie 1986).

$$n\lambda = 2d_{hkl} \sin\theta$$

(A.1)

Where λ is the fixed X-ray wavelength (Cu Kα λ = 1.54056 Å), n is a small number (1, 2, or 3) and is known as the order of reflection, d_{hkl} is the distance between a set of lattice places (*hkl*), and θ is the angle (commonly called the Bragg angle) of incidence and 'reflection' of the X-ray beam from a given lattice plane (*hkl*). From Bragg's law (Eq. A.1) it is possible to determine both the identity and interplaner spacings as a function of θ, which gives rise to a respective diffraction peak intensity. For a simple cubic crystal, Eq. A.2 shows how the interplaner spacings are calculated.

$$d_{hkl} = \frac{a}{\sqrt{(h^2 + k^2 + l^2)}} \tag{A.2}$$

Where *a* is equal to the length of the unit cell, which is the fundamental sub-unit of the lattice plane from which the entire crystal can be constructed by periodic repetition. The terms *h*, *k* and *l* are known as the Miller Indices and these describe a particular lattice plane in the crystal structure. The near integer experimental values for these indices can be calculated when Eq. A.2 is substituted into Braggs law (Eq. A.1) to make Eq. A.3. $\text{Sin}^2\theta$ is then multiplied by a constant. This process is known as indexing (McKie and McKie 1986).

$$\sin^2 \theta = \frac{\lambda^2}{4a^2}\left(h^2 + k^2 + l^2\right) \tag{A.3}$$

Once the cubic powder pattern has been indexed, the unit-cell edge *a* can be determined by application of the expression:

$$a = \frac{\lambda}{2\sin\theta}\sqrt{(h^2 + k^2 + l^2)} \tag{A.4}$$

McKie and McKie (1986) give a comprehensive guide to the theory of powder X-ray diffraction.

A.1.1 Rietveld refinement

In the Rietveld method, direct analysis of the profile intensities allows the maximum amount of information to be extracted from a powder diffraction pattern (Young 1995). It is a crucial feature of the Rietveld method that no effort is made in advance to allocate observed intensity to particular Bragg reflections nor to resolve overlapped reflections. Consequently, a reasonably good starting model is needed. The Rietveld method is one of structure refinement. It is not a structure solution method, *per se*, though it can be a very important part of a structure solution package (Young 1995). The starting model includes parameters that describe the crystal structure, background, and the instrumental characteristics, such as the zero-point error.

In the Rietveld method the least-squares refinements are carried out until the best fit is obtained between the entire observed powder diffraction pattern taken as a whole and the entire calculated pattern based on the simultaneously refined models for the crystal structure, instrumental factors, and other specimen characteristics (e.g. lattice parameters) as may be desired and can be modelled (Young 1995). A key feature is the feedback, during refinement, between improving knowledge of the structure and improving allocation of observed intensity to partially overlapping individual Bragg reflections. The quantity minimised in the least-squares refinement is the residual S_y (Young 1995):

$$S_y = \sum w_i \left(y_{obs}^i - y_{calc}^i \right)^2 \tag{A.5}$$

where y_{obs}^i and y_{calc}^i are the observed and calculated intensities of each data point, w_i is the weighting parameter for each data point ($w_i \propto 1/y_{obs}^i$), and the sum is carried out over all data points where y_{obs}^i is greater than 1 % of the peak height (Young 1995). The best fit is quantitatively determined by a number of R-factors of which the R_{wp}, 'the R-weighted pattern', is the most meaningful as the numerator of the residual is minimised with respect to the observed intensity. A 'goodness of fit' parameter χ^2 is also useful for watching the refinement progress. These functions are described as (Young 1995):

$$R_{wp} = \sqrt{\frac{\sum w_i \left(y_{obs}^i - y_{calc}^i \right)}{\sum w_i \left(y_{obs}^i \right)^2}} \qquad (A.6)$$

$$\chi^2 = \frac{\sum w_i \left(y_{obs}^i - y_{calc}^i \right)^2}{N_{obs} - N_{var}} \qquad (A.7)$$

where N_{obs} is the number of observables and N_{var} is the number of variables to be fitted. While these numerical criteria are important, the refined model should always make chemical sense and attention should always be paid to what the fit is graphically like: a difference plot will show whether an inflated R_{wp} is a result of a poor structural model or a failure to describe the experimental factors (Young 1995).

A more comprehensive discussion on the application of the Rietveld method towards structure refinement of materials and the underlying mathematics of the technique can be found in Young (1995).

A.2 Electron beam methods

Electron beam methods were used to determine the particle morphology of the jarosites and provided an alternative method of calculating the actual formula of synthetic potassium jarosite. A finely focused high-energy electron beam can be used to create an image in a scanning electron microscope (SEM), the electron beam also happens to generate characteristic X-rays in the parts of the specimen exposed to it, and can therefore be used as a 'chemical probe'. An SEM equipped with a suitable X-ray analyser provides a versatile, non-destructive means of analysing chemical variation on a micrometer scale on a specimen's surface. This technique is commonly referred to as electron probe microanalysis (EPMA) (Gill 1997). An SEM can be broadly broken down into four parts: the electron gun, the electron optics, scanning coils, and the energy-dispersive (ED) X-ray spectrometer for EPMA. Each part will be briefly discussed below.

The electron gun is the device that fires the electron beam towards the specimen. Free electrons are generated by thermionic emission from the tip of a hairpin-shaped tungsten filament operated at about 2400°C. The filament acts as the cathode of the

electron gun while the anode consists of a ground plate with an aperture to let the beam pass. A third electrode (the Wehnelt) has a negative bias of a few hundred volts relative to the cathode. This limits the effective emitting area of the filament close to the tip. The emission current is increased until the filament is 'saturated' and stable (Gill 1997).

Modern high-resolution SEMs may use three or even four magnetic lenses to focus the divergent electron beam from the gun to form successively smaller images. Typically, two lenses are sufficient to produce a beam focus less than 1 μm in diameter, which is adequate for conventional SEM imagery and EPMA. The first, the condenser lens, produces an intermediate de-magnifed image. The beam then passes through a smaller objective lens, which produces the final image focused at the specimen surface. Each lens consists of copper wire wound symmetrically around the axis of symmetry of the lens and encased in an iron shell with a gap in the inner cylindrical surface, across which the magnetic field is concentrated (Gill 1997).

An electron image of the specimen surface is essential for locating features of interest and displaying elemental distribution patterns (elemental mapping). To this end, an electron microscope is equipped with a set of scan coils near the objective lens, which scan the beam from side to side. The standard scan is the two-dimensional raster in which an image of an area of the specimen surface is built up of successive line scans like a TV picture (Gill 1997).

When an energy-dispersive (ED) X-ray spectrometer is attached to an SEM for microanalysis (EMPA) the key part of the detector is a Si (Li) crystal. The crystal is typically 3 mm thick and is mounted on a FET preamplifier chip at the end of a long tube extending into the evacuated chamber, pointing directly at the X-ray source. Both devices are cooled with liquid nitrogen to suppress electronic noise (Gill 1997).

General reviews of the theory and the EPMA technique are given by Gill (1997) and Potts (1987).

A.3   Inductively coupled plasma techniques

Inductively coupled plasma techniques were used extensively to provide elemental analysis. They provided total elemental concentrations in solution for the dissolution

experiments and were used to calculate the actual formulas of the synthetic jarosites. The inductively coupled plasma was originally devised as a medium for growing crystals at high temperature (Jarvis 1997), but its potential as a source for emission spectroscopy was soon recognised. Specifically, the very high temperatures of the plasma were noted, and it was appreciated that many spectral lines for the periodic elements could be produced, with atom and ion lines available for even the most refractory of elements (Walsh 1997). There are two types of inductively coupled plasma techniques: optical emission spectroscopy (ICP-OES) and mass spectroscopy (ICP-MS). Essentially the two techniques use the same type of source unit (ICP torch) to ionise elements of interest. The difference in the techniques comes in the form of the spectrometer. In ICP-OES, the spectrometer resolves the light emitted from elements in the tail flame of the ICP. For ICP-MS, the spectrometer detects the mass of ions from the mouth of the ICP torch (Jarvis 1997). Both techniques use computers to interpret the raw data from the spectrometers into numerical concentrations. ICP-OES provides near-simultaneous detection of most elements in the periodic table at levels down to 10 μg kg^{-1} (10 ppb) and ICP-MS down to 10 ng kg^{-1} (10 ppt) (Jarvis 1997). The source unit for the ICP and the two types of spectrometer will be elaborated upon individually below.

A radiofrequency generator (RF) supplies the power for the plasma. The two most important variables in RF generator design are the operating frequency and power output. The ICP torch can either be in axial (ICP-MS and ICP-OES) or radial (ICP-OES only) geometry with respect to the spectrometer, and is made from quartz glass and consists of three concentric tubes. The outermost tube carries the coolant plasma gas, which enters the tube at right angles and swirls upwards in a spiral flow. The plasma is produced when the coolant gas (Ar) reaches the top of the torch where two or three Cu coils are connected to the RF generator supplying an AC current of either 27 or 40 MHz. The temperature at the heart of the plasma is 10 000 K. The solutions to be analysed are introduced into the ICP through the central injector gas tube. The other gas flow is the auxiliary gas flow and the function of this gas inlet is simply to lift the plasma. The most widely used method for introducing the sample is the pneumatic nebuliser. The sample to be analysed is pumped through a capillary tube and converted to an aerosol by a flow of argon gas introduced into the nebuliser. The aerosol then travels up the central injector tube of the ICP torch. The efficiency of

ICP nebulisers are low, only 1-2 % of the solution is converted to useful aerosol, most of the solution goes down the drain (Walsh 1997).

The spectrometer in an ICP-OES has the job of resolving the light emitted in the tail flame of the ICP. Normally a 4 mm window of emitted light between 14 and 18 mm above the load coil is observed. There are two categories of multi-element spectrometers available, either a simultaneous (polychromator) or a sequential (monochromator) spectrometer. Both classes of spectrometer utilise a diffraction grating to disperse the incoming light radiation into separate wavelengths. A polychromator offers 20-30 fixed detector channels that can measure different wavelength components simultaneously. A monochromator detects only one wavelength at a time, but is more versatile for scanning regions of the spectrum (Walsh 1997).

Unlike the optical spectrometer of an ICP-OES instrument, a mass spectrometer must operate under high vacuum. A crucial part of an ICP-MS is the differentially pumped interface region, which transmits ions from the atmospheric pressure plasma into the mass spectrometer (Jarvis 1997). This consists of two conical nickel apertures, the sampling cone, and the skimmer, which allows ions to pass into the mass spectrometer but deflect away a majority of uncharged molecules and atoms.

The commonest form of mass analyser used in ICP-MS is a quadrupole mass filter. The quadrupole allows ions of only one mass/charge ratio (m/z) through to the detector for each combination of potentials applied (Jarvis 1997). By sweeping the potentials the mass spectrometer can be scanned very rapidly; a single scan from m/z = 4 to 240 can be collected in as little as 0.06 s (Jarvis 1997).

Walsh (1997) and Jarvis (1997) explain the theory and nuances of ICP-OES and ICP-MS, respectively, in considerably more detail.

A.4 Ion chromatography

Ion chromatography was used to calculate sulphate (SO_4^{2-}) concentrations in solution for the dissolution experiments. Ion chromatography belongs to that broad sub-classification of chromatography known as liquid chromatography. The term 'liquid chromatography' (LC) is understood to imply at least two constraints: (1) that a liquid

is used as the mobile phase and (2) that the stationary phase is contained in some sort of envelope such as a column or capillary (Small 1989).

A key element of a liquid chromatograph is the column; a tube packed with some sort of solid or gel in a finely divided form, commonly and desirably spherical. This packing is referred to as the stationary phase. A porous plug or filter supports the packing and prevents it from washing out of the tube. The interstitial or void volume of the column, i.e., the space between the packing particles, is filled with a liquid, the mobile phase that is continuously pumped through the column. In a typical chromatographic operation a volume of mobile phase, containing the species to be separated is injected into the flowing mobile phase and carried into the column, at which point the separation begins. To learn something of the composition of the injected mixture some sort of detecting device is attached to the column's terminus to monitor species as they are eluted from the column (Small 1989).

Of all the elements in a chromatographic system, the stationary phase is the key. The stationary phase determines what separation mechanism is operative, and in turn dictates the choice and composition of the mobile phase (Small 1989). Ion exchangers are the most widely used stationary phase in ion chromatography. An ion exchanger comprises of three important elements: (1) an insoluble matrix, which may be organic or inorganic; (2) fixed ionic sites attached to or an integral part of the matrix; and (3) associated with these fixed sites, an equivalent amount of ions oppositely charged to that of the fixed sites (Haddad and Jackson 1990). In this study, sulphate was measured on a DIONEX system with an anion exchange column.

While separation is the central issue in chromatography, detection of the separate species is of comparable importance. A primary requirement of a detector is that it should be responsive over a wide range of concentrations of the monitored solute. Some detectors will respond to changes in solute level when the concentration is low but be prone to 'saturation' effects and become relatively unresponsive when concentrations are high. The range of over which the detector is responsive is termed the dynamic range. There are many types of detectors available, the most common type are conductometric, however, you also can have photometers, spectrophotometers and electrochemical detectors (Haddad and Jackson 1990). The detector used in the DIONEX system was a pulsed electrochemical detector (PED).

Electrochemical detectors in general have great sensitivity and selectivity with respect to which ion(s) are being detected (Small 1989).

Ion chromatography is expanded in detail by Small (1989) and Haddad and Jackson (1990).

A.5   Fourier transform infrared spectroscopy

Over the past 50 years, vibrational spectroscopy has provided a great deal of information about the structure and bonding of molecules and crystals (Johnston and Aochi 1996). The energy of a molecule or crystal can be divided into four parts: electronic, vibrational, rotational, and translational. A large number of vibrational transitions, observed as bands, occur throughout the infrared (IR) region of the electromagnetic spectrum. These bands occur because of the interaction of the molecule or crystal with infrared (IR absorption) or visible (Raman scattering) radiation. The IR spectral range covers 10 to 10 000 cm^{-1} and is subdivided into three sub-regions, Far- (10 – 400 cm^{-1}), Mid- (400 – 4000 cm^{-1}), and Near-IR (4000 – 10 000 cm^{-1}). Most applications of vibrational spectroscopy are in the mid-IR spectral region (Johnston and Aochi 1996).

In the IR region, the wavenumber ($\bar{v}$) is the practical unit of choice of describing the electromagnetic spectrum. Eq. A.8 shows the relationship of this unit to frequency and wavelength:

$$\bar{v} = \frac{v}{(c/n)} = \frac{1}{\lambda}$$

(A.8)

where $\bar{v}$, is the wavenumber (cm^{-1}), v is frequency (s^{-1} or Hz), λ is wavelength (μm), c is velocity of light in a vacuum (2.997×10^8 ms^{-1}), and finally n is the index of refraction (McMillan and Hofmeister 1988).

Molecular vibrations occur at discrete energies in the IR region, and are referred to as vibrational or normal modes. The amount of energy required to excite a particular vibrational mode depends on the type of periodic motion involved. These modes can be divided into two categories: internal vibrational modes and phonon modes. Internal vibrational modes correspond to the periodic motion of atoms within a crystal

or molecule. Three types of motion describe them: (1) bond stretching, (2) bending, and (3) torsional motions. Internal vibrational modes are usually found in the mid-IR range, 400 to 4000 cm^{-1}. Crystalline materials also have vibrational transitions in the far-IR range, 10 to 400 cm^{-1} region, termed phonon modes resulting from the movement of one unit cell or functional unit relative to another (Johnston and Aochi 1996).

Vibrational transitions can occur because of IR absorption and Raman scattering. Direct absorption of IR radiation is the most common method used to study vibrational transitions. In order for infrared absorption to occur, two criteria must be met. Firstly, the frequency of IR radiation must match that of the vibrational mode; and secondly, the vibrational mode must produce a change in the dipole moment (Falmer 1974).

Fourier transform infrared spectrometers (FTIR) have three key components: interferometer, detector, and beamsplitters. Each one will be elaborated upon below.

The interferometer is the central component of an FTIR spectrometer. Light from the IR source is passed onto a beamsplitter, where approximately half of the incident light is reflected onto a moving mirror, and the remainder is transmitted through the beamsplitter onto a fixed mirror. The moving mirror introduces a phase difference between the reflected and transmitted beams by varying the pathlength of one beam relative to the other. Optical interference occurs when the two beams recombine at the beamsplitter. The resulting modulated IR beam is then passed through the sample onto the detector (McMillan and Hofmeister 1988).

Two types of detectors are commonly used in FTIR spectrometers for mid-IR applications, quantum detectors, and thermal detectors. The development of quantum mid-IR detectors, such as the mercury cadmium telluride (MCT) detector, has significantly improved the sensitivity of FTIR spectrometers. The MCT detector is a photoconductive detector that measures an increase in electrical conductivity when illuminated. Pyrolectric devices, such as the deuterated triglycine sulphate (DTGS) detector, measure changes in temperature. They do not require cooling and provide a uniform frequency response from far-IR through the mid-IR region. They are

characterised by lower overall sensitivities and slower response times than MCT detectors (McMillan and Hofmeister 1988).

The most commonly used beamsplitter for the mid-IR spectral region is a KBr beamsplitter with a thin, uniform coating of Ge or Si. Ideally, the beamsplitter should reflect half of the incident light and transmit the remainder (McMillan and Hofmeister 1988).

Wilson et al. (1955), Long (1977), Turrell (1972) and McMillan and Hofmeister (1988) all have excellent discussions on the theory and applications of IR absorption spectroscopy.

A.6   Thermal gravimetric and differential thermal analysis

Whenever a sample of material is to be studied, one of the easiest tests to perform is to heat it. The observation of the behaviour of the sample and the quantitative measurement of the changes on heating can yield a great deal of information on the nature of the material (Haines 2002).

Thermogravimetric analysis (TG) is a technique in which the mass change of a substance is measured as a function of temperature whilst the substance is subjected to a controlled temperature program (Heal 2002). The temperature programme must be taken to include holding the sample at a constant temperature other than ambient, when the mass change is measured against time. Mass loss is only seen if a process where a volatile component is lost. There are, of course, reactions that may take place with no mass loss. These may be detected by allied techniques of differential thermal analysis (DTA) and differential scanning calorimetry (DSC) (Heal 2002).

The modern instrumentation used for any experiment in thermal analysis is usually made up of four parts: (1) The sample and a container or holder; (2) sensors to detect and measure a particular property of the sample and to measure temperature; (3) an enclosure within which the experimental parameters (e.g. temperature, atmospheric gas) may be controlled; and (4) a computer to control the experimental parameters, such as the temperature programme. Each key part will be elaborated upon below.

In the TG apparatus, the sample is placed in a small inert crucible, which is attached to a microbalance and has a furnace positioned around the sample. Furnaces, intended to work up to $1100^{o}C$, use resistive alloy wire or ribbon such as Kanthal or Nichrome, wound on a ceramic or silica tube. For higher temperatures, reaching $1600^{o}C$, platinum or platinum/rhodium alloy is used (Heal 2002). Crucibles are made of various materials. The best ones are made of platinum. These are inert with respect to most gases and molten inorganic materials, and only melt at $1769^{o}C$ (Heal 2002).

The simplest TG experiment would be to heat the sample in static air. However, the sample may react with air by either oxidising or burning. Usually an inert gas such as nitrogen or argon is used. In some cases, a deliberately chosen reactive gas is used. A flowing purge of gas is always used (Heal 2002).

The temperature in the system is measured by thermocouples. These consist of two different metals fused together. One thermocouple is used for measuring the temperature of the sample and a second is used to measure the temperature of a reference, usually at $0^{o}C$ in melting ice. The most common thermocouple in these apparatus is platinum and platinum alloyed with 13% rhodium. As well as the thermocouple system for measurement, a second, entirely separate thermocouple system is proved to sense the furnace temperature (Heal 2002).

Differential thermal analysis (DTA) and differential scanning calorimetry (DSC) are the most widely used of all thermal analysis techniques. The concept underlying the techniques is quite simple: to obtain information on thermal changes in a sample by heating or cooling it alongside an inert reference. Unlike thermogravimetry, DTA and DSC techniques are not dependent on the sample undergoing a change in mass (Laye 2002). DSC is a more recent technique and was developed for quantitative calorimetric measurements. DTA does not lead itself to such measurements and has been progressively replaced by DSC; however, DTA still finds application in the measurement of characteristic temperatures and in quantitative identification of materials (Heal 2002).

Since TG and DTA are extremely complementary techniques, it is logical to combine them together to make a simultaneous thermogravimetric-differential thermal analysis (TG-DTA). TG is inherently quantitative, after appropriate calibration and

corrections, but responds to reactions accompanied by a mass change. DTA is capable in principle of detecting any reaction or transition that entails a change in enthalpy or heat capacity, but requires a good deal of effort before it is truly quantitative (Haines 2002).

Haines (2002) summarises the theory and the potential uses of thermogravimetric and differential thermal analysis.

A.7   Surface area analysis

The physical absorption of gases by non-porous solids gives rise to a Type II absorption isotherm in the vast majority of cases (Gregg and Sing 1982). All the jarosites studied here could be classed as non-porous solids. From the Type II isotherm of a given gas on a particular solid, it is possible in principle to derive a value of the monolayer capacity of the solid, which in turn can be used to calculate the specific surface of the solid. The monolayer capacity is defined as the amount of absorbate, which can be accommodated in a completely filled single molecular layer (a monolayer) on the surface of 1 g of solid (Gregg and Sing 1982).

To obtain the monolayer capacity from the isotherm, it is necessary to interpret the Type II isotherm in quantitative terms. A number of theories have been advanced for this purpose, none it has to be said with complete success. The best known of them and perhaps the most useful in relation to surface area determination is that of Brunauer, Emmett, and Teller. Though based on a model which is admittedly over-simplified and open to criticism on a number of grounds, the theory leads to an mathematical expression, the BET equation, which, when applied with discrimination, has proved remarkably successful in evaluating the specific surface from a Type II isotherm (Gregg and Sing 1982).

The BET treatment (Brunauer et al. 1938) is based on a kinetic model of the absorption process put forward more than sixty years ago by Langmuir (1916), in which the surface of the solid was regarded as an array of absorption sites. The BET equation (A.9) for a Type II isotherm takes the form of:

$$\frac{p}{V_A(p^o - p)} = \frac{1}{V_M C} + \frac{C-1}{V_M C}\frac{p}{p^o} \tag{A.9}$$

where V_A, is the volume of absorbate absorbed (cm^3 g^{-1}), V_M is absorbate monolayer volume (cm^3 g^{-1}), p is the sample pressure (bar), p^o is the saturation pressure (bar), and C is a constant related to the enthalpy of absorption. The surface area of all the synthetic jarosites were obtained by using multi-point analysis, in which the absorbate, N$_2$ gas, was added at five linear relative pressures 0.1-0.3. The BET function (Eq. A.9) [p/V$_A$(p^o-p)] has a directionally proportional relationship between relative pressure (p/p^o). When plotted the straight line has a slope of [C-1/(V$_M$C)] and an intercept of [1/(V$_M$C)]. Due to this relationship, the BET equation (A.9) simplifies down to Eq. A.10 (Gregg and Sing 1982):

$$S_{BET} = \frac{(V_M N_A A_m)}{M_V} \tag{A.10}$$

where S$_{BET}$, is BET surface area (m^2 g^{-1}), V$_M$ is absorbate monolayer volume (cm^3 g^{-1}), N$_A$ is Avogadros number (6.02214 x 10^{23} mol^{-1}), A$_M$ is the cross sectional area of absorbate molecule (N$_2$ gas is 0.162 mol nm^2), and M$_V$ is the gram molecular volume of the absorbate (cm^3).

One of the major criticisms of the BET model is that it assumes all the absorption sites on the surface are energetically identical. Unfortunately, Gregg and Sing (1982) state that homogenous surfaces of this kind are the exception and energetically heterogeneous surfaces are the rule. A second criticism is that the model restricts attention to the forces between the absorbent and the absorbate molecules and neglects the forces between the absorbate molecule and its neighbours in the same layer.

Gregg and Sing (1982) go into detail on the theory behind the BET technique and surface area determination of different solids in general.

Appendix B: X-ray diffraction data on the synthetic jarosites

(*hkl*)	*d*(calc)	(*hkl*)	*d*(calc)	(*hkl*)	*d*(calc)
Synthetic $KFe_3(SO_4)_2(OH)_6$ $a = 7.3137(6)$ $c = 17.0730(5)$		Synthetic $Pb_{0.5}Fe_3(SO_4)_2(OH)_6$ $a = 7.3447(7)$ $c = 16.9700(5)$		Synthetic $PbFe_3(SO_4)(AsO_4)(OH)_6$ $a = 7.3417(8)$ $c = 16.9213(6)$	
101	5.938	101	5.956	101	5.951
00$\underline{3}$	5.691	00$\underline{3}$	5.656	00$\underline{3}$	5.640
102	5.086	102	5.089	102	5.082
110	3.657	110	3.672	110	3.670
10$\underline{4}$	3.539	10$\underline{4}$	3.529	10$\underline{4}$	3.522
201	3.113	201	3.126	201	3.124
11$\underline{3}$	3.076	11$\underline{3}$	3.080	11$\underline{3}$	3.076
105	3.005	105	2.994	105	2.987
202	2.969	00$\underline{6}$	2.828	202	2.975
00$\underline{6}$	2.845	204	2.544	00$\underline{6}$	2.820
204	2.543	21$\underline{1}$	2.380	204	2.541
21$\underline{1}$	2.370	212	2.313	211	2.379
212	2.305	107	2.265	205	2.317
107	2.276	30$\underline{3}$	1.985	107	2.259
303	1.979	207	1.928	116	2.236
009	1.897	009	1.885	300	2.119
220	1.828	220	1.836	214	1.089
208	1.769	208	1.764	220	1.835
223	1.740	223	1.746	223	1.745
312	1.720	312	1.727	217	1.704
119	1.683	217	1.707	306	1.694
10$\underline{1}$0	1.648	119	1.677	119	1.673
31$\underline{4}$	1.624	40$\underline{1}$	1.583	10$\underline{1}$0	1.635
218	1.593	402	1.563	402	1.562
401	1.576	226	1.540	226	1.538
31$\underline{5}$	1.562	2010	1.497	2010	1.493
402	1.566	404	1.489	40$\underline{4}$	1.488
226	1.538			317	1.424
1011	1.507			309	1.406
404	1.484			410	1.387
32$\underline{1}$	1.447			413	1.347
40$\underline{5}$	1.436			1112	1.316
32$\underline{2}$	1.432			1013	1.275
31$\underline{7}$	1.425			327	1.248
309	1.411			3110	1.220
2011	1.393				
410	1.382				
413	1.343				

(*hkl*)	*d*(calc)	(*hkl*)	*d*(calc)
	Synthetic		Synthetic
	$Pb(Fe,Cu)_3(SO_4)_2(OH)_6$		$Pb(Fe,Zn)_3(SO_4)_2(OH)_6$
	a = 7.3208(8)		a = 7.3373(7)
	c = 17.0336(7)		c = 16.9268(7)
101	5.941	101	5.948
00$\underline{3}$	5.677	00$\underline{3}$	5.641
102	5.085	102	5.081
110	3.660	110	3.668
10$\underline{4}$	3.535	10$\underline{4}$	3.531
201	3.116	201	3.122
11$\underline{3}$	3.076	11$\underline{3}$	3.075
105	3.009	105	2.987
202	2.970	202	2.974
00$\underline{6}$	2.838	00$\underline{6}$	2.820
204	2.542	204	2.540
211	2.373	211	2.377
20$\underline{5}$	2.320	20$\underline{5}$	2.136
212	2.306	212	2.310
107	2.271	107	2.259
30$\underline{3}$	1.980	30$\underline{3}$	1.982
21$\underline{5}$	1.960	21$\underline{5}$	1.958
207	1.930	207	1.924
009	1.892	009	1.880
220	1.830	220	1.834
208	1.767	208	1.760
312	1.722	312	1.725
119	1.681	119	1.673
226	1.538	226	1.537
101$\overline{1}$	1.504	101$\overline{1}$	1.495

Appendix C: Dissolution raw data

Appendix C contains the aqueous and residual solid raw elemental data for the acid and alkali dissolutions of potassium jarosite, plumbojarosite, and beudantite. The appendix also contains data on aqueous speciation modelling of both sets of acid and alkali dissolutions.

C.1 Acid dissolution raw data

Raw Data of Acid (pH 2) Dissolution of Potassium Jarosite, Bottle 1

Sample No.	Time (hrs)	pH	Raw ICP Values K_{tot} (ppm)	Fe_{tot} (ppm)	S_{tot} (ppm)	DIONEX $[SO_4^{2-}]$	ICP $[SO_4^{2-}]$	K_{tot} (mmol/L)	Fe_{tot} (mmol/L)	DIONEX $[SO_4^{2-}]$ (mmol/L)	ICP $[SO_4^{2-}]$ (mmol/L)
K-1-1	4.750	2.016	2.092	0.129	0.217	0.42	0.6511	0.0535	0.0023	0.0044	0.0068
K-1-2	8.600	1.982	2.423	0.221	0.291	0.78	0.8709	0.0620	0.0040	0.0081	0.0091
K-1-3	24.833	2.008	2.618	0.720	0.454	1.25	1.3610	0.0670	0.0129	0.0130	0.0142
K-1-4	31.250	2.007	2.874	0.866	0.545	1.42	1.6339	0.0735	0.0155	0.0148	0.0170
K-1-5	55.600	1.985	2.825	1.628	0.878	2.64	2.6297	0.0722	0.0292	0.0275	0.0274
K-1-6	79.250	1.991	3.197	2.319	1.190	3.96	3.5656	0.0818	0.0415	0.0412	0.0371
K-1-7	97.566	2.010	3.383	2.854	1.432	5.03	4.2918	0.0865	0.0511	0.0524	0.0447
K-1-8	103.366	2.005	3.021	2.904	1.423	6.21	4.2627	0.0773	0.0520	0.0646	0.0444
K-1-9	146.083	2.065	4.369	4.758	2.270	6.58	6.8024	0.1118	0.0852	0.0685	0.0708
K-1-10	151.600	2.019	4.071	4.937	2.366	7.05	7.0881	0.1041	0.0884	0.0734	0.0738
K-1-11	175.500	1.994	4.424	5.630	2.718	7.76	8.1439	0.1131	0.1008	0.0808	0.0848
K-1-12	200.083	1.981	4.296	6.132	2.994	9.03	8.9703	0.1099	0.1098	0.0940	0.0934
K-1-13	223.633	1.991	4.799	6.543	3.090	9.24	9.2582	0.1227	0.1172	0.0962	0.0964
K-1-14	247.450	1.993	5.279	6.889	3.293	9.74	9.8660	0.1350	0.1234	0.1014	0.1027
K-1-15	288.016	2.041	5.470	7.838	3.800	12.25	11.3840	0.1399	0.1404	0.1275	0.1185
K-1-16	310.333	2.028	5.627	8.332	4.011	12.03	12.0190	0.1439	0.1492	0.1252	0.1251
K-1-17	338.916	1.972	5.820	8.497	4.197	12.53	12.5758	0.1489	0.1522	0.1304	0.1309
K-1-18	362.500	1.994	5.785	9.117	4.379	12.98	13.1198	0.1480	0.1633	0.1351	0.1366
K-1-19	386.083	1.990	6.029	9.479	4.561	13.38	13.6661	0.1542	0.1697	0.1393	0.1423
K-1-20	1003.628	1.999	7.695	13.907	7.025	21.11	21.0467	0.1968	0.2490	0.2198	0.2191
K-1-21	1209.999	2.007	8.066	15.292	7.566	22.47	22.6702	0.2063	0.2738	0.2339	0.2360
K-1-22	1358.218	2.106	8.238	16.186	7.990	23.83	23.9382	0.2107	0.2898	0.2481	0.2492
K-1-23	1511.817	2.024	8.524	16.811	8.227	24.52	24.6491	0.2180	0.3010	0.2553	0.2566
K-1-24	1756.666	2.033	8.657	17.347	8.384	25.24	25.1198	0.2214	0.3106	0.2627	0.2615
K-1-25	2001.116	2.041	8.717	17.826	8.628	25.73	25.8499	0.2230	0.3192	0.2678	0.2691
K-1-26	2885.833	2.041	9.173	18.397	9.131	27.39	27.3587	0.2346	0.3294	0.2851	0.2848
K-1-27	3026.683	2.046	9.214	18.695	8.952	26.67	26.8207	0.2357	0.3348	0.2776	0.2792
K-1-28	3079.833	2.047	9.504	18.458	8.882	26.48	26.6128	0.2431	0.3305	0.2757	0.2770
K-1-29	3192.500	2.043	9.471	18.935	9.156	27.58	27.4317	0.2422	0.3391	0.2871	0.2856

Raw Data of Acid (pH 2) Dissolution of Potassium Jarosite, Bottle 2

Sample No.	Time (hrs)	pH	Raw ICP Values			DIONEX $[SO_4^{2-}]$	ICP $[SO_4^{2-}]$	K_{tot} (mmol/L)	Fe_{tot} (mmol/L)	DIONEX $[SO_4^{2-}]$ (mmol/L)	ICP $[SO_4^{2-}]$ (mmol/L)
			K_{tot} (ppm)	Fe_{tot} (ppm)	S_{tot} (ppm)						
K-2-1	4.500	2.005	0.545	0.186	0.229	0.43	0.6866	0.0139	0.0033	0.0045	0.0071
K-2-2	8.083	1.972	0.687	0.306	0.342	0.78	1.0261	0.0176	0.0055	0.0081	0.0107
K-2-3	24.383	1.994	0.899	0.921	0.576	1.49	1.7247	0.0230	0.0165	0.0155	0.0180
K-2-4	30.500	1.971	1.100	1.116	0.638	1.62	1.9129	0.0281	0.0200	0.0169	0.0199
K-2-5	55.200	1.967	1.654	2.226	1.081	3.12	3.2375	0.0423	0.0399	0.0325	0.0337
K-2-6	78.800	1.973	1.763	3.057	1.535	4.36	4.5979	0.0451	0.0547	0.0454	0.0479
K-2-7	97.150	2.006	3.183	3.692	1.811	5.30	5.4268	0.0814	0.0661	0.0552	0.0565
K-2-8	102.883	1.996	2.004	3.914	1.902	5.54	5.6988	0.0513	0.0701	0.0577	0.0593
K-2-9	145.566	2.044	2.621	6.335	3.043	8.89	9.1180	0.0670	0.1134	0.0925	0.0949
K-2-10	151.233	2.000	2.613	6.500	3.119	8.27	9.3459	0.0668	0.1164	0.0861	0.0973
K-2-11	175.116	1.970	2.960	7.177	3.307	9.68	9.9078	0.0757	0.1285	0.1008	0.1031
K-2-12	199.833	1.954	3.507	8.046	3.794	11.35	11.3672	0.0897	0.1441	0.1182	0.1183
K-2-13	223.250	1.989	3.357	8.587	4.024	12.13	12.0555	0.0859	0.1538	0.1263	0.1255
K-2-14	247.000	1.974	3.619	9.313	4.257	12.95	12.7543	0.0926	0.1668	0.1348	0.1328
K-2-15	287.583	2.020	4.293	10.507	4.835	13.78	14.4880	0.1098	0.1881	0.1434	0.1508
K-2-16	309.833	2.012	4.187	10.615	5.050	15.35	15.1306	0.1071	0.1901	0.1598	0.1575
K-2-17	338.416	1.952	4.408	11.237	5.256	15.49	15.7467	0.1127	0.2012	0.1612	0.1639
K-2-18	362.000	1.978	4.287	11.402	5.412	16.51	16.2162	0.1096	0.2042	0.1719	0.1688
K-2-19	385.583	1.968	4.455	11.773	5.649	16.39	16.9255	0.1139	0.2108	0.1706	0.1762
K-2-20	1003.245	1.976	6.121	16.202	8.112	24.16	24.3051	0.1565	0.2901	0.2515	0.2530
K-2-21	1209.616	1.984	6.492	17.587	8.654	25.73	25.9285	0.1660	0.3149	0.2678	0.2699
K-2-22	1357.835	1.995	6.664	18.480	9.077	27.35	27.1966	0.1704	0.3309	0.2847	0.2831
K-2-23	1511.434	2.002	6.949	19.106	9.314	27.75	27.9074	0.1777	0.3421	0.2889	0.2905
K-2-24	1756.283	2.009	7.082	19.820	9.471	28.64	28.3781	0.1811	0.3549	0.2981	0.2954
K-2-25	2000.733	2.018	7.403	20.641	9.715	29.21	29.1082	0.1893	0.3696	0.3041	0.3030
K-2-26	2885.333	2.025	8.445	22.109	10.624	31.76	31.8318	0.2160	0.3959	0.3306	0.3314
K-2-27	3026.250	2.023	8.166	22.390	10.740	32.29	32.1800	0.2089	0.4009	0.3361	0.3350
K-2-28	3079.333	2.025	7.758	22.738	10.386	31.83	31.1191	0.1984	0.4072	0.3313	0.3239
K-2-29	3192.083	2.015	8.165	21.779	10.585	32.01	31.7136	0.2088	0.3900	0.3332	0.3301

Raw Data of Acid (pH 2) Dissolution of Potassium Jarosite, Bottle 3

Sample No.	Time (hrs)	pH	Raw ICP Values K_{tot} (ppm)	Fe_{tot} (ppm)	S_{tot} (ppm)	DIONEX $[SO_4^{2-}]$	ICP $[SO_4^{2-}]$	K_{tot} (mmol/L)	Fe_{tot} (mmol/L)	DIONEX $[SO_4^{2-}]$ (mmol/L)	ICP $[SO_4^{2-}]$ (mmol/L)
K-3-1	4.333	2.010	0.477	0.301		0.31	0.000	0.0122	0.0054	0.0032	0.0022
K-3-2	7.916	1.974	0.548	0.431	0.072	0.43	0.216	0.0140	0.0077	0.0045	0.0111
K-3-3	24.283	2.001	0.886	1.014	0.355	1.32	1.064	0.0227	0.0182	0.0137	0.0140
K-3-4	30.416	1.995	1.049	1.272	0.447	1.41	1.341	0.0268	0.0228	0.0147	0.0311
K-3-5	55.100	1.983	1.358	2.384	0.997	3.34	2.987	0.0347	0.0427	0.0348	0.0463
K-3-6	78.700	1.987	1.706	3.304	1.484	4.41	4.446	0.0436	0.0592	0.0459	0.0539
K-3-7	97.083	2.019	2.155	4.003	1.727	5.55	5.174	0.0551	0.0717	0.0578	0.0561
K-3-8	102.716	2.001	2.063	4.117	1.798	5.75	5.388	0.0528	0.0737	0.0599	0.0951
K-3-9	145.416	2.039	2.587	6.566	3.050	8.73	9.137	0.0662	0.1176	0.0909	0.0980
K-3-10	151.083	2.008	2.839	6.765	3.143	9.03	9.416	0.0726	0.1211	0.0940	0.1076
K-3-11	174.916	1.984	2.971	7.770	3.450	10.09	10.337	0.0760	0.1391	0.1050	0.1176
K-3-12	199.583	1.971	3.081	8.210	3.770	11.56	11.296	0.0788	0.1470	0.1203	0.1311
K-3-13	223.000	2.001	3.331	8.915	4.203	12.47	12.593	0.0852	0.1596	0.1298	0.1327
K-3-14	246.833	1.984	3.775	9.342	4.254	13.24	12.746	0.0965	0.1673	0.1378	0.1521
K-3-15	287.333	2.033	4.197	10.692	4.876	14.85	14.609	0.1073	0.1915	0.1546	0.1585
K-3-16	309.666	2.020	4.251	11.204	5.082	15.81	15.228	0.1087	0.2006	0.1646	0.1688
K-3-17	338.250	1.964	4.250	11.603	5.411	16.57	16.213	0.1087	0.2078	0.1725	0.1749
K-3-18	361.833	1.987	4.569	11.969	5.608	16.44	16.802	0.1169	0.2143	0.1711	0.1764
K-3-19	385.416	1.979	4.633	12.342	5.655	16.62	16.942	0.1185	0.2210	0.1730	0.2532
K-3-20	1003.045	1.987	6.299	16.770	8.118	24.12	24.323	0.1611	0.3003	0.2511	0.2701
K-3-21	1209.416	1.995	6.670	18.155	8.660	25.83	25.947	0.1706	0.3251	0.2689	0.2833
K-3-22	1357.635	2.002	6.842	19.049	9.083	27.53	27.215	0.1750	0.3411	0.2866	0.2907
K-3-23	1511.234	2.011	7.128	19.674	9.320	27.62	27.925	0.1823	0.3523	0.2875	0.2956
K-3-24	1756.083	2.019	7.261	20.389	9.477	28.15	28.396	0.1857	0.3651	0.2930	0.3032
K-3-25	2000.533	2.024	7.581	21.210	9.721	29.24	29.126	0.1939	0.3798	0.3044	0.3311
K-3-26	2885.016	2.034	8.075	21.323	10.617	31.52	31.811	0.2065	0.3818	0.3281	0.3300
K-3-27	3026.000	2.029	8.557	21.104	10.579	31.73	31.697	0.2188	0.3779	0.3303	0.3423
K-3-28	3079.167	2.031	8.236	21.921	10.976	32.53	32.886	0.2107	0.3925	0.3386	0.3307
K-3-29	3191.833	2.026	7.993	21.801	10.604	31.74	31.771	0.2044	0.3904	0.3304	0.3307

Raw Data of Acid (pH 2) Dissolution of Plumbojarosite, Bottle 1

Sample No.	Time (hrs)	pH	Raw ICP Values			DIONEX $[SO_4^{2-}]$	ICP $[SO_4^{2-}]$	Pb_{tot} (mmol/L)	Fe_{tot} (mmol/L)	DIONEX $[SO_4^{2-}]$ (mmol/L)	ICP $[SO_4^{2-}]$ (mmol/L)
			Pb_{tot} (ppm)	Fe_{tot} (ppm)	S_{tot} (ppm)						
Pb-1-1	27.666	1.978	0.699	2.077	0.940	2.79	2.816	0.0034	0.0372	0.0290	0.0293
Pb-1-2	68.583	2.040	0.952	3.716	1.637	4.92	4.906	0.0046	0.0665	0.0512	0.0511
Pb-1-3	120.999	1.968	1.522	8.298	3.474	10.23	10.408	0.0073	0.1486	0.1065	0.1083
Pb-1-4	171.583	1.952	1.827	11.047	4.634	13.92	13.884	0.0088	0.1978	0.1449	0.1445
Pb-1-5	188.666	2.016	1.874	11.538	4.804	14.15	14.393	0.0090	0.2066	0.1473	0.1498
Pb-1-6	213.416	2.104	1.962	12.331	5.118	15.43	15.333	0.0095	0.2208	0.1606	0.1596
Pb-1-7	289.166	2.104	2.040	13.144	5.494	16.49	16.461	0.0098	0.2354	0.1717	0.1714
Pb-1-8	335.999	2.081	2.115	13.907	5.786	17.21	17.336	0.0102	0.2490	0.1792	0.1805
Pb-1-9	384.749	1.956	2.113	14.071	5.895	17.73	17.663	0.0102	0.2520	0.1846	0.1839
Pb-1-10	456.915	1.982	2.104	14.209	5.953	17.80	17.835	0.0102	0.2544	0.1853	0.1857
Pb-1-11	529.165	2.008	2.115	14.347	6.010	18.09	18.007	0.0102	0.2569	0.1883	0.1874
Pb-1-12	601.248	2.034	2.127	14.485	6.067	18.21	18.178	0.0103	0.2594	0.1896	0.1892
Pb-1-13	673.748	2.061	2.135	14.622	6.125	18.37	18.350	0.0103	0.2618	0.1912	0.1910
Pb-1-14	744.583	2.114	2.149	14.760	6.182	18.41	18.522	0.0104	0.2643	0.1916	0.1928
Pb-1-15	838.416	2.039	2.153	14.852	6.160	18.53	18.455	0.0104	0.2660	0.1929	0.1921
Pb-1-16	910.249	2.052	2.161	14.940	6.269	18.69	18.782	0.0104	0.2689	0.1946	0.1955
Pb-1-17	1006.166	2.025	2.167	14.991	6.270	18.73	18.787	0.0105	0.2694	0.1950	0.1956
Pb-1-18	1078.249	2.034	2.182	15.017	6.238	18.71	18.691	0.0105	0.2699	0.1948	0.1946
Pb-1-19	1225.166	2.058	2.194	15.042	6.206	18.79	18.596	0.0106	0.2722	0.1956	0.1936
Pb-1-20	1321.249	2.058	2.201	15.072	6.250	18.83	18.725	0.0106	0.2699	0.1960	0.1949
Pb-1-21	1417.499	2.065	2.218	15.203	6.293	18.82	18.855	0.0107	0.2722	0.1959	0.1963
Pb-1-22	1513.832	2.061	2.224	15.335	6.336	18.85	18.984	0.0107	0.2746	0.1962	0.1976
Pb-1-23	1609.916	2.059	2.231	15.467	6.379	18.91	19.114	0.0108	0.2770	0.1969	0.1990
Pb-1-24	1706.082	2.063	2.236	15.599	6.423	18.97	19.243	0.0108	0.2793	0.1975	0.2003
Pb-1-25	1896.583	2.063	2.239	15.613	6.466	18.93	19.373	0.0108	0.2796	0.1971	0.2017
Pb-1-26	2205.249	2.073	2.238	15.621	6.424	18.95	19.248	0.0108	0.2797	0.1973	0.2004

Raw Data of Acid (pH 2) Dissolution of Plumbojarosite, Bottle 2

Sample No.	Time (hrs)	Raw ICP Values				DIONEX [SO$_4^{2-}$]	ICP [SO$_4^{2-}$]	Pb$_{tot}$ (mmol/L)	Fe$_{tot}$ (mmol/L)	DIONEX [SO$_4^{2-}$] (mmol/L)	ICP [SO$_4^{2-}$] (mmol/L)
		pH	Pb$_{tot}$ (ppm)	Fe$_{tot}$ (ppm)	S$_{tot}$ (ppm)						
Pb-2-1	27.833	1.958	0.724	2.187	0.958	2.52	2.872	0.0035	0.0392	0.0262	0.0299
Pb-2-2	68.749	2.030	1.211	5.023	2.134	6.13	6.394	0.0058	0.0899	0.0638	0.0666
Pb-2-3	121.249	1.964	2.218	11.948	5.005	15.04	14.997	0.0107	0.2140	0.1566	0.1561
Pb-2-4	171.749	1.954	2.706	15.551	6.488	19.63	19.439	0.0131	0.2785	0.2044	0.2024
Pb-2-5	188.833	2.012	2.717	15.925	6.627	19.78	19.855	0.0131	0.2852	0.2059	0.2067
Pb-2-6	213.583	2.096	2.849	16.284	6.744	20.15	20.206	0.0138	0.2916	0.2098	0.2103
Pb-2-7	289.333	2.096	3.036	18.391	7.653	23.01	22.929	0.0147	0.3293	0.2395	0.2387
Pb-2-8	336.249	2.081	3.107	19.200	7.924	23.85	23.740	0.0150	0.3438	0.2483	0.2471
Pb-2-9	384.916	1.953	3.126	19.491	8.003	24.11	23.978	0.0151	0.3490	0.2510	0.2496
Pb-2-10	457.165	2.031	3.150	19.885	8.191	24.73	24.541	0.0152	0.3561	0.2574	0.2555
Pb-2-11	529.248	2.056	3.192	20.279	8.379	25.21	25.103	0.0154	0.3631	0.2624	0.2613
Pb-2-12	601.748	2.071	3.234	20.673	8.566	25.88	25.666	0.0156	0.3702	0.2694	0.2672
Pb-2-13	673.998	2.963	3.277	21.067	8.754	26.34	26.229	0.0158	0.3772	0.2742	0.2730
Pb-2-14	744.749	2.108	3.319	21.856	8.942	26.81	26.793	0.0160	0.3914	0.2791	0.2789
Pb-2-15	838.583	2.038	3.308	21.916	9.019	27.12	27.022	0.0160	0.3924	0.2823	0.2813
Pb-2-16	910.416	2.039	3.312	22.073	9.157	27.57	27.437	0.0160	0.3953	0.2870	0.2856
Pb-2-17	1006.333	2.018	3.336	22.321	9.202	27.72	27.571	0.0161	0.3997	0.2886	0.2870
Pb-2-18	1078.853	2.023	3.351	22.541	9.294	27.91	27.845	0.0162	0.4036	0.2905	0.2899
Pb-2-19	1225.333	2.053	3.373	22.924	9.436	28.39	28.272	0.0163	0.4105	0.2955	0.2943
Pb-2-20	1321.416	2.056	3.381	23.084	9.488	28.52	28.426	0.0163	0.4134	0.2969	0.2959
Pb-2-21	1417.583	2.061	3.390	23.244	9.539	28.42	28.580	0.0164	0.4162	0.2958	0.2975
Pb-2-22	1514.083	2.059	3.398	23.403	9.590	28.78	28.734	0.0164	0.4191	0.2996	0.2991
Pb-2-23	1610.166	2.064	3.407	23.563	9.642	28.81	28.889	0.0164	0.4219	0.2999	0.3007
Pb-2-24	1706.333	2.066	3.410	23.654	9.693	29.03	29.043	0.0165	0.4236	0.3022	0.3023
Pb-2-25	1896.916	2.069	3.416	23.723	9.745	28.89	29.197	0.0165	0.4248	0.3007	0.3039
Pb-2-26	2205.416	2.074	3.442	23.578	9.752	28.92	29.220	0.0166	0.4222	0.3011	0.3042

Raw Data of Acid (pH 2) Dissolution of Plumbojarosite, Bottle 3

Sample No.	Time (hrs)	pH	Raw ICP Values			DIONEX [SO$_4^{2-}$]	ICP [SO$_4^{2-}$]	Pb tot (mmol/L)	Fe tot (mmol/L)	DIONEX [SO$_4^{2-}$] (mmol/L)	ICP [SO$_4^{2-}$] (mmol/L)
			Pb tot (ppm)	Fe tot (ppm)	S tot (ppm)						
Pb-3-1	28.083	1.952	0.915	3.998	1.686	4.89	5.052	0.0044	0.0716	0.0509	0.0526
Pb-3-2	68.916	2.011	1.728	8.845	3.704	11.32	11.099	0.0083	0.1584	0.1178	0.1155
Pb-3-3	120.750	1.952	2.962	16.633	6.925	20.83	20.747	0.0143	0.2978	0.2168	0.2160
Pb-3-4	171.333	1.946	3.393	19.814	8.277	24.97	24.800	0.0164	0.3548	0.2599	0.2582
Pb-3-5	188.250	2.002	3.451	20.223	8.478	25.32	25.401	0.0167	0.3621	0.2636	0.2644
Pb-3-6	213.083	2.082	3.584	21.287	8.788	26.89	26.331	0.0173	0.3812	0.2799	0.2741
Pb-3-7	288.916	2.083	3.665	22.114	9.095	27.31	27.251	0.0177	0.3960	0.2843	0.2837
Pb-3-8	335.833	2.071	3.843	23.398	9.585	28.85	28.718	0.0185	0.4190	0.3003	0.2990
Pb-3-9	384.500	1.945	3.864	23.685	9.738	29.22	29.176	0.0186	0.4241	0.3042	0.3037
Pb-3-10	456.666	1.974	3.902	24.128	9.917	29.86	29.712	0.0188	0.4320	0.3108	0.3093
Pb-3-11	528.750	2.003	3.940	24.570	10.096	30.32	30.248	0.0190	0.4400	0.3156	0.3149
Pb-3-12	601.250	2.032	3.978	25.013	10.275	30.87	30.784	0.0192	0.4479	0.3214	0.3205
Pb-3-13	673.333	2.061	4.016	25.456	10.454	31.51	31.321	0.0194	0.4558	0.3280	0.3260
Pb-3-14	744.250	2.090	4.054	25.898	10.632	31.79	31.857	0.0196	0.4638	0.3309	0.3316
Pb-3-15	838.166	2.030	3.977	25.711	10.441	31.68	31.282	0.0192	0.4604	0.3298	0.3256
Pb-3-16	910.000	2.021	4.083	26.174	10.822	32.33	32.424	0.0197	0.4687	0.3366	0.3375
Pb-3-17	1005.916	2.003	4.031	26.063	10.745	32.27	32.195	0.0195	0.4667	0.3359	0.3351
Pb-3-18	1078.082	2.021	4.039	26.214	10.786	32.41	32.316	0.0195	0.4694	0.3374	0.3364
Pb-3-19	1224.916	2.043	4.047	26.364	10.826	32.48	32.437	0.0195	0.4721	0.3381	0.3377
Pb-3-20	1320.999	2.045	4.041	26.401	10.855	32.68	32.524	0.0195	0.4728	0.3402	0.3386
Pb-3-21	1417.165	2.047	4.034	26.438	10.884	32.83	32.610	0.0195	0.4734	0.3418	0.3395
Pb-3-22	1513.415	2.049	4.028	26.475	10.913	32.91	32.697	0.0194	0.4741	0.3426	0.3404
Pb-3-23	1609.499	2.051	4.021	26.878	10.942	33.17	32.784	0.0194	0.4813	0.3453	0.3413
Pb-3-24	1705.582	2.053	4.015	27.107	10.971	33.35	32.870	0.0194	0.4854	0.3472	0.3422
Pb-3-25	1896.500	2.056	4.008	27.146	11.000	33.42	32.957	0.0193	0.4861	0.3479	0.3431
Pb-3-26	2205.000	2.074	4.060	27.212	11.078	33.49	33.193	0.0196	0.4873	0.3487	0.3455

Raw Data of Acid (pH 2) Dissolution of Beudantite, Bottle 1

Sample No.	Time (hrs)	pH	Raw ICP Values				DIONEX [SO$_4^{2-}$]	ICP [SO$_4^{2-}$]	ICP [AsO$_4^{3-}$]	Pb$_{tot}$ (mmol/L)	Fe$_{tot}$ (mmol/L)	DIONEX [SO$_4^{2-}$] (mmol/L)	ICP [SO$_4^{2-}$] (mmol/L)	ICP [AsO$_4^{3-}$] (mmol/L)
			Pb$_{tot}$ (ppm)	Fe$_{tot}$ (ppm)	S$_{tot}$ (ppm)	As$_{tot}$ (ppm)								
PbAs-1-1	29.000	1.991	0.047	3.464	0.459	2.445	1.36	1.376	4.534	0.000225	0.0620	0.0142	0.0143	0.0326
PbAs-1-2	69.833	2.046	0.029	3.718	0.421	2.748	1.25	1.262	5.095	0.000141	0.0666	0.0130	0.0131	0.0367
PbAs-1-3	121.667	1.977	0.025	3.909	0.399	2.939	1.18	1.195	5.450	0.000120	0.0700	0.0123	0.0124	0.0392
PbAs-1-4	172.250	1.961	0.019	3.996	0.398	3.037	1.18	1.191	5.631	0.000090	0.0716	0.0123	0.0124	0.0405
PbAs-1-5	189.167	2.023	0.018	3.963	0.394	2.969	1.17	1.182	5.506	0.000086	0.0710	0.0122	0.0123	0.0396
PbAs-1-6	214.000	2.124	0.018	4.004	0.383	3.043	1.14	1.147	5.642	0.000085	0.0717	0.0118	0.0119	0.0406
PbAs-1-7	289.833	2.107	0.016	3.991	0.389	2.992	1.15	1.165	5.547	0.000075	0.0715	0.0120	0.0121	0.0399
PbAs-1-8	336.750	2.098	0.014	3.993	0.380	2.938	1.13	1.139	5.448	0.000069	0.0715	0.0117	0.0119	0.0392
PbAs-1-9	385.417	1.965	0.014	4.001	0.386	2.993	1.14	1.155	5.550	0.000070	0.0716	0.0119	0.0120	0.0399
PbAs-1-10	457.583	1.994	0.014	4.007	0.394	3.010	1.17	1.181	5.582	0.000069	0.0717	0.0122	0.0123	0.0402
PbAs-1-11	529.667	2.023	0.014	4.012	0.399	3.027	1.18	1.196	5.613	0.000068	0.0718	0.0123	0.0125	0.0404
PbAs-1-12	602.167	2.055	0.014	4.017	0.411	3.044	1.22	1.231	5.645	0.000066	0.0719	0.0127	0.0128	0.0406
PbAs-1-13	674.250	2.079	0.014	4.022	0.424	3.062	1.26	1.269	5.677	0.000066	0.0720	0.0131	0.0132	0.0409
PbAs-1-14	745.167	2.110	0.014	4.028	0.428	3.079	1.27	1.282	5.708	0.000065	0.0721	0.0132	0.0133	0.0411
PbAs-1-15	839.083	2.054	0.013	4.037	0.446	3.016	1.32	1.337	5.592	0.000062	0.0723	0.0138	0.0139	0.0403
PbAs-1-16	910.917	2.046	0.012	4.017	0.448	3.045	1.33	1.341	5.645	0.000060	0.0719	0.0138	0.0140	0.0406
PbAs-1-17	1006.833	2.037	0.012	4.001	0.449	3.031	1.33	1.344	5.621	0.000058	0.0716	0.0139	0.0140	0.0405
PbAs-1-18	1078.999	2.045	0.012	4.017	0.456	3.055	1.35	1.366	5.664	0.000058	0.0719	0.0141	0.0142	0.0408
PbAs-1-19	1225.833	2.059	0.012	4.033	0.461	3.078	1.37	1.381	5.706	0.000058	0.0722	0.0142	0.0144	0.0411
PbAs-1-20	1321.916	2.063	0.012	4.033	0.462	3.076	1.37	1.383	5.703	0.000058	0.0722	0.0143	0.0144	0.0411
PbAs-1-21	1418.082	2.068	0.012	4.033	0.463	3.074	1.37	1.386	5.700	0.000058	0.0722	0.0143	0.0144	0.0410
PbAs-1-22	1514.332	2.072	0.012	4.034	0.463	3.072	1.37	1.389	5.697	0.000058	0.0722	0.0143	0.0145	0.0410
PbAs-1-23	1610.416	2.078	0.012	4.034	0.464	3.071	1.38	1.391	5.694	0.000059	0.0722	0.0143	0.0145	0.0410
PbAs-1-24	1706.499	2.081	0.012	4.035	0.465	3.069	1.38	1.394	5.690	0.000058	0.0722	0.0144	0.0145	0.0410
PbAs-1-25	1897.417	2.086	0.012	4.035	0.466	3.067	1.38	1.396	5.687	0.000058	0.0723	0.0144	0.0145	0.0409
PbAs-1-26	2205.917	2.096	0.012	4.040	0.473	3.026	1.38	1.418	5.611	0.000059	0.0723	0.0144	0.0148	0.0404

Raw Data of Acid (pH 2) Dissolution of Beudantite, Bottle 2

| Sample No. | Time (hrs) | pH | Raw ICP Values | | | | DIONEX [SO$_4^{2-}$] | ICP [SO$_4^{2-}$] | ICP [AsO$_4^{3-}$] | Pb$_{tot}$ (mmol/L) | Fe$_{tot}$ (mmol/L) | DIONEX [SO$_4^{2-}$] (mmol/L) | ICP [SO$_4^{2-}$] (mmol/L) | ICP [AsO$_4^{3-}$] (mmol/L) |
			Pb$_{tot}$ (ppm)	Fe$_{tot}$ (ppm)	S$_{tot}$ (ppm)	As$_{tot}$ (ppm)								
PbAs-2-1	28.666	2.003	0.014	3.384	0.446	2.474	1.35	1.335	4.587	0.000069	0.0606	0.0140	0.0139	0.0330
PbAs-2-2	69.499	2.054	0.014	3.707	0.412	2.758	1.25	1.234	5.114	0.000067	0.0664	0.0130	0.0128	0.0368
PbAs-2-3	121.333	1.984	0.013	3.886	0.403	2.919	1.22	1.208	5.413	0.000061	0.0696	0.0127	0.0126	0.0390
PbAs-2-4	171.916	1.966	0.011	4.041	0.391	3.047	1.18	1.172	5.649	0.000055	0.0724	0.0123	0.0122	0.0407
PbAs-2-5	188.833	2.030	0.010	3.968	0.386	2.994	1.17	1.156	5.551	0.000048	0.0711	0.0121	0.0120	0.0400
PbAs-2-6	213.666	2.130	0.009	4.046	0.390	3.058	1.18	1.169	5.669	0.000045	0.0725	0.0123	0.0122	0.0408
PbAs-2-7	289.499	2.107	0.009	4.039	0.383	3.056	1.16	1.148	5.666	0.000042	0.0723	0.0121	0.0120	0.0408
PbAs-2-8	336.416	2.097	0.008	4.095	0.385	3.087	1.17	1.154	5.724	0.000039	0.0733	0.0121	0.0120	0.0412
PbAs-2-9	385.083	1.966	0.008	4.047	0.389	3.057	1.18	1.167	5.668	0.000039	0.0725	0.0123	0.0121	0.0408
PbAs-2-10	457.249	2.026		4.050	0.389	3.061	1.19	1.167	5.676		0.0725	0.0124	0.0121	0.0409
PbAs-2-11	529.333	2.067		4.053	0.390	3.066	1.21	1.167	5.684		0.0726	0.0126	0.0121	0.0409
PbAs-2-12	601.833	2.091		4.056	0.390	3.070	1.21	1.167	5.692		0.0726	0.0126	0.0122	0.0410
PbAs-2-13	673.916	2.104		4.059	0.390	3.074	1.22	1.168	5.700		0.0727	0.0127	0.0122	0.0410
PbAs-2-14	744.833	2.115		4.062	0.402	3.079	1.25	1.205	5.708		0.0727	0.0130	0.0125	0.0411
PbAs-2-15	838.749	2.056		4.057	0.400	3.072	1.25	1.198	5.696		0.0726	0.0130	0.0125	0.0410
PbAs-2-16	910.583	2.045		4.058	0.421	3.065	1.27	1.261	5.682		0.0727	0.0133	0.0131	0.0409
PbAs-2-17	1006.499	2.035		4.032	0.436	3.050	1.32	1.305	5.656		0.0722	0.0137	0.0136	0.0407
PbAs-2-18	1078.665	2.043		4.037	0.438	3.041	1.33	1.313	5.638		0.0723	0.0138	0.0137	0.0406
PbAs-2-19	1225.499	2.061		4.042	0.441	3.031	1.33	1.321	5.620		0.0724	0.0139	0.0138	0.0405
PbAs-2-20	1321.582	2.065		4.028	0.444	3.023	1.34	1.331	5.604		0.0721	0.0140	0.0139	0.0403
PbAs-2-21	1417.748	2.069		4.014	0.448	3.014	1.35	1.341	5.589		0.0719	0.0141	0.0140	0.0402
PbAs-2-22	1513.998	2.074		4.000	0.451	3.006	1.36	1.352	5.573		0.0716	0.0141	0.0141	0.0401
PbAs-2-23	1610.082	2.078		3.986	0.446	2.997	1.36	1.335	5.557		0.0714	0.0141	0.0139	0.0400
PbAs-2-24	1706.165	2.082		3.972	0.445	2.988	1.36	1.332	5.541		0.0711	0.0142	0.0139	0.0399
PbAs-2-25	1897.083	2.086		3.958	0.448	2.980	1.35	1.342	5.525		0.0709	0.0141	0.0140	0.0398
PbAs-2-26	2205.583	2.098		4.058	0.463	3.043	1.36	1.388	5.643		0.0727	0.0141	0.0144	0.0406

Raw Data of Acid (pH 2) Dissolution of Beudantite, Bottle 3

			Raw ICP Values				DIONEX $[SO_4^{2-}]$	ICP $[SO_4^{2-}]$	ICP $[AsO_4^{3-}]$	Pb_{tot}	Fe_{tot}	DIONEX $[SO_4^{2-}]$	ICP $[SO_4^{2-}]$	ICP $[AsO_4^{3-}]$
Sample No.	Time (hrs)	pH	Pb_{tot} (ppm)	Fe_{tot} (ppm)	S_{tot} (ppm)	As_{tot} (ppm)	$[SO_4^{2-}]$	$[SO_4^{2-}]$	$[AsO_4^{3-}]$	(mmol/L)	(mmol/L)	(mmol/L)	(mmol/L)	(mmol/L)
PbAs-3-1	28.916	1.996	0.014	3.381	0.453	2.474	1.37	1.358	4.587	0.000069	0.0605	0.0142	0.0141	0.0330
PbAs-3-2	69.749	2.048	0.015	3.688	0.424	2.742	1.28	1.269	5.085	0.000071	0.0660	0.0133	0.0132	0.0366
PbAs-3-3	121.583	1.982	0.012	3.950	0.405	2.975	1.22	1.212	5.515	0.000060	0.0707	0.0127	0.0126	0.0397
PbAs-3-4	172.166	1.966	0.010	4.032	0.403	3.058	1.21	1.208	5.671	0.000049	0.0722	0.0126	0.0126	0.0408
PbAs-3-5	189.083	2.025	0.009	3.984	0.396	3.000	1.19	1.185	5.563	0.000043	0.0713	0.0124	0.0123	0.0400
PbAs-3-6	213.916	2.120	0.009	4.024	0.394	3.057	1.19	1.180	5.669	0.000045	0.0721	0.0123	0.0123	0.0408
PbAs-3-7	289.749	2.096	0.008	4.098	0.392	3.102	1.20	1.176	5.752	0.000037	0.0734	0.0124	0.0122	0.0414
PbAs-3-8	336.666	2.097	0.007	4.073	0.392	3.099	1.20	1.175	5.746	0.000035	0.0729	0.0125	0.0122	0.0414
PbAs-3-9	385.333	1.963	0.007	3.999	0.402	3.044	1.21	1.204	5.645	0.000034	0.0716	0.0126	0.0125	0.0406
PbAs-3-10	457.499	2.010		4.015	0.404	3.054	1.21	1.212	5.663		0.0719	0.0126	0.0126	0.0408
PbAs-3-11	529.583	2.023		4.031	0.407	3.064	1.24	1.219	5.681		0.0722	0.0129	0.0127	0.0409
PbAs-3-12	602.083	2.047		4.047	0.409	3.074	1.23	1.227	5.699		0.0725	0.0128	0.0128	0.0410
PbAs-3-13	674.166	2.055		4.064	0.412	3.083	1.26	1.234	5.717		0.0728	0.0131	0.0128	0.0412
PbAs-3-14	745.083	2.088		4.080	0.414	3.093	1.28	1.241	5.735		0.0731	0.0133	0.0129	0.0413
PbAs-3-15	838.999	2.053		3.996	0.426	3.034	1.28	1.277	5.625		0.0716	0.0134	0.0133	0.0405
PbAs-3-16	910.833	2.055		4.075	0.441	3.093	1.33	1.320	5.734		0.0730	0.0138	0.0137	0.0413
PbAs-3-17	1006.749	2.063		4.082	0.436	3.103	1.31	1.306	5.754		0.0731	0.0137	0.0136	0.0414
PbAs-3-18	1078.915	2.055		4.088	0.450	3.107	1.35	1.347	5.761		0.0732	0.0141	0.0140	0.0415
PbAs-3-19	1225.749	2.058		4.093	0.463	3.111	1.36	1.388	5.768		0.0733	0.0142	0.0144	0.0415
PbAs-3-20	1321.832	2.065		4.095	0.463	3.111	1.38	1.387	5.769		0.0733	0.0144	0.0144	0.0415
PbAs-3-21	1417.998	2.071		4.097	0.463	3.112	1.38	1.387	5.771		0.0734	0.0144	0.0144	0.0415
PbAs-3-22	1514.248	2.077		4.098	0.463	3.113	1.39	1.386	5.772		0.0734	0.0145	0.0144	0.0416
PbAs-3-23	1610.332	2.083		4.100	0.463	3.114	1.38	1.386	5.774		0.0734	0.0144	0.0144	0.0416
PbAs-3-24	1706.415	2.081		4.102	0.462	3.115	1.39	1.385	5.776		0.0734	0.0145	0.0144	0.0416
PbAs-3-25	1897.333	2.085		4.103	0.462	3.116	1.39	1.385	5.777		0.0735	0.0145	0.0144	0.0416
PbAs-3-26	2205.833	2.098		4.106	0.466	3.117	1.39	1.395	5.779		0.0735	0.0145	0.0145	0.0416

C.2 Alkali dissolution raw data

Raw Data of Alkali (pH 8) Dissolution of Potassium Jarosite, Bottle 1

Sample No.	Time (hrs)	pH	Raw ICP Values			DIONEX $[SO_4^{2-}]$	ICP $[SO_4^{2-}]$	K_{tot} (mmol/L)	Fe_{tot} (mmol/L)	DIONEX $[SO_4^{2-}]$ (mmol/L)	ICP $[SO_4^{2-}]$ (mmol/L)
			K_{tot} (ppm)	Fe_{tot} (ppm)	S_{tot} (ppm)						
A-K-1-1	25.250	4.047	2.384	0.068	1.558	4.7	4.668	0.0610	0.0012	0.0486	0.0486
A-K-1-2	30.750	3.916	2.492	0.034	1.699	5.1	5.092	0.0637	0.0006	0.0527	0.0530
A-K-1-3	49.166	3.870	2.787	0.037	2.210	6.9	6.622	0.0713	0.0007	0.0723	0.0689
A-K-1-4	55.000	3.853	2.798	0.037	2.267	7.8	6.793	0.0716	0.0007	0.0807	0.0707
A-K-1-5	73.083	3.826	2.963	0.038	2.458	7.5	7.364	0.0758	0.0007	0.0781	0.0767
A-K-1-6	79.667	3.775	3.017	0.039	2.571	7.4	7.702	0.0772	0.0007	0.0766	0.0802
A-K-1-7	96.667	3.718	3.228	0.042	2.789	8.2	8.357	0.0826	0.0008	0.0851	0.0870
A-K-1-8	149.250	3.668	3.490	0.042	3.249	9.9	9.735	0.0893	0.0007	0.1026	0.1013
A-K-1-9	167.167	3.582	3.548	0.051	3.284	9.7	9.840	0.0907	0.0009	0.1005	0.1024
A-K-1-10	174.750	3.562				10.0				0.1042	
A-K-1-11	192.333	3.661	3.785	0.053	3.576	10.5	10.713	0.0968	0.0010	0.1092	0.1115
A-K-1-12	217.167	3.527	3.783	0.051	3.630	11.2	10.877	0.0968	0.0009	0.1165	0.1132
A-K-1-13	223.916	3.532	3.834	0.049	3.744	11.4	11.217	0.0981	0.0009	0.1190	0.1168
A-K-1-14	240.416	3.510	3.896	0.051	3.874	11.6	11.608	0.0997	0.0009	0.1212	0.1208
A-K-1-15	336.833	3.606	4.169	0.053	4.360	13.4	13.063	0.1066	0.0010	0.1394	0.1360
A-K-1-16	344.000	3.610	4.285	0.054	4.573	14.1	13.701	0.1096	0.0010	0.1463	0.1426
A-K-1-17	363.250	3.631	4.355	0.058	4.678	14.4	14.018	0.1114	0.0010	0.1499	0.1459
A-K-1-18	838.667	3.435	5.492	0.097	6.425	20.6	19.252	0.1405	0.0017	0.2143	0.2004
A-K-1-19	934.583	3.413	5.668	0.076	6.690	21.5	20.045	0.1450	0.0014	0.2236	0.2087
A-K-1-20	1103.250	3.397	5.965	0.084	7.186	22.6	21.531	0.1526	0.0015	0.2353	0.2241
A-K-1-21	1224.083	3.442	6.186	0.138	7.287	23.5	21.834	0.1582	0.0025	0.2448	0.2273
A-K-1-22	1367.583	3.344	6.349	0.107	7.606	24.9	22.790	0.1624	0.0019	0.2590	0.2372
A-K-1-23	1512.583	3.344	6.753	0.101	8.302	26.1	24.875	0.1727	0.0018	0.2720	0.2589
A-K-1-24	1704.583	3.323	6.901	0.100	8.408	27.9	25.192	0.1765	0.0018	0.2901	0.2622
A-K-1-25	2015.916	3.285	7.180	0.103	8.736	29.1	26.175	0.1836	0.0018	0.3026	0.2725
A-K-1-26	3221.833	3.295	7.980	0.130	10.529	31.5	31.548	0.2041	0.0023	0.3279	0.3284

Raw Data of Alkali (pH 8) Dissolution of Potassium Jarosite, Bottle 2

| Sample No. | Time (hrs) | pH | Raw ICP Values | | | DIONEX $[SO_4^{2-}]$ | ICP $[SO_4^{2-}]$ | K_{tot} (mmol/L) | Fe_{tot} (mmol/L) | DIONEX $[SO_4^{2-}]$ (mmol/L) | ICP $[SO_4^{2-}]$ (mmol/L) |
			K_{tot} (ppm)	Fe_{tot} (ppm)	S_{tot} (ppm)						
A-K-2-1	26.000	4.032	2.467	0.025	1.489	4.3	4.460	0.0631	0.0004	0.0451	0.0464
A-K-2-2	30.583	3.962	2.523	0.026	1.681	4.7	5.037	0.0645	0.0005	0.0494	0.0524
A-K-2-3	48.916	3.832	2.763	0.040	2.103	5.8	6.301	0.0707	0.0007	0.0609	0.0656
A-K-2-4	45.833	3.813	2.859	0.042	2.234	6.2	6.694	0.0731	0.0007	0.0650	0.0697
A-K-2-5	72.833	3.811	2.979	0.037	2.396	7.0	7.179	0.0762	0.0007	0.0729	0.0747
A-K-2-6	79.416	3.707	3.060	0.038	2.497	7.5	7.483	0.0783	0.0007	0.0777	0.0779
A-K-2-7	96.500	3.735	3.288	0.056	2.742	8.1	8.217	0.0841	0.0010	0.0839	0.0855
A-K-2-8	149.000	3.660	3.542	0.051	3.200	9.8	9.589	0.0906	0.0009	0.1018	0.0998
A-K-2-9	167.083	3.584	3.608	0.054	3.317	10.0	9.937	0.0923	0.0010	0.1044	0.1034
A-K-2-10	174.500	3.573	3.700	0.046	3.328	10.0	9.971	0.0946	0.0008	0.1046	0.1038
A-K-2-11	192.083	3.660	3.809	0.057	3.483	10.5	10.437	0.0974	0.0010	0.1089	0.1086
A-K-2-12	216.916	3.517	3.887	0.052	3.725	11.2	11.161	0.0994	0.0009	0.1165	0.1162
A-K-2-13	223.667	3.521	3.834	0.089	3.679	11.1	11.023	0.0981	0.0016	0.1154	0.1147
A-K-2-14	240.250	3.507	4.017	0.125	3.926	11.9	11.762	0.1028	0.0022	0.1242	0.1224
A-K-2-15	336.667	3.598	4.367	0.062	4.447	13.7	13.323	0.1117	0.0011	0.1430	0.1387
A-K-2-16	343.750	3.596	4.410	0.077	4.521	14.2	13.546	0.1128	0.0014	0.1478	0.1410
A-K-2-17	363.083	3.621	4.548	0.061	4.623	14.1	13.850	0.1163	0.0011	0.1468	0.1442
A-K-2-18	838.500	3.425	5.666	0.093	6.599		19.773	0.1449	0.0017		0.2058
A-K-2-19	934.333	3.425	5.906	0.082	6.967	21.2	20.874	0.1511	0.0015	0.2207	0.2173
A-K-2-20	1103.083	3.398	6.208	0.088	7.408	23.0	22.195	0.1588	0.0016	0.2399	0.2310
A-K-2-21	1223.833	3.427	6.367	0.089	7.516	23.1	22.518	0.1629	0.0016	0.2408	0.2344
A-K-2-22	1367.416	3.341	6.582	0.092	7.823	24.6	23.440	0.1684	0.0017	0.2558	0.2440
A-K-2-23	1512.333	3.338	6.840	0.098	8.228	25.7	24.653	0.1750	0.0017	0.2673	0.2566
A-K-2-24	1704.416	3.315	7.064	0.106	8.528	26.9	25.553	0.1807	0.0019	0.2802	0.2660
A-K-2-25	2015.750	3.299	7.278	0.107	8.894	28.5	26.649	0.1861	0.0019	0.2972	0.2774
A-K-2-26	3221.500	3.271	7.978	0.110	10.201	31.1	30.563	0.2041	0.0020	0.3237	0.3182
A-K-2-27	3384.083	3.290	8.094	0.110	10.183	31.9	30.511	0.2070	0.0020	0.3321	0.3176
A-K-2-28	3552.500	3.288	8.163	0.120	10.076	32.1	30.190	0.2088	0.0021	0.3342	0.3143
A-K-2-29	3774.416	3.283	8.140	0.140	10.516	32.0	31.508	0.2082	0.0025	0.3331	0.3280
A-K-2-30	3942.083	3.275	8.220	0.140	10.599	32.2	31.757	0.2102	0.0025	0.3352	0.3306

Raw Data of Alkali (pH 8) Dissolution of Potassium Jarosite, Bottle 3

Sample No.	Time (hrs)	pH	Raw ICP Values K_{tot} (ppm)	Fe_{tot} (ppm)	S_{tot} (ppm)	DIONEX $[SO_4^{2-}]$	ICP $[SO_4^{2-}]$	K_{tot} (mmol/L)	Fe_{tot} (mmol/L)	DIONEX $[SO_4^{2-}]$ (mmol/L)	ICP $[SO_4^{2-}]$ (mmol/L)
A-K-3-1	24.750	4.021	2.478	0.074	1.424	4.13	4.267	0.0634	0.0013	0.0429	0.0444
A-K-3-2	30.250	3.960	2.486	0.031	1.586	4.63	4.753	0.0636	0.0006	0.0482	0.0495
A-K-3-3	48.667	3.835	2.757	0.034	1.992	6.13	5.967	0.0705	0.0006	0.0638	0.0621
A-K-3-4	54.500	3.815	2.882	0.035	2.081	6.25	6.234	0.0737	0.0006	0.0650	0.0649
A-K-3-5	72.583	3.803	3.015	0.036	2.386	7.13	7.149	0.0771	0.0006	0.0743	0.0744
A-K-3-6	79.083	3.753	3.013	0.038	2.459	7.14	7.367	0.0771	0.0007	0.0743	0.0767
A-K-3-7	96.167	3.732	3.173	0.043	2.703	8.18	8.100	0.0812	0.0008	0.0851	0.0843
A-K-3-8	148.667	3.635	3.471	0.049	3.106	9.52	9.306	0.0888	0.0009	0.0991	0.0969
A-K-3-9	166.580	3.580	3.583	0.045	3.379	10.17	10.123	0.0916	0.0008	0.1058	0.1054
A-K-3-10	174.167	3.564	3.592	0.073	3.427	10.02	10.267	0.0919	0.0013	0.1043	0.1069
A-K-3-11	191.750	3.664	3.786	0.102	3.694	10.81	11.068	0.0968	0.0018	0.1126	0.1152
A-K-3-12	216.583	3.529	3.852	0.058	3.866	11.17	11.584	0.0985	0.0010	0.1162	0.1206
A-K-3-13	223.333	3.514	4.091	0.057	3.875	11.44	11.610	0.1046	0.0010	0.1191	0.1209
A-K-3-14	239.916	3.496	3.883	0.205	3.905	11.41	11.700	0.0993	0.0037	0.1188	0.1218
A-K-3-15	336.250	3.576	4.342	0.056	4.563	13.70	13.671	0.1111	0.0010	0.1426	0.1423
A-K-3-16	343.416	3.592	4.399	0.056	4.679	14.09	14.020	0.1125	0.0010	0.1467	0.1459
A-K-3-17	362.833	3.609	4.529	0.057	4.799	14.49	14.380	0.1158	0.0010	0.1508	0.1497
A-K-3-18	838.167	3.420	5.747	0.079	6.831	20.54	20.467	0.1470	0.0014	0.2138	0.2131
A-K-3-19	934.000	3.412	6.023	0.082	7.211	21.57	21.604	0.1540	0.0015	0.2246	0.2249
A-K-3-20	1102.750	3.401	6.260	0.092	7.563	23.04	22.659	0.1601	0.0016	0.2399	0.2359
A-K-3-21	1223.500	3.419	6.546	0.089	7.866	23.84	23.567	0.1674	0.0016	0.2482	0.2453
A-K-3-22	1367.083	3.347	6.876	0.102	8.260	25.35	24.750	0.1759	0.0018	0.2639	0.2576
A-K-3-23	1512.000	3.340	7.084	0.099	8.505	25.99	25.483	0.1812	0.0018	0.2706	0.2653
A-K-3-24	1704.083	3.303	7.346	0.102	8.868	27.09	26.570	0.1879	0.0018	0.2820	0.2766
A-K-3-25	2015.416	3.286	7.574	0.111	9.255	29.03	27.730	0.1937	0.0020	0.3022	0.2887
A-K-3-26	3221.250	3.270	8.131		10.250	31.30	30.711	0.2080		0.3258	0.3197
A-K-3-27	3384.833	3.268	8.175	0.120	10.447	31.80	31.300	0.2091	0.0021	0.3310	0.3258
A-K-3-28	3552.250	3.266	8.292	0.110	10.422	31.50	31.227	0.2121	0.0020	0.3279	0.3251
A-K-3-29	3774.083	3.264	8.310	0.130	10.668	32.20	31.964	0.2125	0.0023	0.3352	0.3327
A-K-3-30	3942.750	3.264	8.300	0.130	10.799	32.50	32.357	0.2123	0.0023	0.3383	0.3368

Raw Data of Alkali (pH 8) Dissolution of Plumbojarosite, Bottle 1

Sample No.	Time (hrs)	Raw ICP Values pH	Pb_{tot} (ppm)	Fe_{tot} (ppm)	S_{tot} (ppm)	DIONEX $[SO_4^{2-}]$	ICP $[SO_4^{2-}]$	Pb_{tot} (mmol/L)	Fe_{tot} (mmol/L)	DIONEX $[SO_4^{2-}]$ (mmol/L)	ICP $[SO_4^{2-}]$ (mmol/L)
A-Pb-1-1	27.833	4.582	0.029	0.008	0.569	1.54	1.704	0.0001	0.0001	0.0160	0.0177
A-Pb-1-2	68.749	4.930	0.027	0.007	0.691	2.12	2.070	0.0001	0.0001	0.0221	0.0215
A-Pb-1-3	121.249	4.524	0.054	0.008	0.945	2.68	2.833	0.0003	0.0001	0.0279	0.0295
A-Pb-1-4	171.749	4.426	0.100	0.007	0.965	2.74	2.892	0.0005	0.0001	0.0285	0.0301
A-Pb-1-5	188.833	4.390	0.112	0.006	0.985	3.21	2.950	0.0005	0.0001	0.0334	0.0307
A-Pb-1-6	213.583	4.283	0.136	0.006	1.071	3.48	3.209	0.0007	0.0001	0.0362	0.0334
A-Pb-1-7	289.333	4.258	0.180	0.007	1.158	3.65	3.471	0.0009	0.0001	0.0380	0.0361
A-Pb-1-8	336.249	4.184	0.206	0.006	1.228	3.79	3.678	0.0010	0.0001	0.0395	0.0383
A-Pb-1-9	384.916	4.223	0.235	0.006	1.294	3.83	3.876	0.0011	0.0001	0.0399	0.0403
A-Pb-1-10	457.165	4.156	0.276	0.006	1.390	4.23	4.165	0.0013	0.0001	0.0440	0.0434
A-Pb-1-11	529.248	4.135	0.317	0.007	1.486	4.55	4.453	0.0015	0.0001	0.0474	0.0464
A-Pb-1-12	601.748	4.088	0.352	0.008	1.585	4.73	4.749	0.0017	0.0001	0.0492	0.0494
A-Pb-1-13	673.998	4.031	0.398	0.008	1.680	4.96	5.033	0.0019	0.0001	0.0516	0.0524
A-Pb-1-14	744.749	3.995	0.440	0.009	1.778	5.42	5.326	0.0021	0.0002	0.0564	0.0554
A-Pb-1-15	838.583	3.955	0.481	0.009	1.873	5.59	5.612	0.0023	0.0002	0.0582	0.0584
A-Pb-1-16	910.416	3.965	0.553	0.010	2.019	5.91	6.049	0.0027	0.0002	0.0615	0.0630
A-Pb-1-17	1006.333	3.965	0.611	0.010	2.227	6.55	6.672	0.0029	0.0002	0.0682	0.0695
A-Pb-1-18	1078.853	3.934	0.666	0.010	2.267	6.87	6.792	0.0032	0.0002	0.0715	0.0707
A-Pb-1-19	1225.333	3.854	0.715	0.011	2.398	7.31	7.185	0.0034	0.0002	0.0761	0.0748
A-Pb-1-20	1321.416	3.710	0.799	0.012	2.557	7.78	7.662	0.0039	0.0002	0.0810	0.0798
A-Pb-1-21	1417.583	3.681	0.878	0.014	2.723	8.34	8.159	0.0042	0.0002	0.0868	0.0849
A-Pb-1-22	1514.083	3.664	0.956	0.014	2.889	8.82	8.657	0.0046	0.0003	0.0918	0.0901
A-Pb-1-23	1610.166	3.641	1.027	0.016	3.055	9.35	9.154	0.0050	0.0003	0.0973	0.0953
A-Pb-1-24	1706.333	3.618	1.112	0.017	3.221	9.97	9.651	0.0054	0.0003	0.1038	0.1005
A-Pb-1-25	1896.916	3.595	1.191	0.018	3.387	10.57	10.148	0.0057	0.0003	0.1100	0.1056
A-Pb-1-26	2205.416	3.538	1.371	0.023	3.429	11.47	10.275	0.0066	0.0004	0.1194	0.1070

Raw Data of Alkali (pH 8) Dissolution of Plumbojarosite, Bottle 2

Sample No.	Time (hrs)	pH	Raw ICP Values Pb tot (ppm)	Fe tot (ppm)	S tot (ppm)	DIONEX $[SO_4^{2-}]$	ICP $[SO_4^{2-}]$	Pb tot (mmol/L)	Fe tot (mmol/L)	DIONEX $[SO_4^{2-}]$ (mmol/L)	ICP $[SO_4^{2-}]$ (mmol/L)
A-Pb-2-1	28.033	4.760	0.044	0.005	0.575	1.53	1.723	0.0002	0.0001	0.0159	0.0179
A-Pb-2-2	68.949	4.560	0.042	0.014	0.642	2.04	1.924	0.0002	0.0002	0.0212	0.0200
A-Pb-2-3	121.449	4.518	0.066	0.005	0.872	2.46	2.614	0.0003	0.0001	0.0256	0.0272
A-Pb-2-4	171.949	4.433	0.120	0.006	1.096	3.38	3.285	0.0006	0.0001	0.0352	0.0342
A-Pb-2-5	189.033	4.336	0.135	0.005	1.016	3.52	3.045	0.0007	0.0001	0.0366	0.0317
A-Pb-2-6	213.783	4.220	0.167	0.011	1.176	3.71	3.523	0.0008	0.0002	0.0386	0.0367
A-Pb-2-7	289.533	4.187	0.227	0.009	1.284	3.92	3.846	0.0011	0.0002	0.0408	0.0400
A-Pb-2-8	336.449	4.106	0.262	0.007	1.309	4.11	3.922	0.0013	0.0001	0.0428	0.0408
A-Pb-2-9	385.116	4.165	0.300	0.007	1.407	4.35	4.215	0.0014	0.0001	0.0453	0.0439
A-Pb-2-10	457.365	4.118	0.350	0.007	1.519	4.68	4.550	0.0017	0.0001	0.0487	0.0474
A-Pb-2-11	529.448	4.071	0.400	0.008	1.630	4.98	4.884	0.0019	0.0001	0.0518	0.0508
A-Pb-2-12	601.948	4.024	0.450	0.009	1.742	5.12	5.219	0.0022	0.0002	0.0533	0.0543
A-Pb-2-13	674.198	3.977	0.500	0.010	1.854	5.63	5.554	0.0024	0.0002	0.0586	0.0578
A-Pb-2-14	744.949	3.930	0.550	0.010	1.965	5.99	5.889	0.0027	0.0002	0.0624	0.0613
A-Pb-2-15	838.783	3.883	0.600	0.011	2.077	6.32	6.223	0.0029	0.0002	0.0658	0.0648
A-Pb-2-16	910.616	3.913	0.661	0.011	2.179	6.76	6.527	0.0032	0.0002	0.0704	0.0679
A-Pb-2-17	1006.533	3.921	0.742	0.013	2.425	7.17	7.266	0.0036	0.0002	0.0746	0.0756
A-Pb-2-18	1079.053	3.387	0.799	0.013	2.491	7.53	7.465	0.0039	0.0002	0.0784	0.0777
A-Pb-2-19	1225.533	3.565	0.870	0.014	2.636	7.78	7.899	0.0042	0.0003	0.0810	0.0822
A-Pb-2-20	1321.616	3.742	0.940	0.016	2.781	8.41	8.334	0.0045	0.0003	0.0875	0.0868
A-Pb-2-21	1417.783	3.697	1.016	0.017	2.943	8.92	8.818	0.0049	0.0003	0.0929	0.0918
A-Pb-2-22	1514.283	3.652	1.092	0.018	3.105	9.43	9.302	0.0053	0.0003	0.0982	0.0968
A-Pb-2-23	1610.366	3.606	1.169	0.019	3.266	9.87	9.786	0.0056	0.0003	0.1027	0.1019
A-Pb-2-24	1706.533	3.561	1.245	0.021	3.428	10.33	10.271	0.0060	0.0004	0.1075	0.1069
A-Pb-2-25	1897.116	3.516	1.321	0.022	3.590	10.98	10.755	0.0064	0.0004	0.1143	0.1120
A-Pb-2-26	2205.616	3.461	1.415	0.022	3.731	11.78	11.178	0.0068	0.0004	0.1226	0.1164

Raw Data of Alkali (pH 8) Dissolution of Plumbojarosite, Bottle 3

Sample No.	Time (hrs)	pH	Raw ICP Values Pb tot (ppm)	Fe tot (ppm)	S tot (ppm)	DIONEX $[SO_4^{2-}]$	ICP $[SO_4^{2-}]$	Pb tot (mmol/L)	Fe tot (mmol/L)	DIONEX $[SO_4^{2-}]$ (mmol/L)	ICP $[SO_4^{2-}]$ (mmol/L)
A-Pb-3-1	26.867	4.818	0.043	0.004	0.561	1.55	1.681	0.0002	0.0001	0.0161	0.0175
A-Pb-3-2	67.783	4.710	0.030	0.004	0.652	2.01	1.954	0.0001	0.0001	0.0209	0.0203
A-Pb-3-3	120.283	4.550	0.064	0.004	0.828	2.53	2.482	0.0003	0.0001	0.0263	0.0258
A-Pb-3-4	170.783	4.428	0.119	0.005	1.025	3.11	3.072	0.0006	0.0001	0.0324	0.0320
A-Pb-3-5	187.867	4.357	0.145	0.007	1.081	3.38	3.238	0.0007	0.0001	0.0352	0.0337
A-Pb-3-6	212.617	4.205	0.171	0.007	1.134	3.45	3.399	0.0008	0.0001	0.0359	0.0354
A-Pb-3-7	288.367	4.155	0.240	0.008	1.306	3.89	3.912	0.0012	0.0001	0.0405	0.0407
A-Pb-3-8	335.283	4.166	0.282	0.007	1.336	4.07	4.003	0.0014	0.0001	0.0424	0.0417
A-Pb-3-9	383.950	4.177	0.329	0.007	1.455	4.46	4.359	0.0016	0.0001	0.0464	0.0454
A-Pb-3-10	456.199	4.125	0.382	0.009	1.564	4.79	4.687	0.0018	0.0002	0.0499	0.0488
A-Pb-3-11	528.282	4.073	0.436	0.010	1.674	5.09	5.016	0.0021	0.0002	0.0530	0.0522
A-Pb-3-12	600.782	4.021	0.489	0.012	1.783	5.41	5.344	0.0024	0.0002	0.0563	0.0556
A-Pb-3-13	673.032	3.968	0.543	0.013	1.893	5.73	5.672	0.0026	0.0002	0.0596	0.0590
A-Pb-3-14	743.783	3.916	0.597	0.015	2.003	6.16	6.000	0.0029	0.0003	0.0641	0.0625
A-Pb-3-15	837.617	3.864	0.650	0.016	2.112	6.52	6.328	0.0031	0.0003	0.0679	0.0659
A-Pb-3-16	909.450	3.896	0.734	0.014	2.257	6.85	6.762	0.0035	0.0003	0.0713	0.0704
A-Pb-3-17	1005.367	3.909	0.787	0.015	2.492	7.72	7.468	0.0038	0.0003	0.0804	0.0777
A-Pb-3-18	1077.887	3.860	0.869	0.017	2.571	7.96	7.704	0.0042	0.0003	0.0829	0.0802
A-Pb-3-19	1224.367	3.767	0.942	0.018	2.714	8.24	8.132	0.0045	0.0003	0.0858	0.0847
A-Pb-3-20	1320.450	3.673	1.015	0.019	2.857	8.86	8.560	0.0049	0.0003	0.0922	0.0891
A-Pb-3-21	1416.617	3.636	1.095	0.020	3.024	9.19	9.060	0.0053	0.0004	0.0957	0.0943
A-Pb-3-22	1513.117	3.598	1.174	0.021	3.191	9.67	9.561	0.0057	0.0004	0.1007	0.0995
A-Pb-3-23	1609.200	3.561	1.254	0.023	3.358	10.21	10.061	0.0061	0.0004	0.1063	0.1047
A-Pb-3-24	1705.367	3.523	1.333	0.024	3.525	10.94	10.561	0.0064	0.0004	0.1139	0.1099
A-Pb-3-25	1895.950	3.486	1.413	0.024	3.692	11.58	11.062	0.0068	0.0004	0.1205	0.1152
A-Pb-3-26	2204.450	3.440	1.471	0.025	3.907	12.19	11.706	0.0071	0.0004	0.1269	0.1219

Raw Data of Alkali (pH 8) Dissolution of Beudantite, Bottle 1

Sample No.	Time (hrs)	pH	Raw ICP Values Pb tot (ppm)	Fe tot (ppm)	S tot (ppm)	As tot (ppm)	DIONEX [SO$_4^{2-}$]	ICP [SO$_4^{2-}$]	ICP [AsO$_4^{3-}$]	Pb tot (mmol/L)	Fe tot (mmol/L)	DIONEX [SO$_4^{2-}$] (mmol/L)	ICP [SO$_4^{2-}$] (mmol/L)	ICP [AsO$_4^{3-}$] (mmol/L)
A-PbAs-1-1	27.867	5.234	0.015	0.0025	0.387	0.062	1.17	1.161	0.115	0.000070	0.000044	0.0122	0.0121	0.0008
A-PbAs-1-2	68.783	5.194		0.0013	0.359	0.087	1.09	1.075	0.161		0.000023	0.0113	0.0112	0.0012
A-PbAs-1-3	121.283	5.171		0.0010	0.377	0.098	1.14	1.130	0.182		0.000017	0.0119	0.0118	0.0013
A-PbAs-1-4	171.783	5.141		0.0008	0.362	0.105	1.10	1.085	0.194		0.000014	0.0114	0.0113	0.0014
A-PbAs-1-5	188.867	5.088		0.0008	0.378	0.106	1.14	1.132	0.196		0.000015	0.0119	0.0118	0.0014
A-PbAs-1-6	213.617	4.919		0.0009	0.361	0.105	1.09	1.083	0.194		0.000016	0.0114	0.0113	0.0014
A-PbAs-1-7	289.367	4.996		0.0012	0.356	0.107	1.08	1.067	0.199		0.000021	0.0112	0.0111	0.0014
A-PbAs-1-8	336.283	4.932		0.0012	0.360	0.106	1.09	1.079	0.196		0.000021	0.0113	0.0112	0.0014
A-PbAs-1-9	384.950	5.051		0.0014	0.362	0.108	1.09	1.084	0.200		0.000025	0.0114	0.0113	0.0014
A-PbAs-1-10	457.199	5.015		0.0015	0.362	0.109	1.10	1.085	0.202		0.000027	0.0114	0.0113	0.0015
A-PbAs-1-11	529.282	4.975		0.0018	0.358	0.112	1.08	1.073	0.207		0.000032	0.0113	0.0112	0.0015
A-PbAs-1-12	601.782	5.002		0.0018	0.365	0.112	1.11	1.094	0.208		0.000033	0.0115	0.0114	0.0015
A-PbAs-1-13	674.032	4.907		0.0020	0.375	0.113	1.13	1.123	0.210		0.000036	0.0118	0.0117	0.0015
A-PbAs-1-14	744.783	4.872		0.0022	0.378	0.115	1.14	1.133	0.213		0.000040	0.0119	0.0118	0.0015
A-PbAs-1-15	838.617	4.836		0.0025	0.392	0.114	1.18	1.173	0.211		0.000045	0.0123	0.0122	0.0015
A-PbAs-1-16	910.450	4.979		0.0031	0.413	0.117	1.25	1.237	0.217		0.000056	0.0130	0.0129	0.0016
A-PbAs-1-17	1006.367	5.025		0.0031	0.442	0.120	1.34	1.324	0.223		0.000056	0.0139	0.0138	0.0016
A-PbAs-1-18	1078.887	4.983		0.0034	0.447	0.121	1.35	1.338	0.224		0.000061	0.0141	0.0139	0.0016
A-PbAs-1-19	1225.367	4.926		0.0036	0.456	0.122	1.38	1.367	0.225		0.000065	0.0144	0.0142	0.0016
A-PbAs-1-20	1321.450	4.860		0.0038	0.461	0.123	1.40	1.382	0.228		0.000068	0.0145	0.0144	0.0016
A-PbAs-1-21	1417.617	4.854		0.0040	0.466	0.124	1.41	1.395	0.230		0.000071	0.0147	0.0145	0.0017
A-PbAs-1-22	1514.117	4.848		0.0043	0.470	0.125	1.42	1.408	0.232		0.000077	0.0148	0.0147	0.0017
A-PbAs-1-23	1610.200	4.839		0.0044	0.476	0.128	1.44	1.426	0.237		0.000078	0.0150	0.0148	0.0017
A-PbAs-1-24	1706.367	4.836		0.0046	0.480	0.129	1.45	1.438	0.239		0.000082	0.0151	0.0150	0.0017
A-PbAs-1-25	1896.950	4.831		0.0048	0.482	0.129	1.46	1.443	0.239		0.000085	0.0152	0.0150	0.0017
A-PbAs-1-26	2205.450	4.783		0.0048	0.483	0.130	1.45	1.448	0.242		0.000087	0.0151	0.0151	0.0017

Raw Data of Alkali (pH 8) Dissolution of Beudantite, Bottle 2

Sample No.	Time (hrs)	pH	Raw ICP Values Pb tot (ppm)	Fe tot (ppm)	S tot (ppm)	As tot (ppm)	DIONEX [SO₄²⁻]	ICP [SO₄²⁻]	ICP [AsO₄³⁻]	Pb tot (mmol/L)	Fe tot (mmol/L)	DIONEX [SO₄²⁻] (mmol/L)	ICP [SO₄²⁻] (mmol/L)	ICP [AsO₄³⁻] (mmol/L)
A-PbAs-2-1	27.583	5.068		0.0043	0.3891	0.0586	1.18	1.1657	0.1087		0.000077	0.0123	0.0121	0.0008
A-PbAs-2-2	68.499	5.003		0.0033	0.3690	0.0744	1.12	1.1055	0.1379		0.000059	0.0116	0.0115	0.0010
A-PbAs-2-3	120.999	5.025		0.0024	0.3735	0.0828	1.13	1.1190	0.1535		0.000043	0.0118	0.0116	0.0011
A-PbAs-2-4	171.499	5.012		0.0016	0.3540	0.0888	1.07	1.0607	0.1647		0.000028	0.0112	0.0110	0.0012
A-PbAs-2-5	188.583	4.959		0.0014	0.3629	0.0881	1.10	1.0872	0.1634		0.000025	0.0114	0.0113	0.0012
A-PbAs-2-6	213.333	4.779		0.0012	0.3533	0.0889	1.07	1.0586	0.1648		0.000021	0.0111	0.0110	0.0012
A-PbAs-2-7	289.083	4.866		0.0011	0.3476	0.0893	1.05	1.0413	0.1655		0.000020	0.0109	0.0108	0.0012
A-PbAs-2-8	335.999	4.846		0.0012	0.3533	0.0905	1.07	1.0587	0.1677		0.000021	0.0111	0.0110	0.0012
A-PbAs-2-9	384.666	4.933		0.0012	0.3517	0.0907	1.06	1.0538	0.1682		0.000022	0.0111	0.0110	0.0012
A-PbAs-2-10	456.915	4.898		0.0014	0.3454	0.0932	1.05	1.0349	0.1729		0.000025	0.0109	0.0108	0.0012
A-PbAs-2-11	528.998	4.862		0.0018	0.3554	0.0948	1.08	1.0648	0.1757		0.000032	0.0112	0.0111	0.0013
A-PbAs-2-12	601.498	4.827		0.0022	0.3498	0.0953	1.06	1.0481	0.1767		0.000039	0.0110	0.0109	0.0013
A-PbAs-2-13	673.748	4.791		0.0024	0.3546	0.0959	1.07	1.0624	0.1777		0.000043	0.0112	0.0111	0.0013
A-PbAs-2-14	744.499	4.756		0.0029	0.3632	0.0973	1.10	1.0882	0.1804		0.000052	0.0114	0.0113	0.0013
A-PbAs-2-15	838.333	4.720		0.0030	0.3756	0.0984	1.14	1.1253	0.1825		0.000054	0.0118	0.0117	0.0013
A-PbAs-2-16	910.166	4.872		0.0033	0.3952	0.0950	1.20	1.1842	0.1761		0.000059	0.0125	0.0123	0.0013
A-PbAs-2-17	1006.083	4.909		0.0034	0.4109	0.1021	1.24	1.2310	0.1894		0.000061	0.0129	0.0128	0.0014
A-PbAs-2-18	1078.603	4.838		0.0037	0.4198	0.1003	1.27	1.2577	0.1859		0.000067	0.0132	0.0131	0.0013
A-PbAs-2-19	1225.083	4.723		0.0042	0.4235	0.1010	1.28	1.2689	0.1873		0.000075	0.0133	0.0132	0.0013
A-PbAs-2-20	1321.166	4.716		0.0046	0.4216	0.1015	1.28	1.2632	0.1882		0.000083	0.0133	0.0131	0.0014
A-PbAs-2-21	1417.333	4.684		0.0052	0.4256	0.1029	1.29	1.2752	0.1907		0.000094	0.0134	0.0133	0.0014
A-PbAs-2-22	1513.833	4.638		0.0055	0.4286	0.1042	1.30	1.2842	0.1932		0.000098	0.0135	0.0134	0.0014
A-PbAs-2-23	1609.916	4.614		0.0059	0.4311	0.1056	1.30	1.2917	0.1957		0.000106	0.0136	0.0134	0.0014
A-PbAs-2-24	1706.083	4.523		0.0065	0.4342	0.1069	1.31	1.3009	0.1982		0.000116	0.0137	0.0135	0.0014
A-PbAs-2-25	1896.666	4.546		0.0068	0.4366	0.1096	1.32	1.3080	0.2032		0.000121	0.0138	0.0136	0.0015
A-PbAs-2-26	2205.166	4.579		0.0071	0.4359	0.1109	1.31	1.3061	0.2057		0.000127	0.0136	0.0136	0.0015

Raw Data of Alkali (pH 8) Dissolution of Beudantite, Bottle 3

Sample No.	Time (hrs)	pH	Raw ICP Values Pb$_{tot}$ (ppm)	Fe$_{tot}$ (ppm)	S$_{tot}$ (ppm)	As$_{tot}$ (ppm)	DIONEX [SO$_4^{2-}$]	ICP [SO$_4^{2-}$]	ICP [AsO$_4^{3-}$]	Pb$_{tot}$ (mmol/L)	Fe$_{tot}$ (mmol/L)	DIONEX [SO$_4^{2-}$] (mmol/L)	ICP [SO$_4^{2-}$] (mmol/L)	ICP [AsO$_4^{3-}$] (mmol/L)
A-PbAs-3-1	27.767	5.053	0.0008	0.371	0.060	1.12	1.112	0.111		0.000015	0.0116	0.0116	0.0008	
A-PbAs-3-2	68.683	5.015	0.0007	0.373	0.069	1.13	1.117	0.128		0.000013	0.0116	0.0116	0.0009	
A-PbAs-3-3	121.183	5.030	0.0009	0.351	0.080	1.06	1.053	0.147		0.000015	0.0110	0.0110	0.0011	
A-PbAs-3-4	171.683	5.019	0.0005	0.353	0.085	1.07	1.059	0.158		0.000009	0.0110	0.0110	0.0011	
A-PbAs-3-5	188.767	4.986	0.0007	0.351	0.086	1.06	1.051	0.159		0.000013	0.0109	0.0109	0.0011	
A-PbAs-3-6	213.517	4.790	0.0006	0.368	0.083	1.12	1.104	0.154		0.000010	0.0115	0.0115	0.0011	
A-PbAs-3-7	289.267	4.890	0.0009	0.343	0.085	1.04	1.028	0.158		0.000015	0.0107	0.0107	0.0011	
A-PbAs-3-8	336.183	4.829	0.0008	0.344	0.086	1.04	1.031	0.160		0.000014	0.0107	0.0107	0.0012	
A-PbAs-3-9	384.850	4.934	0.0011	0.334	0.087	1.01	1.001	0.161		0.000020	0.0104	0.0104	0.0012	
A-PbAs-3-10	457.099	4.925	0.0013	0.335	0.087	1.01	1.003	0.161		0.000023	0.0104	0.0104	0.0012	
A-PbAs-3-11	529.182	4.873	0.0015	0.338	0.089	1.02	1.011	0.164		0.000027	0.0105	0.0105	0.0012	
A-PbAs-3-12	601.682	4.852	0.0019	0.337	0.090	1.02	1.010	0.166		0.000034	0.0105	0.0105	0.0012	
A-PbAs-3-13	673.932	4.827	0.0023	0.343	0.091	1.04	1.029	0.169		0.000041	0.0107	0.0107	0.0012	
A-PbAs-3-14	744.683	4.794	0.0026	0.355	0.093	1.07	1.062	0.172		0.000047	0.0111	0.0111	0.0012	
A-PbAs-3-15	838.517	4.768	0.0030	0.377	0.092	1.14	1.131	0.171		0.000054	0.0118	0.0118	0.0012	
A-PbAs-3-16	910.350	4.896	0.0031	0.396	0.093	1.20	1.187	0.172		0.000056	0.0124	0.0124	0.0012	
A-PbAs-3-17	1006.267	4.876	0.0033	0.415	0.095	1.25	1.242	0.177		0.000058	0.0129	0.0129	0.0013	
A-PbAs-3-18	1078.787	4.789	0.0035	0.416	0.097	1.26	1.247	0.180		0.000063	0.0130	0.0130	0.0013	
A-PbAs-3-19	1225.267	4.749	0.0039	0.414	0.097	1.25	1.242	0.180		0.000070	0.0129	0.0129	0.0013	
A-PbAs-3-20	1321.350	4.735	0.0041	0.417	0.097	1.26	1.250	0.180		0.000074	0.0130	0.0130	0.0013	
A-PbAs-3-21	1417.517	4.703	0.0042	0.416	0.098	1.26	1.247	0.183		0.000075	0.0130	0.0130	0.0013	
A-PbAs-3-22	1514.017	4.689	0.0043	0.419	0.100	1.27	1.256	0.185		0.000077	0.0131	0.0131	0.0013	
A-PbAs-3-23	1610.100	4.647	0.0046	0.424	0.102	1.28	1.271	0.190		0.000082	0.0132	0.0132	0.0014	
A-PbAs-3-24	1706.267	4.591	0.0045	0.429	0.102	1.30	1.285	0.190		0.000081	0.0134	0.0134	0.0014	
A-PbAs-3-25	1896.850	4.543	0.0047	0.431	0.103	1.30	1.291	0.192		0.000085	0.0134	0.0134	0.0014	
A-PbAs-3-26	2205.350	4.615	0.0055	0.429	0.108	1.30	1.286	0.200		0.000098	0.0134	0.0134	0.0014	

C.3 Raw elemental data on the residual solids

Wet Chemical Analysis Data of the Residual Solids from the Acid/Alkali Dissolutions

Sample*	K tot (ppm)	Pb tot (ppm)	Fe tot (ppm)	S tot (ppm)	As tot (ppm)	ICP [SO_4^{2-}]	ICP [AsO_4^{3-}]	K tot (mmol/L)	Pb tot (mmol/L)	Fe tot (mmol/L)	ICP [SO_4^{2-}] (mmol/L)	ICP [AsO_4^{3-}] (mmol/L)
Acid K 1	6.059		34.329	14.866		44.538		0.1552		0.6147	0.4636	
Acid K 2	6.178		35.433	15.113		45.277		0.1582		0.6345	0.4713	
Acid K 3	6.155		34.993	15.014		44.981		0.1576		0.6266	0.4682	
Acid Pb 1		5.650	20.263	7.395		22.153			0.0273	0.3628	0.2306	
Acid Pb 2		5.651	20.789	7.619		22.827			0.0273	0.3723	0.2376	
Acid Pb 3		5.726	20.685	7.562		22.655			0.0276	0.3704	0.2358	
Acid PbAs 1		19.064	37.302	11.567	2.511	34.653	4.656		0.0920	0.6680	0.3607	0.0335
Acid PbAs 2		19.202	37.720	11.682	2.549	34.998	4.726		0.0927	0.6754	0.3643	0.0340
Acid PbAs 3		19.063	37.193	11.511	2.551	34.484	4.731		0.0920	0.6660	0.3590	0.0341
Alkali K 1	4.769		48.838	11.588		34.715		0.1221		0.8745	0.3614	
Alkali K 2	4.939		49.760	11.907		35.671		0.1265		0.8910	0.3713	
Alkali K 3	4.838		49.941	11.817		35.402		0.1239		0.8943	0.3685	
Alkali Pb 1		7.356	40.583	12.808		38.370			0.0355	0.7267	0.3994	
Alkali Pb 2		7.496	40.817	12.866		38.544			0.0362	0.7309	0.4012	
Alkali Pb 3		7.577	40.894	12.785		38.301			0.0366	0.7323	0.3987	
Alkali PbAs 1		17.478	38.807	11.088	4.117	33.217	7.633		0.0844	0.6949	0.3458	0.0549
Alkali PbAs 2		17.722	39.319	11.214	4.145	33.595	7.685		0.0855	0.7041	0.3497	0.0553
Alkali PbAs 3		17.698	39.199	11.147	4.163	33.394	7.719		0.0854	0.7019	0.3476	0.0556

* K: Potassium Jarosite; Pb: Plumbojarosite; PbAs: Beudantite; Numbers (1-3) correspond to replicate bottle numbers.

C.4 Aqueous speciation data from the acid and alkali dissolutions

All Aqueous species calculated were in concentrations of $> 10^{-8}$ mol L^{-1}.

C.4.1 Acid dissolutions

Potassium Jarosite

Aqueous species	log activities (Q/K)		
	Bottle 1	Bottle 2	Bottle 3
H^+	-2.0430	-2.0150	-2.0260
K^+	-3.6658	-3.7314	-3.7404
Fe^{3+}	-4.0208	-3.9573	-3.9589
$FeOH^{2+}$	-4.1679	-4.1324	-4.1231
$Fe(OH)_2^+$	-5.6051	-5.5976	-5.5772
$FeCl_2^+$	-5.9917	-5.9305	-5.9316
$FeSO_4^+$	-6.0394	-5.9251	-5.9254
$Fe_2(OH)_2^{4+}$	-6.9059	-6.8349	-6.8162
$FeCl^{2+}$	-6.8820	-6.8197	-6.8210
Cl^-	-2.0504	-2.0516	-2.0513
SO_4^{2-}	-3.9462	-3.8954	-3.9573
HSO_4^-	-4.0101	-3.9313	-3.9410
KSO_4^-	-6.7324	-6.7473	-6.7549
O_2 (aq)	-3.5973	-3.5973	-3.5973
HCl (aq)	-4.7634	-4.7366	-4.7473
CO_2 (aq)	-4.9689	-4.9689	-4.9689
KCl (aq)	-7.2109	-7.2776	-7.2863

Plumbojarosite

Aqueous species	log activities (Q/K)		
	Bottle 1	Bottle 2	Bottle 3
H^+	-2.0703	-2.0740	-2.0740
Fe^{3+}	-4.0996	-3.9298	-3.8715
$FeOH^{2+}$	-4.2167	-4.0460	-3.9876
Pb^{2+}	-5.2143	-5.0316	-4.9618
$Fe(OH)_2^+$	-5.6239	-5.4521	-5.3937
$PbCl^+$	-5.8705	-5.6892	-5.6201
$FeCl_2^+$	-6.1569	-5.9900	-5.9329
$FeSO_4^+$	-6.2624	-5.9130	-5.7929
$Fe_2(OH)_2^{4+}$	-7.0035	-6.6619	-6.5452
$FeCl^{2+}$	-7.0040	-6.8357	-6.7780
Cl^-	-2.0537	-2.0551	-2.0557
SO_4^{2-}	-4.0904	-3.9108	-3.8490
HSO_4^-	-4.1843	-4.0057	-3.9439
O_2 (aq)	-3.5973	-3.5973	-3.5973
HCl (aq)	-4.8367	-4.8391	-4.8397
CO_2 (aq)	-4.9689	-4.9689	-4.9689
$PbCl$ (aq)	-7.3990	-7.2191	-7.1506

Beudantite

Aqueous species	log activities (Q/K)		
	Bottle 1	Bottle 2	Bottle 3
H^+	-2.0960	-2.0980	-2.0980
Fe^{3+}	-4.6716	-4.6702	-4.6651
$FeOH^{2+}$	-4.7657	-4.7623	-4.7573
$Fe(OH)_2^+$	-6.1499	-6.1444	-6.1394
$FeCl_2^+$	-6.8232	-6.8217	-6.8167
Pb^{2+}	-7.4656	-7.6415	-7.6995
$Fe_2(OH)_2^{4+}$	-8.1015	-8.0946	-8.0845
$FeCl^{2+}$	-7.6232	-7.6218	-7.6167
$FeSO_4^+$	-7.9521	-7.9562	-7.9417
Cl^-	-2.0518	-2.0518	-2.0518
$H_2AsO_4^-$	-4.7959	-4.7923	-4.7820
SO_4^{2-}	-5.2081	-5.2136	-5.2042
HSO_4^-	-5.3250	-5.3325	-5.3231
$O_{2\ (aq)}$	-3.5973	-3.5973	-3.5973
$H_3AsO_{4\ (aq)}$	-4.6427	-4.6411	-4.6308
$HCl_{(aq)}$	-4.9068	-4.9088	-4.9088
$CO_{2\ (aq)}$	-4.9689	-4.9689	-4.9689

C.4.2 Alkali dissolutions

Potassium Jarosite

Aqueous species	log activities (Q/K)		
	Bottle 1	Bottle 2	Bottle 3
H^+	-3.2950	-3.2750	-3.2640
K^+	-3.7117	-3.6941	-3.6900
Ca^{2+}	-5.4726	-5.4737	-5.4742
$FeOH^{2+}$	-5.9208	-5.8836	-5.9131
$Fe(OH)_2^+$	-6.1058	-6.0886	-6.1291
Fe^{3+}	-7.0258	-6.9686	-6.9871
SO_4^{2-}	-3.5657	-3.5579	-3.5548
HSO_4^-	-4.8816	-4.8538	-4.8397
KSO_4^-	-6.3978	-6.3724	-6.3652
$O_{2\ (aq)}$	-3.5973	-3.5973	-3.5973
$CO_{2\ (aq)}$	-4.9689	-4.9689	-4.9689
$CaSO_{4\ (aq)}$	-6.9273	-6.9205	-6.9178

Plumbojarosite

Aqueous species	log activities (Q/K)		
	Bottle 1	Bottle 2	Bottle 3
H^+	-3.5380	-3.4610	-3.4400
Pb^{2+}	-5.2193	-5.2072	-5.1911
Ca^{2+}	-5.4434	-5.4451	-5.4460
$Fe(OH)_2^+$	-6.6933	-6.7557	-6.7130
$FeOH^{2+}$	-6.7513	-6.7367	-6.6730
Fe^{3+}	-	-8.0077	-7.9230
SO_4^{2-}	-3.9743	-3.9664	-3.9530
HSO_4^-	-5.5332	-5.4483	-5.4139
HCO_3^-	-7.7756	-7.8526	-7.8736
$O_{2\,(aq)}$	-3.5973	-3.5973	-3.5973
$CO_{2\,(aq)}$	-4.9689	-4.9689	-4.9689
$CaSO_{4\,(aq)}$	-7.3066	-7.3004	-7.2879

Beudantite

Aqueous species	log activities (Q/K)		
	Bottle 1	Bottle 2	Bottle 3
H^+	-4.7830	-4.5790	-4.6150
Ca^{2+}	-5.4132	-5.4134	-5.4132
$Fe(OH)_2^+$	-7.1024	-6.9405	-7.0494
Pb^{2+}	-7.1548	-7.6320	-7.6318
SO_4^{2-}	-4.8361	-4.8808	-4.8839
$H_2AsO_4^-$	-5.7684	-5.8374	-5.8503
HCO_3^-	-6.5306	-6.7346	-6.6986
HSO_4^-	-7.6400	-7.4807	-7.5198
$HAsO4^{2-}$	-7.7437	-	-7.9936
$O_{2\,(aq)}$	-3.5973	-3.5973	-3.5973
$CO_{2\,(aq)}$	-4.9689	-4.9689	-4.9689